MODULATION OF EAST ASIAN PRESSURE SURGES

by

GILBERT PENNOYER COMPO

B.S., Duke University, 1992

M.S., University of Colorado, 1994

A thesis submitted to the

Faculty of the Graduate School of the

University of Colorado in partial fulfillment

of the requirements for the degree of

Doctor of Philosophy

Program in Atmospheric and Oceanic Sciences

1997

This thesis entitled:

Modulation of East Asian Pressure Surges

written by Gilbert Pennoyer Compo

has been approved for the Program in Atmospheric

and Oceanic Sciences by

_____

Peter J. Webster

_____

Andrew Moore

Date _____

The final copy of this thesis has been examined by the signatories, and we find that both the content and the form meet acceptable presentation standards of scholarly work in the above mentioned discipline.

Compo, Gilbert Pennoyer (Ph. D., Astrophysical, Planetary, and
Atmospheric Sciences)

Modulation of East Asian Pressure Surges

Thesis directed by Professor Peter J. Webster

The variability of East Asian pressure surges is diagnosed using objective methods. The dominant timescales associated with pressure surges are found to be between 2 and 30 days (submonthly). East Asian pressure surges are characterized by southward propagating positive pressure anomalies and are in phase with low-level negative temperature and northerly wind anomalies. The propagation of pressure surges is interpreted as a topographic Rossby wave or shelf wave. The importance of intermediate timescale (6-30 day), rather than previously discussed synoptic timescale (2-6 day), upper-level wave activity to pressure surges is discussed.

An objective index for pressure surges is derived from an orthogonal rotated principal component analysis (ORPCA) of East Asian sea level pressure (SLP) anomalies. Several of the dominant modes of the ORPCA correspond to previously studied circulation anomalies in the summer and winter monsoons but are analyzed with few a priori assumptions. A new mode is found to describe East Asian pressure surges that effect the tropical circulation.

The seasonal cycle of surge frequency is quantified using wavelet analysis. Maximum surge activity is found in boreal spring, with a relative maximum in late fall and a distinct mid-winter minimum. The frequency distribution unifies the disparate findings of several studies that employed subjective analysis techniques. The seasonal modulation of surge activity correlates well with an observed modulation of intermediate timescale upper-level wave activity. The modulation is hypothesized to arise from seasonal variations in the strength of the upper-level circulation over

northern Asia.

A previously hypothesized relationship between pressure surges and the Madden-Julian Oscillation (MJO) is quantified and statistically tested using newly developed techniques for analyzing variance. An apparent interplay between intraseasonal (30-70 day) convective and circulation anomalies and a 40-day modulation of surge activity is found. Increased surge activity is strongly related to reduced intraseasonal convective activity in the equatorial western Pacific and precedes increased intraseasonal convective activity in the Indonesian region. A reduction in surge activity is related to enhanced intraseasonal convective activity in the equatorial western Pacific. The tropical-midlatitude interaction appears to occur through atmospheric circulation anomalies forced by tropical heating anomalies associated with the MJO.

ACKNOWLEDGMENTS

I would like to thank my great advisors Peter Webster and George Kiladis for their wise guidance and limitless patience as this work unfolded. I would like to thank them for allowing me to pursue directions that did not seem immediately viable and still may not. I would like to thank them for the freedom and encouragement to pursue the research on wavelet analysis and its application to the study of atmospheric modulation. I am grateful for the support and confidence they have displayed in me at all times.

I would like to thank my thesis committee members: Peter Webster, George Kiladis, Judy Curry, Andy Moore, and Klaus Weickmann for their time and commitment.

I would like to thank Peter Webster, Judy Curry, Maggie Tolbert, and Murry Salby for being inspirational teachers and scientists. Special thanks to Cecile Pénland and Prashant Sardeshmukh for thought-provoking questions that led to the development of the wavelet significance tests. Thanks to Paquita Zuidema, Dave Lawrence, Johannes Loschnigg, Jen Kolar, John Fasullo, Geoffrey Considine, and Matt Wheeler for helpful comments and discussions on this work. Thanks to Andrew Siegal for helpful discussions on wavelet analysis. Thanks to Hai-Ru Chang, Sanjay Dixit, and Bob Tomas for guidance and support. Thanks to Chris Boozer for providing moral support and a spot on the bench.

Thanks to Chris Torrence for wanting to investigate wavelet analysis further, writing many useful IDL routines, and introducing me to Brillig Works (now Prufrocks), which provided much of the caffeine used in this work.

Thanks to Klaus Weickmann, Jerry Meehl, Jeffery Weiss, Dave Gutzler, Adrian Matthews, and Leslie Hartten for sharing their expertise on many aspects of this work.

The support of the PAOS office staff of Bonnie Grebe, Kelly Duong, and Robert Lambeth was greatly appreciated.

This work would not have been undertaken without the encouragement of my parents Betty and Louis Compo. This work would not have been completed without the love of my wife Pam. I am eternally indebted to her for her unfailing support, encouragement, and unwavering belief in me.

This work was supported under the TOGA COARE project grant through the NOAA Office of Global Programs and the Division of Atmospheric Sciences of the National Science Foundation, ATM-9526030; and NOAA Office of Global Programs, DOC NA56GP0230. Computing was performed at the PAOS Computing Facility and the NOAA Climate Diagnostics Computer Facility using Fortran, IDL, and the ISML mathematical package. Data was obtained from the NOAA Climate Diagnostics Center archives (www.cdc.noaa.gov), the National Center for Atmospheric Research archives, and the United States Geological Survey. NCAR is supported by the National Science Foundation.

CONTENTS

FIGURES

FIGURE

TABLES

TABLE

CHAPTER 1

INTRODUCTION

While the longitudinal and latitudinal variations of the seasonal cycle of tropical circulation and convective regions are generally well understood in terms of the atmospheric response to variations in orography, sea surface temperature gradients, and land-sea temperature contrasts, the subseasonal variability of the tropical circulation and convective activity remains comparatively poorly understood. For instance, only recently has the importance of tropical-extratropical interaction in organizing tropical convective activity been recognized. One observed tropical-extratropical mechanism for organizing transient tropical convective activity is through midlatitude upper-level Rossby waves propagating into the deep tropics via Rossby wave dispersion through tropical upper-level mean westerlies (Webster and Holton 1982; Kiladis and Weickmann 1992; Tomas and Webster 1994; Kiladis and Weickmann 1997b). The upper-level troughs associated with the upper-level waves induce rising motion on their equatorward side that can lead to enhanced convective activity (Kiladis and Weickmann 1992; Kiladis and Weickmann 1997b).

Another tropical-extratropical mechanism for organizing tropical convective activity is the transient low-level East Asian **pressure surge** associated with fluctuations in the East Asian winter monsoon. Pressure surges are associated with periods of strong northerly winds, anomalously high pressure, and anomalously low temperatures that dominate the synoptic weather from Siberia to the South China Sea. The low-level wind, pressure, and temperature perturbations associated with

surges occur on timescales from 2 to 30 days (submonthly) (See Sec. B.3) and form a major contribution to the low-level poleward heat, momentum, and mass flux that occurs over East Asia during northern hemisphere winter (Boyle 1986).

Separate studies have shown that convective activity increases in the South China Sea region coincident with pressure surge episodes (Ramage 1971; Chang *et al.* 1979; Chang and Lau 1980; Chang and Lau 1982; Murakami 1980; Houze *et al.* 1981; Johnson and Priegnitz 1981; Lau 1982; Kiladis *et al.* 1994; Meehl *et al.* 1996). Some studies have also shown that the Australian monsoon becomes active following East Asian pressure surges (Murakami 1980; Webster 1981; Williams 1981; Love 1985a; Webster 1987). However, McBride (1987) found no obvious association between tropical cyclones, an important component of monsoon activity, and surge occurrence for the Winter MONEX year. In contrast, Love (1985b) presented a composite study and case analysis of East Asian surges that suggests surges do appear to have an effect on Southern Hemisphere tropical cyclogenesis north of Australia. In Sec. B.1, a review of the literature of East Asian pressure surges is given.

Conclusions about East Asian pressure surges depend on different datasets which extend over different time periods. In many of the composite studies performed, the use of different surge definitions leads to completely different statistics of surge episodes even within the same year (Boyle and Chen 1987). Several of the studies depend on data from Winter MONEX, which was a weak year for surge activity (Lau and Chang 1987), and, thus, may not accurately represent the surge relationship to tropical activity in general. In Appendix B, the relationship between surges and tropical convective activity is objectively quantified using long records and objective analysis techniques.

The difficulty in unifying previous conclusions made about pressure surges is illustrated by examining how the use of different definitions in the literature leads to a surprising diversity of surge episode dates and thus to the annual frequency of surges and their distribution as a function of the annual cycle. Joung and Hitchman (1982) used the 24-hour temperature drop and a strong surface pressure gradient over South Korea and found 16 cases over 10 years (1.6 per year) with 87.5% of the cases nearly uniformly distributed over December-February (29.2% each) and 12.5% in November. With 8-years of data and using a strength threshold of the meridional wind over Hong Kong, Lai (1989) found 128 cases over 7 years (18.3 per year) with a nearly symmetric distribution of episodes peaking in December at 23.4%, January had 19.5%, February and November tie with 16%, October had 11.7%, and March had 9.4%. Yet, Wu and Chan (1995), using 4 years of data and a temperature change and wind threshold definition, found an entirely different distribution of only 15 cases (3.75 per year), with January and November accounting equally for 10 of the 15 cases and December and October having 2 cases each, with one in February. Recently, Zhang *et al.* (1997) employed a multi-variate index of anticyclone strength and temperature tendency in several regions over China to find 189 cases over 17 years (11.1 per year), with 22% in November, 19% in December, nearly equal percentages in January and March (16.4% and 16.9%), decreasing to a relative minimum in February (12.7%), with October and April having some cases (8.5% and 4.8%).

While each study purports to be representative of surge episodes, the different frequency distributions based on different definitions cast doubt on the utility of arbitrarily defined indices for understanding the dynamics of pressure surges and their variability. The use of single grid point indices does not provide information on the large-scale amplitude of a pressure surge. Combining multiple location indices

introduces added subjectivity to the analysis. Possible phase differences between variables in an event must be accounted for in the multi-index with some flexibility in the definition which serves to increase the subjectivity entering the analysis. A study that is independent of definition is needed to find the basic relationships on the submonthly timescale between variables associated with East Asian pressure surges. A linear regression analysis is performed in Appendix B to determine these basic relationships. An objective index for surges can then be developed that accounts for the basic relationships identified. Then, the variability of pressure surges over the seasonal cycle can be quantified. In particular, changes in the amplitude of East Asian pressure anomalies over the course of the seasonal cycle can be measured by forming a time series of the temporal variations in the variance of pressure anomalies.

The analysis of Hsu and Wallace (1985) is suggestive of an objective method to derive an index of pressure surge activity over East Asia that would not suffer from the difficulties seen using subjective definitions. Hsu and Wallace (1985) performed an orthogonal rotated principal component analysis (ORPCA) on 5-day mean SLP anomalies during the northern hemisphere cool season over the northern hemisphere north of 20°N. Two modes that associated with pressure surges appear in their objective analysis. The modes have a significant relationship to 500 hPa height variations consistent with cold-air outbreaks. Composites of both positive and negative periods of the principal component time series indicate that an enhancement of the mean cold-air advection is associated with positive SLP anomalies and a weakening of mean cold-air advection is associated with negative SLP anomalies. The composites show propagation of SLP anomalies that was interpreted as orographically guided waves along the Tibetan Plateau. However, the principal component time series could not be directly related to episodes of surges because of the 5 day

averaging. The relationship of the modes to the tropical circulation was also not studied because of the 20°N limit of their dataset.

Using daily SLP anomalies over East Asia for the entire record of 1971–1996 NCEP Reanalysis, an ORPCA is performed in Chap. 3. Using the entire record instead of a seasonally stratified subset has the advantage of allowing the seasonality of the dominant modes to emerge directly from the data with few a priori assumptions. The principal component time series of one of the dominant modes is shown to be an objective index for episodes of East Asian pressure surges.

Wavelet analysis is then performed on the index in Chap. 4. Wavelet analysis (see Appendix C for a review of wavelet analysis) provides an unbiased method of examining the variations in variance of a time series compared to the biased method of the windowed Fourier transform (Kaiser 1994). (See Sec. C.3.1). The recently developed statistical tests of Torrence and Compo (1997) (see Appendix C) provide a quantitative means of measuring significant periods of variance over a frequency band compared to a noise model, such as white or red-noise. Changes in variance can be related directly to amplitude modulation of the original time series (Lau and Weng 1995).

In addition to a direct relationship between pressure surges and tropical convective activity at submonthly timescales, some researchers have shown a connection between strong pressure surges and the movement of convective activity between the eastern Indian and western Pacific Oceans associated with the 30-to-70 day timescale or the Madden-Julian Oscillation (see Madden and Julian (1994) for a complete review of the MJO) (Hsu *et al.* 1990; Weickmann and Khalsa 1990;

Meehl *et al.* 1996). Weickmann and Khalsa (1990) documented an MJO event during November/December, 1981, in which an intense pressure surge and cold air outbreak precedes the shift of intraseasonal convection from the eastern Indian Ocean to the western Pacific by 12 days. They concluded that a surge initiated convection in the region of 110°E and was important to the overall eastward movement of this MJO case. Hsu *et al.* (1990) documented a case of a pressure surge occurring in response to a subtropical wave-train in the western Pacific forced by MJO convection in the eastern Indian Ocean. The Indonesian convection activated by the pressure surge was thought to be enhanced by favorable upper level conditions that developed as part of the MJO. Meehl *et al.* (1996) used case and correlation comparison studies on the 6-to-30 and 30-to-70 day timescale to suggest that MJO-enhanced convective activity in the eastern equatorial Indian Ocean leads to favorable conditions for episodes of pressure surges over East Asia by enhancing the climatological upper level trough over Japan. The pressure surges lead to an enhancement of convective activity in the vicinity of Indonesia.

The case studies of Hsu *et al.* (1990) and Weickmann and Khalsa (1990) and the comparative study of Meehl *et al.* (1996) are highly suggestive of an interaction between the MJO and the East Asian pressure surges. However, a quantitative assessment to further evaluate the hypothesized interaction of the MJO and East Asian pressure surges has not been performed. Using the objective index for surge activity developed in Chap. 3 and the wavelet-derived time series of variance for the index from Chap. 4, the modulation of submonthly pressure surges on a 40-day timescale is demonstrated and related to variability in circulation and convective anomalies on the 30-70 day timescale.

In summary, the outline of the present study is as follows. A new method of

diagnosing modulation and assessing the statistical significance of modulation is introduced in Chap. 2. As an extension of the study of Hsu and Wallace (1985), an ORPCA of SLP over East Asia is performed in Chap. 3. From the ORPCA the principal component time series of a significant mode over East Asia, termed the South China Sea Mode, is found to be an objective index of East Asian pressure surges and significant anomalies termed "East Asian pressure lulls." The seasonality, timescales, and circulation and convective anomalies associated with several modes are investigated to verify that the ORPCA modes are physically meaningful. The degree of linearity present in the pressure perturbations over the East Asian winter monsoon region is also investigated. In Chap. 4, wavelet analysis is used to objectively determine the seasonality of the submonthly variance of East Asian pressure surges. The seasonal frequency distribution of pressure surges is found to relate directly to seasonal variations in the submonthly variance of the South China Sea mode. In Chap. 5, intraseasonal modulation of the East Asian pressure surges is examined and the relationship to the MJO is investigated.

CHAPTER 2

DATA AND METHOD

2.1 Data

Several datasets are employed in this study. The NCEP/NCAR Reanalysis (Kalnay *et al.* 1996) from 1971–1996 is used as a self-consistent description of the state of the atmospheric circulation. The Reanalysis uses the same data assimilation model throughout the entire period and so is free of spurious interannual variability arising from changes in the assimilation scheme. The Reanalysis is available at 4 times per day resolution on a 2.5° global grid. Fields of SLP, winds, and air temperature are used in this study.

A description of the known regional and temporal problems associated with the NCEP/NCAR Reanalysis is given in Appendix A. A brief analysis of the temporal correlations between variables that are important to this study: SLP, air temperature, and low-level wind and a few of the underlying observing platforms in the Pacific region is performed in Sec. A.3. Temporal correlations between Reanalysis SLP and East Asian and western Pacific surface stations are generally high, but a noticeable trend towards decreasing correlation with decreasing latitude is found. The near-surface eastern Pacific observing platforms and 0.995 sigma level Reanalysis have moderate-to-poor anomaly correlations. In contrast, over the same region, upper air temperatures are seen to correlate best with satellite-derived estimates compared to the correlations in the rest of the Tropical belt. Conclusions drawn from data in the trouble areas are buttressed by using independent data.

Two independent datasets are used as proxies for tropical convective activity. Outgoing Longwave Radiation (OLR) data from the NOAA satellites are used as one proxy for tropical convection (Liebmann and Smith 1996). The data are available from 1973-1996, with all data missing from 17 Mar 1978 through the remainder of 1978. Other gaps have been interpolated by Liebmann and Smith (1996). The OLR data are available at daily resolution on the same 2.5° global grid as the Reanalysis. A blend of Microwave Sounding Unit (MSU) and rain-gauge precipitation estimates (Magaña *et al.* 1997) is also used as a convective proxy independent of the OLR dataset. The precipitation data are available at daily resolution from 1979–1995 on a 1° grid globally from 60°N to 60°S. MSU radiances are assimilated into the Reanalysis, with heavy weighting over the oceans (Basist and Chelliah 1997), so the Reanalysis and the precipitation dataset cannot be considered entirely independent. The Reanalysis does not employ the MSU precipitation estimates directly, however, nor does it use the rain gauge data.

Anomaly time series are constructed by removing the first three harmonics (periods of 365.25, 182.625, and 121.75 days) of the climatological seasonal cycle using a least squares fit to the entire record of available for each dataset. The complete record of the anomaly data are temporally filtered into an intraseasonal (30–70 day) frequency band using a Lanczos digital filter (Duchon 1979) with 481 4-times-a-day weights or 121 daily weights. The high number of weights helps eliminate Gibb's ringing in the response of the filter.

2.2 Methods

2.2.1 Orthogonally Rotated Principal Component Analysis As discussed in the introduction, an objective index describing large-scale episodes of East Asian pressure surges is needed to investigate some of the conflicting findings of

previous studies of pressure surges that used subjectively determined indices. Principal component analysis (PCA) provides an objective method of separating the spatial and temporal variability of a dataset to determine its dominant modes. However, as reviewed by Richman (1986), PCA has several undesirable properties when the purpose of PCA is to be a physical interpretation of the modes. Many of these disadvantages of PCA are overcome by rotating the results of PCA, as discussed below. The more physically motivated rotated principal component analysis (RPCA), when rotation is successful and robust, serves as an excellent method of objectively classifying atmospheric modes of variation and their temporal variability and has been successfully employed in several other studies (Horel 1981; Hsu and Wallace 1985; Richman 1986; Barnston and Livezey 1987; Lau and Lau 1990).

To perform PCA, the anomaly data in the selected region are normalized by the standard deviation at each grid point. The cross-correlation between all grid points within the domain is then computed. The eigenvectors and eigenvalues of the cross-correlation matrix are computed. The loading vectors are formed by multiplying the eigenvectors by the square root of the respective eigenvalue. The principal component time series (PC) is formed by matrix multiplying the loading vector times the normalized data. The loading vectors or modes and the PCs are related such that the modes correspond exactly to the correlation coefficient between the PCs and the original anomaly data. The PCs are normalized, by construction, to unit variance. As PCA is a linear analysis, the sign of both the modes and the PCs is entirely arbitrary. The signs used in the modes presented are purely for convenience.

Rotation of the results of principal component analysis, a rotated principal component analysis (RPCA) has been successfully utilized in several studies in atmospheric sciences (Horel 1981; Hsu and Wallace 1985; Richman 1986;

Barnston and Livezey 1987; Lau and Lau 1990). Rotation (a linear transformation of the PCA) is performed to minimize the number modes needed to explain the variance at each grid point. Richman (1986) has provided a thorough review of the merits and pitfalls associated with RPCA. Summarized by Horel (1981) and reviewed by Richman (1986), the spatial and temporal orthogonality constraint of the unrotated PCA can lead to the undesirable effect that modes differ strongly as different subdomains, even overlapping ones, are employed in an analysis. The changing of solutions as the subdomain is varied makes physical interpretation of modes tenuous (Thurstone 1947). As demonstrated by Richman (1986) using Monte Carlo simulation, and borne out by several reports (Horel 1981; Hsu and Wallace 1985; Barnston and Livezey 1987), RPCA is highly stable to changes in the subdomain used in the analysis. A second highly desirable property of RPCA is that each PC is highly correlated with times series in only a few geographical regions and, simultaneously, each grid point time series is described by as few as possible PCs. These properties are sought after in the RPCA, and the various algorithms available use different methods to attempt to achieve these goals of ”simple structure” (Thurstone 1947).

Rotation can be performed so that the PCs remain temporally orthogonal while the spatial orthogonality constraint of the PCA modes is removed. Rotation with several different methods was employed and little difference was found. Under orthogonal rotated principal component analysis (ORPCA), the loading vector associated with the rotated principal component time series still corresponds to the correlation coefficient between the rotated principal component time series and the original anomaly data. As the varimax method of rotation (Harman 1967) has been most employed in the atmospheric sciences literature and little difference was found

by using other, more sophisticated rotation techniques, the varimax method is utilized here (see Richman (1986) for a complete review). For the remainder of the paper, the orthogonally rotated principal component time series are referred to as the PCs, while the loading vectors are referred to as the modes.

Several arbitrary choices are made in the ORPCA, including rotation method, number of unrotated modes retained, and the subdomain utilized. The modes shown in Fig. 3.1 are robust to these choices. The modes are calculated by rotating the first 18 components of the principal component analysis, using the 1% criterion of Guttman (1954). All of the unrotated modes that explain more than 1% of the original variance are retained for rotation. The modes described here are reproducible using at least the first 10 of unrotated components. As noted by Richman (1986), ORPCA is highly stable to the choice of subdomain. Various subdomains were tested, from the northern section of eastern hemisphere to a tropical belt symmetric about the equator. The modes shown here are readily discernible in all of the subdomains examined, even to the point of matching at boundaries. The subdomain employed was chosen to emphasize variability over East Asia. The modes were also reproduced by taking 10-year independent subsets of the data. The modes display strong-to-moderate pair-wise simple structure based on the visible categories of Richman (1986), providing confirmation of the value of performing the ORPCA. If at least moderate simple structure is not found, the unrotated modes should be used based on the Monte Carlo results of Richman (1986) for identifying dominant patterns present in dataset.

2.2.2 Composites based on Principal Components To describe the circulation and convective anomalies associated with the ORPCA modes, composites of the circulation and convective anomaly fields are constructed by taking the

mean of the fields on the ”key dates” at which the PC is at a relative maximum and exceeds 2.0 (twice the standard deviation, which is unity). Key dates must be at least 10 days separated. At least 40 key dates from the period of the precipitation data (1979–1995) are used to form a meaningful sample from which to take a mean. All data from the available record for each dataset are used. If less than 40 events are found, then the threshold criterion is lowered to 1.5. The largest and smallest value found in the sample at each grid point are eliminated from the composite so that outliers in the data do not unduly influence the composite. The local statistical significance of the composite is evaluated from the test of the significance of a sample mean at the 95% level (Spiegel 1975).

In the composite maps, wind vectors are plotted where the the zonal (u) or meridional (v) wind composite locally meets or exceeds the 95% confidence level, while maps of OLR and precipitation indicate only those composite values that locally meet or exceed the 95% confidence level. Contours of SLP and streamfunction are shown without regard to significance.

2.2.3 Wavelet-derived Variance Time Series A method for computing estimates and testing the significance of periods of high and low variance in the high-frequency fluctuations of a variable is discussed. Seasonal cycles of variance are derived. A new method for compositing periods of high and low variance and determining their significance compared to the seasonal cycle background is developed.

(1) **The wavelet power spectrum is computed.**

Wavelet analysis, as described in Sec. C.3, is performed on a time series by applying (C.3) on each variable at each grid point using a Morlet wavelet

(Fig. C.2a). The wavelet transform is applied to the complete record available at daily resolution. The wavelet power spectrum (Sec. C.3.4) is then calculated. For the missing period of the OLR data, zeroes are inserted and the spectra of periods from good data that lie within the cone-of-influence are removed (see Sec. C.3.7 for a discussion of the COI).

(2) **A variance time series is constructed.**

By averaging the wavelet spectrum over a range of scales, a time series of the local fluctuations in power or variance is formed, as discussed in Sec. C.5.2. The units of this variance time series are fractional variance. The average of the variance time series equals the fraction of the total variance in the selected band (see (C.14) and (C.24)). The significant fluctuations in the variance time series describe the modulation of the variance in the band by a longer time scale.

The use of wavelet-derived variance, in lieu of squared-bandpass filtered data (e.g., Nakamura 1992; Hendon and Liebmann 1994), permits small timescale fluctuations to be analyzed with a small window and large timescale fluctuation with a large window, both at the limit of the uncertainty principle (Kaiser 1994; Lau and Weng 1995). The width of the analyzing window in scale and time is maximized. In addition, in Sec. C.5.2, the variance time series is shown to be chi-squared distributed with the degrees of freedom given by (C.28). Therefore, the significance of each point in the variance time series can be assessed compared to some noise process (such as red noise) or some other background spectrum.

Averaging the wavelet power in scale forms an estimate of the instantaneous variance with as much temporal resolution retained as possible while

providing a single time series describing temporal fluctuations in power that can be analyzed with newly developed statistical significance tests (see Sec. C.5.2 for further details).

(3) **The annual cycle of the variations or modulation of the scale-averaged variance is calculated**

Examining the variance time series formed over the submonthly (2 to 30 day) shows significant modulation at the time scales of the annual cycle and its harmonics. A least-squares fit of the variance time series to the first four harmonics of the annual cycle is used to produce an annual cycle of the variance.

(4) **Significant periods of large variance are determined.** The variance time series is compared against the 95% significance level using a red-noise background spectrum and the chi-squared distribution as in (C.26). Key dates are selected based on when the variance time series is maximum and exceeds the 95% significance level. Dates must be separated by the distance of the COI to be considered significant.

(5) **Composites of anomaly data are constructed.**

Composites of anomaly or filtered data are computed based on the key dates and significance of the composite is tested at the local 95% level as in Sec. 2.2.2.

(6) **Composites of variance are constructed**

Wavelet-derived variance time points are averaged based on the key dates. The largest and smallest value of the variance time points are removed to eliminated the effect of outlying points.

To test the significance of the composite variance, a new test is developed to account for the seasonal modulation of the variance. The time points forming the members of the composite are chi-squared distributed and can be considered to be independent if they are separated by more than the COI decorrelation distance. The degrees of freedom (DOF) for the composite variance can be calculated directly (Spiegel 1975) by multiplying the number of composite time points by the averaged-in-scale DOF from (C.28). The 95% confidence interval on the composite variance can then be calculated from (C.20) with the DOF equal to the variance composite DOF.

The time points from the annual cycle of variance corresponding to the key dates are averaged, just as the variance time points themselves are averaged. The composite of the annual cycle forms the background variance that is compared to the confidence interval of the composite variance. If the background variance lies outside the confidence interval, then the composite variance is significantly reduced or enhanced compared to the background. Composite maps are plotted by subtracting the background from the composite variance to indicate the regions of reduced or enhanced variance and the level of the confidence interval that is exceeded by the composite value is indicated. Composite variance time series are also plotted, with the confidence interval and background variance indicated.

CHAPTER 3

DESCRIPTION OF ROTATED PRINCIPAL COMPONENTS

The results of an orthogonal rotated principal component analysis (ORPCA) of the sea level pressure (SLP) anomaly field over East Asia are presented. The purpose of the ORPCA is to provide an objective time series for determining the structure and seasonality of East Asian pressure surges.

The ORPCA derives several modes that appear interesting and are studied in some detail. The first two modes appear to be related to active and break periods in the summer and winter monsoons. Three other of the dominant modes have features associated with East Asian pressure surges. The spectra of the principal component time series are described and used to stratify the modes by season and timescale.

3.1 Loading Vectors

Figure 3.1 shows the first seven loading vectors of an ORPCA of the SLP anomaly field using the domain 60°N-10°S, 60°E-160°E. The loading vectors represent the correlation coefficient between the original SLP anomaly data and the principal component time series (PC). The percent of the variance explained by each PC is indicated. As ORPCA is a linear analysis, the sign of the modes is arbitrary, and the signs chosen are for convenience. It should be noted that the localized amount of variance explained by each PC is much higher than the total variance explained. The 0.5 correlation coefficient contour is thickened in each panel to illustrate the region where more than 25% of the total variance is explained by the relationship between the grid point SLP anomaly and the PC.

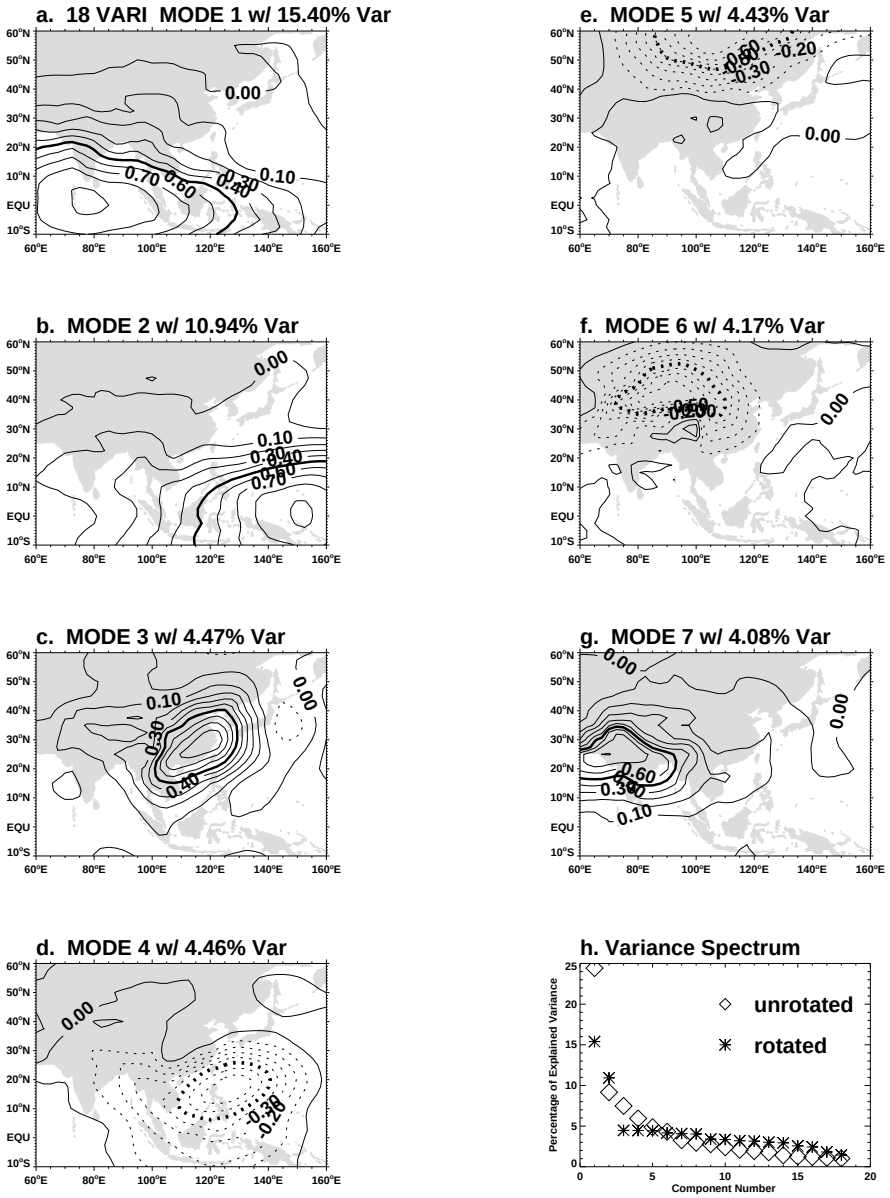

Figure 3.1. (a)-(g) Correlation coefficient (loading vector) between the ORPCA time series and the anomaly SLP indicated at interval 0.1. Positive (negative) correlation is solid (dashed). The ± 0.5 contour is thickened. The amount of variance explained by each PC is indicated. (h) Percent variance spectrum for the first 18 unrotated and rotated principal components derived from the normalized anomaly SLP field.

The majority of the modes in Fig. 3.1 have identifiable similarities to patterns found separately in other studies using PCA (Hsu and Wallace 1985; Lau and Lau 1990; Lau and Lau 1992; Dixit and Webster 1997). The modes shown in Fig. 3.1, unlike the previous work, are derived from a long record of high-resolution unfiltered data. In addition, the data have not been seasonally stratified prior to the analysis. The complete record from 1971-1996 has been used. We can therefore examine the seasonality of the PCs and the spectral characteristics of the PCs, having made only the a priori assumption of the choice of region.

A physical discussion of the modes appears below. The physical discussion is used to establish that the ORPCA modes correspond to physically realizable circulation and convective anomalies, some of much larger extent than the modes themselves. These physical structures have been examined in detail in previous studies and, thus, the circulations found here will only be briefly described in comparison to the relevant studies. Noting the similarities between the spatial pattern of the modes of Fig. 3.1 and the previous work will aid in the discussion. Modes 1 and 2 (Fig. 3.1a and b) are not readily identified from previous work and will be discussed further below. In contrast, Modes 3, 5, and 6 (Fig. 3.1c, e, and f) bear strong similarities to modes found by Hsu and Wallace (1985), which were identified with the East Asian pressure surges. Mode 3 (Fig. 3.1c) does not have a direct correspondence with any of the components of Hsu and Wallace (1985) because their grid only extended over the northern hemisphere southward to 20°N, but Mode 3 does resemble the time-lagged correlation with their ”Chinese Mode.” Following Hsu and Wallace (1985), we will refer to Mode 5 as the Siberian Mode and Mode 6 as the Chinese Mode. Mode 3 will be referred to as the South China Sea Mode. Mode 4 (Fig. 3.1d)

appears to be related to the synoptic-scale disturbances in the western Pacific examined by Lau and Lau (1990) and Lau and Lau (1992) and will be referred to as the western Pacific mode. As with Modes 1 and 2, Mode 7 (Fig. 3.1g) has no obvious connection to previously found modes.

3.2 Spectra of Modes

Before discussing the circulation anomalies associated with the ORPCA modes, the seasonality of the spectrum of the PC associated with each mode is described. Fig. 3.2 shows the global wavelet spectrum (GWS) for each PC. The GWS is computed from (C.21). Points within the COI have been excluded (see Sec. C.3.7 for a complete discussion of the COI). The red-noise spectrum is included as the thin solid line. The 95% confidence level is indicated as the thin dashed line. The DOF are calculated from (C.23). The development of the significance testing employed here is discussed in Sec. C.5.1.

Several regions of the component spectra are significant compared to red-noise spectra. For PC 1 (Fig. 3.2a), broad significant regions are seen between periods of 3 and 6 days and also between 32 and 45 days. The spectrum for PC 2 (Fig. 3.2b) also shows significant power between periods of 3 to 6 days and 16 to 32 days. The South China Sea Mode (Fig. 3.2c) has significant power from 3 to 15 days, somewhat similar to the spectra shown for SLP anomalies along 110°E in Fig. B.3. The western Pacific Mode (Fig. 3.2d) broadly departs above the 95% significance threshold from 3 days to 30 days. The Siberian Mode (Fig. 3.2e) has broad significant power from 3 to 16 days, while the Chinese Mode (Fig. 3.2f) has significant power only from 3 to 10 days. Finally, Mode 7 shows significant power over the range of 5 to 10 days and 32 to 50 days (Fig. 3.2g).

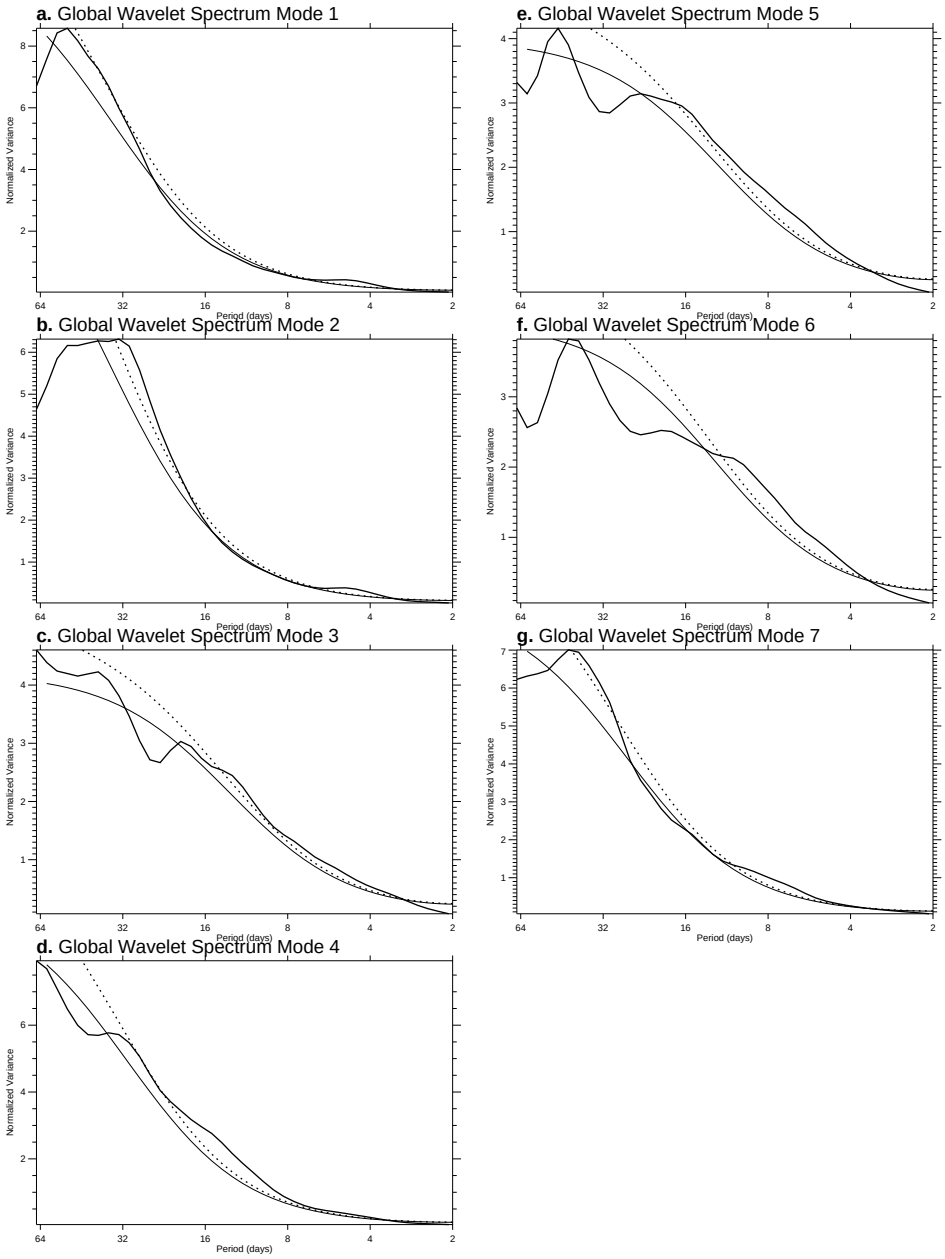

Figure 3.2. Global wavelet spectra for ORPCA mode principal component time-series 1-7 (a-g, respectively) shown by the thick solid line. The GWS are calculated from (C.21). Points within the cone-of-influence have been excluded. The lag-1 red-noise spectrum for each mode is indicated by thin solid line. The 95% confidence level is indicated by the thin dashed line, with the number of degrees of freedom calculated according to (C.23).

Fig. 3.3 shows the seasonally-averaged wavelet spectra for November-March and May-September. These spectra are calculated for each season according to (C.21) and averaged over all years to form 2 seasonally-averaged wavelet spectra for each PC. Note that the average of the two seasonal spectrum is not equal to the GWS because April and October have not been included. To test the significance of each spectrum, a red-noise model is again employed, where the amount of variance in each noise spectrum and the lag-1 autocorrelation is calculated separately for each season. The GWS for each PC from Fig. 3.2 is also reproduced to allow a comparison of the power between the seasons with that of the annual average. Figure 3.3 shows that significant seasonality exists in the dominant scales associated with several of the PCs. The seasonally-averaged wavelet spectra for PC 1 (Fig. 3.3a) show that the warm season is dominated by significant power exceeding the annual average in the 20-40 day range, while in the cool season significant power shifts to longer periods of 40-50 days. The spectra for PC 2 (Fig. 3.3b) contain a similar shift in power, though the 20-40 day power is significant at the 95% level during the warm season, more power at periods longer than 20 days is present in the cool season. The 3-to-6 day peak seen in Fig. 3.2 is a well defined 4.9-day significant feature for both PC 1 and 2 in Fig. 3.4. The 5-day peak has larger amplitude in the warm season than the cool season for both modes, though the difference is more pronounced for PC 1 (Fig. 3.4a).

The Siberian, Chinese, and South China Sea modes (Fig. 3.3c, e, and f) all reveal themselves as strongly cool-season modes. All three PCs associated with these modes have significant power between 2 and 16 days in both seasons but show a dramatic seasonal change in the amount of variance throughout the spectrum. The Chinese and South China Sea PCs (Fig. 3.3c and f) also show a produced peak at 40

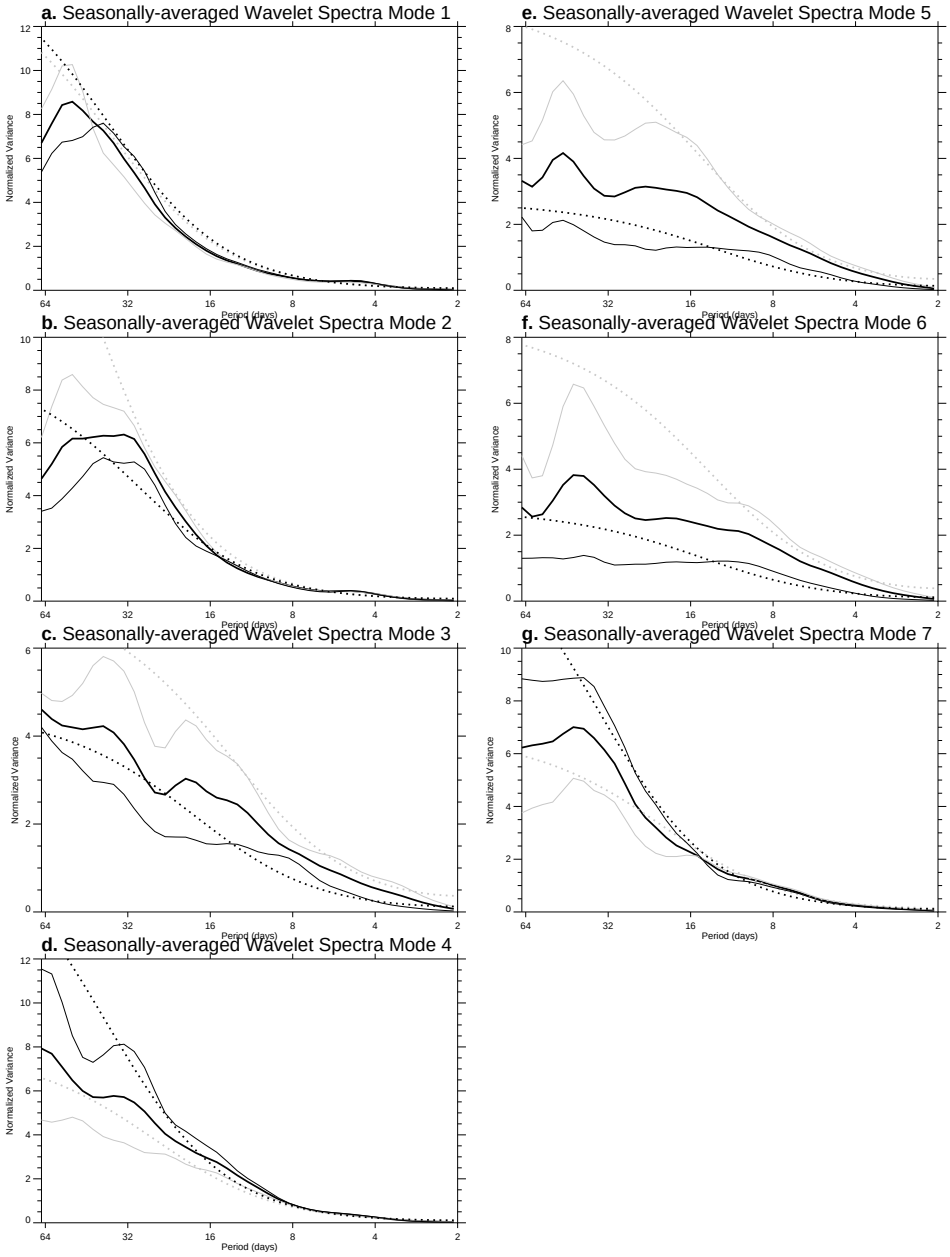

Figure 3.3. November-March (May-September) seasonally-averaged wavelet spectra for ORPCA mode principal component timeseries 1-7 (a-g, respectively) shown by the light (dark) solid line. The GWS for each mode from Fig. 3.2 is indicated by the thick black line. A 95% significance level is indicated by the light (dark) thin dashed line, with the number of degrees of freedom calculated according to (C.23).

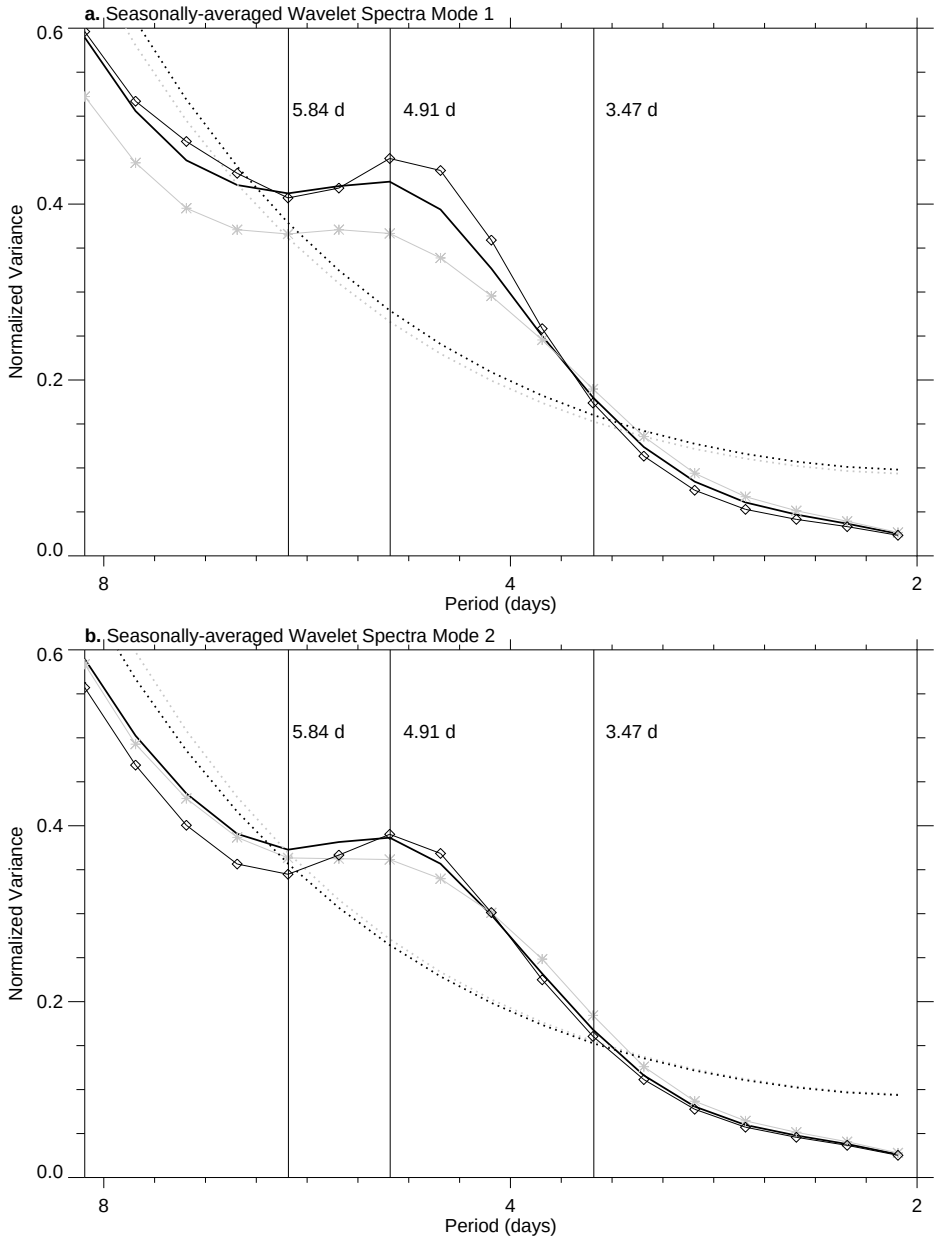

Figure 3.4. Seasonally averaged wavelet spectra for (a) PC 1 and (b) PC 2 as in Fig. 3.3 but only showing periods 2 to 8 days. The resolved wavelet scales are also indicated with diamonds for May-September and stars for November-March.

days, though not statistically significant.

The PCs associated with the western Pacific mode and Mode 7 (Fig. 3.3d and g) have their variance dominated by the warm season. In addition to the broad significant power seen in the GWS of the western Pacific PC (Fig. 3.2d), the warm season spectrum shows significant power between 20 and 32 days. PC 7 (Fig. 3.3f) shows a similar significant peak. Comparing the warm season spectra of Modes 1, 2, 4, and 7, all four show significant power roughly between 20 and 40 days.

3.3 Warm Season Composites

Spatial patterns of upper and lower tropospheric circulation, SLP, OLR, and precipitation anomalies associated with the ORPCA modes of Fig. 3.1 during the warm season are presented based on the composite analysis technique described in Sec. 2.2.2. PCs 2, 3, 5, and 6 did not have sufficient large positive maxima to meet the minimum criteria for a meaningful composite. The circulation and convective anomalies associated with PCs 1, 4, and 7 are described.

Figure 3.5a shows the composite lower tropospheric circulation, SLP, and precipitation anomalies associated with the warm season Day 0 key dates for PC 1. The PC 1 key dates are listed in Table 3.1. While the equatorial structure of Mode 1 has not been previously identified, the circulation and precipitation composite bears strong similarity to the ”break” period of the Indian summer monsoon observed and modeled in several studies (Sikka and Gadgil 1980; Webster and Chou 1980b; Webster and Chou 1980a; Srinivasan *et al.* 1993; Dixit and Webster 1997) and recently reviewed in Webster *et al.* (1997). Positive maxima in PC 1 correspond to negative precipitation anomalies over the whole of the eastern and central northern Indian Ocean while positive precipitation anomalies extend over the equatorial western Pacific Ocean. Large-scale easterly and westerly anomalies extend over the

equatorial eastern hemisphere, with westerly wind anomalies also over subtropical India associated with the negative precipitation anomaly there. Note the excellent agreement between the precipitation (Fig. 3.5a) and OLR (Fig. 3.5b) anomalies. The significant upper tropospheric circulation in Fig. 3.5b is more regionalized than the lower tropospheric circulation.

The active and break phases of the summer monsoon are associated with northward propagating positive and negative precipitation anomalies over the South Asian region that propagate with a timescale of 20-40 days (Webster *et al.* 1997). Figure 3.6 shows a hovmöller diagram of composite precipitation anomalies along 90°E for 30 days before the key date to 30 days after. Composite values that are locally significant at the 95% level are shaded. Positive precipitation anomalies displaying both northwards and southwards propagation are seen to precede the arrival of the northward propagating negative precipitation anomalies. A weak indication of a return of positive precipitation anomalies about 22 days after the first appearance can be seen around day +10. Note that the north-south orientation of the anomalies changes from Day -10 to Day +15, with like-signed anomalies from the equator to 15° being replaced by oppositely signed anomalies at Day +15.

The active and break phases of the summer monsoon have also been associated with eastward-moving anomalies on the 20-40 day timescale (Madden and Julian 1994). Figure 3.7 shows a composite hovmöller diagram of SLP anomalies along the equator for 30 days before the key date to 30 days after. The monsoon break associated with Mode 1 appears to be related to a global, somewhat eastward, shift of wavenumber 1 pressure anomalies. In addition to lower frequency changes in the equatorial SLP anomaly, several rapid westward-moving positive and negative anomalies from Day -5 to Day +7 can be seen. The longitudinal extent of the

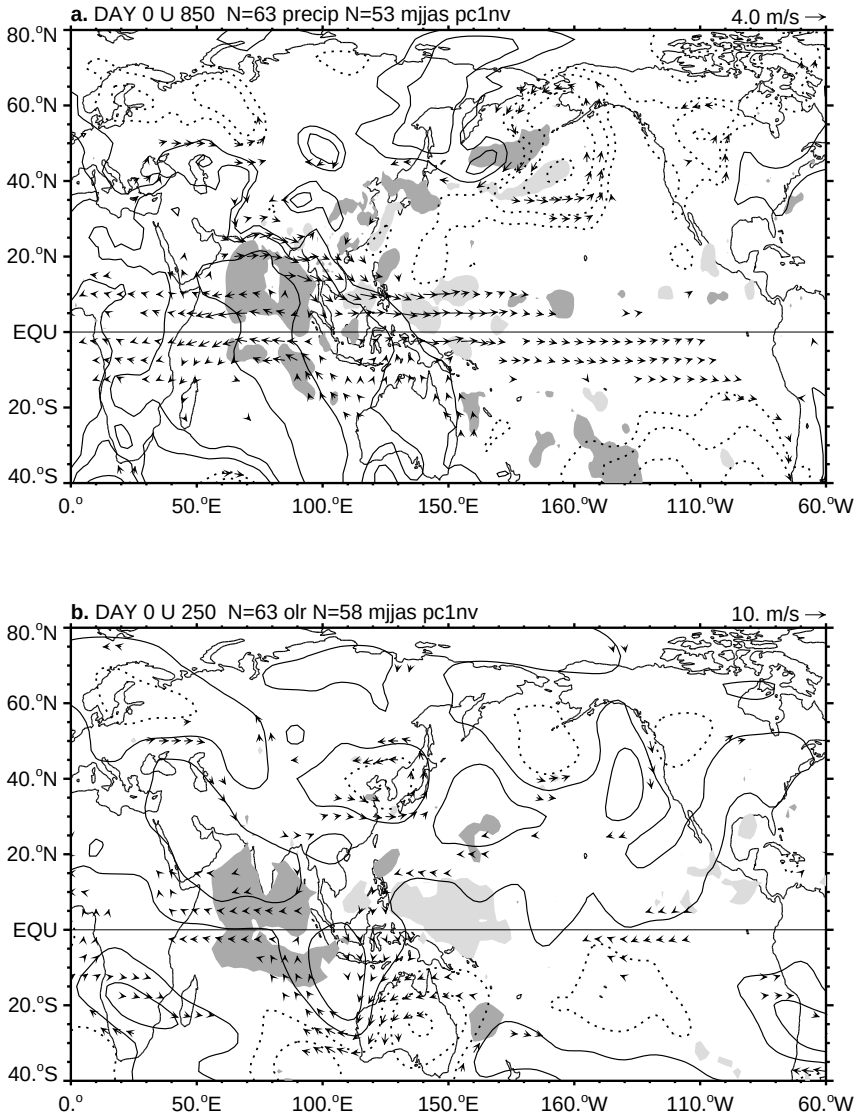

Figure 3.5. Composite of (a) 850 hPa wind, SLP, and precipitation anomalies and (b) 250 hPa wind, streamfunction, and OLR anomalies for May–September PC 1 exceeding 1.5. The number of episodes used in the composite of the NCEP Reanalysis variables (SLP and wind), OLR, and precipitation is indicated. Wind vectors are shown where either u or v is locally significant at the 95% level. Precipitation and OLR anomalies are only contoured where they are locally significant at the 95% level. Contour level is 1.5mm for precipitation and 8.0W m^2 for OLR. Positive (negative) anomalies of OLR (precip) are shaded dark. Negative (positive) anomalies of OLR (precip) are shaded light. The SLP contour interval is 1.0 hPa, and the 0.5 hPa contour also included. The streamfunction contour interval is 2.0×10^6 m^2 s^{-2}.

Table 3.1: Date of Maximum PC 1 equal to or exceeding 1.5 for May–September.

Sep	11	1971	Jul	5	1982	Jul	5	1991
May	20	1972	Jul	25	1982	Sep	6	1991
Jun	4	1974	May	9	1983	Jul	6	1992
May	14	1976	Jul	1	1983	Aug	9	1992
Jun	8	1976	Jun	19	1984	Sep	16	1992
Jul	18	1976	Sep	16	1984	Jun	18	1993
Sep	11	1976	Jun	10	1985	Jul	22	1993
Sep	20	1977	Jul	1	1985	Aug	7	1993
May	28	1978	Jul	28	1985	Aug	19	1993
Sep	13	1978	May	15	1986	Sep	12	1993
May	21	1979	Jul	8	1986	May	9	1994
Jun	30	1979	Jul	31	1986	Jul	10	1994
Aug	17	1979	Aug	24	1986	Aug	27	1994
Sep	10	1979	Sep	18	1986	Sep	18	1994
Jun	24	1980	May	9	1987	Sep	22	1995
Jul	18	1980	Jun	17	1987			
Aug	6	1980	Jul	6	1987			
Aug	27	1980	Aug	4	1987			
Sep	26	1980	Jun	13	1988			
Jun	6	1981	Jun	19	1989			
Jun	29	1981	Jul	31	1989			
May	4	1982	Sep	30	1989			
Jun	22	1982	Jun	12	1990			
Jul	5	1982	Jul	15	1990			

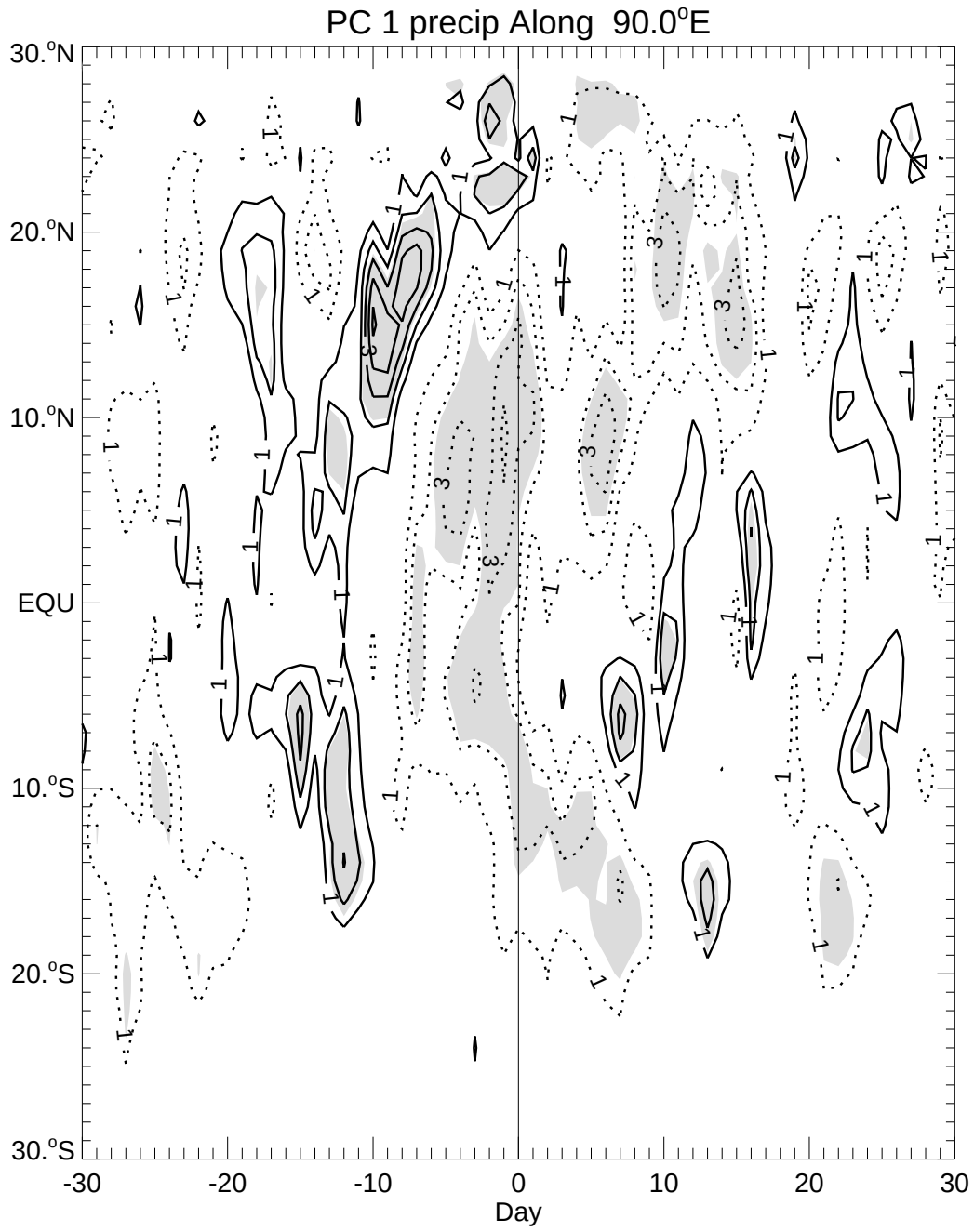

Figure 3.6. Latitude-time composite of precipitation anomalies for May–September PC 1 exceeding 1.5. Shading indicates where precipitation anomalies are locally significant at the 95% level. Dashed (solid) lines indicated negative (positive) anomalies. Contour interval is 1.0mm. The zero contour has been suppressed

anomalies indicates that, like the lower-frequency perturbation, they too are zonal wavenumber 1. Calculations of the westward propagation indicate about 72° of longitude per day. These anomalies appear to have a timescale of about 5 days, consistent with the 5-day spectral peak seen in Figs. 3.4a and b.

The rapid westward moving 5-day pressure perturbations seen in Fig. 3.7 appear to be related to a global 5-day pressure wave discussed by Madden and Julian (1972a). Using cross-spectra of 5-10 years of station pressure records and composites of spatially and temporally filtered SLP data, Madden and Julian reported a global, 5-day pressure wave with maximum amplitude in the mid-latitudes. The cross-spectral results of Madden and Julian (1972a) indicated the largest significant coherence between the stations at a period of 4.9 days, the period at which Fig. 3.4a and b indicate a significant spectral peak in the PCs of Modes 1 and 2. To further investigate if the 5-day, global wave seen in the composite of Fig. 3.7 and the spectra of Fig. 3.4a and b has a similar time-evolution and structure to that found by Madden and Julian (1972a), a time-latitude diagram along 10°W is presented in Fig. 3.8. To better isolate the 5-day wave feature, 10°W is presented as a representative latitude not strongly influence by the strong, slower evolving positive pressure anomaly seen over the Indian Ocean in Fig. 3.7. Figure 3.8 shows that significant subtropical and mid-latitude pressure perturbations are observed. The magnitude of the extratropical perturbations is larger than those at the equator. Madden and Julian (1972a) identified the 5-day pressure wave with one of the solutions of Laplace's tidal equations on a sphere, that of the zonal wavenumber 1, meridional wave number 2.

Figure 3.9 shows the composite circulation and convective anomalies associated with large positive maxima in PC 4, the western Pacific mode. The key dates for PC 4 are given in Table 3.2. The circulation shows a low-level cyclonic anomaly

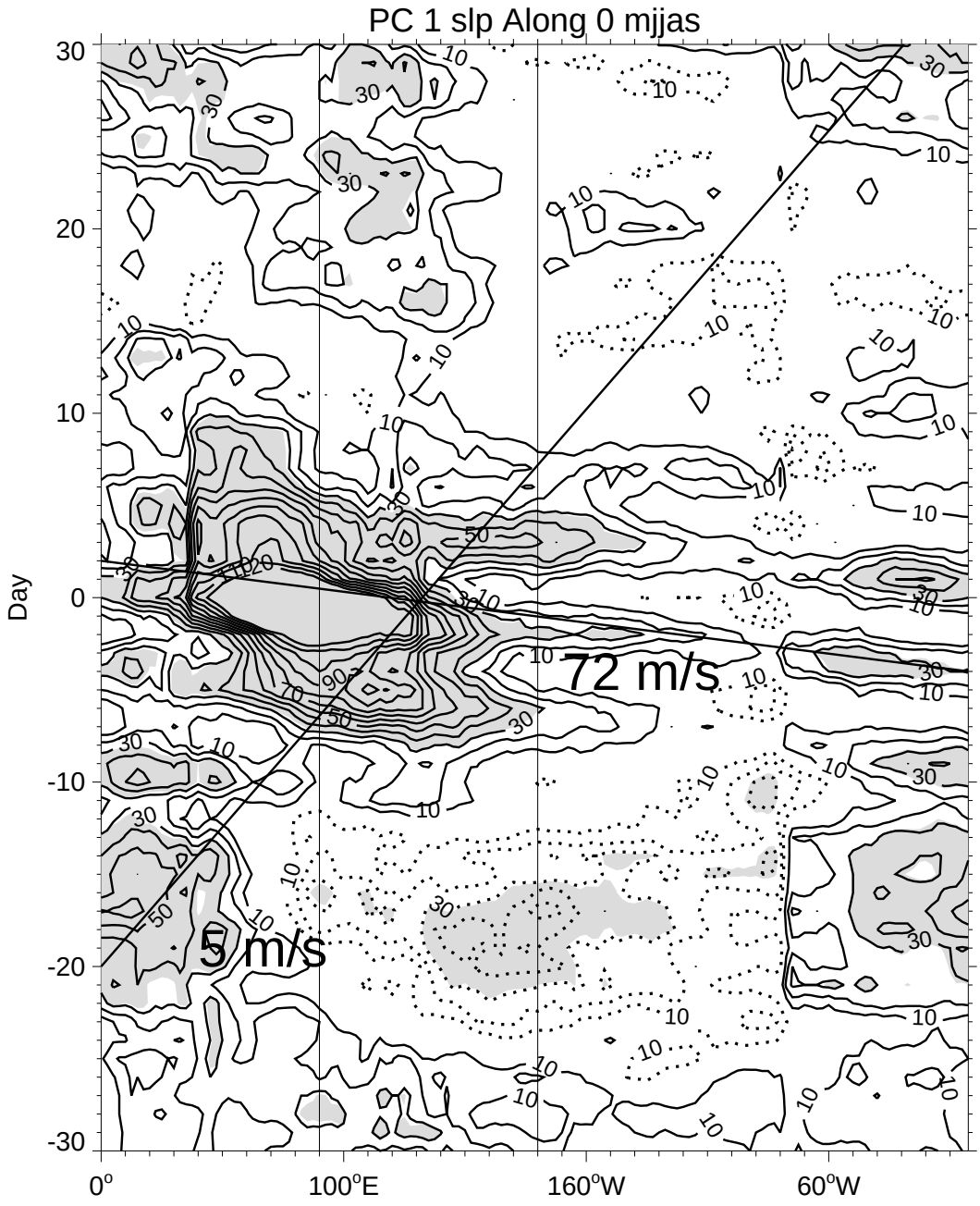

Figure 3.7. Longitude-time composite of SLP anomalies for May–September PC 1 exceeding 1.5 along the equator. Shading indicates where SLP anomalies are locally significant at the 95% level. Dashed (solid) lines indicated negative (positive) anomalies. Contour interval is 10hPa. The zero contour has been suppressed. The phase lines indicate speeds of 5 m s^{-1} eastward and 72 m s^{-1} westward.

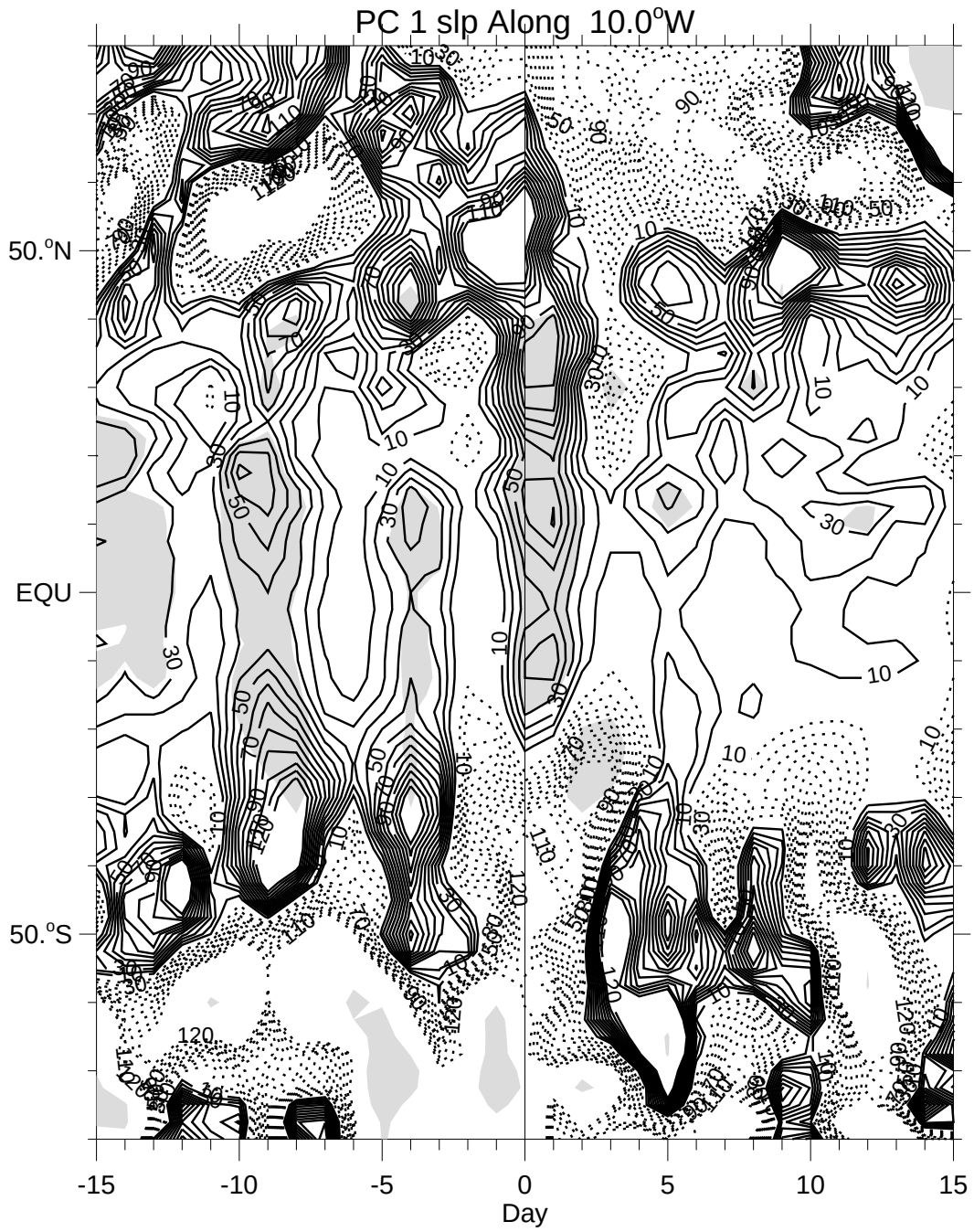

Figure 3.8. Latitude-time composite along 10°W of SLP anomalies for May–September PC 1 exceeding 1.5 along the equator. Shading indicates where SLP anomalies are locally significant at the 95% level. Dashed (solid) lines indicated negative (positive) anomalies. Contour interval is 10hPa. The zero contour has been suppressed

with positive precipitation anomalies in the westerly flow. Significant negative precipitation anomalies are found over India, southern China, and eastern Indonesia. The circulation and convective anomalies, combined with the significant spectral power at less than 20 days (Fig. 3.3d), suggests that the western Pacific mode reflects previously documented westward-moving features along 20°N. The timescale seen here is similar to the timescale of 10-20 days previously identified as another type of active/break period of the monsoon (Krishnamurti and Ardanuy 1980; Dixit and Webster 1997). Time-lagged composites show significant northwestward movement of the anomalies, similar to the more synoptic (3-8 day) disturbances discussed by Lau and Lau (1990) and Lau and Lau (1992). The composite suggests that unlike the 20-40 day timescale break period, the 10-20 timescale has like-signed positive convective anomalies in a broad region flanking the negative anomalies. Recently, Kiladis and Weickmann (1997a) found a similar circulation pattern as the significant linear association with active convection in the South China Sea. They found these circulations to be ubiquitous in the summer hemisphere of the Australasian monsoon region and western Pacific. However, none of these studies has reported on the suppression of convective activity around the active region. Recently, Dixit and Webster (1997) have also found a similar circulation and convective anomaly pattern using PCA of 7-20 day bandpass filtered OLR and winds. The significant presence of these strong circulation and convective anomalies even in unfiltered fields demonstrates the robustness and reproducibility of the disturbances affecting the South Asia monsoon region.

The circulation and convective anomalies associated with Mode 7 (Fig. 3.10) are similar to the oppositely signed subtropical and equatorial precipitation and wind anomalies typically associated with a break

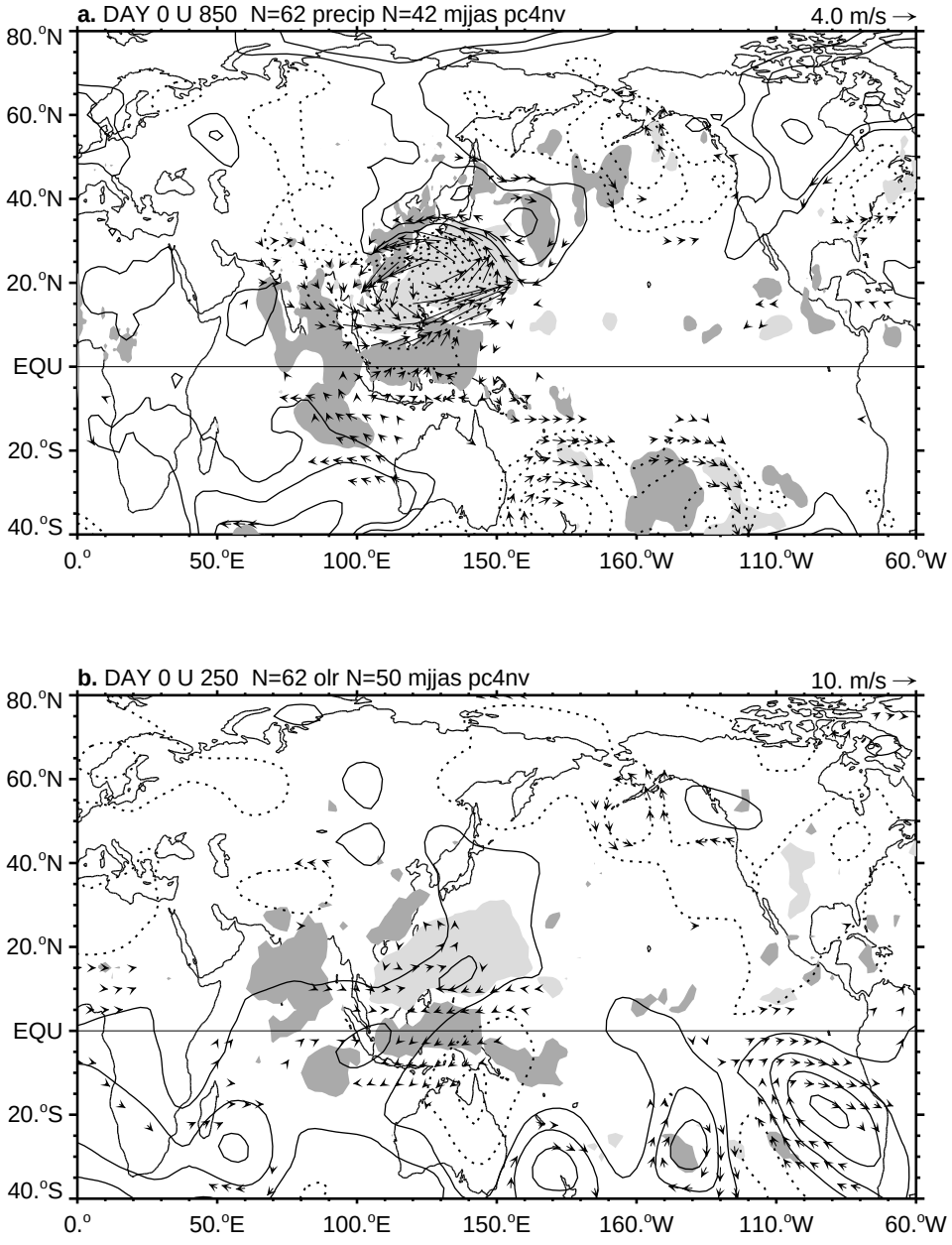

Figure 3.9: As in Fig. 3.5 but for May–September PC 4 exceeding 2.0.

Table 3.2: Date of Maximum PC 4 equal to or exceeding 1.5 for May–September.

Jul	23	1971	May	19	1980	Jun	22	1989
Jul	13	1972	Sep	9	1980	Jul	29	1989
Jul	31	1972	Jun	13	1981	Sep	9	1989
Jul	15	1973	Aug	2	1981	Jun	21	1990
Aug	22	1973	Aug	16	1981	Aug	17	1990
Jun	10	1974	Jun	25	1982	Sep	16	1990
Jul	3	1974	Jul	29	1982	Aug	18	1991
Aug	17	1974	Aug	24	1982	Sep	16	1991
Aug	2	1975	Sep	6	1982	Jun	26	1992
Aug	14	1975	Sep	21	1982	Aug	29	1992
May	23	1976	Aug	12	1983	Aug	7	1993
Jun	30	1976	Jun	20	1984	May	15	1994
Jul	22	1976	Aug	18	1984	Jul	10	1994
Aug	8	1976	Jun	18	1985	Jul	29	1994
Aug	16	1977	May	26	1986	Sep	26	1994
Sep	16	1977	Jul	9	1986	May	21	1995
May	25	1978	Aug	2	1986	Sep	15	1995
Jul	28	1978	Aug	25	1986			
Aug	13	1978	Sep	16	1986			
Aug	25	1978	Jun	14	1987			
Jul	5	1979	Jul	12	1987			
Aug	1	1979	Sep	9	1987			
Aug	13	1979	Jun	2	1988			

phase of the south Asian monsoon (Krishnamurti and Surgi 1987; Webster *et al.* 1997). The key dates for PC 7 are shown in Table 3.3. Easterly anomalies over all of South Asia are associated with negative precipitation anomalies, while a small positive precipitation anomaly along the equatorial eastern Indian Ocean lies to the north of westerly anomalies. The figure is precisely the opposite sign from the active minus break composites discussed in Webster *et al.* (1997), suggesting that a strong measure of linearity between certain stages of the active/break periods is present. In latitude-time cross-sections, northward and southward propagating positive and negative precipitation anomalies are observed, similar to Fig. 3.6, furthering the association of Mode 7 with the active/break periods of the summer monsoon.

3.4 Warm Season Cross–correlations between Modes

Figure 3.11 shows the significant lag cross-correlations between the first seven ORPCA PCs using data from May to September. By construction, the ORPCA PCs are temporally orthogonal for simultaneous correlations using the entire record. Correlations that are seasonally stratified , however, can have non-zero correlation at zero lag. Employing the significance tests of Livezey and Chen (1983), whereby the lagged autocorrelations of the two cross-correlated time series are used to determine the number of DOF present in the cross-correlation, correlation coefficients between 0.08-0.14 are found to be statistically significant at the 99.95% level. To be conservative, those PCs that have at least 3% of their variance described by the cross-correlation ($r > \|0.172\|$, but no $r < \|0.20\|$ is found) are shown.

PCs 1, 2, 4 and 7 (Fig. 3.11a-e) have significant lagged cross-correlations during the warm season. Figure 3.11a shows that PCs 1 and 2 have significant positive and negative correlation over the course of 35-40 days. The jump and drop in

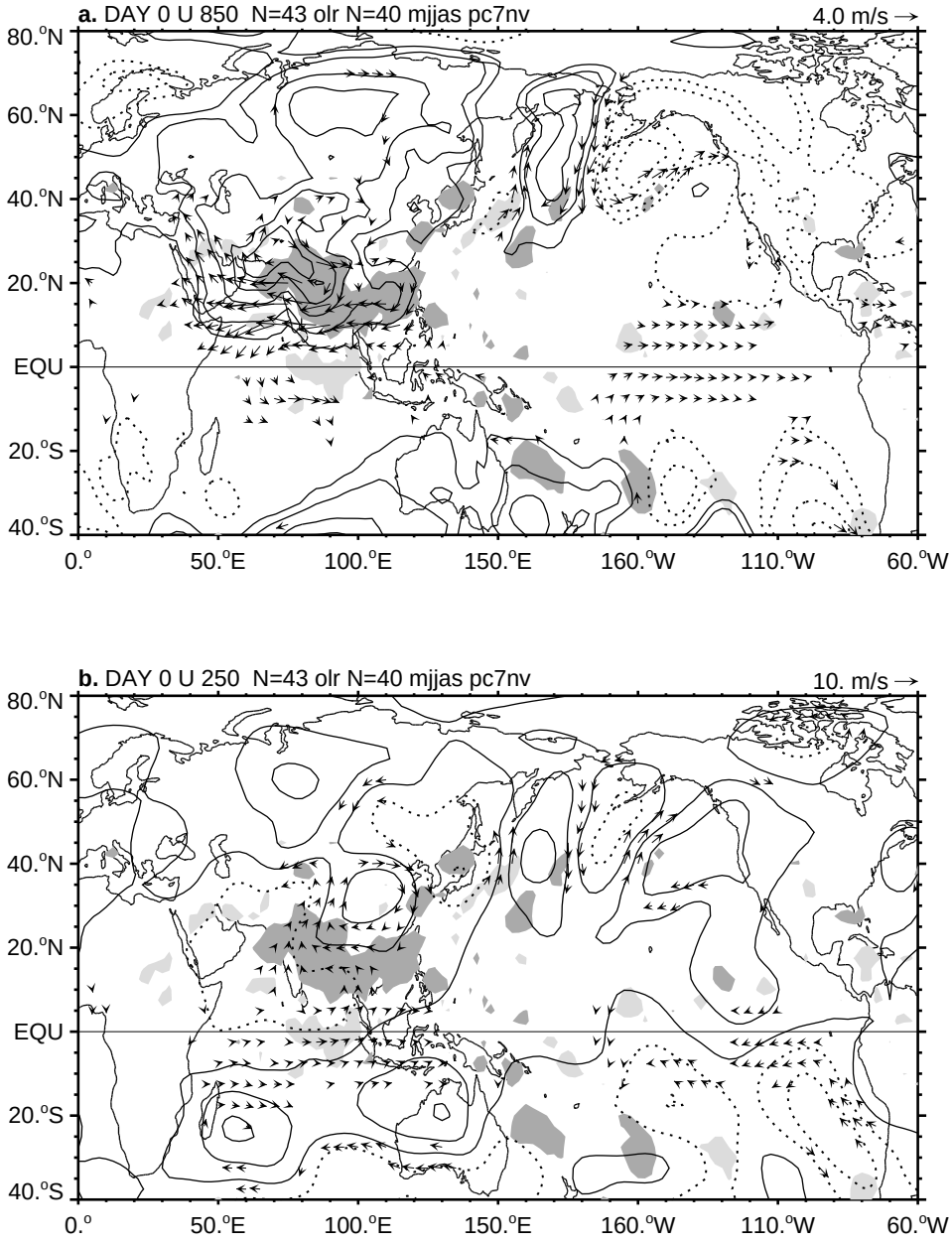

Figure 3.10: As in Fig. 3.5 but for May–September PC 7 exceeding 1.5.

Table 3.3: Date of Maximum PC 7 equal to or exceeding 1.5 for May–September.

Jun	1	1973	May	31	1987
Jun	28	1974	Jun	23	1987
Jul	24	1975	Aug	6	1987
Jun	21	1976	Jul	10	1988
Jul	12	1977	May	8	1989
Aug	10	1977	Jun	2	1989
Jul	16	1978	Jul	9	1989
May	30	1979	May	12	1991
Jul	25	1979	May	30	1991
Aug	29	1979	Jun	22	1991
Sep	15	1979	May	6	1992
May	1	1981	Jun	5	1992
Sep	14	1981	Jul	6	1992
May	17	1982	Aug	5	1992
Jun	14	1983	Sep	20	1992
Jul	7	1983	Jul	20	1993
Jul	10	1984	Aug	7	1993
Sep	21	1984	May	15	1994
Jul	23	1985	Sep	24	1994
Jun	1	1986	May	26	1995
Jul	2	1986	Aug	11	1995
Jul	31	1986			
Sep	2	1986			
May	14	1987			

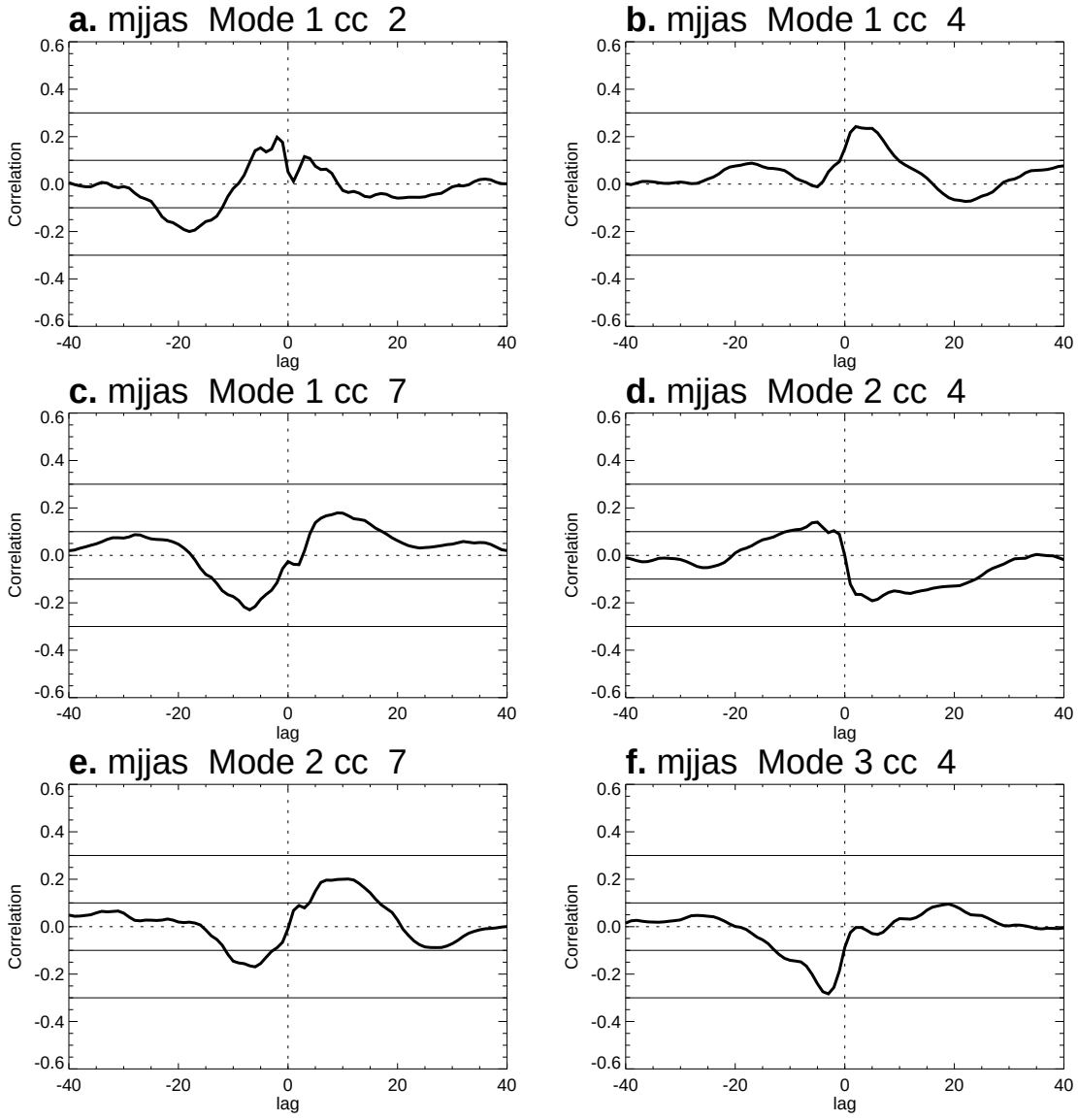

Figure 3.11. Lagged cross-correlation coefficient for May–September between (a) Mode 1 and 2, (b) Mode 1 and 4, (c) Mode 1 and 7, (d) Mode 2 and 4, (e) Mode 2 and 7, and (f) Mode 3 and 4. The time convention is such that the positive lag indicates that the first mode leads the second. The thin solid lines denote correlation coefficients of 0.1 and 0.3. Using the statistical significance tests of Livezey and Chen (1983), as discussed in Sec. 3.4 a correlation coefficient of at most 0.14 is significant at the 99.95% level.

the correlation around zero-lag reflects the 5-day spectral peak noted in Fig. 3.4. The 5-day time scale is associated with global-scale westward moving pressure perturbations observed in Fig. 3.7. Modes 1 and 2, combined, represent the equatorial SLP perturbations associated with the monsoon active/break periods observed in many studies (e.g., Webster *et al.* 1997). The equatorial signature of the summer monsoon active/break periods has been previously associated with the summer realization of the MJO (e.g., Madden and Julian 1994). However, the results here indicate that the active/break periods of the summer monsoon have a shorter period than that of the winter (Fig. 3.3a and b), in contrast to previous results (Madden and Julian 1994). The summer active/break periods also do not show a clear 4-5 m s^{-1} eastward progression associated with the MJO during the northern hemisphere winter (Figs. 3.11a and 3.7) (Salby and Hendon 1994; Madden and Julian 1994). Whether the summer 20-40 day timescale active/break fluctuations should be considered as having similar enough characteristics to that of the winter 40-50 day MJO should be researched further.

Figure 3.11c and e provide further support for the Indian Ocean equatorial-subtropical relationship between summer monsoon active/break periods discussed above. The time-lagged relationship implies that a negative SLP anomaly over India is at a minimum seven days before the maximum SLP anomalies in the equatorial regions of PCs 1 and 2. As indicated by the composite for Mode 7 (Fig. 3.10), a negative SLP anomaly is associated with westerly anomalies and deep convection over India, an active period of the monsoon. The time-lagged cross-correlation implies a somewhat oscillatory relationship between PCs 1, 2, and 7 with a period of between 35-40 days. The warm season spectra of all three modes show a significant peak in this timescale (Fig. 3.3). The relationship between PCs 1, 2, and 7 is consistent with

the hypothesis that equatorial anomalies lead same-signed subtropical anomalies, as part of a northward movement of active and break periods (Webster *et al.* 1997). The relationship between Modes 2 and 4 (Fig. 3.11d) is also consistent with this hypothesis. However, the relationship between PCs 1 and 4 (Fig. 3.11b) stands in marked contrast, as a positive correlation between PCs 1 and 4 implies that positive anomalies in the equatorial Indian Ocean are followed by negative anomalies in the western subtropical Pacific. The negative correlation at positive lags between PCs 2 and 4 (Fig. 3.11d) implies that positive anomalies in the equatorial western Pacific are followed by positive anomalies in the subtropical western Pacific. As PCs 1 and 2 have nearly simultaneous positive correlation, the conflicting lagged-correlations with PC 4 demonstrate the variety of the anomaly circulations in this region.

While the variance of PC 3 is dominated by the cool season, the significant negative lag correlation between PCs 3 and 4 (Fig. 3.11f), with PC 4 leading PC 3 demonstrates the northwestward propagation of the synoptic-timescale anomalies associated with Mode 4. The lag correlation has a broad significant correlation from -10 days to simultaneous, with a minimum at a 2-day lag. The 2-10 day correlation for northward moving anomalies from the subtropical western Pacific to the South China Sea and coastal China broadly agrees with the 3-8 day timescale for similar anomalies described by Lau and Lau (1990) and Lau and Lau (1992).

3.5 Cool Season Composites

Figure 3.12 shows the composite SLP, circulation, and precipitation anomalies associated with the cool season Day 0 key dates for PC 1. The PC 1 key dates are listed in Table 3.4. The upper and lower tropospheric circulation and convective anomalies are readily identified with previous studies of the characteristic circulation of the MJO (Madden and Julian 1972b; Kiladis and Weickmann 1992;

Kiladis *et al.* 1994; Salby and Hendon 1994; Meehl *et al.* 1996). In the lower troposphere, equatorial westerly anomalies are associated with positive precipitation anomalies. Negative precipitation anomalies are associated with locally weak winds and easterly anomalies further east. Strong mid-latitude anomalies are present in the upper-troposphere, with upper-level westerly anomalies in the Asian exit region. Significant positive precipitation anomalies extend from the East China Sea to the central North Pacific.

The composite of PC 2 (Figure 3.13) appears to correspond to the break phase of the Australia monsoon or the suppressed phase of the MJO. Key dates for PC 2 are listed in Table 3.5. The extensive regions of liked-signed precipitation and OLR anomalies, coincident with the significant wind anomalies, suggest the dominant nature of the MJO during the northern hemisphere cool season. A large-scale significant upper-tropospheric circulation is associated with positive maxima of PC 2. In particular, two subtropical gyres are evident.

Several differences are observed between the warm season (Fig. 3.5) and cool season (Fig. 3.12) composites of PC 1. Over South Asia, the cool season composite has no significant lower- tropospheric wind or precipitation anomalies. For both seasons, the significant upper tropospheric circulation is in the winter hemisphere. The cool season propagation characteristics of PC 1, shown in Fig. 3.14, are quite different from those of the warm season (Fig. 3.7). The 5-day pressure wave is much less discernible in the cool season composite, while an overall large-scale eastward propagation at about 5 m s^{-1} of a 40-50 day pressure anomaly is more evident.

The composite of PC 3 (Fig. 3.15) is directly comparable to the anomaly circulation associated with the structure of an East Asian pressure surge seen at Day

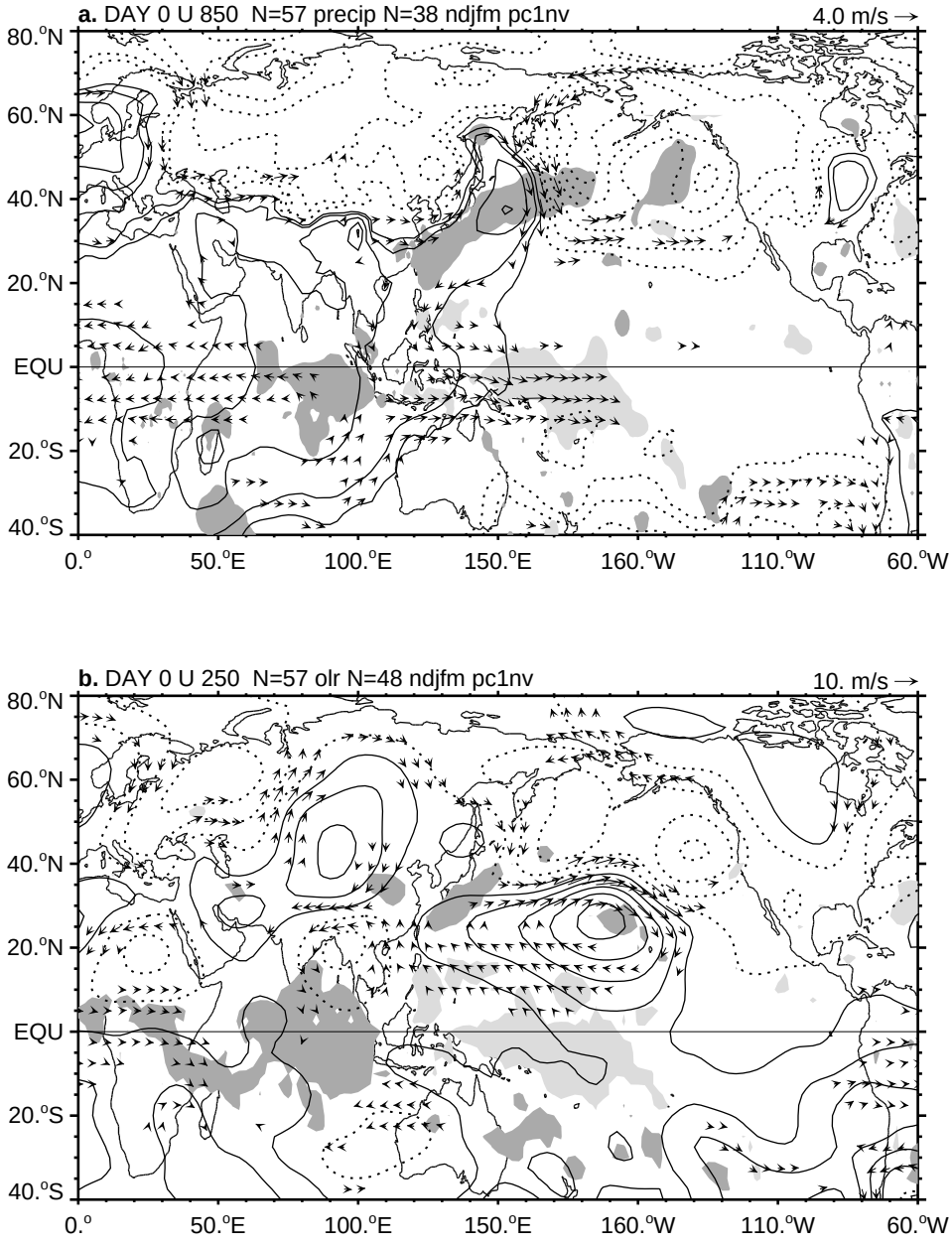

Figure 3.12: As in Fig. 3.5 but for November–March PC 1 exceeding 1.5.

Table 3.4. Date of Maximum PC 1 equal to or exceeding 1.5 for November–March.

Jan	1	1972	Jan	9	1985
Mar	15	1972	Mar	5	1985
Dec	26	1972	Nov	13	1986
Feb	4	1973	Dec	21	1986
Feb	25	1973	Feb	1	1987
Nov	20	1973	Feb	25	1987
Mar	24	1975	Nov	15	1987
Jan	23	1976	Dec	22	1987
Dec	13	1976	Dec	3	1988
Jan	14	1977	Nov	26	1989
Mar	7	1977	Dec	7	1989
Nov	30	1977	Mar	11	1990
Dec	16	1977	Nov	10	1990
Jan	2	1978	Feb	23	1991
Feb	20	1978	Nov	7	1991
Dec	1	1978	Dec	7	1991
Jan	7	1979	Jan	4	1992
Dec	2	1979	Mar	8	1992
Feb	21	1980	Nov	24	1992
Mar	22	1980	Jan	1	1993
Nov	1	1980	Feb	5	1993
Jan	17	1981	Mar	23	1993
Feb	6	1981	Dec	26	1993
Mar	2	1981	Mar	31	1994
Dec	10	1981	Dec	22	1994
Jan	27	1982	Jan	8	1995
Mar	30	1982	Nov	27	1995
Jan	28	1983	Dec	28	1995
Mar	1	1983			
Nov	1	1983			
Nov	17	1983			

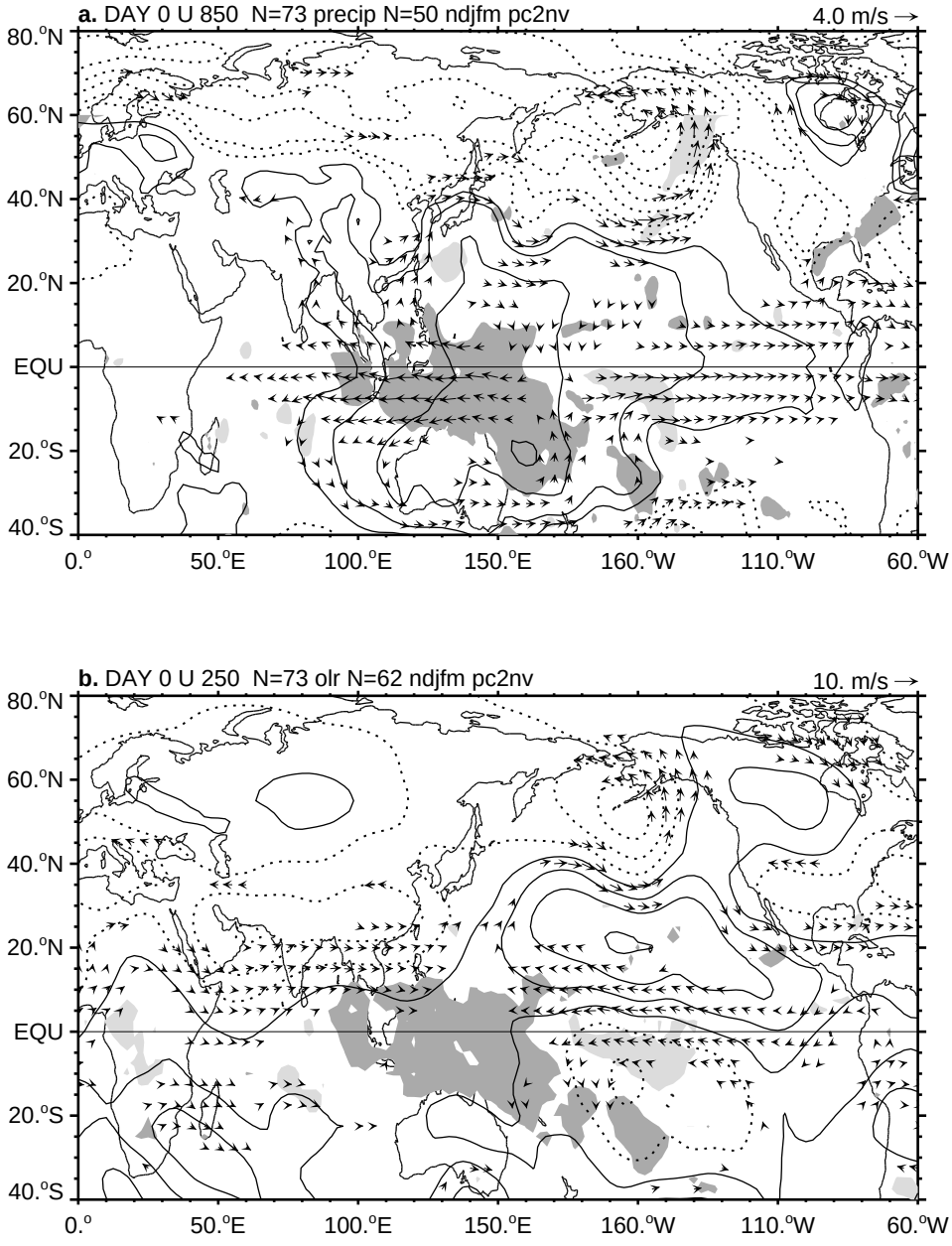

Figure 3.13: As in Fig. 3.5 but for November–March PC 2 exceeding 1.5.

Table 3.5. Date of Maximum PC 2 equal to or exceeding 1.5 for November–March.

Feb	11	1972	Dec	28	1982	Mar	28	1991
Dec	26	1972	Jan	27	1983	Nov	16	1991
Jan	16	1973	Feb	9	1983	Dec	9	1991
Feb	10	1973	Feb	24	1983	Jan	25	1992
Feb	21	1973	Mar	15	1983	Feb	14	1992
Mar	31	1973	Nov	4	1983	Mar	20	1992
Dec	3	1973	Jan	4	1984	Nov	28	1992
Mar	23	1974	Mar	11	1984	Dec	12	1992
Nov	23	1975	Nov	1	1984	Jan	12	1993
Dec	31	1975	Jan	27	1985	Mar	22	1993
Nov	14	1977	Dec	24	1985	Nov	2	1993
Dec	15	1977	Feb	5	1986	Jan	7	1994
Jan	2	1978	Mar	8	1986	Feb	1	1994
Jan	15	1978	Dec	23	1986	Nov	27	1994
Mar	1	1978	Mar	2	1987	Dec	28	1994
Nov	5	1978	Mar	25	1987	Feb	7	1995
Jan	17	1979	Dec	3	1987	Feb	23	1995
Mar	1	1979	Jan	21	1988	Mar	17	1995
Mar	23	1979	Feb	25	1988	Nov	9	1995
Dec	20	1979	Mar	10	1988	Dec	15	1995
Jan	18	1980	Nov	30	1989	Dec	31	1995
Feb	2	1980	Dec	28	1989	Mar	12	1996
Feb	29	1980	Feb	9	1990			
Mar	18	1981	Mar	28	1990			
Feb	18	1982	Dec	2	1990			
Nov	17	1982	Jan	16	1991			

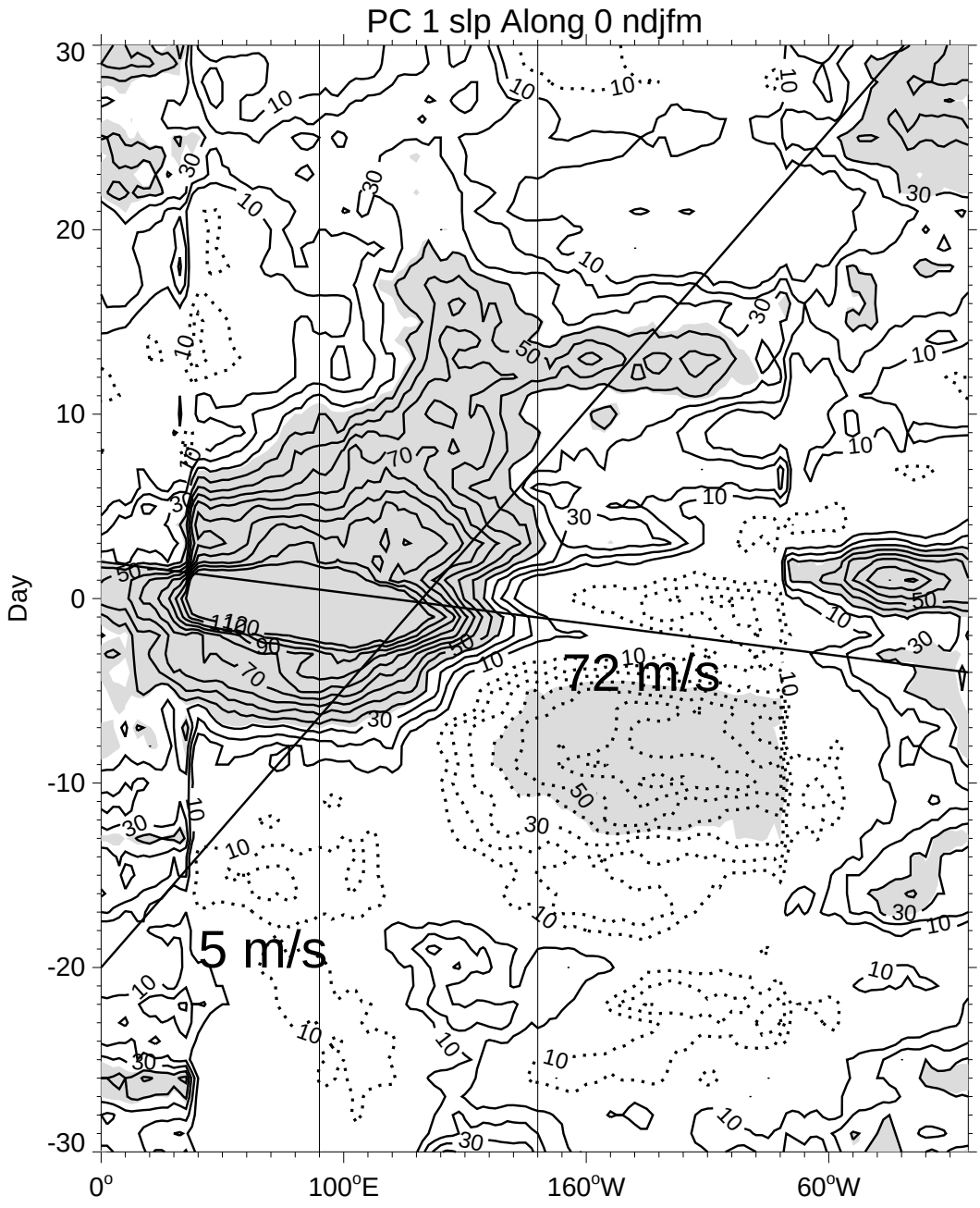

Figure 3.14. As in fig. 3.7 but for SLP anomalies for November–March PC 1 exceeding 1.5 along the equator.

-2 in Figs. B.5b and B.7b. The key dates for PC 3 are given in Table 3.6. The composite indicates that PC 3 is well-associated with occurrences of pressure surges, including the enhanced northeasterly flow over the South China Sea and positive precipitation anomaly in that region. A well-defined midlatitude wave pattern over the North Pacific at both upper and lower tropospheric levels is observed. The concurrent positive and negative precipitation anomalies with the wave train provide additional support for the robustness of the wave train feature. The upper-level wave train pattern over northern central Siberia in Fig. 3.15b appears to be a significant feature associated with surges and is quite similar to the upper-level anomaly found in the linear regression at Day -2 in Fig. B.7b. The reproducibility of the wave-train pattern using two different analysis techniques suggests that the association between surges and upper-level wave activity over Asia is a robust one. In the tropics, significant wind anomalies and convective anomalies are seen extending to the equator. The precipitation and OLR anomalies associated with the pressure surge cover most of the South and East China Seas.

Figure 3.16 shows the time evolution of the SLP anomaly along 110°E. An approximate southward propagation speed of 11 m s^{-1} is indicated. The lagged and lead composite about the key date is quite similar in evolution to the linear regression in Fig. B.9. The SLP anomaly penetrates deeply into the tropics. Greater than a 50 Pa statistically significant anomaly penetrates well into the southern hemisphere, providing further evidence for the cross-equatorial influence of surges previously observed (Murakami 1980; Webster 1981; Lau 1982; Love 1985a; Webster 1987) and noted in Fig. B.5.

The time evolution of the composite meridional wind anomaly along 110°E (Fig. 3.17) provides further support for the argument of Sec. B.4.3 that pressure

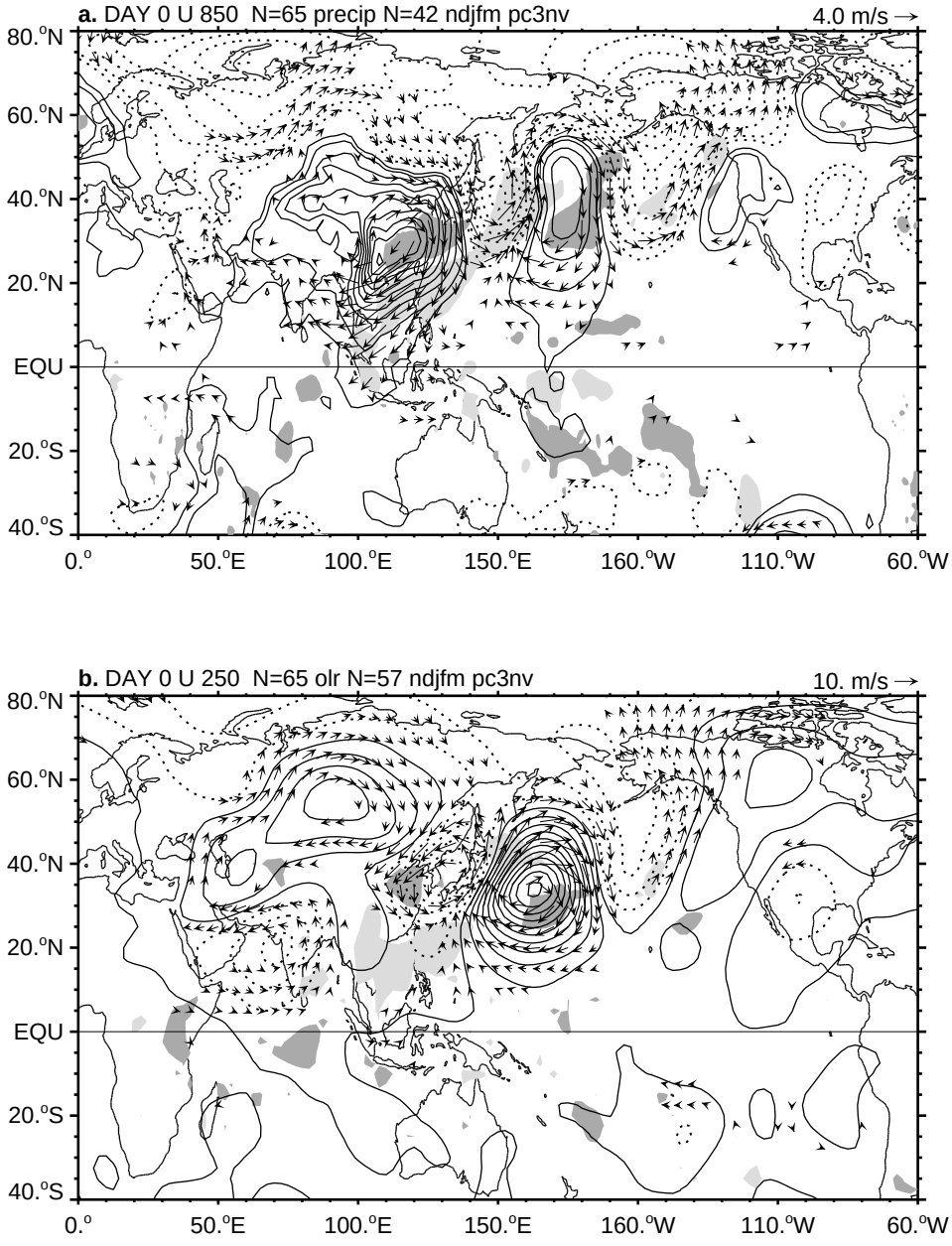

Figure 3.15: As in Fig. 3.5 but for November–March PC 3 exceeding 2.0.

Table 3.6. Date of Maximum PC 3 equal to or exceeding 2.0 for November–March. Dates that correspond to 1 week after the key dates of Joung and Hitchman (1982) are indicated by jh. Dates that correspond to ± 3.0 days within the key dates of Lai (1989) are indicated with l. Dates that correspond to ± 6.0 days of Wu and Chan (1995) are indicated with wc.

Mar	4	1972		Nov	8	1981	l	Mar	8	1989	
Feb	8	1973	jh	Dec	2	1981	l	Nov	19	1989	wc
Dec	25	1973	jh	Dec	18	1981	l	Feb	1	1990	wc
Feb	11	1974		Dec	6	1982	l	Nov	21	1990	wc
Feb	27	1974	jh	Jan	22	1983		Dec	3	1990	
Mar	12	1974		Feb	21	1983	l	Feb	25	1991	
Feb	22	1975	jh	Mar	5	1983	l	Jan	14	1992	
Nov	23	1975		Nov	26	1983	l	Jan	28	1993	
Dec	17	1975		Feb	7	1984	l	Mar	1	1993	
Jan	30	1976		Mar	3	1984	l	Mar	21	1993	
Mar	3	1976		Jan	30	1985	l	Dec	17	1993	
Mar	20	1976		Mar	15	1985	l	Mar	10	1994	
Nov	23	1976		Mar	31	1985	l	Mar	27	1994	
Feb	21	1977		Jan	5	1986	l	Feb	1	1995	
Mar	4	1977		Mar	1	1986	l	Mar	18	1995	
Mar	24	1977		Nov	29	1986	l	Dec	25	1995	
Nov	11	1977		Jan	13	1987	l	Feb	2	1996	
Dec	2	1977		Feb	3	1987	l	Feb	21	1996	
Feb	17	1978		Mar	26	1987	l				
Dec	2	1978		Dec	2	1987					
Nov	23	1979		Feb	18	1988					
Feb	15	1980		Mar	8	1988					
Mar	24	1980		Nov	5	1988	wc				
Feb	26	1981	l	Dec	9	1988	wc				

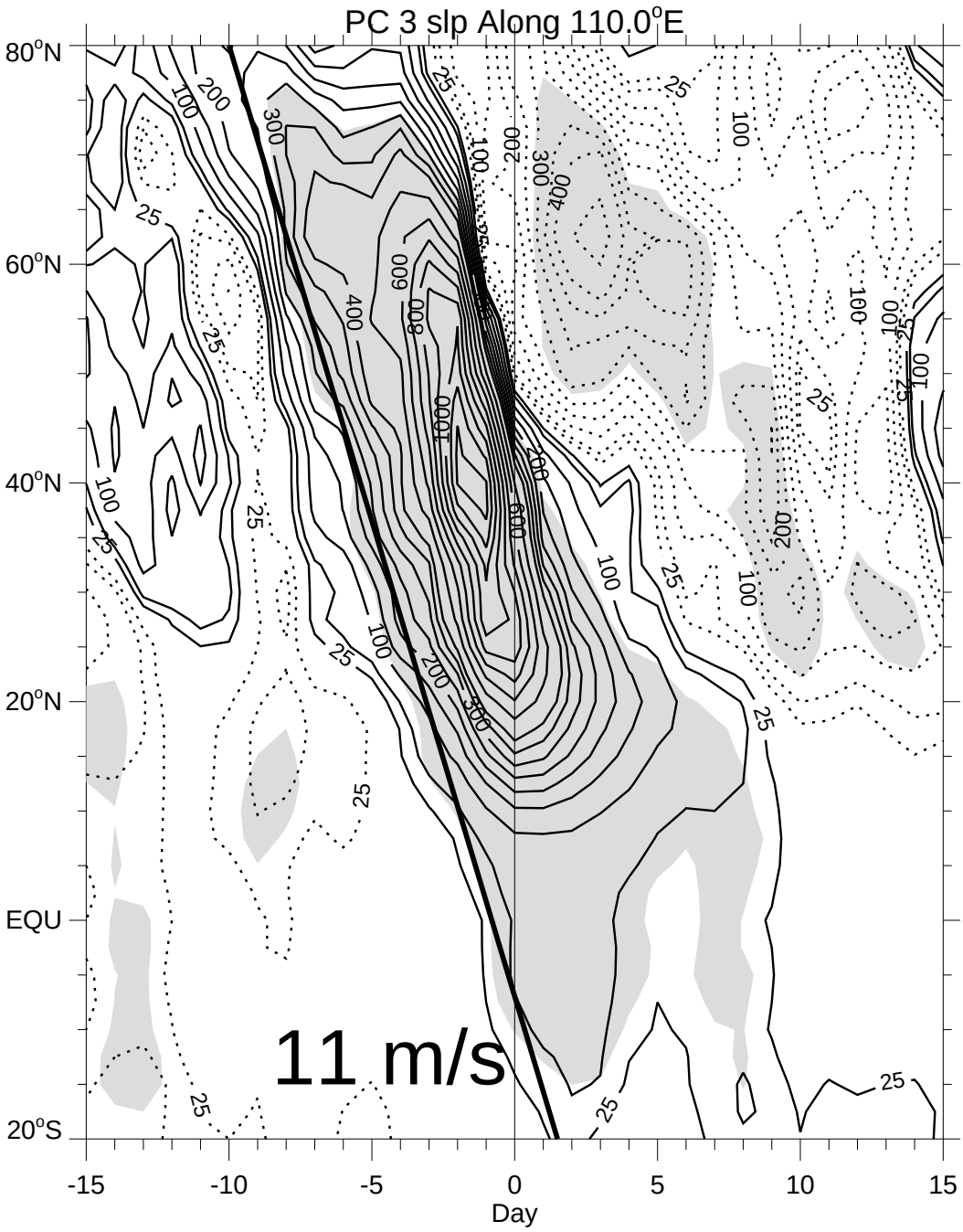

Figure 3.16. Latitude-time composite along 110°E of SLP anomalies for November–March PC 3 exceeding 2.0. Shading indicates where SLP anomalies are locally significant at the 95% level. Dashed (solid) lines indicated negative (positive) anomalies. Contour interval is 50 Pa to 500 Pa and then 100 Pa thereafter. The zero contour has been suppressed, and a ± 25 Pa contour has been added. The phase line indicates a speed of 11.0 m s^{-1} southward.

surges, at least in part, are propagated by a shelf-wave or topographic Rossby wave type mechanism, rather than non-linear advection by the meridional wind anomaly as hypothesized by Colle and Mass (1995) for surges occurring along the Rocky Mountains. Recently, Davis (1997) presented model results of surges along the Rocky Mountains that also suggested a topographic Rossby wave mechanism was responsible for much of the low-level southward propagation of surge-related anomalies in pressure, wind, and temperature. Under an advection mechanism, meridional wind and pressure anomalies should be nearly in quadrature rather than nearly in phase. The consistent southward phase propagation of 11 m s^{-1} is much larger than the composite meridional wind anomaly and originates well north of the significant meridional wind anomaly.

For the topographic Rossby wave mechanism to be a reasonable dynamical explanation for the southward propagation of surges, negative pressure anomalies should also propagate southward. Figure 3.18 shows the composite SLP anomaly using key dates based on episodes of relative minima of PC 3 less than -2.0. As previously observed by Hsu (1987), significant negative pressure anomalies also propagate southward at approximately 11 m s^{-1}. Positive meridional wind anomalies, nearly opposite to the negative anomalies of Fig. 3.17, propagate southward (not shown), providing further evidence that advection is not the dominant process for the southward progression of pressure anomalies over East Asia.

The association between Mode 3 and occurrences of East Asian pressure surges is strengthened in Table 3.6 by a comparison of the key dates where PC 3 is at a maximum and greater than 2.0 with the key dates of other studies of East Asian surges using various definitions (Joung and Hitchman 1982; Lai 1989; Wu and Chan 1995). Joung and Hitchman (1982) used a definition for cold surges occurring over

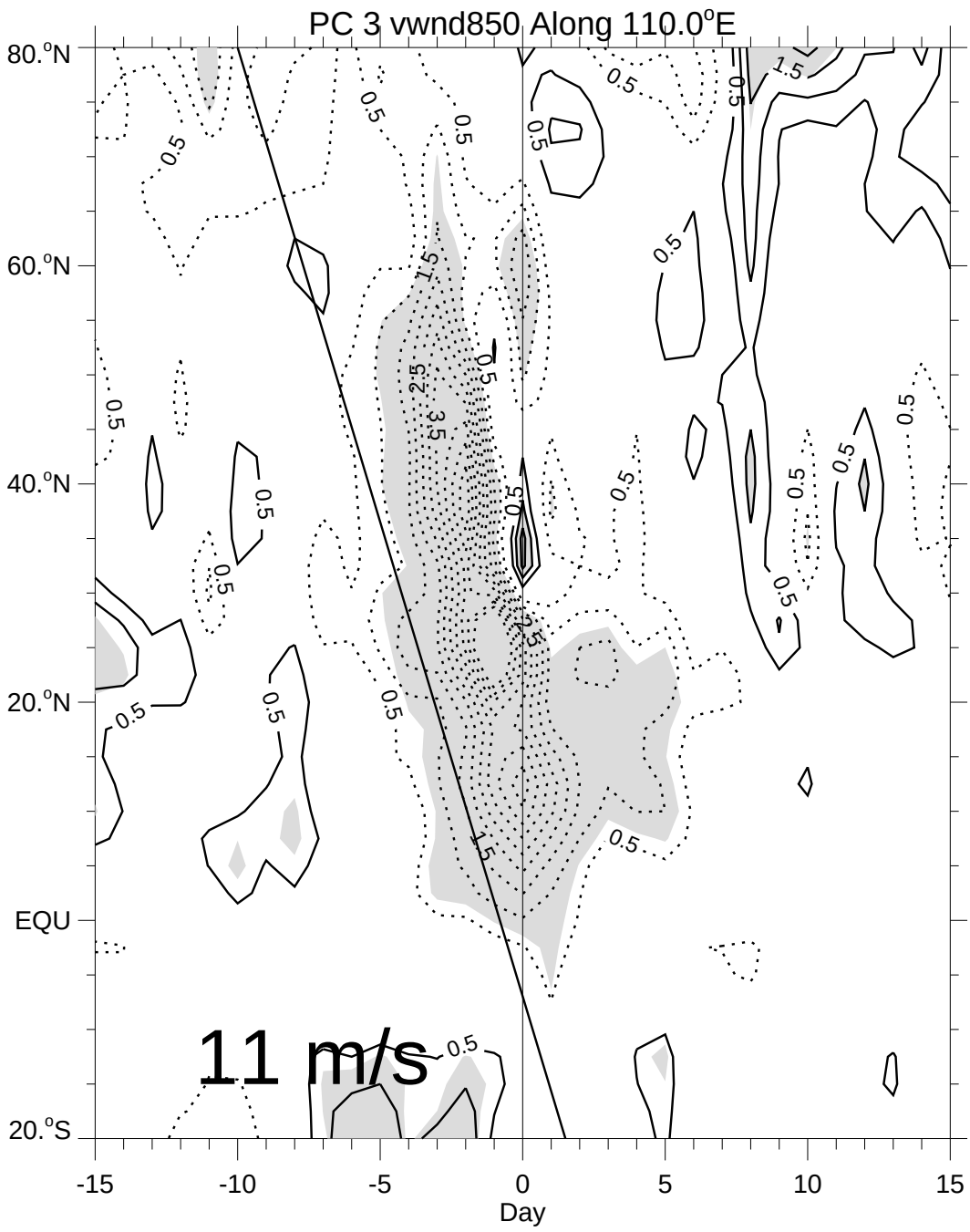

Figure 3.17. As in Fig. 3.16but for 850 hPa meridional wind anomalies. Contour interval is 0.5 m s^{-1}.

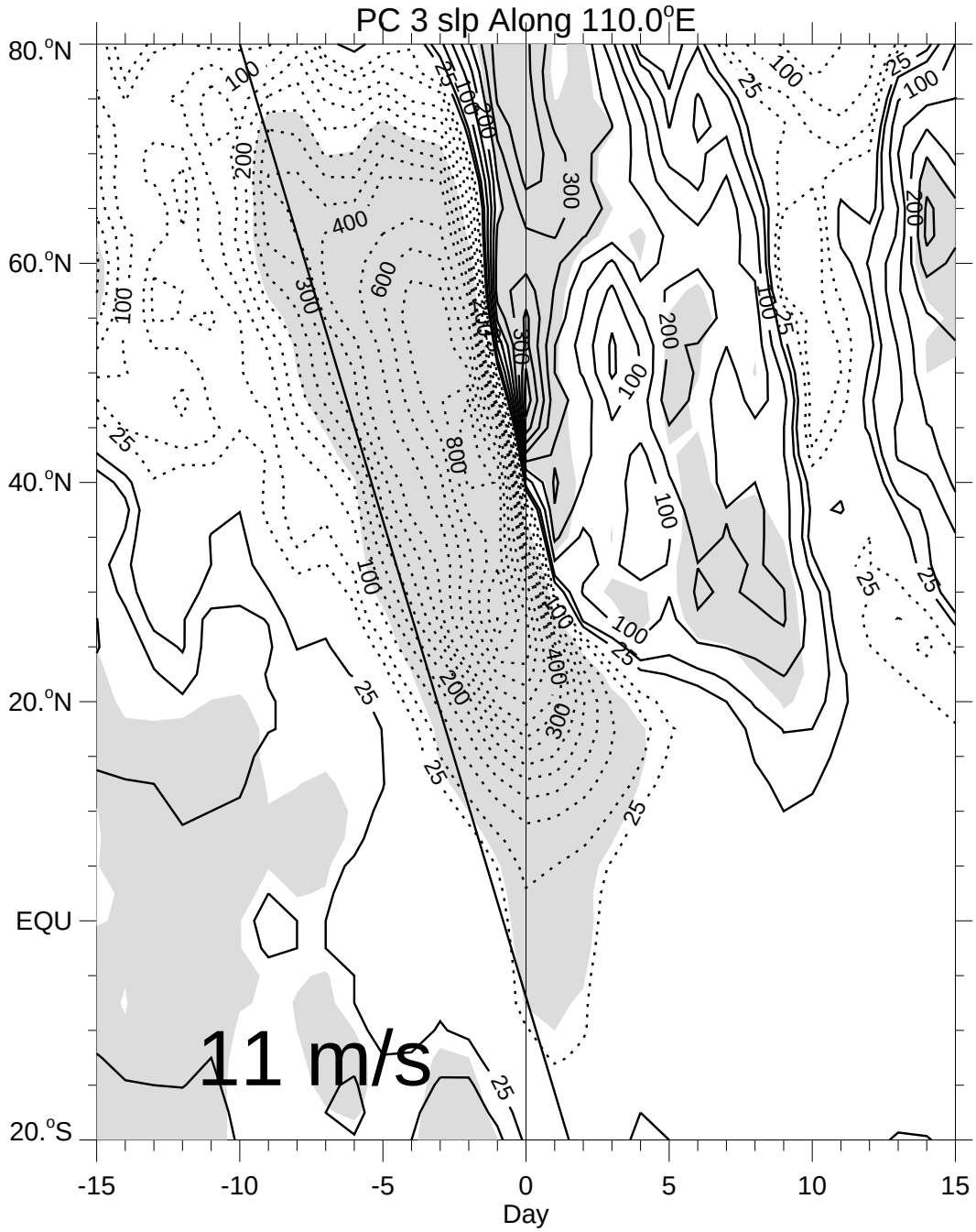

Figure 3.18: As in Fig. 3.16 but for November–March PC 3 less than -2.0.

Table 3.7: Date of Minimum PC 3 less than or equal to -2.0 for November–March.

Nov	27	1971	Jan	28	1980	Feb	16	1989
Jan	31	1972	Feb	26	1980	Jan	9	1990
Nov	14	1972	Nov	7	1980	Feb	22	1990
Dec	11	1972	Dec	11	1980	Nov	8	1990
Dec	28	1972	Feb	12	1981	Nov	29	1990
Jan	24	1973	Feb	23	1981	Dec	20	1990
Feb	22	1973	Mar	24	1981	Dec	31	1990
Feb	22	1974	Dec	28	1981	Jan	21	1991
Nov	8	1974	Mar	4	1982	Feb	14	1991
Dec	2	1974	Mar	15	1982	Mar	20	1991
Jan	15	1975	Nov	13	1982	Feb	15	1992
Feb	6	1975	Nov	29	1982	Mar	2	1992
Dec	4	1975	Dec	31	1982	Dec	7	1992
Jan	3	1976	Feb	1	1983	Dec	20	1992
Feb	14	1976	Mar	23	1983	Feb	6	1993
Feb	28	1976	Jan	14	1984	Feb	21	1993
Mar	17	1976	Feb	22	1984	Mar	14	1993
Dec	24	1976	Nov	10	1984	Jan	16	1994
Mar	1	1977	Feb	9	1985	Feb	11	1994
Dec	15	1977	Mar	27	1985	Mar	7	1994
Dec	31	1977	Nov	22	1985	Dec	11	1994
Jan	13	1978	Jan	30	1986	Jan	22	1995
Jan	26	1978	Feb	14	1986	Mar	16	1995
Feb	9	1978	Mar	18	1986	Jan	7	1996
Mar	3	1978	Jan	2	1987	Feb	13	1996
Jan	6	1979	Feb	11	1987	Mar	16	1996
Jan	29	1979	Mar	17	1987			
Feb	22	1979	Nov	26	1987			
Mar	10	1979	Dec	29	1987			
Mar	29	1979	Jan	21	1988			
Nov	4	1979	Feb	5	1988			
Dec	19	1979	Mar	14	1988			

Korea. For the overlapping data period, the PC 3 key dates include all the key dates used in their study. Lai (1989) constructed a definition of surges based on entirely on the strength of the low-level meridional wind at Hong Kong. During the overlapping period of 1981–1987, all of the PC 3 key dates, with one exception appear within 3 days of the Lai northerly surge cases. The excepted date appears 5 days after the Lai date. Inspection of the PC 3 time series shows two relative maxima, with a relative maximum 3 days after the Lai date and a second, larger maximum 2 days following. The northerly wind definition of Lai produced many more events than the 2.0 PC 3 criterion used here, suggesting that the overall statistics of Lai contained many weak anomaly events. Similarly, the multi-variable Hong Kong based definition of Wu and Chan (1995) also produced many more events over the 1988-1990 period than found here. Curiously, the time difference between the 6 overlapping Wu and Chan events is larger than that of the northerly surge definition of Lai, with 2 of the events separated from the key dates used here by 6 days, one by 4 days, one by 3 days, and the other two by 1 day. The differences between the multi-variable definition suggest that the broad, flexible definition of Wu and Chan should produce composite results with a larger variance in the ensemble and, perhaps, smaller statistically significant regions than those shown here. However, none of the composite studies discussed the statistical significance of their results, so this speculation cannot be addressed. Other composite studies (Hsu and Wallace 1985; Hsu 1987; Zhang *et al.* 1997) did not list their key dates.

Figure 3.19 shows the composite SLP, circulation, and convective anomalies associated with PC 5. The key dates used in the composite are given in Table 3.8. The composite shows that positive anomalies in PC 5 are associated primarily with large-scale midlatitude circulations over the Asian continent. Significant positive

precipitation anomalies and negative OLR anomalies are observed in the Indonesian region. The lack of significant wind or pressure anomalies, however, raises the question of whether these convective anomalies can be regarded as dynamically significant. Similar to Fig. 3.18, the negative SLP anomaly, associated with southerly wind anomalies, propagates southward over East Asia at approximately 11 m s^{-1} (not shown).

Figure 3.20 shows the composite SLP, circulation, and convective anomalies associated with PC 6. The key dates used in the composite are given in Table 3.9. The composite shows that positive anomalies in PC 6 are associated primarily with large-scale midlatitude circulations over the Asian continent, somewhat south of those seen in Fig. 3.19. The upper level features associated with PC 6 over the Asian continent and North Pacific bear a strong similarity to those of Fig. B.7e. The similarity between the linear regression using a base point in the South China Sea and the composite of negative pressure anomalies over the Chinese regions further suggests a high degree of symmetry between positive and negative SLP anomalies and their associated circulations. The time evolution of SLP anomalies over East Asia associated with PC 6 show southward propagation extending into the deep tropics and across the equator similar to Fig. 3.18 (not shown).

3.6 Cool Season Cross–correlations between Modes

Figure 3.21 shows the significant lag cross-correlations between the first seven ORPCA modes using data from November to March. Significance is determined as in Fig. 3.11. As in the warm season cross-correlations of Sec. 3.4, no $r < \|0.20\|$ is found when a 3% variance threshold is employed.

Comparing Figs. 3.21a and 3.11a, a definite shift is observed in the phase relationship between PCs 1 and 2. Such a phase shift, with PC 1 now leading PC

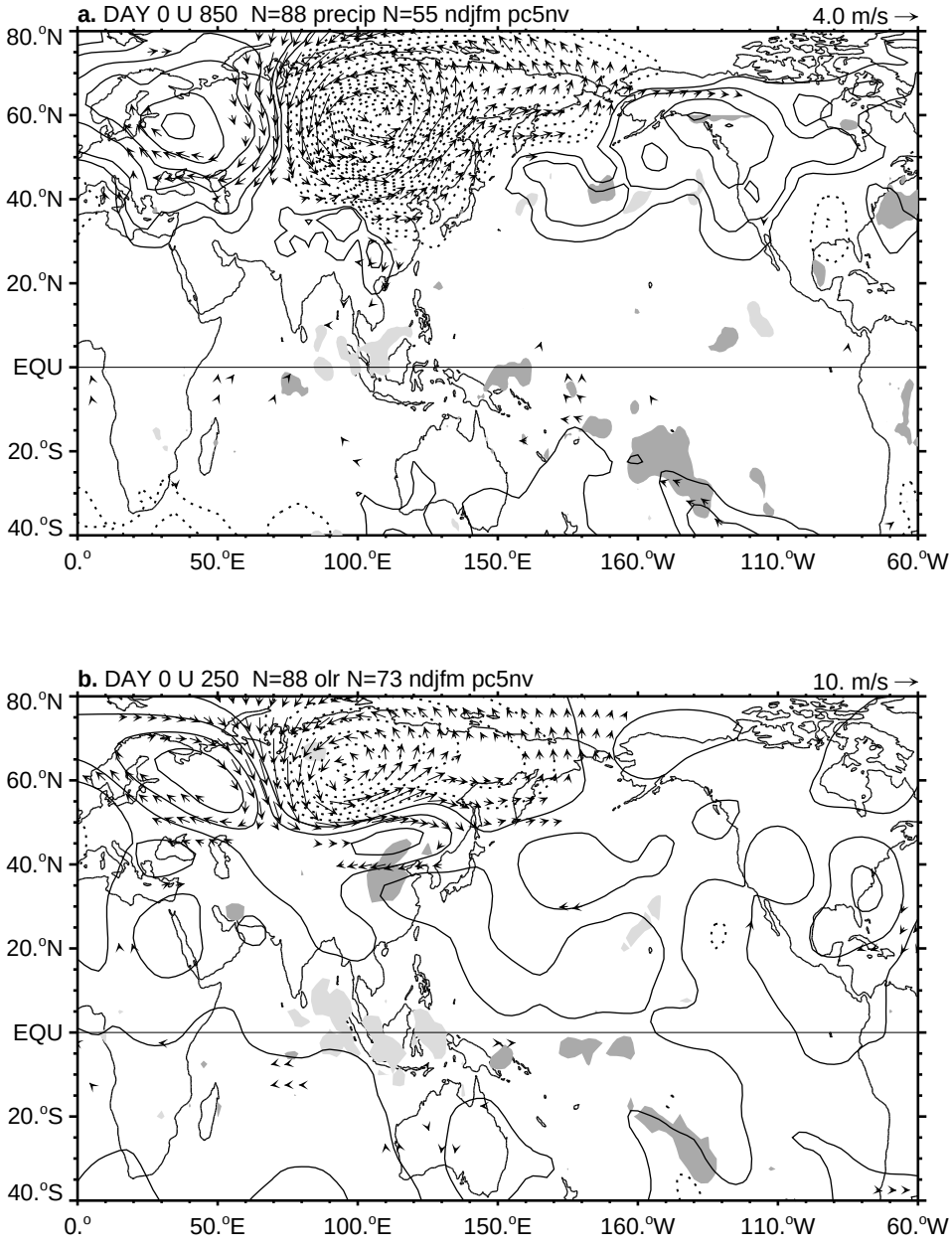

Figure 3.19: As in Fig. 3.5 but for November–March PC 5 exceeding 2.0.

Table 3.8. Date of Maximum PC 5 equal to or exceeding 2.0 for November–March.

Dec	2	1971	Nov	30	1980	Feb	11	1989
Dec	15	1971	Jan	31	1981	Mar	11	1989
Jan	16	1972	Jan	7	1982	Nov	15	1989
Feb	3	1972	Mar	8	1982	Mar	29	1990
Mar	21	1972	Nov	28	1982	Nov	12	1990
Dec	7	1972	Dec	25	1982	Dec	5	1990
Jan	6	1973	Mar	30	1983	Dec	18	1990
Feb	13	1973	Jan	8	1984	Jan	24	1991
Nov	6	1973	Feb	22	1984	Feb	9	1991
Nov	30	1973	Dec	1	1984	Mar	21	1991
Dec	31	1973	Dec	18	1984	Nov	28	1991
Feb	17	1974	Jan	9	1985	Feb	26	1992
Nov	23	1974	Jan	31	1985	Nov	20	1992
Jan	21	1975	Mar	22	1985	Dec	18	1992
Mar	16	1975	Nov	4	1985	Jan	23	1993
Nov	13	1975	Nov	19	1985	Nov	24	1993
Nov	25	1975	Jan	14	1986	Dec	24	1993
Dec	31	1975	Nov	8	1986	Jan	14	1994
Feb	22	1976	Nov	29	1986	Nov	4	1994
Mar	9	1976	Dec	10	1986	Jan	6	1995
Nov	20	1976	Dec	22	1986	Jan	23	1995
Dec	16	1976	Jan	13	1987	Mar	5	1995
Mar	6	1977	Feb	7	1987	Nov	11	1995
Jan	20	1978	Dec	8	1987	Nov	27	1995
Jan	5	1979	Dec	26	1987	Dec	31	1995
Jan	21	1979	Jan	19	1988	Jan	25	1996
Feb	8	1979	Feb	3	1988	Feb	11	1996
Feb	24	1979	Mar	12	1988			
Nov	22	1979	Nov	11	1988			
Dec	27	1979	Dec	5	1988			
Feb	27	1980	Jan	14	1989			

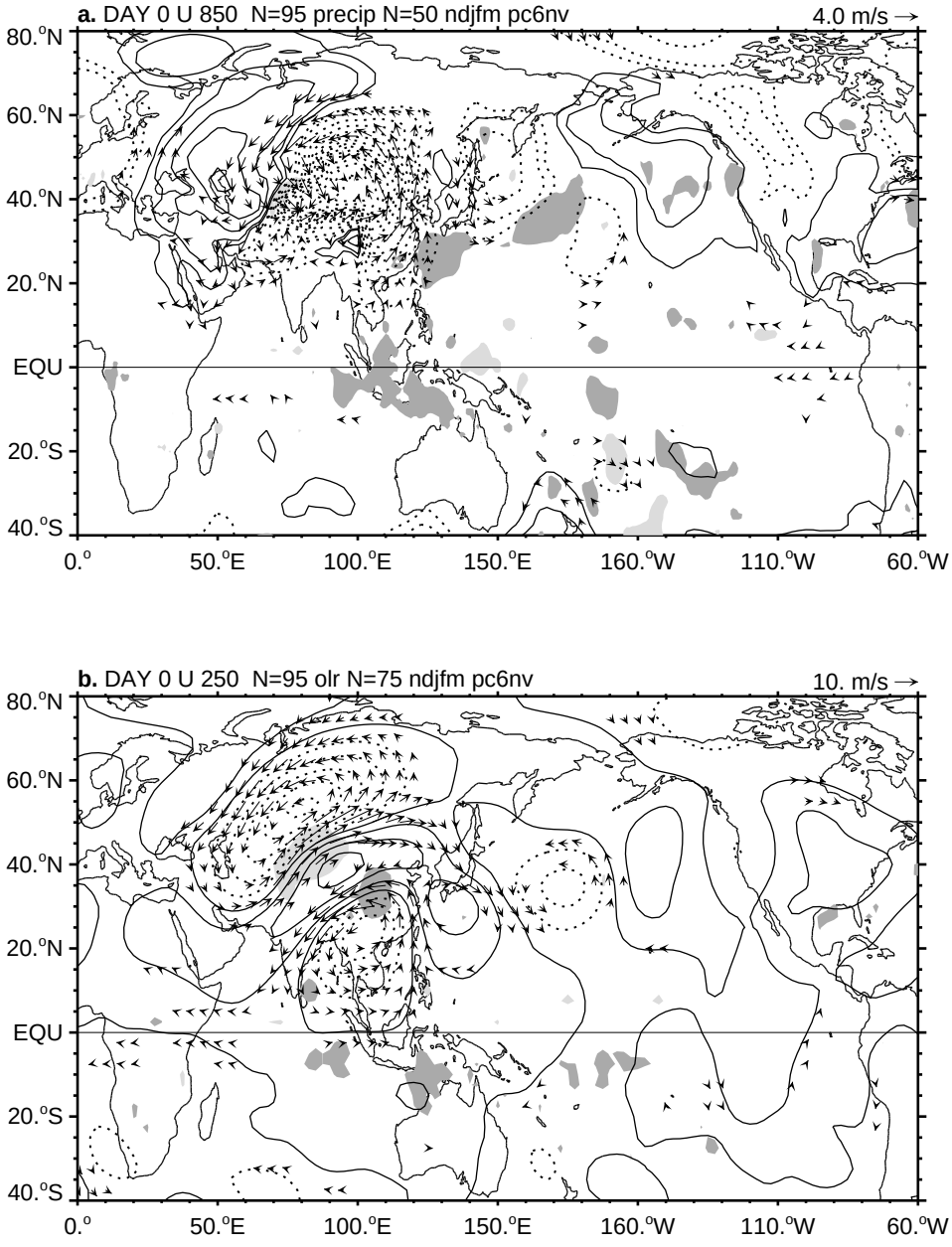

Figure 3.20: As in Fig. 3.5 but for November–March PC 6 exceeding 2.0.

Table 3.9. Date of Maximum PC 6 equal to or exceeding 2.0 for November–March.

Dec	22	1971	Feb	5	1978	Feb	24	1989
Jan	21	1972	Mar	15	1978	Nov	1	1989
Feb	23	1972	Dec	18	1978	Dec	6	1989
Mar	12	1972	Jan	8	1979	Dec	18	1989
Nov	1	1972	Jan	26	1979	Jan	26	1990
Dec	3	1972	Feb	19	1979	Feb	13	1990
Jan	20	1973	Nov	7	1979	Nov	14	1990
Feb	2	1973	Dec	18	1979	Dec	27	1990
Feb	24	1973	Mar	6	1980	Feb	6	1991
Mar	8	1973	Nov	19	1980	Mar	8	1991
Nov	21	1973	Dec	14	1980	Nov	4	1991
Jan	26	1974	Jan	20	1981	Dec	14	1991
Feb	20	1974	Feb	13	1981	Feb	26	1992
Mar	22	1974	Mar	30	1981	Nov	17	1992
Nov	1	1974	Dec	26	1981	Dec	11	1992
Nov	26	1974	Jan	19	1982	Dec	24	1992
Dec	7	1974	Feb	16	1982	Mar	12	1993
Dec	25	1974	Mar	21	1982	Nov	13	1993
Jan	5	1975	Jan	28	1983	Feb	10	1994
Feb	13	1975	Nov	15	1984	Mar	10	1994
Mar	4	1975	Dec	1	1984	Nov	7	1994
Mar	25	1975	Feb	28	1985	Dec	6	1994
Nov	6	1975	Mar	11	1986	Dec	22	1994
Nov	30	1975	Dec	7	1986	Nov	16	1995
Dec	25	1975	Jan	1	1987	Jan	10	1996
Feb	12	1976	Feb	12	1987	Feb	12	1996
Feb	25	1976	Mar	6	1987	Mar	15	1996
Mar	15	1976	Nov	9	1987	Mar	28	1996
Nov	7	1976	Nov	24	1987			
Dec	20	1976	Dec	30	1987			
Jan	22	1977	Mar	12	1988			
Feb	27	1977	Dec	5	1988			
Dec	9	1977	Dec	22	1988			
Dec	25	1977	Jan	6	1989			

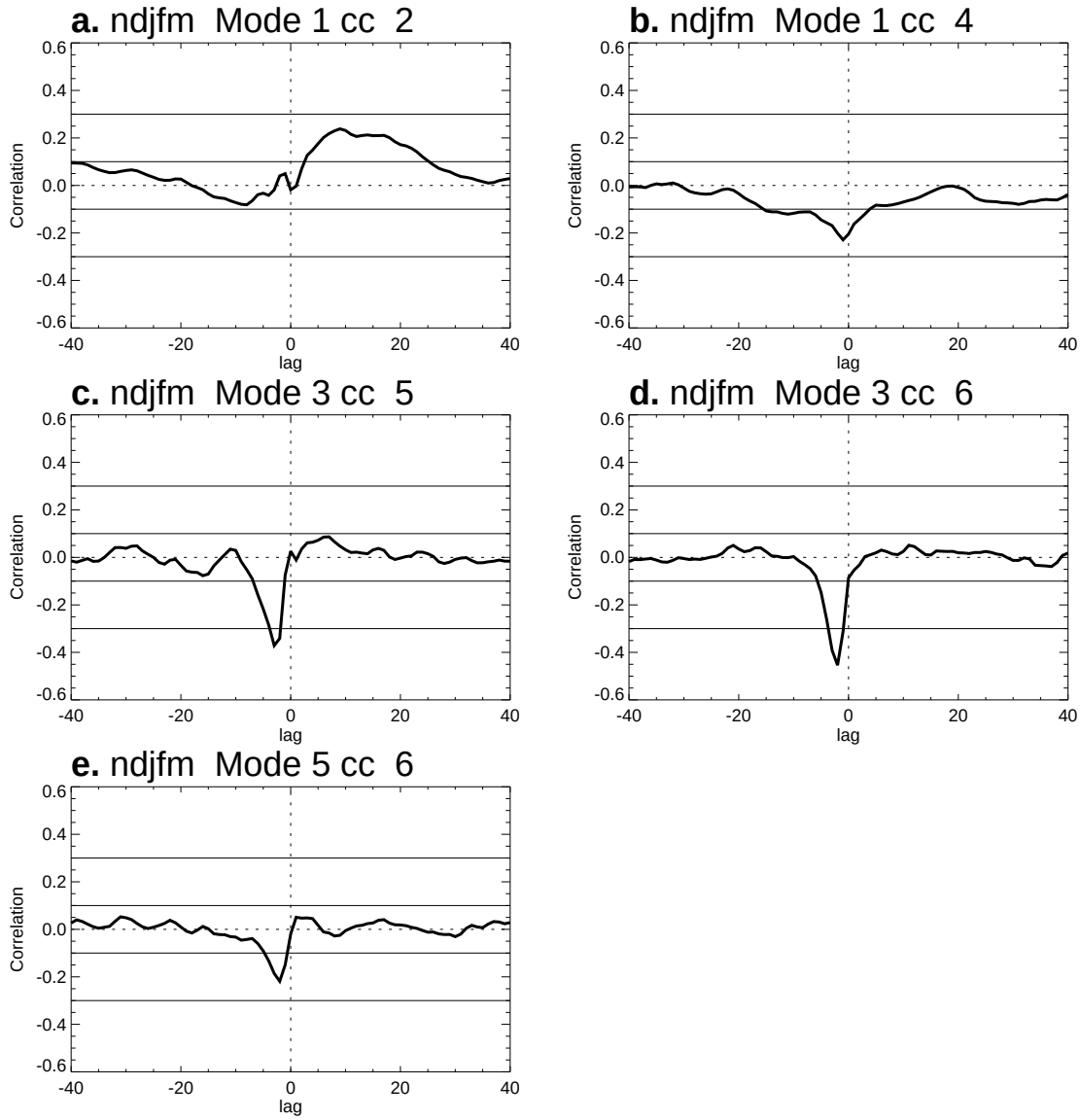

Figure 3.21. As in Fig. 3.11 but for November–March between (a) Modes 1 and 2, (b) Modes 1 and 4, (c) Modes 3 and 5, (d) Modes 3 and 6, and (e) Modes 5 and 6.

2 is consistent with the slow eastward propagation of positive SLP anomalies seen in Fig. 3.14, where positive SLP anomalies are largely east of 90°E after Day +10. Combining the evidence of the cool season spectra of PCs 1 and 2 (Fig. 3.3a and b), composite circulation and convective anomalies (Figs. 3.12 and 3.13), and the lag relationship between the two modes, leads to the strong identification of Modes 1 and 2 with the MJO, based on the consistency with many other observational studies (e.g., Madden and Julian 1972b; Weickmann *et al.* 1985; Kiladis and Weickmann 1992; Madden and Julian 1994; Salby and Hendon 1994; Meehl *et al.* 1996).

The midlatitude-tropical connection associated with Modes 3, 5, and 6 is further solidified by examining the lagged cross-correlations between these modes (Fig. 3.21c, d, and e). Southward progression of both positive and negative pressure anomalies over East Asia from the midlatitudes to the tropics is observed in the principal component time series composites (Figs. 3.16 and 3.18), and case studies (Fig. B.2). The dominance of the East Asian pressure surges associated with these southward progressing pressure anomalies is reflected in the magnitude of correlation coefficients between PCs 3 and 5 (Fig. 3.21c) and PCs 3 and 6 (Fig. 3.21d). The negative correlation between PCs 5 and 6 (Fig. 3.21e), however, suggests that East Asian pressure surges may have two origins: that anomalies beginning in the Siberian region and progressing southward may be unrelated to anomalies progressing from northwest of the Tibetan Plateau to the South China Sea.

Hsu (1987) presented evidence from one-point correlation analysis suggesting that two orographic waveguides existed over the Himalayas mountain region. The first waveguide stretches north-south from the region of Mode 5 to Mode 3, (Fig. 3.1e and c) while the second runs along the Tibetan Plateau east-west until 105°E, where it turns southward, as indicated by the curved shape of Mode 6

(Fig. 3.1f) around the Plateau (see Fig. B.1 for a diagram of the large-scale orography). The high correlations between PCs 3 and 5 and PCs 3 and 6 (Fig. 3.21c and d) support the hypothesis that these waveguides influence both positive and negative pressure anomalies from the mid-latitudes to the deep Tropics.

Recent studies have suggested that a build-up of the Siberian High is the primary mechanism for surge activation (Ding 1990; Wu and Chan 1997). The evidence presented in the symmetry between positive and negative pressure anomalies suggests that, in addition to the study of pressure surges, the dynamics of the negative pressure anomalies, pressure "lulls," should also be addressed further. Lau and Li (1984) noted that cold-air outbreaks and northerly surges were often preceded or followed by lulls in the winter monsoon. Most research on pressure surges has not addressed these lulls in formulating theories of the dynamics of surges. Few studies have noted the existence of negative SLP anomalies of nearly equal magnitude to the positive SLP anomalies associated with surges. That lulls have not been recognized as an important part of the same dynamics as surges may be because surges bring an enhancement of the climatological winter monsoon northeasterlies over Southern China. The increased wind speed and drop in temperatures and humidity can have important socio-economic impacts, such as increasing fire hazards (Zhang *et al.* 1997). Lulls bring a weakening of the climatological conditions, and so may not appear to be as important to forecasters. However, future dynamical theories for pressure surges should also include a mechanism for the lulls, as a large amount of linearity appears to exist between the two perturbations.

3.7 Summary of Modes

Seven dominant modes of the ORPCA analysis in Fig. 3.1 have been identified with previously studied circulation anomalies in the summer and winter monsoons. The composite and spectral analysis of the ORPCA PCs demonstrates that the PCs correspond to physically meaningful structures.

The ORPCA using the entire 1971–1996 SLP anomaly record at full spatial resolution has demonstrated that the signature of dominant dynamical structures of the atmosphere can be obtained as statistically significant features in the data when a long record is available. The composites help confirm the reproducibility and robustness of several previous results, both in the warm and cool seasons over the Indian-Pacific Ocean regions. The use of a long continuous record of unfiltered, daily data has allowed the seasonality and timescales associated with several previously studied tropical and midlatitudes circulations to be identified a posteriori, providing support for previous associations with few assumptions prior to the analysis.

The seasonal comparison of circulation and spectra provides support for some differences in the MJO between the cool and warm seasons: a frequency shift toward longer periods in the cool season (Fig. 3.3). A 5-day global pressure wave using the anomaly data in both the composites of PC 1 in the warm season (Fig. 3.7 and 3.8) and in the wavelet spectra of PCs 1 and 2 (Fig. 3.4) is shown to have greater variance in the warm season.

Cool season Mode 2 does not have a significant 30-60 day spectral peak. However, composites of circulation, SLP, and convective anomalies strongly resemble previous studies of the MJO in fields of the global circulation and convective activity (Madden and Julian 1972b; Kiladis and Weickmann 1992; Kiladis *et al.* 1994; Meehl *et al.* 1996). Modes 1 and 2 can be associated with the large-scale

variations in the summer monsoon and winter monsoon.

Mode 4 appears to be associated with monsoon depression disturbances. Mode 7 appears to project onto the active and break periods over all of South Asia during the summer monsoon.

Modes 3, 5, and 6 describe East Asian pressure surges. Modes 5 and 6 are quite similar to the previously found Siberian and Chinese modes of Hsu and Wallace (1985). Mode 3, the newly identified South China Sea mode, captures the signal of pressure surges that have a robust statistically significant relationship to tropical convective and circulation anomalies. Mode 3 also appears to capture the winter monsoon ”lulls.” As such, PC 3 provides an objective time series for measuring the activity of surges and lulls.

CHAPTER 4

SEASONAL MODULATION OF EAST ASIAN PRESSURE SURGES

4.1 Spatial Distribution of Submonthly SLP Variance

Figure 4.1a shows the global distribution of the standard deviation of SLP anomalies for the entire 1971–1996 record of NCEP/NCAR Reanalysis. The well-known "storm tracks" (e.g., Blackmon 1976; Blackmon *et al.* 1977; Blackmon *et al.* 1984) are visible as high variance regions over the oceans on the poleward side of the upper level jet streams of both hemispheres. Also evident are wedges of high variance on the eastern side of the major orographic features of the Himalayas, the Rockies, the Andes, and to a lesser extent, along the South African Highlands.

Figure 4.1b shows the percent variance of the SLP anomalies in the submonthly (2-30 day) band. The dark shading indicates where more than 60% of the total anomaly variance is within the submonthly band. The distinctive wedges of high variance seen along the major orographic features of Fig. 4.1a have a majority of their variance in the submonthly timescale. Over East Asia, in particular, Fig. 4.1b shows that the majority of the variance associated with the South China Sea Mode (3), the Siberian Mode (5), and the Chinese Mode (6) is within the submonthly band. A description of the seasonal evolution of the variance in the submonthly band accounts for the majority of the variance in this region.

4.2 Modulation of PC 3 Submonthly Variance

As shown in Fig. 3.3c, submonthly variance of the South China Sea Mode (3) is large during the northern hemisphere cool season compared to the annual

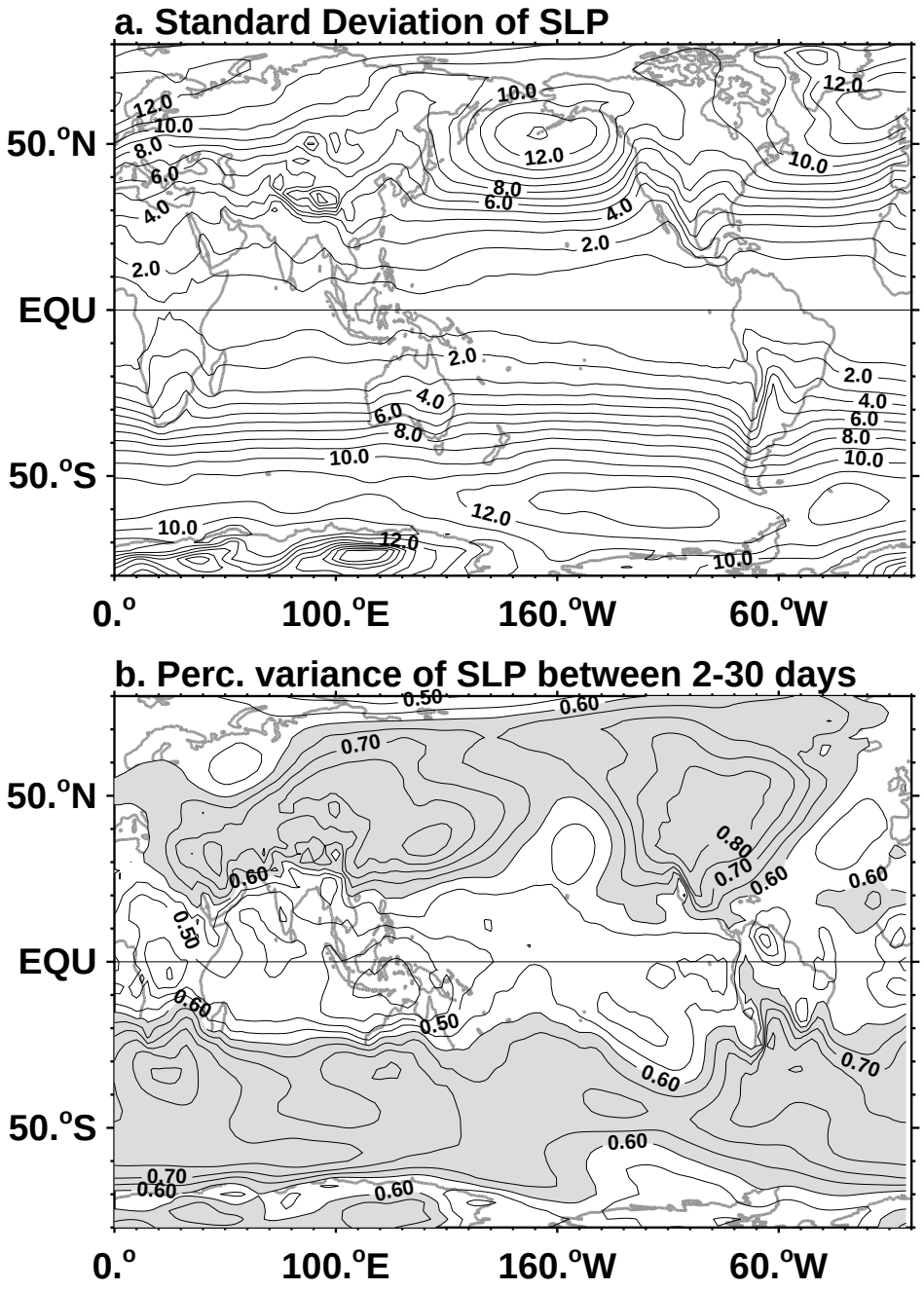

Figure 4.1. Map of (a) SLP anomaly standard deviation. The standard deviation is calculated from the 1971–1996 after a 3-harmonic annual cycle has been removed. Contour interval is 1.0 mb, with a 1.5 mb contour added. Map of (b) fractional variance of SLP anomaly in the 2-30 day band. Variance is estimated using (C.14) over periods corresponding to 2-30 days. Contour interval is 0.05. Fractional values larger than 0.6 are shaded.

mean. PC 3 appears to describe tropically-influential pressure surge and lull episodes (Chap. 3). An examination of the seasonal cycle of submonthly variance of PC 3 may help illuminate the conflicting modulation of surge activity seen in other studies (Joung and Hitchman 1982; Lai 1989; Ding 1990; Wu and Chan 1995; Zhang *et al.* 1997).

Figure 4.2 shows the time series of PC 3 submonthly variance, constructed by averaging the wavelet power spectrum of PC 3 between periods of 2-to-30 days using (C.24). The 95% confidence level from (C.26) is shown assuming red noise with $\alpha = 0.61$. The percent of the total variance of PC 3 in the submonthly band (73.1%) is indicated as a fraction. Considerable variability exists in the amplitude and duration of episodes of 2-to-30 day fluctuations. In particular, a strong annual modulation is evident throughout the record. Submonthly fluctuations in PC 3 during the northern hemisphere warm season are considerably weaker than those of the cool season, consistent with the seasonal variation of power seen in the seasonally-averaged wavelet spectra shown in Fig. 3.3c.

Modulation of submonthly power of PC 3 also occurs interannually. For example 1974-75 and 1992-93 show considerably less overall amplitude than the rest of the record. The winter MONEX experiment during 1978-79 was noted for its weak surges (Lau and Chang 1987) and the winter period of December 1978 and January 1979 shows amplitude near the mean and much weaker than many of the other years. The subsequent increase in power in the late spring of 1979 corresponds primarily to several large-amplitude negative anomalies in PC 3 (lulls) that propagated from the north. These dates can be seen in Tables 3.8 and 3.9 of key dates for PCs 5 and 6. The example illustrates that the modulation of variance occurs on both negative and positive fluctuations of PC 3. Fluctuations in variance must therefore be

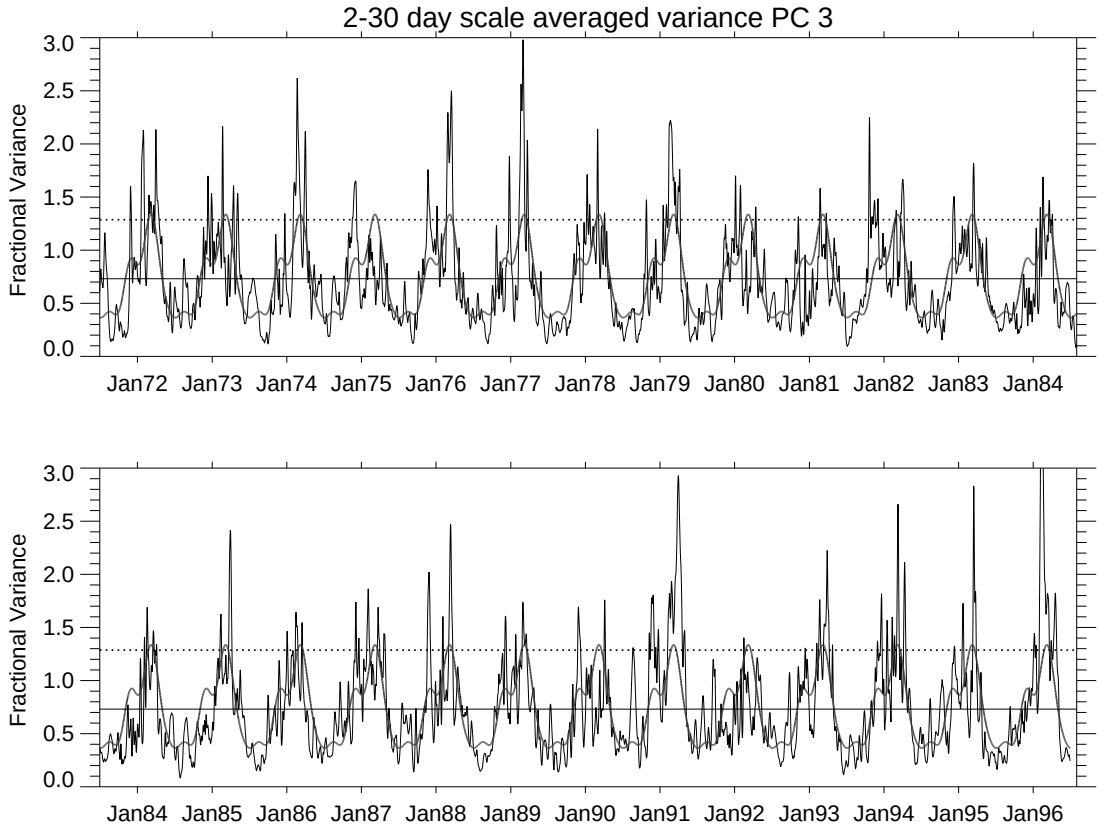

Figure 4.2. Time series of the scale-averaged wavelet spectrum, the submonthly variance time series, (C.24) for PC 3 from 1971–1996 is shown by the varying black curve. Power is averaged over the submonthly (2-30 day) band. The thin dashed line indicates the 95% confidence level from (C.26) for PC 3 (assuming red noise $\alpha = 0.61$). The thin black line is the mean of the variance time series (percent variance of PC 3 in the submonthly band is 73.1%). The gray curve shows a 4-harmonic fit to the annual cycle of the variance time series. 1983–1984 are reproduced in the second panel.

interpreted as changes in episodes of both pressure surges and lulls. Since surges and lulls appear to have similar dynamics over East Asia (Sec. 3.5) identifying the time periods of enhanced and reduced submonthly variance may help in understanding more about the mechanisms responsible for their occurrence.

Modulation of the submonthly power in PC 3 also occurs at periods shorter than annual in Fig. 4.2. By visual inspection, it is difficult to distinguish between modulation occurring from the seasonal cycle (the harmonics of the annual) or from higher frequencies. To quantify the interannual to subseasonal timescales of the modulation of submonthly variance Figure 4.3 shows a power spectrum of the PC 3 submonthly variance time series. Fourier analysis of the scale-averaged variance time series quantifies the timescales of the modulation of the variance. The dashed gray bars indicate a period of 18 and 22 months. Tomita and Yasunari (1996) found significant spectral peaks in this band for interannual variations in the monthly pressure difference between the Siberian High and the Aleutian Low and interannual variations of the monthly mean low-level meridional wind over the South China Sea. Tomita and Yasunari (1996) also found significant spectral peaks at 24 and 40 months in these variables and hypothesized that this biennial or quasi-biennial variation was associated with changes in surge activity. With the power spectrum of Fig. 4.3 it is difficult to tell if the spectral features at periods longer than 22-months are significant or meaningful. These longer timescale features are certainly less pronounced than the 18-22 month peak, suggesting that the argument of Tomita and Yasunari (1996) that quasi-biennial variations in monthly mean variables over the East Asian region are indicative of changes in surge activity should investigated more throughly with a longer record since a modulation at longer than 22 months appears as a weak signal at best here. A quasi-biennial oscillation in the summer and winter

monsoons has been investigated in many previous studies using monthly mean data and modeling efforts (e.g., Nicholls 1978; Brier 1978; Meehl 1987; Yasunari 1989; Ropelewski *et al.* 1992; Meehl 1994; Shen and Lau 1995). The significance of the apparent observed 18-22 month modulation will be the subject of future study.

The solid gray curve in Fig. 4.3 indicates the first four harmonics of the annual cycle (periods of 365, 182.5, 121.667, and 91.25 days). Dominant spectral peaks occur at all four of these periods. The seasonal modulation of the PC 3 submonthly variance is more complicated than the visually identified annual modulation described above. The comparative amplitudes of the peaks at 1/2 and 1/3 of the annual period indicate that significant asymmetry in the modulation of the variance may exist over the course of the seasonal cycle.

The thick gray curve in Fig. 4.2 is the least-squares fit of the PC 3 submonthly variance time series to the first four harmonics of the annual cycle. The amplitude of the spectral peaks of the harmonic fit is shown in Fig. 4.3 by the solid gray spectrum. The amplitude of the harmonic fit is close to the amplitude of the seasonal modulation, except at the fourth harmonic, where some of the modulation must not correspond as well to a sinusoid.

The seasonal variance time series for PC 3 is reproduced in Fig. 4.4a. The seasonal cycle of PC 3 submonthly variance is maximum in the spring and minimum in mid-summer. A relative maximum in late November is followed by a relative minimum in January. The seasonal modulation of the submonthly variance of PC 3 relates directly to the episodes of surges listed in Table 3.6. Figure 4.4b shows the monthly frequency distributions of the key dates of surges of PC 3. All months have been used. The monthly distribution of strong surge episodes mirrors the distribution of submonthly variance seen in Fig. 4.4a. The seasonal cycle of the PC 3 submonthly

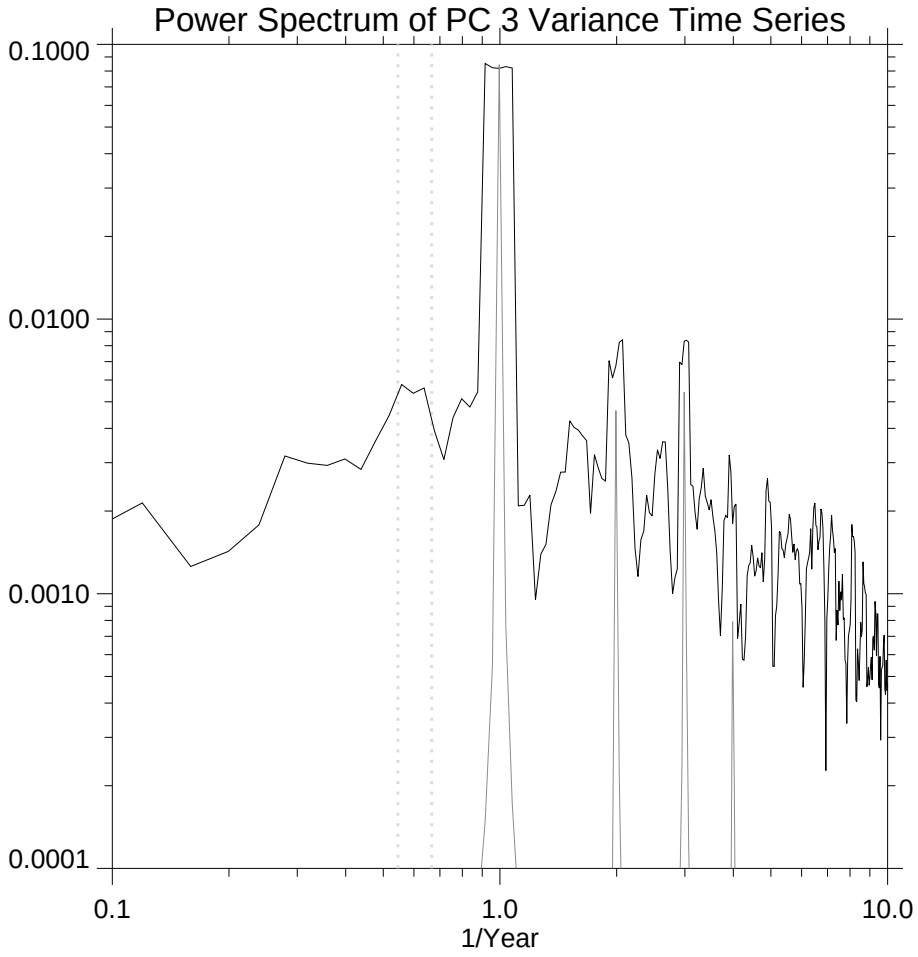

Figure 4.3. Log-log fourier power spectrum plotted versus frequency in $years^{-1}$ of the PC 3 submonthly variance time series shown in Fig. 4.2. The solid gray lines indicate the periods of the first four harmonics of the annual cycle (1, 0.5, 0.33, and 0.25 years). The dashed gray line indicates a period of 22 months.

variance forms a good proxy for the expected seasonal distribution for the occurrence of large positive values of PC 3.

The strong similarity in the submonthly seasonal variance and PC 3 key date distributions seen in Fig. 4.4 suggests that large-scale positive pressure anomalies over East Asia have a minimum occurrence in January. If it can be assumed that large departures from the climatological mean are of interest dynamically, then such a finding is useful and should be explored further. Studies using threshold-based definitions have found a variety of seasonal distributions, with a maximum or relative maximum in frequency of "surges" reported in November (Wu and Chan 1995; Zhang *et al.* 1997), December (Lai 1989), January (Wu and Chan 1995), and March (Zhang *et al.* 1997) and a minimum or relative minimum in frequency found in November (Joung and Hitchman 1982), December (Wu and Chan 1995), February (Zhang *et al.* 1997), and March (Lai 1989). Joung and Hitchman (1982) reported equal frequency in December-February.

The surge definitions that use absolute thresholds of a variable are biasing the statistics of events by directly incorporating the variations of the winter circulation seasonal cycle. For example, Fig. 4.5 shows the seasonal cycle of SLP averaged over the eastern edge of the Siberian High (50°N- 40°N, 100°E-110°E) and the seasonal cycle of the submonthly variance for PC 6, the mode which dominates this region (Fig. 3.1f). Criterion for surge occurrence based on a threshold of pressure intensity (Ding 1990; Zhang *et al.* 1997) are introducing a bias in January, when the mean Siberian High reaches its maximum (Fig. 4.5a). However, the submonthly variance of PC 6, like PC 3 (Fig. 4.4a), has relative maximum in December and March, with a relative minimum in January. The similarity in the

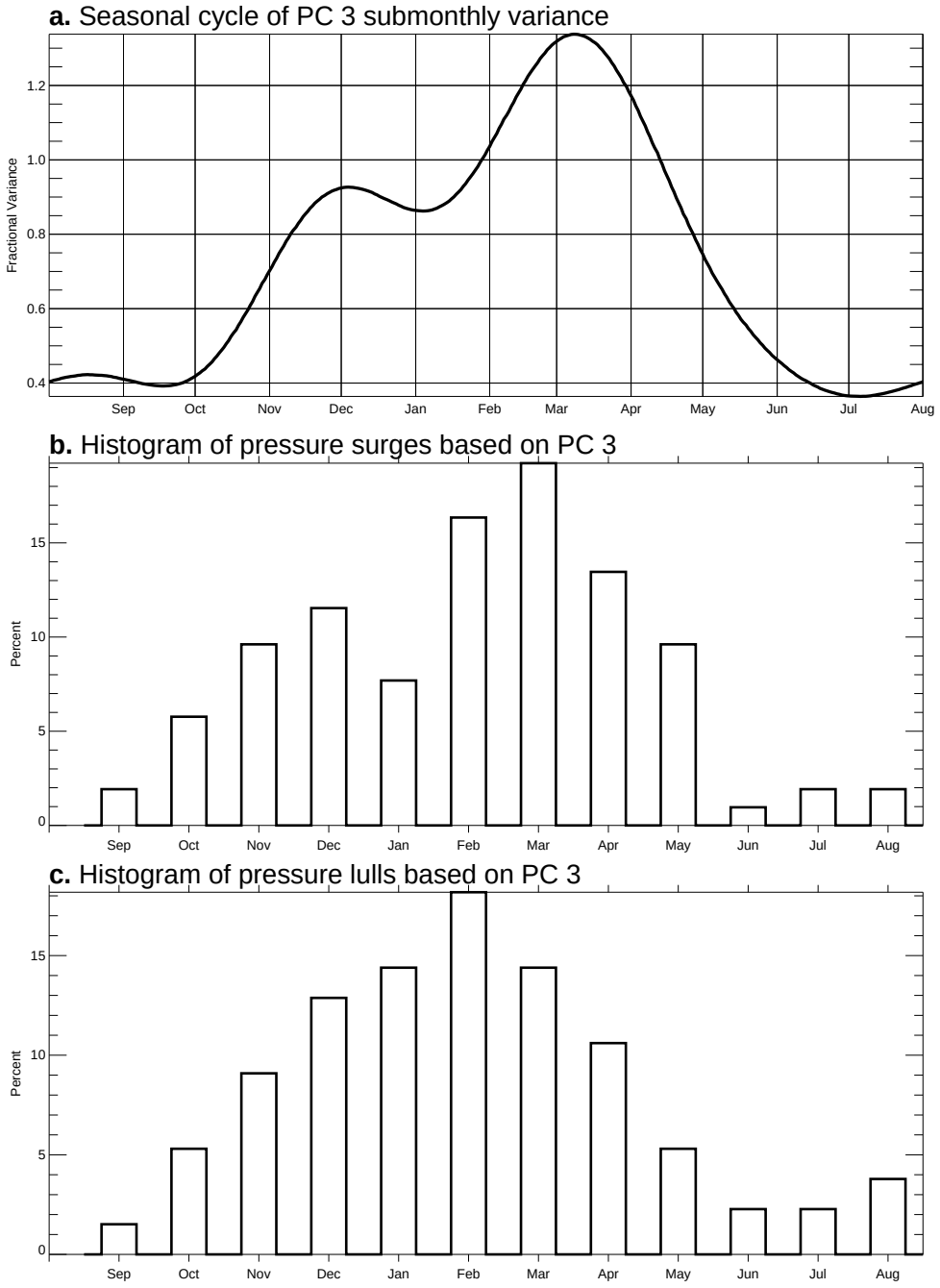

Figure 4.4. (a) Time series of the 4-harmonic fit to the annual cycle of the variance time series in Fig. 4.2. (b) Frequency distribution of relative maxima of PC 3 greater than 2.0.

seasonal cycles of submonthly variance of both PCs 3 and 6 and the correspondence with PC 3 key dates strongly suggests that large-scale atmospheric perturbations associated with pressure surges have a relative minimum in January. For the same threshold, defined events in March represent a much larger perturbation to the atmospheric circulation than events in January, with a larger contribution to the anomaly fluxes of heat and momentum associated with the East Asian region (Blackmon *et al.* 1977; Boyle 1986). Similarly, studies determining surge frequency using a definition that incorporates a wind magnitude threshold over South China or Hong Kong (e.g, Chang and Lau 1982; Lau 1982; Lau *et al.* 1983; Lau and Lau 1984; Lau and Chang 1987; Lai 1989; Ding 1990; Wu and Chan 1995; Zhang *et al.* 1997) are including a bias in November and December, when the northeasterlies reach their minimum over this region (not shown). Studies of the interannual variability of surge frequency using a biased frequency will be directly incorporating interannual timescale variations, such as a weakening of the monthly mean northeasterlies over the South China Sea during El Nino events (Rasmusson and Carpenter 1982), into the statistics of variations in the much higher-frequency perturbations that are associated with surges (Figs. 3.3c, e, and f).

4.3 Modulation of Upper Level Wave Activity over Asia

Figure 4.6 shows the seasonal cycle of scale-averaged variance of 500 hPa geopotential height averaged over the bands of 2-30, 2-6, and 6-30 days in the vicinity of the Siberian High. The seasonal cycle submonthly variance of PC 3 is also shown. As discussed in Sec. B.4.2 and seen in Fig. 3.15b, midlatitude wave activity in the vicinity and to the east of the Siberian High appears important for the development of pressure surges, a result similar to that found in several studies (Chang and Lau 1982; Joung and Hitchman 1982; Lau and Lau 1984; Boyle 1986;

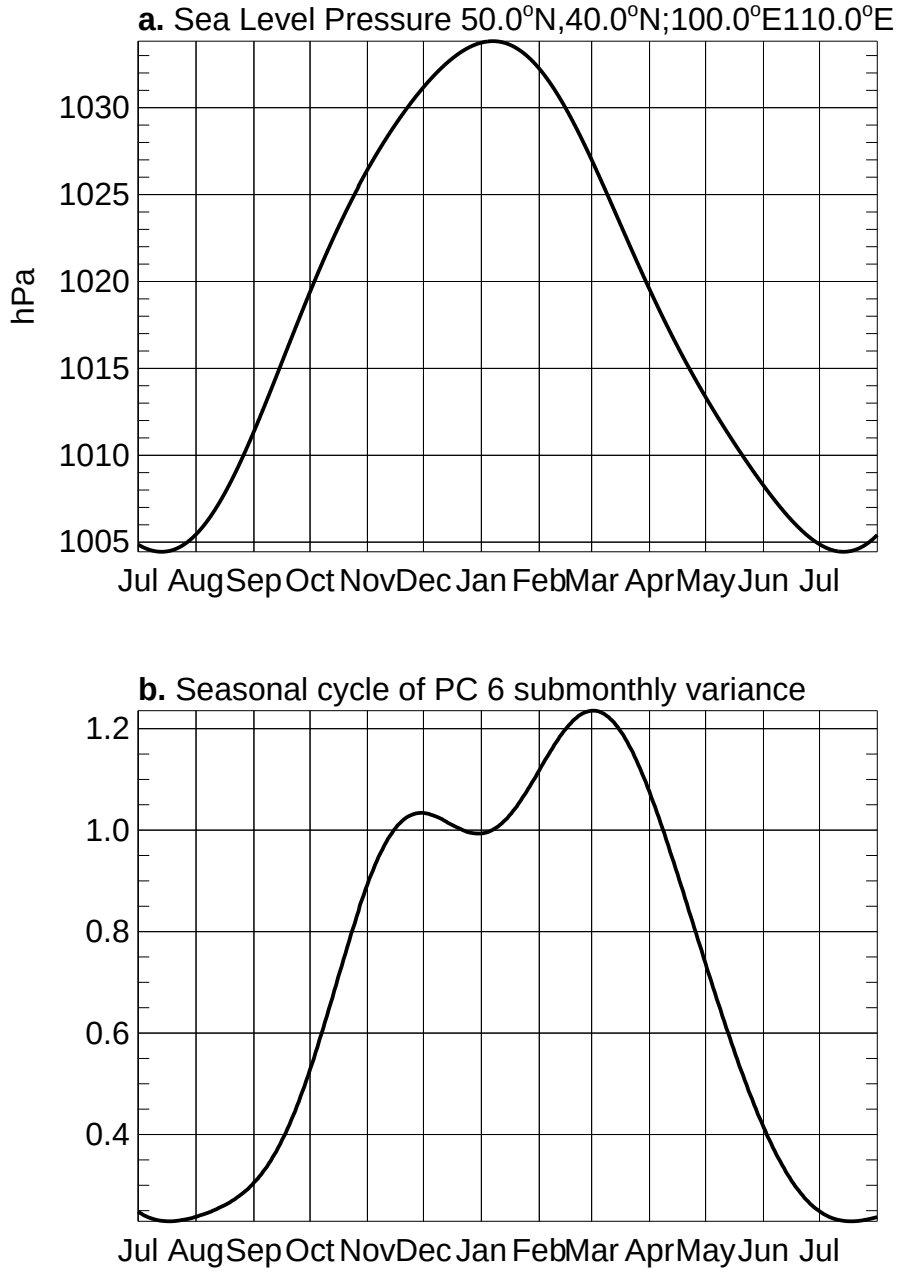

Figure 4.5. (a) Time series of seasonal cycle of SLP averaged over 50°N- 40°N, 100°E-110°E. (b) Time series of the 4-harmonic fit to the seasonal cycle of the PC 6 submonthly variance time series.

Hsu 1987). However, the 6-30 day timescale used in Sec. B.4.2 is longer than the timescale usually associated with baroclinic wave activity and more related to the ”intermediate” timescale waves associated with two-dimensional Rossby-wave dispersion (Hoskins *et al.* 1977; Hoskins and Karoly 1981; Hoskins 1983; Blackmon *et al.* 1984; Kiladis and Weickmann 1992; Tomas and Webster 1994; Kiladis 1996). The correspondence between the seasonal cycles of the 6-30 day variance of 500 height and 2-30 day variance of PC 3 in Fig. 4.6b suggests that the observed modulation of the PC 3 variance is closely related to the modulation of intermediate timescale wave activity during mid-winter. Note that this mid-winter minimum is not the same as (Nakamura 1992) found in baroclinic wave activity (2-6 days) which was related to the winter increase in the East Asia jet being unfavorable for the growth of baroclinic waves. The minimum seen in 2-6 day variance in 4.6b is related to the Pacific baroclinic wave activity minimum of (Nakamura 1992) and occurs at the same time of the year as observed in that study. (Nakamura 1992) hypothesized that some of the reduction in Pacific baroclinic wave activity might be related to a decrease in the seeding from the Asian continent.

As shown in Fig. 4.5a, the Siberian High attains maximum amplitude during early January, the period corresponding to decreased variance in intermediate timescale wave activity and decreased variance in PC 3 (Fig. 4.6c) and PC 6 (Fig. 4.5b). The increased stability of the lower atmosphere may play a role in diminishing the amplitude of the intermediate timescale wave activity creating an unfavorable environment for the activation of surges, even though the high-frequency wave activity associated with surge activation has not diminished (Fig. 4.6b).

Figure 4.7 shows the 250 hPa annual cycle of meridional wind to the northwest and zonal wind to the south of the modulated region of intermediate timescale

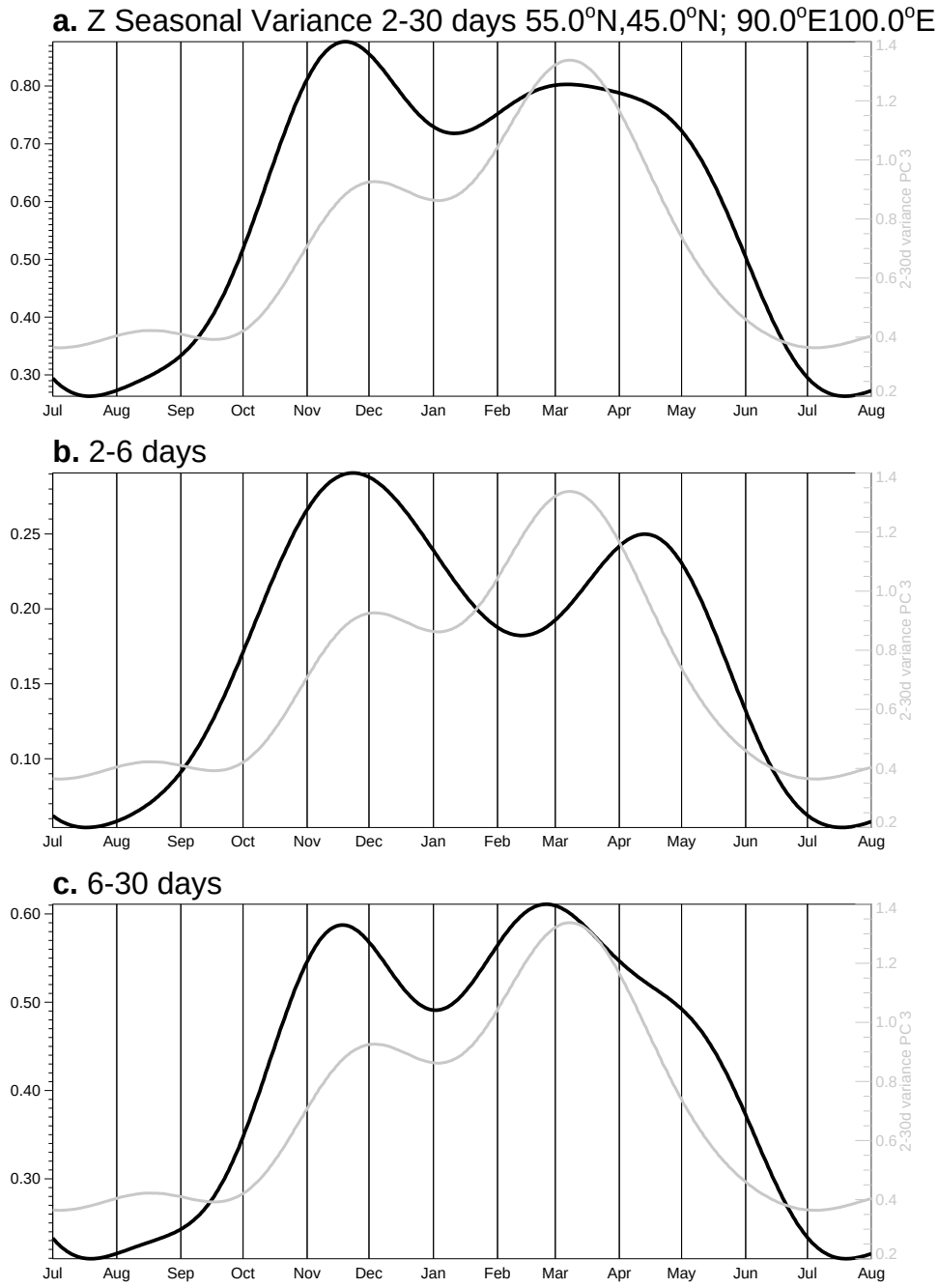

Figure 4.6. (a) Time series of seasonal cycle of geopotential height scale-averaged over 2-30 days in the region 55°N- 45°N, 90°E-100°E. (b) same as a but scale averaged over 2-6 day. (c) same as (a) but scale averaged over 6-30 days. The gray curve indicates the submonthly variance of PC 3 from Fig. 4.4a.

wave activity. Blackmon *et al.* (1977) suggested that the intermediate timescale wave activity was controlled by the entrance regions of the jet streams. Figure 4.7 shows that the northlies over northern central Siberia vary coincidentally, albeit weakly, with the submonthly variance of the upper-level wave activity and surge activity while the westerlies to the south do not vary sympathetically, suggesting that another mechanism, perhaps seasonal variations in the stationary wave amplitude over this region may cause the modulation of intermediate timescale upper-level wave activity that appears directly linked to the seasonal modulation of surge activity.

4.4 Summary

Observations of the seasonal modulation of pressure variance over East Asia have been reported. A maximum amplitude in PCs 3 and 6 in March and minimum amplitude in the warm season are evident. A relative maximum in November-December followed by a relative minimum in December-January is also observed. Episodes of large anomalies in pressure show a similar seasonal cycle to that of the variance suggesting that the submonthly variance of PC 3 well describes the modulation of surge activity.

The overall seasonal modulation of surge activity appears well correlated to the seasonal modulation of intermediate timescale upper level wave activity over northern Asia. As the activation of surges has been linked to upper level midlatitude waves, the relationship between the two is strengthened by the observed sympathetic modulation. However, the sympathetic modulation of upper-level wave activity occurs on the 6-30 day timescale, rather than the usual synoptic timescale reported as the direct link to surge activation.

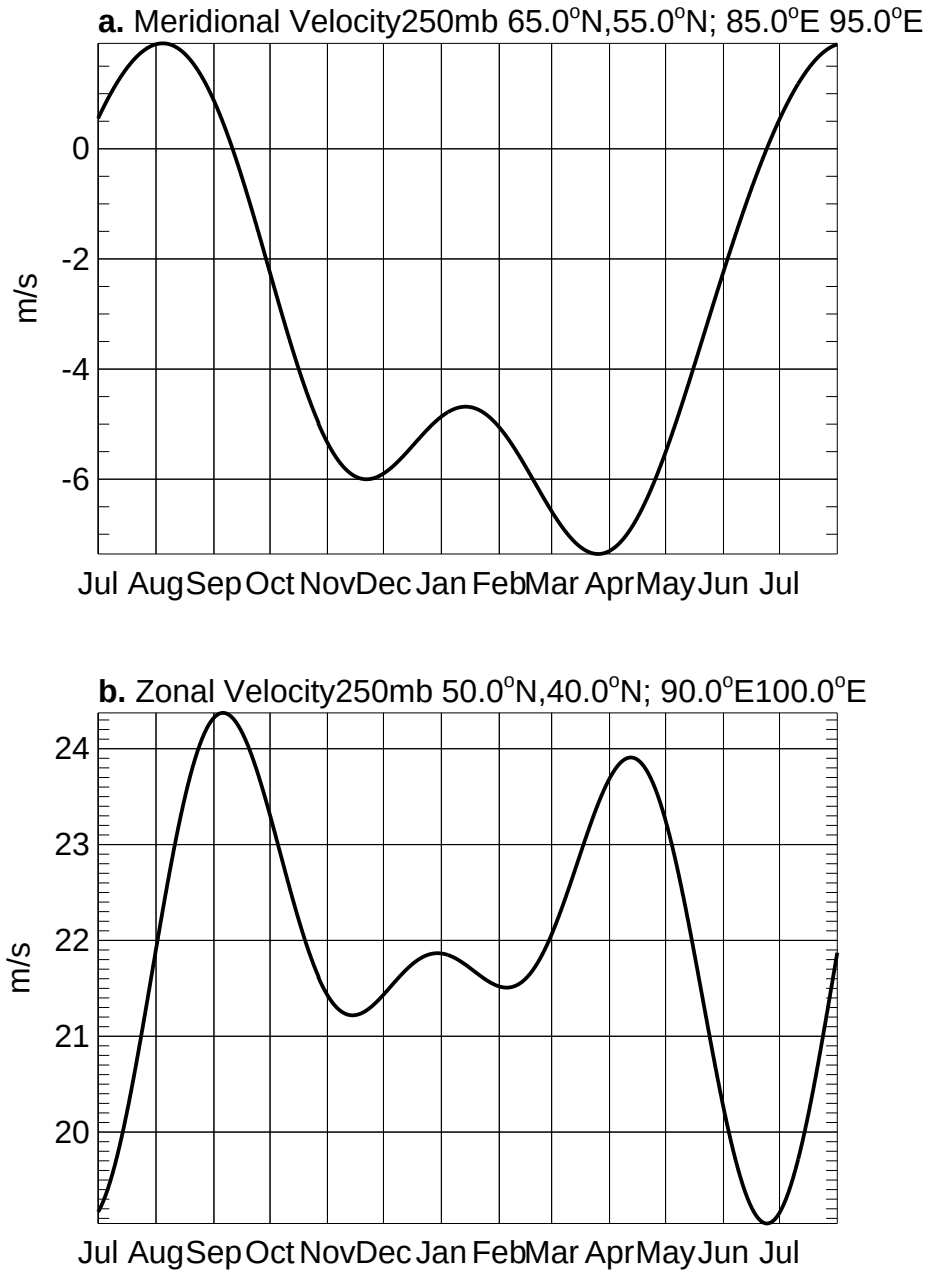

Figure 4.7. (a) Time series of seasonal cycle of 250 hPa v averaged over $65°$N- $55°$N, $85°$E-$95°$E. (b) as in (a) but for 250 hPa u averaged over $50\circ$N- $40°$N, $90°$E-$100°$E.

Changes in the lower tropospheric stability and changes in the upper tropospheric circulation may provide a dynamical mechanism for the observed modulation of intermediate timescale wave activity during midwinter. The changes in the upper level winds reported appear small, however, compared to their overall scale. The sensitivity of wave amplitude to small changes in the upper level zonal winds and moderate variations in the upper level meridional wind is needed to provide further evaluation of the importance of seasonal changes in the intensity of the jet entrance region or changes in the stationary wave amplitude. Further investigation is also needed to determine the mechanisms behind these sympathetic modulations of upper level wave and surge activity on preferred timescales.

CHAPTER 5

INTRASEASONAL MODULATION OF EAST ASIAN PRESSURE SURGES

In this chapter, East Asian pressure surges, as represented by the South China Sea Mode (Fig. 3.1c), are shown to be modulated at a 35-40 day time scale. The modulation of East Asian pressure surges is associated with changes in the submonthly variance of SLP, low-level winds, and upper level wave activity. The enhanced periods of submonthly variance in East Asian pressure surges precede development of the active phase of the MJO in the Indonesian and Australian regions. The development of the active phase of the MJO appears subsequently to create upper-level circulation anomalies that are unfavorable for surges, resulting in a modulation of surge activity.

5.1 Modulation of Submonthly Variance

As shown in Fig. 3.3c, submonthly variance of the South China Sea Mode is large compared to the mean variance at all scales during the northern hemisphere cool season. As discussed in Sec. 3.7, the PC associated with the South China Sea Mode is an objective indicator of episodes of pressure surges and lulls that have a significant tropical influence. To examine the intraseasonal modulation of these episodes, a wavelet analysis is performed on the complete record of PC 3 and the submonthly variance (2 to 30 days) is constructed by averaging the wavelet power spectrum in scale according to (C.24).

Figure 5.1 shows the composite South China Sea PC (3) submonthly variance based on days of maximum statistically significant submonthly variance during November-March using 1971/72–1995/96 (time series and significance level are shown in Fig. 4.2). The thick solid line indicates the composite variance lagged and lead about the day of maximum significant variance. The thin dashed lines denote the 95% confidence interval for the composite using (C.20) with the DOF calculated from (C.28). The thin solid line indicates the background variance (see Sec. 2.2.3 for calculation of composite background variance). Key dates used in forming the composite are given in Table 5.1. The time periods where the background variance lies outside of the confidence interval are considered significant at the 95% level. Aside from the periods near Day 0 that are significantly different from the background, a statistically significant reduction in variance is observed around Day +20. The 7-10 day period of low submonthly variance is followed by an increase in variance. Periods prior to Day 0 are seen to also show an increase and a reduction in variance, but these estimates cannot be confidently distinguished from the background variance. The composite shows that the submonthly variance in the South China Sea PC is significantly modulated at a period of about 35-40 days.

To determine whether any individual scales are dominate during the modulated periods, Fig. 5.2 shows the composite local spectrum based on the key dates in Table 5.1. Assuming the global wavelet spectrum of PC 3 (Fig. 3.2c) as the appropriate background, the regions where GWS lies outside the 95% confidence interval of the composite spectrum are indicated by the white contours. The 40-day modulation of submonthly variance is seen to be largely confined to periods less than 20 days, the same time scales identified directly with occurrences of pressure surges in Appendix B. As the PC of the South China Sea Mode is identified with pressure surges

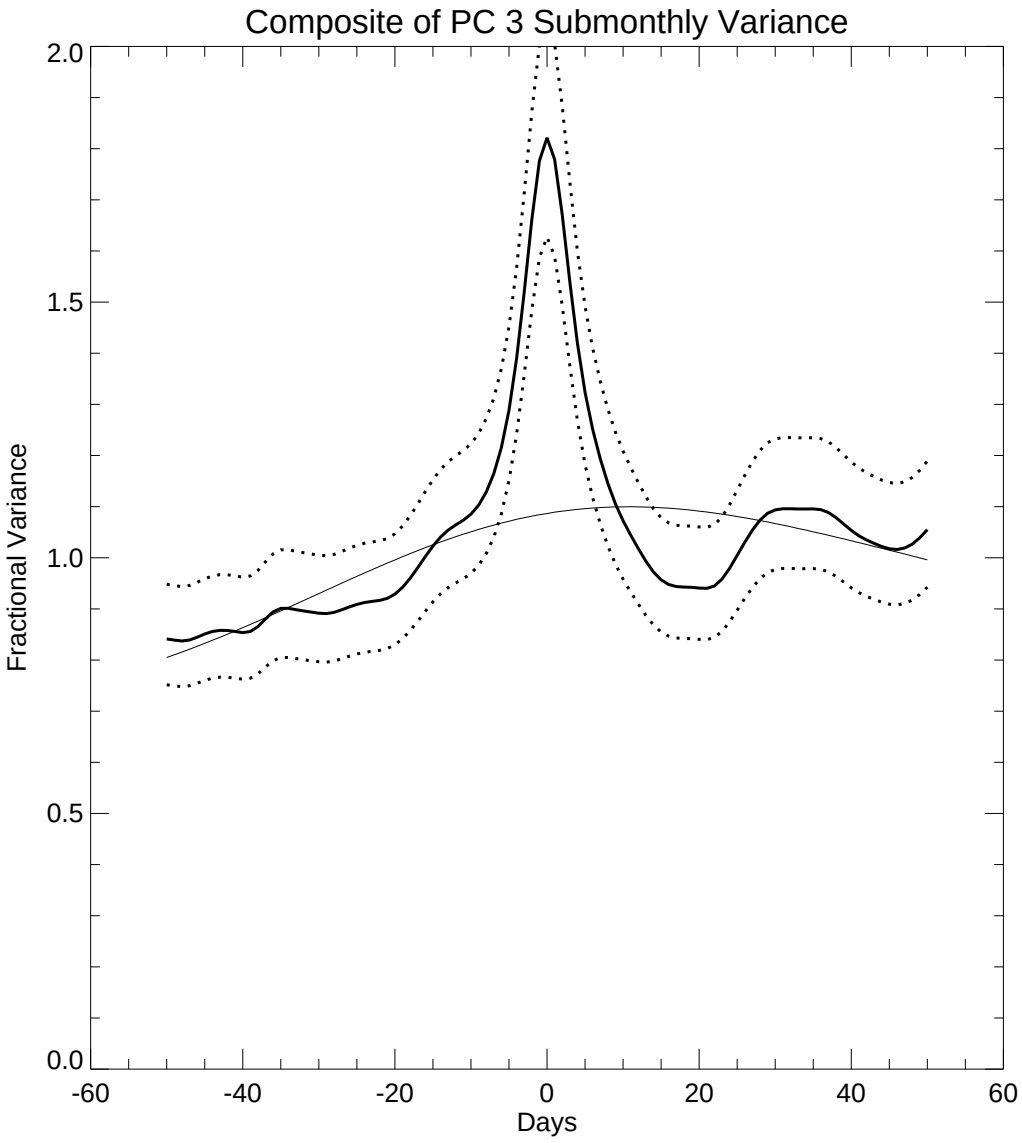

Figure 5.1. Time-lag composite of the PC 3 submonthly (2-30 day) variance based on periods when the PC 3 submonthly variance is maximum and significant at the 95% level compared to red noise The dashed curves indicate the composite 95% confidence interval from (C.20). The thin black curve is the background variance appropriate for each time point.

Table 5.1. Date of Maximum PC 3 submonthly (2-30) day variance exceeding the 95% significance level compared to red-noise for November–March.

Nov	29	1971	Feb	15	1986
Jan	30	1972	Mar	17	1986
Feb	27	1972	Dec	5	1986
Dec	12	1972	Feb	4	1987
Feb	21	1973	Mar	24	1987
Dec	22	1973	Nov	28	1987
Feb	21	1974	Feb	4	1988
Dec	4	1974	Mar	12	1988
Nov	23	1975	Dec	6	1988
Jan	6	1976	Jan	25	1989
Mar	17	1976	Mar	1	1989
Dec	25	1976	Nov	28	1989
Mar	2	1977	Nov	28	1990
Jan	10	1978	Dec	24	1990
Mar	2	1978	Feb	26	1991
Feb	21	1979	Feb	15	1992
Jan	6	1980	Dec	12	1992
Jan	30	1980	Feb	21	1993
Nov	8	1980	Mar	29	1993
Feb	23	1981	Dec	20	1993
Mar	25	1981	Jan	16	1994
Dec	2	1981	Feb	10	1994
Mar	2	1982	Mar	11	1994
Dec	10	1982	Dec	12	1994
Mar	16	1983	Jan	23	1995
Feb	18	1984	Mar	16	1995
Mar	19	1984	Jan	7	1996
Feb	13	1985	Feb	10	1996
Mar	31	1985			
Jan	3	1986			

on the submonthly timescale, the 40-day modulation indicates a modulation of surge episodes, with the period of low variance corresponding to reduced surge activity, as well as reduced amplitude of negative anomalies. Note that the composite wavelet spectrum also shows enhanced power between timescales of 40 and 50 days, with maximum amplitude coinciding with the minimum amplitude in submonthly variance.

Power at 40-50 days is not just a result of the observed modulation as the scales exceeding multiples of the square root of two (20 days and 40 days) are well separated for the Morlet wavelet and only a discrete 40-50 day variation in the time series will produce power at that scale, while modulation appears as oscillatory increases and decreases in the power of the smaller scale occurring at the period of the larger scale.

5.2 Variance Composites

Coincident with the enhanced submonthly variance seen in the composite of the South China Sea Mode submonthly variance (Fig. 5.1), a regional enhancement of submonthly SLP variance is expected. Figure 5.3a shows the submonthly SLP variance composite based on the key dates in Table 5.1. Enhanced and reduced regions of SLP 2-30 day variance are shown relative to each gridpoint's background variance. Light shading indicates enhanced variance; dark shading indicates reduced. The shaded regions show the enhanced or reduced regions locally significant at the 80% confidence level. The line contours indicate the regions that are locally significant at the 95% level. A region of enhanced submonthly SLP variance extends from midlatitude Siberia around the Tibetan Plateau and across China into the South China. The region of the enhancement is much larger than the scale of the South China Sea Mode itself (compare with Fig. 3.1c).

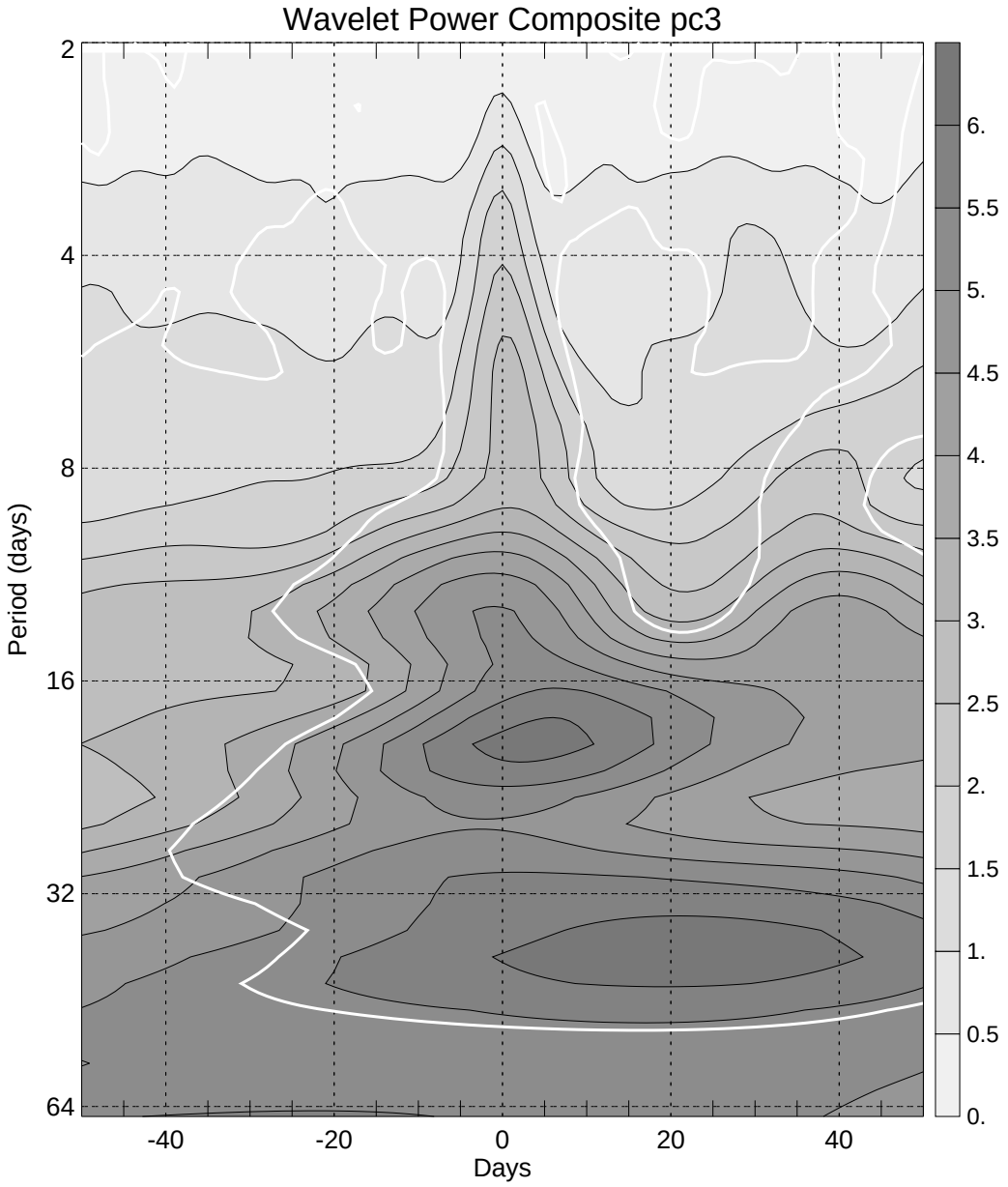

Figure 5.2. Time-lag composite wavelet spectrum of the PC 3 corresponding to Fig. 5.2. The white lines indicate the composite where the global wavelet spectrum (Fig. 3.2c), taken as the background spectrum, lies outside of 95% confidence interval from (C.20). The units are fractional variance. The contour interval is 0.05.

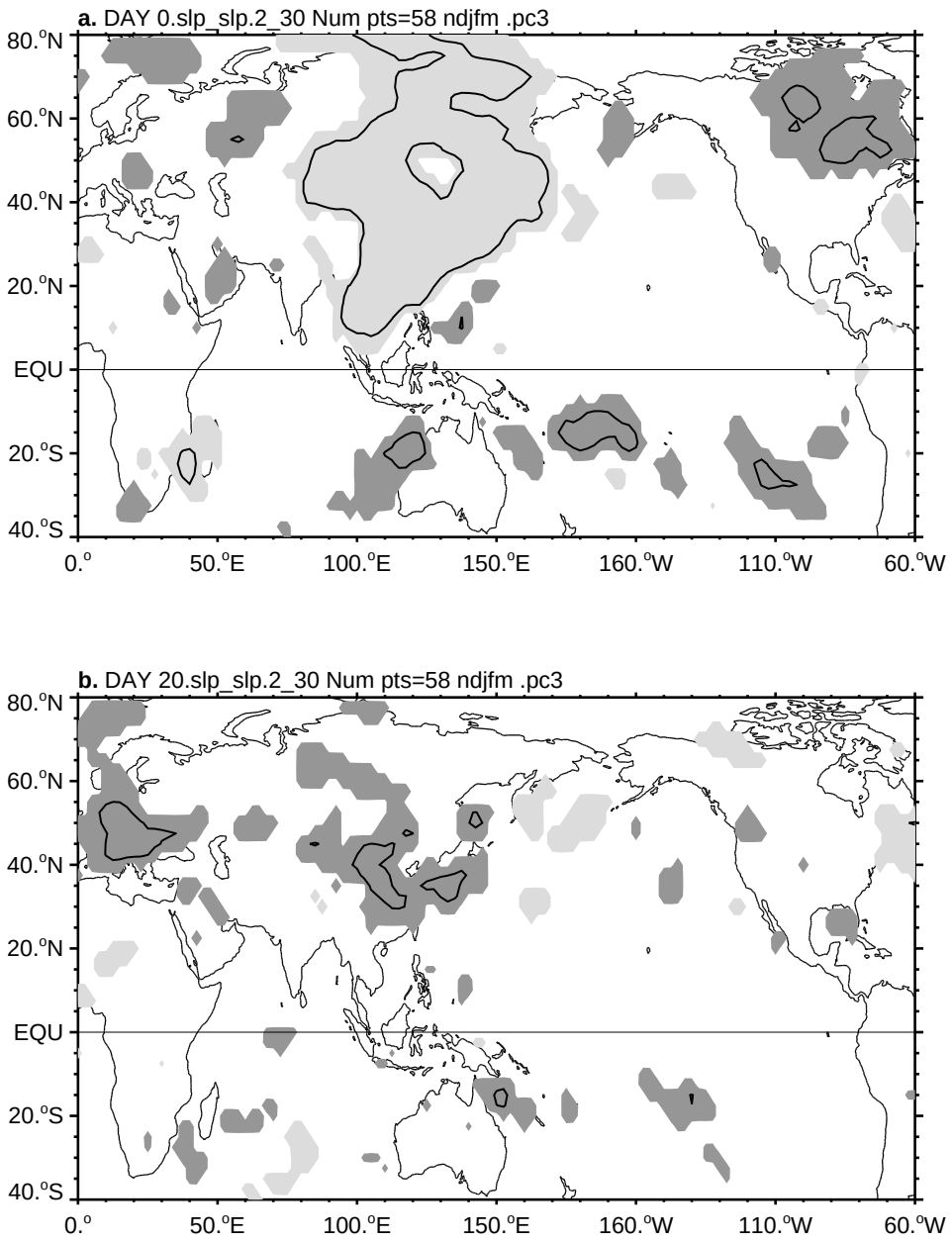

Figure 5.3. (a) Composite of the submonthly (2-30 day) SLP variance for Day 0 corresponding to Fig. 5.1. (b) corresponding to Day +20 of Fig. 5.1. The dark (light) shading indicates where the local background variance at each grid point lies below (above) the composite 80% confidence interval from (C.20). Line contours indicate where the local background variance at each grid point lies outside composite 95% confidence interval.

Figure 5.3b shows the composite submonthly SLP variance 20 days after the maximum submonthly variance in the South China Sea PC. The reduced submonthly variance of the South China Sea PC seen in Fig. 5.1 is associated with reduced submonthly SLP variance over much of the East Asian region. Notably, variance is significantly reduced over the East China Sea, the dominant region for the path of the anticyclone associated with pressure surges as seen in Fig. B.5. In previous days, the region of reduced variance is confined to the midlatitudes and in subsequent days, the region of reduced variance never extends as far into the tropics as that seen for the enhanced variance in Fig. 5.3a.

The changes in the submonthly variance of the South China Sea Mode are also associated with significant changes in the variance of lower tropospheric winds (Fig. 5.4). Figure 5.4a shows the composite submonthly 850 hPa meridional wind variance associated with Day 0 of Fig. 5.1. The region of enhanced meridional wind variance largely coincides with that seen in the SLP variance. Figure 5.4b shows that the significantly enhanced composite submonthly 850 hPa zonal wind variance extends well into the deep tropics over the South China Sea. Both variables show a significant reduction in variance over the tropical South Pacific.

As discussed in Sec. B.4.2 and seen in Fig. 3.15b, midlatitude upper-level wave activity in the vicinity and to the east of the Siberian High appears important for the development of pressure surges, a result similar to that found in several studies (Chang and Lau 1982; Joung and Hitchman 1982; Lau and Lau 1984; Boyle 1986; Hsu 1987). Figure 5.5 shows the composite submonthly 500 hPa geopotential height and 250 hPa meridional wind variance associated with Day 0 of Fig. 5.1. Significant enhanced upper-level wave activity coincident with the enhanced variance of the South China Sea mode is indicated throughout the midlatitudes from the Asian

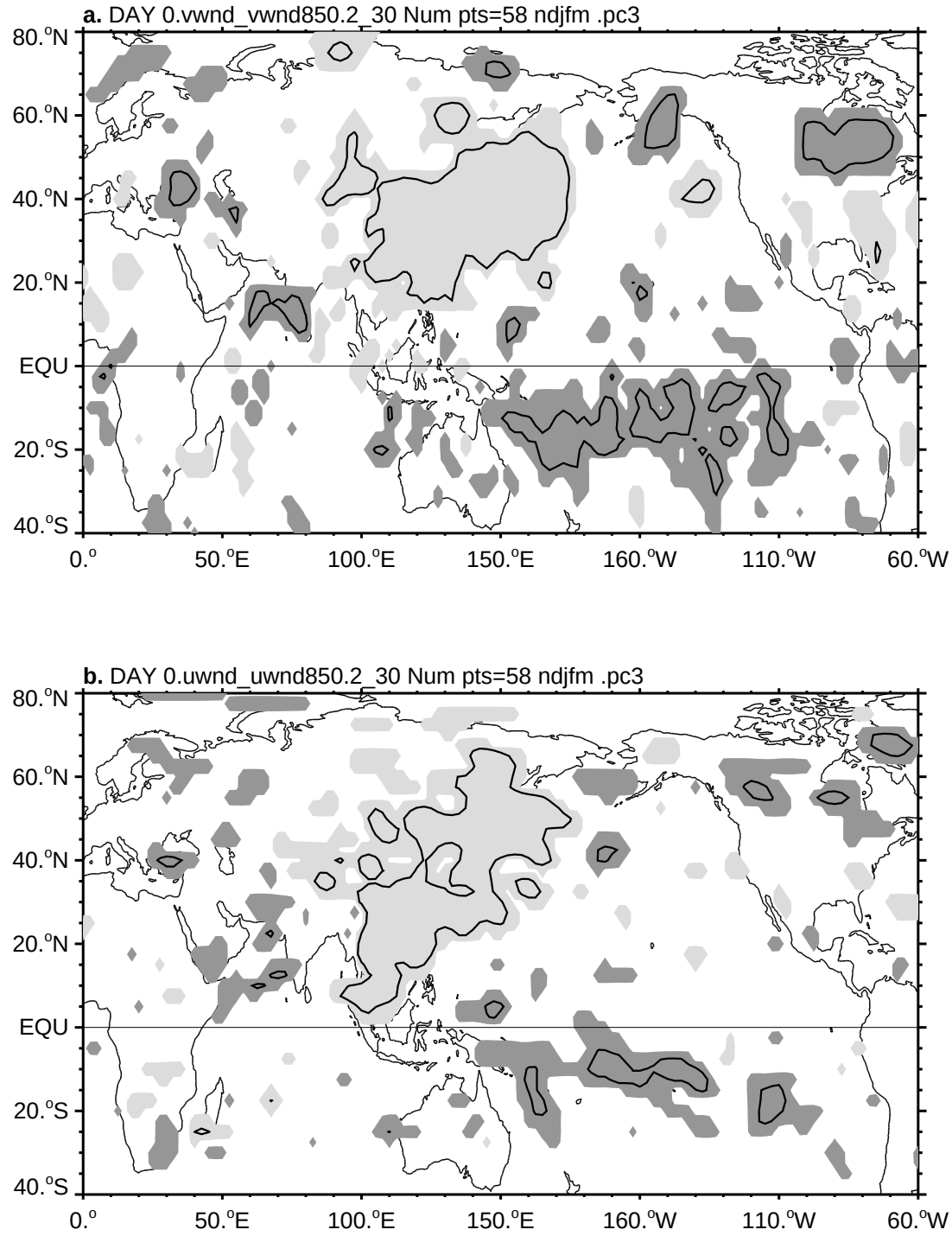

Figure 5.4. As in Fig. 5.3 but for (a) submonthly 850 hPa v variance for Day 0. (b) for submonthly 850 hPa u variance for Day 0.

continent into the Pacific.

The separation of the enhanced upper-level wave activity from the enhanced SLP variance over China seen by comparing Figs. 5.3a and 5.5a is further indication that the low-level surges become separate from the midlatitude upper-level waves as the surges penetrate into the tropics (Sec. B.4.2) The enhancement of the upper-level wave activity at the time of enhanced pressure variance is consistent with the hypothesis found in the sympathetic seasonal modulation of PC 3 submonthly variance and intermediate timescale upper-level wave activity in Fig. 4.6c. However, in Fig. 5.5a, wave activity across the 2-30 day band is enhanced. Composites using only 6-30 day variance of 500 hPa height indicate that the intermediate timescale wave activity increases in variance over the continent but does not show a significant increase over the Pacific (not shown). The exact nature of the relationship between upper-level wave activity in the intermediate timescale band and SLP anomalies in the submonthly band should be investigated further.

5.3 Intraseasonal Composites

Figure 5.6 shows the time evolution of the composite 30-70 filtered OLR along $5°$S corresponding to Fig. 5.1. The composite shows that a large significant positive OLR anomaly in the western Pacific, indicating suppressed convective activity, precedes the maximum submonthly variance in PC 3 by about two weeks. A large negative OLR anomaly develops south of Indonesia at Day -2 and progresses eastward at about 4-5 m s^{-1}. A small negative anomaly in the Indian Ocean is seen to precede the development of the Indonesian anomaly by about 10 days. In subsequent days, a strong positive anomaly propagates coherently from the central Indian Ocean to the central Pacific. The timescale for the apparent oscillation in OLR anomalies is about 40 days. Composites of unfiltered OLR anomalies (not shown) have a similar

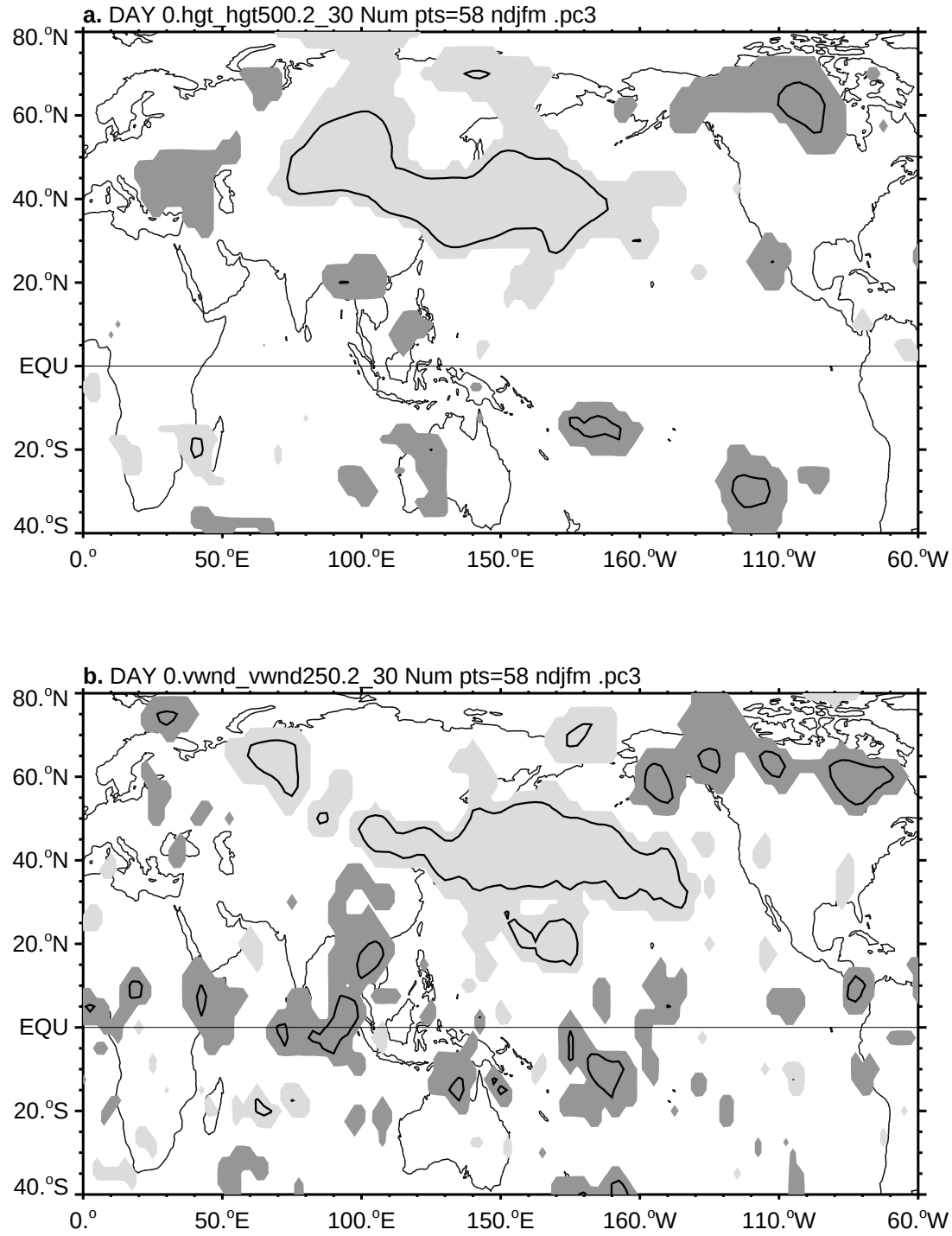

Figure 5.5. As in Fig. 5.3 but for (a) submonthly 500 hPa height variance for Day 0. (b) for submonthly 250 hPa v variance for Day 0.

eastward propagation

Figure 5.7 shows composite maps of 30-70 day 250 hPa circulation anomalies and 30-70 day filtered OLR anomalies corresponding to Fig. 5.1 for two of the composite days. The maps show that enhanced submonthly variance in PC 3 is preceded by a wave pattern in the subtropical circulation, enhanced northwesterly from over northern China, and easterly anomalies south of Japan. The midlatitude wind anomalies along 35°N over East Asia indicating a weakened or retracted East Asia jet. The configuration is similar to that found by Boyle (1986) in the monthly mean of December 1974, a month of large-amplitude surges. Day 0 (Fig. 5.7b) shows a strengthening of the pattern seen 5 days earlier, with the exception of a reduction in the strength of the positive OLR anomaly in the Pacific and the development of negative OLR anomalies around Indonesia. The wave pattern shows an arc of positive and negative circulation anomalies over East Asia.

The significant increase in upper-level wave activity in Fig. 5.5 over norther Central Siberia occurs in a region of 30-70 day timescale upper-level northwesterly anomalies (Fig. 5.7)b, which supports the hypothesis of Meehl *et al.* (1996) that such anomalies would be favorable for the development of upper-level wave activity. The northwesterly anomalies and increase in upper-level wave activity are similar to the seasonal modulation of upper-level wave activity in this region (Fig. 4.6) coincident with similar variations in the seasonal upper-level northerly flow (Fig. refclimuplev.fig). The similarity between the increase in upper-level wave activity in northerly flow on both the seasonal and intraseasonal timescales suggests that the dynamical mechanism for the modulation may be similar. Whether the hypothesized changes in the jet entrance region or changes in the stationary wave or some other mechanism are the dominant process for modulating the upper-level

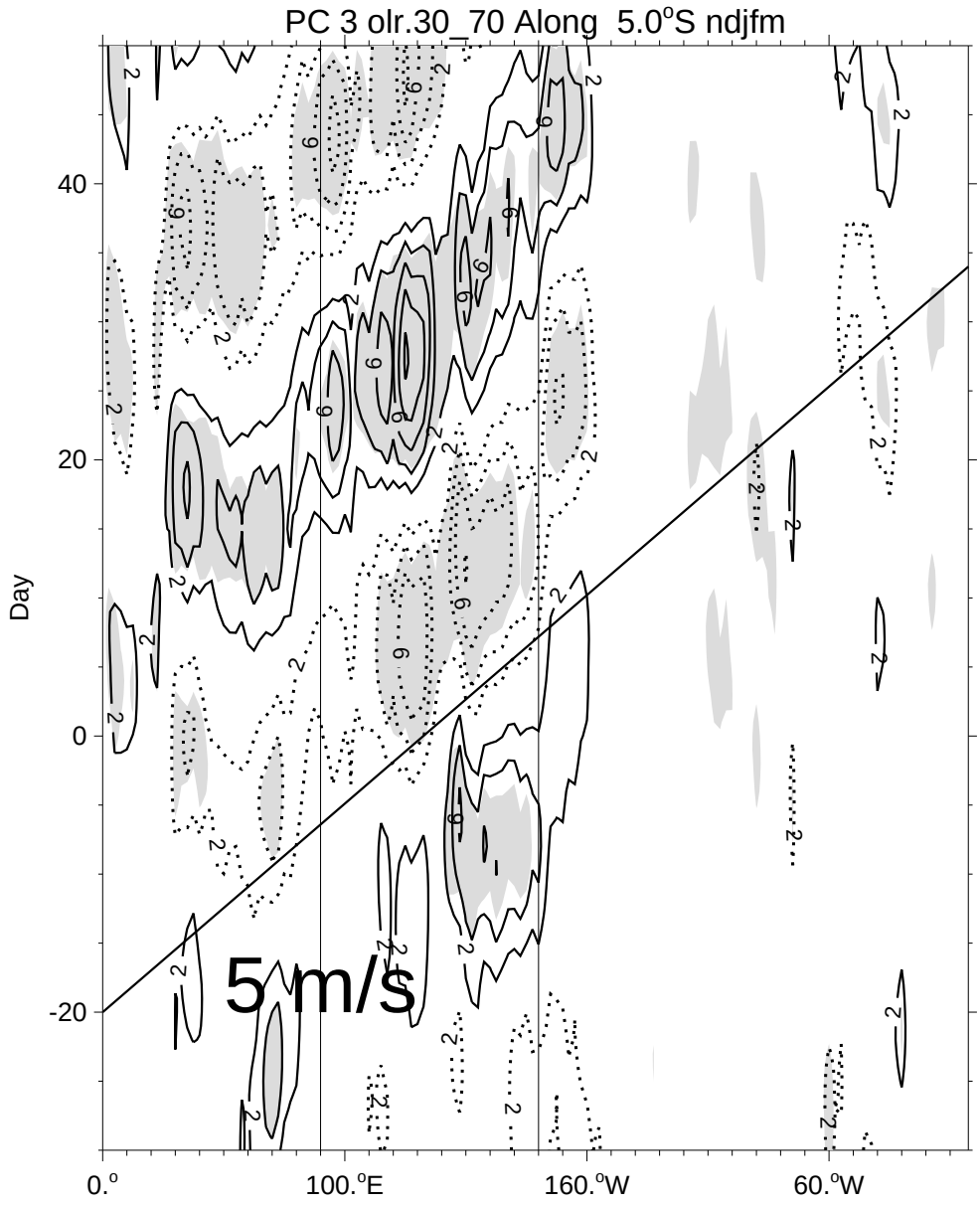

Figure 5.6. Composite of the 30-70 day filtered OLR along $5°$S corresponding to Fig. 5.1. Shading indicates where the composite value is locally significant at the 95% level. The contour interval is 2.0 W m^2 with the zero contour suppressed.

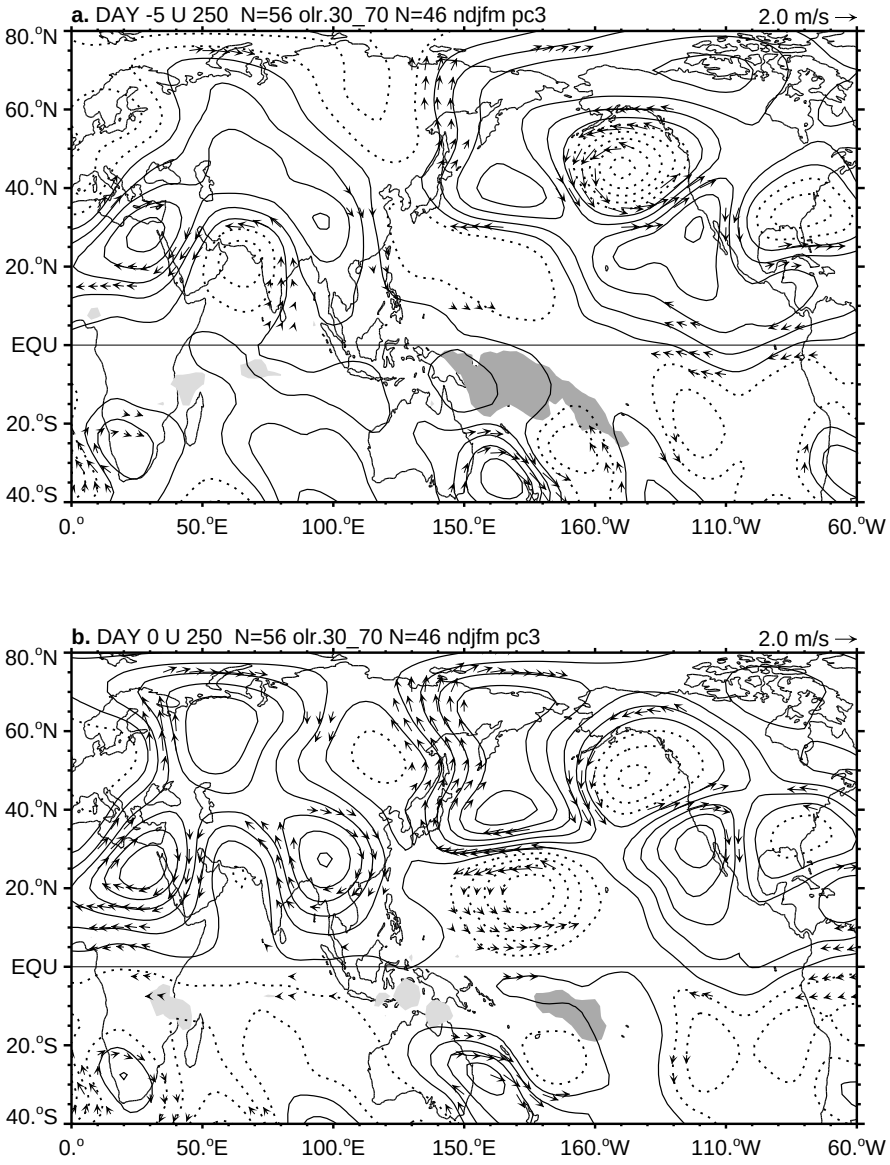

Figure 5.7. Composite (a) 250 hPa wind, streamfunction, and OLR anomalies corresponding to Fig. 5.1 Day -5. (b) Day 0. The number of episodes used in the composite of the NCEP Reanalysis variables (wind) and OLR is indicated. Wind vectors are shown where either u or v is locally significant at the 95% level. OLR anomalies are only contoured where they are locally significant at the 95% level. Contour level is $4.0\mathrm{Wm}^2$ for OLR. Positive (negative) anomalies of OLR are shaded dark (light). The streamfunction contour interval is $4.0 \times 10^5 \mathrm{m}^2\mathrm{s}^{-2}$.

wave activity should be investigated further.

Figure 5.8a shows the Day +5 circulation with the midlatitude Pacific easterly anomaly at its maximum and enhanced convective activity in the Indonesian-Australian region. The composite circulation has evolved to nearly the oppositely signed circulation pattern and convective anomalies of Fig. 5.7a. By Day +15 (Fig. 5.8b), the circulation anomalies in the midlatitudes are nearly opposite to those of Day -5, with an enhanced Pacific jet and southeasterly upper-level flow indicated over north central Siberia. Upper-level wave submonthly variance is significantly reduced in this region (not shown) and SLP submonthly variance is reduced over continental China (Fig. 5.3b) by Day +20, furthering the association between changes in the upper-level circulation modulating upper-level wave activity which then reduces surge activity.

The large-scale eastward moving anomalies seen in the composites of 30-70 day filtered data (Figs. 5.7 and 5.8) bear a strong resemblance to the cool season composites of PCs 1 and 2 in Figs. 3.12b and 3.13b with opposite sign. As discussed in Sec. 3.6, the circulation and convective anomalies seen in the composites of PCs 1 and 2 appear to be related to the MJO. The circulation and convective anomalies seen corresponding to the evolution of significantly enhanced submonthly variance in PC 3 similarly can be identified with the circulation and convective anomaly patterns in previous studies of the MJO (e.g., Madden and Julian 1972b; Weickmann *et al.* 1985; Kiladis and Weickmann 1992; Madden and Julian 1994; Salby and Hendon 1994; Meehl *et al.* 1996).

The development of the negative OLR anomalies around Day 0 of maximum surge activity provides statistical evidence documenting a relationship between the convective activity associated with the MJO and East Asian pressure surges

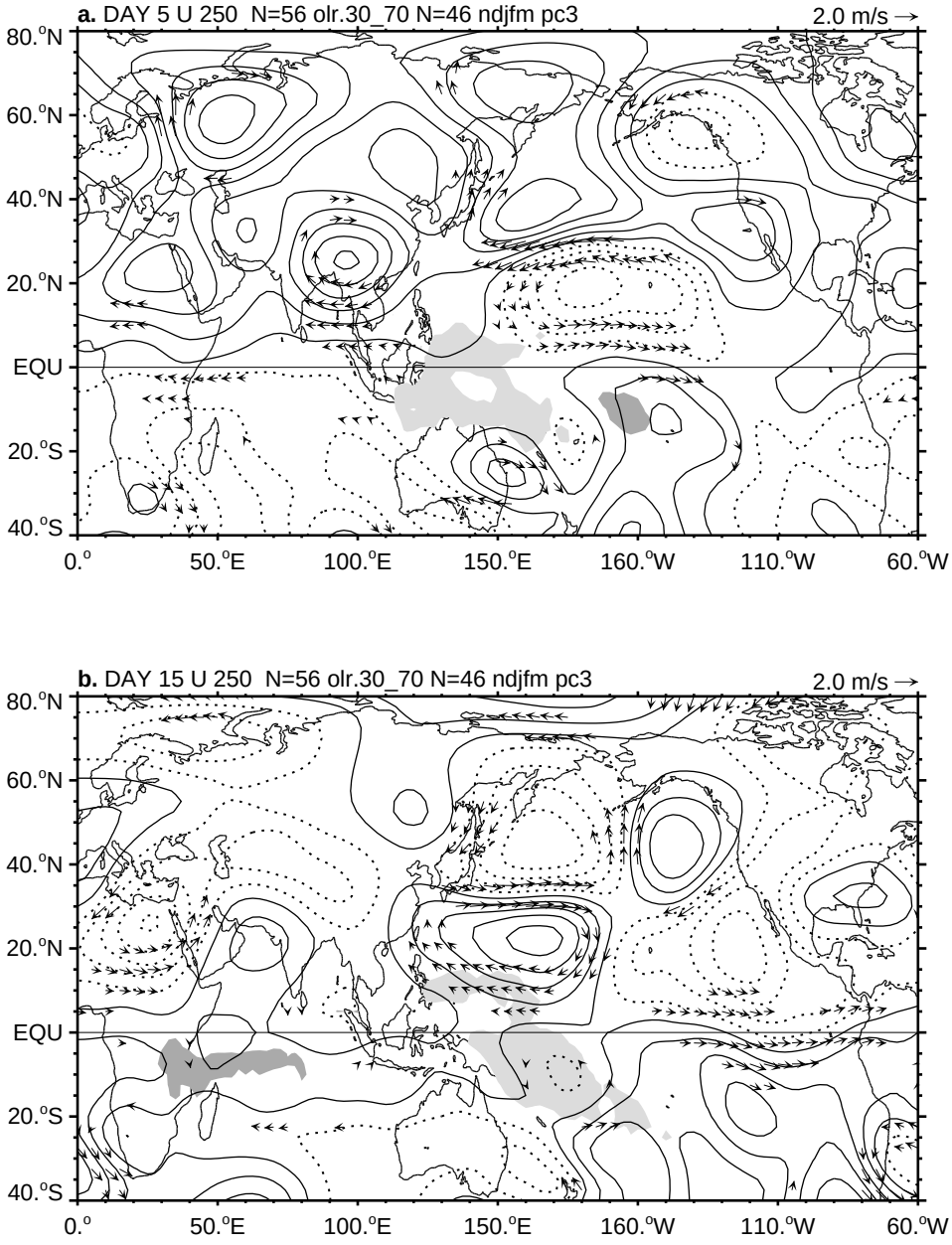

Figure 5.8: As in Fig. 5.7 but for (a) Day +5. (b) Day +15.

similar to previous case studies (Hsu *et al.* 1990; Weickmann and Khalsa 1990; Meehl *et al.* 1996). Unlike those studies and other diagnostic studies of the MJO, however, only a weak precursor of large-scale negative OLR anomalies in the Indian Ocean is observed, but a wave-pattern that leads to enhanced northwesterlies over northern Asia is seen (Fig. 5.7a). Large-scale negative OLR anomalies in the equatorial Indian Ocean are observed in the composite days following the reduced surge variance (Fig. 5.6). The evidence therefore suggests that the 35-40 day modulation of the South China Sea mode observed in Fig. 5.1 has a significant relationship to the intraseasonal variability related to the MJO. Whether the increased occurrence of pressure surges indicated by the increase in the South China Sea PC submonthly variance acts as an important mechanism for stimulating convective activity on the timescale of the MJO will need to be investigated further. Also, the apparent interplay between tropical heating anomalies and midlatitude circulation anomalies that modulate submonthly transients which, in turn, effect the tropical heating anomalies should be evaluated further based on the strength of the statistical relationship seen here and the several previous case studies. Composites of SLP submonthly variance using positive and negative anomalies in the Asian jet show a similar evolution of submonthly variance and 30-70 day timescale circulationa anomalies as that shown here (not shown).

In addition to the direct identification of the circulation and convective anomaly patterns described above, some secondary evidence is also observed linking the 35-40 day modulation of surge activity with the MJO. The enhanced low-level wind variance in Fig. 5.4 suggests that the direct mechanism of increased moisture convergence or increased evaporation from the wind anomalies associated with surges may play a role in stimulating convective activity that directly impacts the

movement of the envelope of convective activity associated with the MJO. Also, in Fig. 5.5b, an enhanced region of 250 hPa meridional wind variance extends well into the tropics around the dateline, similar to the recent results of Matthews and Kiladis (1997) who found deep tropical penetration of upper-level wave activity is preferred when the upper-level wind perturbations associated with the MJO are in a retracted jet anomaly similar to Fig. 5.7b.

CHAPTER 6

CONCLUSIONS

In this study, the variability of East Asian pressure surges has been diagnosed using objective methods. The dominant structure and anomalies associated with pressure surges have been documented. An objective index for East Asian pressure surges has been presented. The use of an objective index allows some of the inconsistencies seen in the statistics of surges from studies using subjective methods to be overcome. Using the objective index, the previous hypothesis from case studies that increased surge activity plays a role in the eastward transition of the MJO is evaluated statistically. A statistically significant signal supporting the hypothesis is found.

6.1 Dominant Modes of Pressure Variability over East Asia

An orthogonal rotated principal component analysis (ORPCA) of SLP over East Asia is performed in Chap. 3. Several of the dominant modes of the ORPCA analysis in Fig. 3.1 correspond to previously studied circulation anomalies in the summer and winter monsoons but have been analyzed with few a priori assumptions, suggesting the high degree of reproducibility of the analyzed circulation patterns. A new mode, the South China Sea mode, has been introduced and shown to correspond to a large-scale objective index of East Asian pressure surges.

The composite and spectral analysis of the ORPCA PCs demonstrates that the modes correspond to physically meaningful structures. A seasonal comparison

of circulation and spectra of PCs 1 and 2, identified with the monsoon active/break periods and the MJO provides support for some differences in the MJO between the cool and warm seasons: a frequency shift toward longer periods in the cool season (Fig. 3.3). A 5-day global pressure wave is found using anomaly data in composites of PC 1 in the warm season (Figs. 3.7 and 3.8) and the wavelet spectra of PCs 1 and 2 (Fig. 3.4). The wavelet spectra of PCs 1 and 2 (Fig. 3.4) show that the 5-day pressure wave is more pronounced in the warm season.

Mode 4 appears to be associated with monsoon depression disturbances. Mode 7 appears to project onto the active and break periods over all of South Asia during the summer monsoon.

Modes 3, 5, and 6 appear to be related to the East Asian pressure surges. Modes 5 and 6 are quite similar to the previously found Siberian and Chinese modes of Hsu and Wallace (1985). Mode 3, the newly identified South China Sea mode, captures the signal of tropically-influential pressure surges. Mode 3 also appears to capture the winter monsoon ”lulls.” As such, the PC corresponding Mode 3 provides an objective time series for measuring the high-frequency activity of surges and lulls.

Examination of composites based on the PCs associated with the pressure surge modes demonstrates the robustness and reproducibility of conclusions reached about surges in the linear regression study of Appendix B.

In particular, the previous result that upper-level wave activity over central Siberia is associated with East Asian pressure surges is verified. However, the timescale of the upper-level wave activity significantly correlating with pressure surges is longer (6-30 days) than the synoptic (2-6 days) usually associated with upper-level waves that force pressure surges (Boyle 1986; Wu and Chan 1997). The similarity of the composite unfiltered upper-level circulation and the regressed 6-30

day bandpass filtered circulation suggests that intermediate timescale upper-level circulation variations are important for the activation of surges and should be examined further.

The high degree of symmetry displayed in the southward propagation of both positive and negative pressure anomalies, in the suppression and enhancement of convective activity, and in the reversals of wind anomalies found in the composite studies of the East Asian pressure surge modes provides support for the linearity assumption made in the linear regression study of Appendix B.

The dynamical argument that surges may be described as a topographic Rossby wave or shelf wave presented in Appendix B is consistent with the observed in-phase southward propagation of southerly wind anomalies with negative SLP anomalies and northerly wind anomalies with positive SLP anomalies seen in the composite of the PC of the South China Sea Mode (3), and further evidence is presented that non-linear advection of surge-associated anomalies does not explain the temporal relationships observed.

6.2 Seasonal Modulation of East Asian Pressure Surges

A new method of diagnosing modulation and assessing its statistical significance is introduced in Chap. 2. Composites of wavelet-derived variance time series allow rigorous statistical tests to be applied to modulated time series at the limit of the uncertainty principal. Background variance can be computed from the seasonal cycle of variance as in Fig. 5.1. Wavelet spectra can also be examined directly, as in Fig. 5.2.

In Chap. 4, the seasonality of the submonthly (2-to-30 day) variance of SLP anomalies associated with pressure surges is investigated. The occurrence of pressure surges displays a late fall and early spring maximum with a mid-winter

minimum. Using an objective index for surges has allowed an unbiased estimate of the seasonal cycle of surge activity compared to previous works that used subjectively based definitions (Joung and Hitchman 1982; Lai 1989; Wu and Chan 1995; Zhang *et al.* 1997).

The strong connection between upper-level wave activity and surge episodes seen in Figs. 3.15 and B.7 is also observed in the similar seasonal cycles of intermediate (6-30 day) timescale wave activity at 500 hPa over northern Asia (Fig. 4.6) and surge activity. That synoptic timescale wave activity does not appear to by coincidentally modulated with surge activity suggests, in contrast to the findings of Wu and Chan (1997), that synoptic timescale waves may not be solely responsible for surge episodes. Further, variations in intermediate timescale wave activity may also have to be accounted for in a theory for the activation of surges.

6.3 Intraseasonal Modulation of East Asian Pressure Surges

In Chap. 5, the intraseasonal modulation of the East Asian pressure surges is examined and the relationship to the MJO is investigated. The composites of convection and circulation anomalies in the 30-70 day band appear to provide evidence that variations in surge activity are associated with large-scale changes in tropical convection and global circulation. The composites of circulation patterns can be associated with distinct phases of the Madden-Julian Oscillation. The phase relationship between an observed increase in tropical convective activity following an increase in surge activity suggests that a direct link between submonthly pressure surges and the eastward transition of intraseasonal convective activity may exist.

An observed increase in submonthly upper-level wave activity over central Siberia preceding and coincident with the increase in SLP variance associated with pressure surges furthers the hypothesis that surges and the modulation of surge

activity are directly linked to changes in the upper-level wave activity over northern Central Siberia. The significant increase in upper-level wave activity occurs in a region of 30-70 day timescale upper-level northwesterly anomalies, which supports the hypothesis of Meehl *et al.* (1996) that such anomalies would be favorable for the development of upper-level wave activity.

The modeling results of Hsu *et al.* (1990) suggested that an atmospheric circulation anomaly similar to that of Fig. 5.7 could be forced by heating anomalies in the tropical Indian Ocean. However, the significant OLR anomaly seen preceding the largest amplitude surge activity shows only suppressed convective activity in the western Pacific and only a weak signal of enhanced convective activity in the Indian Ocean (Fig. 5.6). The weakness of the negative OLR anomaly in the Indian Ocean and the strength of the positive OLR anomaly preceding the enhanced surge activity suggests that heating anomalies in the Indian Ocean hypothesized to force the upper-level circulation do not have a definite phase relationship with enhanced surge activity in time or location, while the suppression of convective activity in the western Pacific does have a clear, robust relationship. The sensitivity of the mid-latitude atmospheric response to heating anomalies in various locations along the near-equatorial Indian Ocean should be evaluated to see if a circulation pattern similar to that observed here is possible from a multiplicity of heating anomalies in the equatorial Indian Ocean. In particular, whether northwesterly anomalies over central Siberia are sensitive or robust to variously located heating anomalies in the equatorial Indian Ocean should be examined.

That submonthly convective activity in the Indonesian and Australian regions increases in direct response to an individual East Asian pressure surge is seen in Figs. 3.15 and B.5 and confirms previous case studies and statistical work suggesting

such a relationship. The increase in 30-70 day timescale convective activity in the Indonesian region coincident with and following a period of increased surge activity or groups of surge episodes had previously been hypothesized on the basis of case and comparative studies and has been demonstrated here as a statistically significant result. The relative importance of the link between surge activity and MJO timescale enhancement of convective activity compared to other mechanisms hypothesized for the eastward progression of the MJO should be investigated further.

An apparent interplay, similar to previous case study and comparative analysis work (Hsu *et al.* 1990; Weickmann and Khalsa 1990; Meehl *et al.* 1996), between intraseasonal convective and circulation anomalies and changes in submonthly variance of upper-level and low-level transients over East Asia has been documented. The statistical analysis presented here supports the previous hypothesis that tropical heating anomalies force midlatitude circulation anomalies that modulate submonthly transients which,in turn, effect intraseasonal tropical heating anomalies. That the development of convective anomalies in the western Pacific may subsequently force upper-level circulation anomalies that reduce submonthly transient activity in upper-level waves and pressure surges over East Asia has not been previously observed, however. This hypothesis of tropical-extratropical interaction on multiple timescales deserves theoretical further investigation based on the strength of the statistical relationship seen here and the previous case studies that have identified similar relationships.

6.4 Future Research

Several parts of this study provided observations that require further investigation to determine the dynamics underlying the observations.

(1) The suggestive relationships between modulation of upper-level wave activity and modulation of surge activity on both the seasonal and intraseasonal timescales should be investigated with a modeling effort.

(2) In this study, new statistical tests are presented to evaluate the significance of composites of variance based on wavelet spectra averaged in time and in scale. The tests presented here are local only. As suggested by Livezey and Chen (1983), global tests for the significance of the maps presented should also be employed to ensure that the regional coverage observed is beyond chance.

(3) The modulation of the warm season mode should also be investigated with the same method applied here for the South China Sea mode.

(4) The East Asian pressure surges should be compared with apparently similar phenomena along the Rockies and Andes to test the assertion in the cold surge review of (Murakami 1987) that ”A phenomenon unique to this area [East Asia] is the frequent occurrence of low-level cold surges bursting out of Siberia.” The methods employed here are directly transferable to the other orographic regions seen to have high submonthly variance in Fig. 4.1

BIBLIOGRAPHY

Baliunas, S., P. Frick, D. Sokoloff, and W. Soon, 1997: Time scales and trends in the Central England Temperature data (1659–1990): A wavelet analysis. *Geophy. Res. Lett.*, **24**, 1351–54.

Barnston, A. G., and R. E. Livezey, 1987: Classification, seasonality , and persistence of low-frequency atmospheric circulation patterns. *Mon. Wea. Rev.*, **115**, 1083–1126.

Basist, A. N., and M. Chelliah, 1997: Comparison of tropospheric temperatures derived from the NCEP/NCAR reanalysis, NCEP operational analysis, and the microwave sounding unit. *Bull. Am. Meteor. Soc.*, **78**, 1431–1447.

Bergman, J. W., and H. H. Hendon, 1996: The impact of cloud distributions on the seasonal cycle of radiative heating at the surface and in the atmosphere. *Proceedings of the 21st Annual Climate Diagnostics Workshop*, 356–359, Huntsville, AL, 28 October–1 November 1996.

Blackmon, M. L., 1976: A climatological spectral study of the 500-mb geopotential height of the northern hemisphere. *J. Atmos. Sci.*, **33**, 1607–1623.

Blackmon, M. L., Y.-H. Lee, and J. M. Wallace, 1984: Horizontal structure of 500-mb height fluctuations with long, intermediate, and short time scales. *J. Atmos. Sci.*, **41**, 961–979.

Blackmon, M. L., J. M. Wallace, N.-C. Lau, and S. L. Mullen, 1977: An observational study of the northern hemisphere wintertime circulation. *J. Atmos. Sci.*, **34**, 1040–1053.

Boyle, J. S., 1986: Comparison of the synoptic conditions in mid-latitudes accompanying cold surges over eastern Asia for the months of December 1974 and 1978. part I: Monthly mean fields and individual events. *Mon. Wea. Rev.*, **114**, 903–918.

Boyle, J. S., and T.-J. Chen, 1987: Synoptic aspects of the wintertime East Asian monsoon. *Monsoon Meteorology*, Chang, C. P., and T. N. Krishnamurti, Eds., Oxford University Press, 125–160.

Brier, G.W., 1978: The quasi-biennial oscillation and feedback processes in the atmosphere-ocean-earth system. *Mon. Wea. Rev.*, **106**, 938–946.

Chang, C. P., and J.-M. Chen, 1992: A statistical study of winter monsoon cold surges over the South China Sea and the large-scale equatorial divergence. *J. Met. Soc. Japan*, **70**, 287–301.

Chang, C. P., J. E. Erickson, and K.-M. Lau, 1979: Northeasterly cold surges and near-equatorial disturbances over the Winter MONEX area during December 1974. part I: Synoptic aspects. *Mon. Wea. Rev.*, **107**, 813–829.

Chang, C. P., and K.-M. Lau, 1982: Short-term planetary-scale interaction over the Tropics and Midlatitudes during northern winter. Part I: Contrasts between active and inactive periods. *Mon. Wea. Rev.*, **110**, 933–946.

Chang, C. P., and K. M. W. Lau, 1980: Northeasterly cold surges and near-equatorial disturbances over the Winter MONEX area during December 1974. Part II: Planetary-scale aspects. *Mon. Wea. Rev.*, **108**, 299–312.

Chang, C. P., and H. Lim, 1988: Kelvin-wave cisk: A possible mechanism for the 30-50 day oscillation. *J. Atmos. Sci.*, **45**, 298–312.

Chang, C. P., and K. G. Lum, 1985: Tropical-Midlatitude interaction over Asia and the western Pacific Ocean during the 1983/84 northern winter. *Mon. Wea. Rev.*, **113**, 1345–1358.

Chang, C. P., J. E. Miller, and G. T. J. Chen, 1983: Gravitational character of cold surges during Winter MONEX. *Mon. Wea. Rev.*, **111**, 293–307.

Chatfield, C., 1989: *The Analysis of Time Series: An Introduction*, 4th ed. Chapman and Hall, 241 pp.

Chu, P.-S., 1988: Extratropical forcing and the burst of equatorial westerlies in the western Pacific: A synoptic study. *J. Met. Soc. Japan*, **66**, 549–564.

Chu, P.-S., and J. Frederick, 1990: Westerly wind bursts and surface heat fluxes in the equatorial western Pacific in May 1982. *J. Met. Soc. Japan*, **68**, 523–537.

Chu, P.-S., and S.-U. Park, 1984: Regional circulation characteristics associated with a cold surge event over East Asia during Winter MONEX. *Mon. Wea. Rev.*, **112**, 955–965.

Colle, B. A., and C. F. Mass, 1995: The structure and evolution of cold surges east of the Rocky Mountains. *Mon. Wea. Rev.*, **123**, 2577–2610.

Compo, G. P., G. N. Kiladis, and P. J. Webster, 1997: East Asian pressure surges and their relationship to tropical variability. *Quart. J. Roy. Meteor. Soc.*, submitted.

Daubechies, I., 1990: The wavelet transform, time-frequency localization and signal analysis. *IEEE Trans. Inform. Theory*, **36**, 961–1004.

Daubechies, I., 1992: *Ten Lectures on Wavelets*. Society for Industrial and Applied Mathematics, 357 pp.

Davidson, N., J. L. McBride, and B. J. McAvaney, 1984: Divergent circulations during the onset of the 1978-79 Australian monsoon. *Mon. Wea. Rev.*, **112**, 1684–1696.

Davis, C. A., 1997: The modification of baroclinic waves by the Rocky Mountains. *J. Atmos. Sci.*, **54**, 848–868.

Ding, Y., 1990: Build-up, air mass transformation and propagation of Siberian high and its relation to cold surge in East Asia. *Meteor. Atmos. Phys.*, **44**, 281–292.

Dixit, S., and P. J. Webster, 1997: Structure of intraseasonal variability in the Asian summer monsoon. *J. Climatology*, to be submitted.

Donoho, D. L., and I. M. Johnstone, 1994: Ideal spatial adaptation by wavelet shrinkage. *Biometrika*, **81**, 425–455.

Duchon, C. E., 1979: Lanczos filtering in one and two dimensions. *J. Appl. Meteor.*, **18**, 1016–1022.

Farge, M., 1992: Wavelet transforms and their applications to turbulence. *Ann. Rev. Fluid Mech.*, **24**, 395–457.

Farge, M., E. Goirand, Y. Meyer, F. Pascal, and M. V. Wickerhauser, 1992: Improved predictability of two-dimensional turbulent flows using wavelet packet compression. *Fluid Dyn. Res.*, **10**, 229–250.

Folland, C.K., D.E. Parker, and F.E. Kates, 1984: Worldwide marine temperature fluctuations 1856-1981. *Nature*, **310**, 670–673.

Foufoula-Georgiou, E., and P. Kumar, Eds., 1995: *Wavelets in Geophysics*. Academic Press, 373 pp.

Gamage, N., and W. Blumen, 1993: Comparative analysis of low-level cold fronts: Wavelet, Fourier and empirical orthogonal function decompositions. *Mon. Wea. Rev.*, **121**, 2867–2878.

Giese, B. S., and D. E. Harrison, 1990: Aspects of the Kelvin wave response to episodic wind forcing. *J. Geophys. Res.*, **95**, 7289–7312.

Gilman, D. L., F. J. Fuglister, and Jr. J. M. Mitchell, 1963: On the power spectrum of "red noise". *J. Atmos. Sci.*, **20**, 182–184.

Gu, D., and S.G.H. Philander, 1995: Secular changes of annual and interannual variability in the tropics during the past century. *J. Climate*, **8**, 864–876.

Guttman, L., 1954: Some necessary conditions for common-factor analysis. *Psychometrika*, **19**, 149–161.

Harman, H. H., 1967: *Modern Factor Analysis*. The University of Chicago Press.

Hendon, H. H., and B. Liebmann, 1994: Organization of convection within the Madden-Julian Oscillation. *J. Geophys. Res.*, **99**, 8073–8083.

Higgins, R. W., Y.-P. Yao, M. Chelliah, W. Ebisuzaki, J. E. Janowiak, C. F. Ropelewski, and R. E. Kistler, 1996: Inter-comparison of the NCEP/NCAR and the NASA/DAO Reanalyses (1985–1993). Technical report, NCEP/Climate Prediction Center Atlas No. 2, Camp Springs, MD.

Horel, J. D., 1981: A rotated principal component analysis of the interannual variability of the northern hemisphere 500 mb height field. *Mon. Wea. Rev.*, **109**, 2080–2092.

Hoskins, B. J., 1983: Dynamical processes in the atmosphere and the use of models. *Quart. J. Roy. Meteor. Soc.*, **109**, 1–21.

Hoskins, B. J., and D. J. Karoly, 1981: The steady linear response of a spherical atmosphere to thermal and orographic forcing. *J. Atmos. Sci.*, **38**, 1179–1196.

Hoskins, B. J., A. J. Simmons, and D. G. Andrews, 1977: Energy dispersion in a barotropic atmosphere. *Quart. J. Roy. Meteor. Soc.*, **103**, 553–567.

Houze, R. A., S. G. Geotis, F. D. Marks, and A. K. West, 1981: Winter monsoon convection in the vicinity of North Borneo. Part I: Structure and time variation of the clouds and precipitation. *Mon. Wea. Rev.*, **109**, 1595–1614.

Hsu, H. H., 1987: Propagation of low-level circulation features in the vicinity of mountain ranges. *Mon. Wea. Rev.*, **115**, 1864–1892.

Hsu, H. H., B. J. Hoskins, and F.-F. Jin, 1990: The 1985/86 intraseasonal oscillation and the role of the extratropics. *J. Atmos. Sci.*, **47**, 823–839.

Hsu, H. H., and J. M. Wallace, 1985: Vertical structure of wintertime teleconnnection patterns. *J. Atmos. Sci.*, **42**, 1693–1719.

Hudgins, L., C. A. Friehe, and M. E. Mayer, 1993: Wavelet transforms and atmospheric turbulence. *Phys. Rev. Let.*, **71**, 3279–3282.

Huthnance, J. M., 1978: On coastal trapped waves : Analysis and numerical calculations by inverse iteration. *J. Phys. Ocean.*, **8**, 74–92.

Jenkins, G. M., and D. G. Watts, 1968: *Spectral Analysis and its Applications*. Holden-Day.

Johnson, R. H., and D. L. Priegnitz, 1981: Winter monsoon convection in the vicinity of north Borneo. Part II: Effects on large-scale fields. *Mon. Wea. Rev.*, **109**, 1615–1628.

Joung, C. H., and M. H. Hitchman, 1982: On the role of successive downstream development in East Asian polar air outbreaks. *Mon. Wea. Rev.*, **110**, 1224–1237.

Kaiser, G., 1994: *A Friendly Guide to Wavelets*. Birkhäuser, Boston, 300 pp.

Kalnay, E., M. Kanamitsu, R. Kistler, W. Collins, D. Deaven, L. Gandin, M. Iredell, S. Saha, G. White, J. Woolen, Y. Zhu, M. Chelliah, W. Ebisuzaki, W. Higgins, J. Janowiak, K. C. Mo, C. Ropelewski, J. Wang, A. Leetmaa, R. Reynolds, R. Jenne, and D. Joseph, 1996: The NCEP/NCAR 40-year Reanalysis Project. *Bull. Am. Meteor. Soc.*, **77**(3), 437–471.

Keen, R. A., 1982: The role of cross-equatorial tropical cyclone pairs in the southern oscillation. *Mon. Wea. Rev.*, **110**, 1405–1416.

Kestin, T. A., D. J. Karoly, J.-I. Yano, and N. Rayner, 1998: Time-frequency analysis of ENSO and stochastic simulations. *J. Climate*, **11**, in press.

Kiladis, G. N., 1996: Observations of Rossby waves linked to convection over the eastern tropical Pacific. Submitted to J. Atmos. Sci.

Kiladis, G. N., G. A. Meehl, and K. M. Weickmann, 1994: Large-scale circulation associated with westerly wind bursts and deep convection over the western equatorial Pacific. *J. Geophys. Res.*, **99**, 18,527–18,544.

Kiladis, G. N., and K. M. Weickmann, 1992: Circulation anomalies associated with tropical convection during northern Winter. *Mon. Wea. Rev.*, **120**, 1900–1923.

Kiladis, G. N., and K. M. Weickmann, 1997: Horizontal structure and seasonality of large-scale circulations associated with submonthly tropical convection. *Mon. Wea. Rev.*, **125**, 1997–2013.

Kiladis, G.N., and K. M. Weickmann, 1997: Vertical sturcture and seasonality of large-scale circulations associated with submonthly tropical convection. Submitted to *Mon. Wea. Rev.*

Kiladis, G.N., and M. Wheeler, 1995: Horizontal and vertical structure of observed tropospheric equatorial Rossby waves. *J. Geophys. Res.*, **100**, 22,981–22,997.

Kindle, J. C., and P. A. Phoebus, 1995: The ocean response to operational westerly wind bursts. *J. Geophys. Res.*, **100**, 4893–4920.

Knox, R. A., and D. Halpern, 1982: Long range Kelvin wave propagation of transport variations in Pacific Ocean equatorial currents. *J. Mar. Res.*, **40**, 329–339.

Krishnamurti, T. N., and P. Ardanuy, 1980: The 10 to 20-day westward propagating mode and Breaks in the Monsoon. *Tellus*, **32**, 15–26.

Krishnamurti, T. N., and N. Surgi, 1987: Observational aspects of summer monsoon. *Monsoon Meteorology*, Chang, C.-P., and T. N. Krishnamurti, Eds., number 7 in Oxford Monographs on Geology and Geophysics, Oxford University Press, Ch. 1.

Lai, S. T., 1989: Short-range forecasting of northerly surges. Technical Report 83, Royal Observatory, Hong Kong.

Lau, K.-H., and N.-C Lau, 1990: Observed structure and propagation chracteristics of tropical summertime synoptic scale disturbances. *Mon. Wea. Rev.*, **118**, 1888–1913.

Lau, K.-H., and N.-C. Lau, 1992: The energetics and propagation dynamcis of tropical summertime synoptic-scale disturbances. *Mon. Wea. Rev.*, **120**, 2523–2539.

Lau, K. M., 1982: Equatorial responses to northeasterly cold surges as inferred from satellite cloud imagery. *Mon. Wea. Rev.*, **110**, 1306–1313.

Lau, K. M., and C. P. Chang, 1987: Planetary scale aspects of the winter monsoon and atmospheric teleconnection. *Monsoon Meteorology*, Chang, C. P., and T. N. Krishnamurti, Eds., Oxford University Press, 161–202.

Lau, K. M., C. P. Chang, and P. H. Chan, 1983: Short-term planetary-scale interactions over the Tropics and Midlatitudes. Part II: Winter-MONEX period. *Mon. Wea. Rev.*, **111**, 1372–1388.

Lau, K. M., and M. T. Li, 1984: The monsoons of East Asia and its global associations - a survey. *Bull. Am. Meteor. Soc.*, **65**, 114–124.

Lau, K.-M., and H.-Y. Weng, 1995: Climate signal detection using wavelet transform: How to make a time series sing. *Bull. Am. Meteor. Soc.*, **76**, 2391–2402.

Lau, N. C., and K.-M. Lau, 1984: The structure and energetics of midlatitude distrubances accompanying cold-air outbreaks over East Asia. *Mon. Wea. Rev.*, **112**, 1309–1327.

Leathers, D. L., 1986: Edge wave characteristics of East Asian cold surges. Master's thesis, The Pennsylvania State University, University Park, PA.

Liebmann, B., and C. A. Smith, 1996: Description of a complete (interpolated) outgoing longwave radiation dataset. *Bull. Am. Meteor. Soc.*, **77**, 1275–1277.

Lim, H., and C. P. Chang, 1981: A theory for midlatitude forcing of tropical motions during winter monsoons. *J. Atmos. Sci.*, **38**, 2377–2392.

Lindsay, R. W., D. B. Percival, and D. A. Rothrock, 1996: The discrete wavelet transform and the scale analysis of sea ice. *IEEE Trans. Geosci. Remote Sensing*, **34**(3), 771–787.

Liu, P. C., 1994: Wavelet spectrum analysis and ocean wind waves. *Wavelets in Geophysics*, Foufoula-Georgiou, E., and P. Kumar, Eds., Wavelet Analysis and its Applications, Academic Press, 151–166.

Livezey, R. E., and W. Y. Chen, 1983: Statistical field significance and its determination by Monte Carlo techniques. *Mon. Wea. Rev.*, **111**, 46–50.

Love, G., 1985: Cross-equatorial influence of winter hemisphere subtropical cold surges. *Mon. Wea. Rev.*, **113**, 1487–1498.

Love, G., 1985: Cross-equatorial interactions during tropical cyclogensis. *Mon. Wea. Rev.*, **113**, 1499–1509.

Lukas, R., and E. Lindstrom, 1991: The mixed layer of the Western equatorial Pacific Ocean. *J. Geophys. Res.*, **96**, 3343–3357.

Madden, R., and P. Julian, 1972: Further evidence of global-scale, 5-day pressure waves. *J. Atmos. Sci.*, **29**, 1464–1469.

Madden, R. A., and P. R. Julian, 1972: Description of global-scale circulation cells in the tropics with a 40–50–day period. *J. Atmos. Sci.*, **29**, 1109–1123.

Madden, R. A., and P. R. Julian, 1994: Observations of the 40-50-day tropical oscillation - a review. *Mon. Wea. Rev.*, **122**, 814–837.

Magaña, V., J. A. Amador, and S. Medina, 1997: The mid-summer drought over mexico and central america. submitted to J. Clim.

Mak, M., 1995: Orthogonal wavelet analysis: Interannual variability in the sea surface temperature. *Bull. Am. Meteor. Soc.*, **76**, 2179–2186.

Matthews, A. J., and G. N. Kiladis, 1997: The tropical-extratropical interaction between high-frequency transients and the Madden-Julian Oscillation. submitted to Mon. Wea. Rev.

McBride, J. L., 1987: The Australian summer monsoon. *Monsoon Meteorology*, Chang, C. P., and T. N. Krishnamurti, Eds., Oxford University Press, 203–231.

McPhaden, M. J., F. Bahr, Y. du Penhoat, E. Firing, S.P. Hayes, P.P. Niiler, P.L. Richardson, and J.M. Toole, 1992: The response of the western equatorial Pacific Ocean to westerly wind bursts during November 1989 to January 1990. *J. Geophys. Res.*, **97**, 14289–14303.

McPhaden, M. J., H. P. Freitag, S. P. Hayes, and B. A. Taft, 1988: The response of the equatorial Pacific Ocean to a westerly wind burst in May 1986. *J. Geophys. Res.*, **93**, 10589–10603.

Meehl, G. A., 1987: The annual cycle and interannual variability in the tropical Pacific and Indian ocean regions. *Mon. Wea. Rev.*, **115**, 27–50.

Meehl, G. A., 1994: Coupled land-ocean-atmosphere processes and South Asian monsoon variability. *Science*, **266**, 263–267.

Meehl, G. A., G. N. Kiladis, K. M. Weickmann, M. Wheeler, D. S. Gutzler, and G. P. Compo, 1996: Modulation of equatorial subseasonal convective episodes by tropical-extratropical interaction in the Indian and Pacific Ocean regions. *J. Geophys. Res.*, **101**, 15,033–15,049.

Meyers, S. D., B. G. Kelly, and J. J. O'Brien, 1993: An introduction to wavelet analysis in oceanography and meteorology: With application to the dispersion of Yanai waves. *Mon. Wea. Rev.*, **121**, 2858–2866.

Murakami, T., 1979: Winter monsoonal surges over East and Southeast Asia. *J. Met. Soc. Japan*, **57**, 133–158.

Murakami, T., 1980: Temporal variations of satellite-observed outgoing longwave radiation over the winter monsoon region. Part I: Long-period (15-30 day) oscillations. *Mon. Wea. Rev.*, **108**, 408–426.

Murakami, T., 1987: Orography and monsoons. *Monsoon Meteorology*, Chang, C. P., and T. N. Krishnamurti, Eds., Oxford University Press, 331–364.

Murakami, T., and W. L. Sumathipala, 1989: Westerly bursts during the 1982/83 ENSO. *J. Climatology*, **2**, 71–85.

Mysak, L. A., 1980: Recent advances in shelf wave dynamics. *Rev. Geophys. and Space Phys.*, **18**, 211–241.

Nakamura, H., 1992: Midwinter suppression of baroclinic wave activity in the Pacific. *J. Atmos. Sci.*, **49**, 1629–1642.

Nicholls, N., 1978: Air-sea interaction and the quasi-biennial oscillation. *Mon. Wea. Rev.*, **106**(1505–1508).

Pedlosky, J., 1987: *Geophysical Fluid Dynamics*. Springer-Verlag.

Percival, D. P., 1995: On estimation of the wavelet variance. *Biometrika*, **82**, 619–631.

Perrier, V., T. Philipovitch, and C. Basdevant, 1995: Wavelet spectra compared to Fourier spectra. *J. Math. Phys.*, **36**, 1506–19.

Qiu, L.-J., and M.-H. Er, 1995: Wavelet spectrogram of noisy signals. *Int. J. Elec.*, **79**, 665–677.

Ramage, C., 1971: *Monsoon Meteorology*, Vol. 15, *International Geophysics Series*. Academic Press, 296 pp.

Rasmusson, E. M., and T. H. Carpenter, 1982: Variations in tropical sea surface temperature and surface wind fields associated with the Southern Oscillation/El Niño. *Mon. Wea. Rev.*, **110**, 354–384.

Rayner, N. A., E. B. Horton, D. E. Parker, C. K. Folland, and R. B. Hackett, 1996: Version 2.2 of the Global sea-Ice and Sea Surface Temperature data set, 1903-1994. Technical report, CRTN 74, Hadley Centre for Climate Prediction and Research, Meteorological Office, London Road, Bracknell, Berkshire, RG12 2SY.

Reason, C. J. C., 1994: Orographically trapped disturbances in the lower atmosphere: scale analysis and simple models. *Meteor. Atmos. Phys.*, **53**, 131–136.

Richman, M. B., 1986: Rotation of principal components. *J. Climatology*, **6**, 293–335.

Ropelewski, C. F., M. S. Halpert, and X. Wang, 1992: Observed tropospheric biennial variability and its relationship to the Southern Oscillation. *J. Climate*, **5**, 594–614.

Salby, M. L., and H. H. Hendon, 1994: Intraseasonal behavior of clouds, temperature, and motion in the Tropics. *J. Atmos. Sci.*, **51**, 2207–2224.

Shen, S., and K.-M. Lau, 1995: Biennial oscillation associated with the East Asian summer monsoon and tropical sea surface temperatures. *J. Met. Soc. Japan*, **73**, 105–124.

Sikka, D. R., and S. Gadgil, 1980: On the maximum cloud zone and the ITCZ over Indian longitudes during the southwest monsoon. *Mon. Wea. Rev.*, **108**, 1840–1853.

Smull, B. F., and M. J. McPhaden, 1996: Comparison of NCEP/NCAR reanalyzed fields and surface observations over the TOGA-TAO array. *Proceedings of the 21st Annual Climate Diagnostics Workshop*, 57–60, Huntsville, AL, 28 October–1 November 1996.

Spencer, R. W., and J. R. Christy, 1992: Precision and radiosonde validation of satellite gridpoint temperature anomalies, part II: A tropospheric retrieval and trends 1979–90. *J. Climate*, **5**, 858–866.

Spencer, R. W., J. R. Christy, and N. C. Goody, 1990: Global atmospheric temperature monitoring with satellite microwave measurements: methods and results 1979–84. *J. Climate*, **3**, 1111–1128.

Spiegel, M. R., 1975: *Schaum's Outline of Theory and Problems of Probability and Statistics*. McGraw-Hill.

Srinivasan, J., S. Gadgil, and P. J. Webster, 1993: Meridional propagation of large-scale monsoon convective zones. *Meteor. Atmos. Phys.*, **52**, 15–35.

Thurstone, L. L., 1947: *Multiple Factor Analysis*. University of Chicago Press.

Tilley, J. S., 1990: *On the application of edge wave theory to terrain-bounded cold surges: A numerical study*. PhD thesis, The Pennsylvania State University, University Park, PA.

Tomas, R.A., and P. J. Webster, 1994: Horizontal and vertical structure of cross-equatorial wave propagation. *J. Atmos. Sci.*, **51**, 1417–1430.

Tomita, T., and T. Yasunari, 1996: Role of the northeast winter monsoon on the biennial oscillation of the ENSO/Monsoon system. *J. Met. Soc. Japan*, **74**, 399–413.

Torrence, C., and G. P. Compo, 1997: A practical guide to wavelet analysis. To appear in *Bull. Am. Met. Soc.*

Torrence, C., and P. J. Webster, 1997: The annual cycle of persistence in the El Niño-Southern Oscillation. To appear in *Quart. J. Roy. Meteor. Soc.*

Trenberth, K. E., 1991: Climate diagnostics from global analyses: conservation of mass in ECMWF analyses. *J. Climatology*, **4**, 707–722.

Trenberth, K. E., 1992: Global analyses from ecmwf and atlas of 1000 to 10 mb circulation statistics. Technical Report NCAR/TN-373+STR, NCAR Tech. Note.

Trenberth, K. E., and C. J. Guillemot, 1995: Evaluation of the global atmospheric moisture budget as seen from analyses. *J. Climatology*, **8**, 2255–2272.

Trenberth, K. E., and C. J. Guillemot, 1996: Evaluation of the atmospheric moisture and hydrological cycle in the NCEP Reanalysis. Technical Report NCAR/TN-430+STR, NCAR Tech. Note.

Trenberth, K.E., 1976: Spatial and temporal variations of the Southern Oscillation. *Quart. J. Roy. Meteor. Soc.*, **102**, 639–653.

Wang, B., 1995: Interdecadal changes in El Niño onset in the last four decades. *J. Climate*, **8**, 267–285.

Wang, B., and Y. Wang, 1996: Temporal structure of the Southern Oscillation as revealed by waveform and wavelet analysis. *J. Climate*, **9**, 1586–1598.

Wang, D. P., and K. C. N. Mooers, 1976: Coastal-trapped waves in a continuously stratified ocean. *J. Phys. Ocean.*, **6**, 853–863.

Webster, P. J., 1981: Mechanisms determining the atmospheric response to sea surface temperature anomalies. *J. Atmos. Sci.*, **38**, 554–571.

Webster, P. J., 1987: The variable and interactive monsoon. *Monsoons*, Fein, J., and P. L. Stephens, Eds., John Wiley & Sons, New York, 269–330.

Webster, P. J., and L. C. Chou, 1980: Low-frequency transitions of a simple monsoon system. *J. Atmos. Sci.*, **37**, 368–382.

Webster, P. J., and L. C. Chou, 1980: Seasonal structure of a simple monsoon system. *J. Atmos. Sci.*, **37**, 354–367.

Webster, P. J., and J. R. Holton, 1982: Cross-equatorial response to middle-latitude forcing in a zonally varying basic state. *J. Atmos. Sci.*, **39**, 723–733.

Webster, P. J., V. Maga na, T. N. Palmer, J. Shukla, R. Tomas, T. M. Yanai, and T. Yasunari, 1997: The monsoon: Processes, predictability and the prospects for prediction. To appear in *J. Geophys. Res.*

Weickmann, K. M., and S. J. S. Khalsa, 1990: The shift of convection from the Indian Ocean to the western Pacific Ocean during a 30–60 day oscillation. *Mon. Wea. Rev.*, **118**, 964–978.

Weickmann, K. M., G. R. Lussky, and J. E Kutzbach, 1985: Intraseasonal (30–60 day) fluctuations of outgoing longwave readiation and 250 mb streamfucntion during northern winter. *Mon. Wea. Rev.*, **113**, 941–961.

Weng, H., and K.-M. Lau, 1994: Wavelets, period doubling, and time-frequency localization with application to organization of convection over the tropical western Pacific. *J. Atmos. Sci.*, **51**, 2523–2541.

Williams, M., 1981: Interhemispheric interaction during Winter MONEX. *Proc. of the International Conference on Early Results of FGGE and Large Scale Aspects of Its Monsoon Experiment*, Geneva. World Meteorological Organization.

Wu, M. C., and J. C. L. Chan, 1995: Surface features of winter monsoon surges over South China. *Mon. Wea. Rev.*, **123**, 662–680.

Wu, M. C., and J. C. L. Chan, 1997: Upper level features associated with winter monsoon surges over South China. *Mon. Wea. Rev.*, **125**, 317–340.

Yasunari, T., 1989: A possible link of the QBOs between the stratosphere, troposphere and sea surface temperature in the tropics. *J. Met. Soc. Japan*, **67**, 483–493.

Zhang, C., and P. J. Webster, 1992: Laterally forced equatorial perturbations in a linear model part I: stationary transient forcing. *J. Atmos. Sci.*, **49**, 585–607.

Zhang, Y., K. R. Sperber, and J. S. Boyle, 1997: Climatology and interannual variation of the East Asian winter monsoon: Results from the 1979–1995 NCEP/NCAR Reanalysis. *Mon. Wea. Rev.*, **125**, 2605–2619.

APPENDIX A

BRIEF COMPARISON OF NCEP/NCAR REANALYSIS AND OBSERVATIONS

Several NCEP/NCAR Reanalysis variables are considered to be highly reflective of the underlying observations. Among these are sea level pressure (SLP), zonal and meridional wind, and air temperature. In this study, the temporal correlation between NCEP Reanalysis fields and three observing platforms is examined. The correlation field of SLP with surface station measurements in the Pacific Basin suggests that total SLP and SLP anomalies, even at 6 hour resolution, are represented well in the global Reanalysis. In contrast, the Reanalysis tropical Pacific low–level air temperature field and its anomalies correlates poorly with surface station air temperature measurements. In the western Pacific, SLP and low-level winds appear to be well represented by the Reanalysis compared to in-situ measurements by surface stations and the Tropical Ocean Global Atmosphere (TOGA) Tropical Atmosphere Ocean (TAO) buoy measurements. However, Reanalysis deep layer tropospheric temperature in the western Pacific compares poorly with satellite estimations from the Microwave Sounding Unit (MSU). The differences appear to arise from the effect of deep convection. In the eastern Pacific, SLP is well represented in the Reanalysis, but low-level wind and temperature anomalies correlate poorly with in-situ measurements from surface stations and TAO buoys. However, eastern Pacific Reanalysis deep layer tropospheric temperature in the eastern Pacific compares well with satellite estimations from MSU.

A.1 Introduction

The recently released 1979-1995 NCEP/NCAR Reanalysis provides a state-of-the art analysis of the global atmosphere using a comprehensive suite of observations. The Reanalysis system is described in detail by Kalnay *et al.* (1996). The products of the Reanalysis are not equally influenced by observations. Variables that are well defined by the observations provide a better estimate of the state of the atmosphere than observations alone, given the statistical interpolation and use of a first guess. Wind, temperature, and sea level pressure (SLP) are three such variables and are classified as A variables. Variables that are partially defined by the observations but also strongly influenced by the model characteristics are labeled B. Quantities that are not assimilated (such as precipitation), and thus entirely dependent on the model, are labeled C.

Studies using the Reanalysis dataset have identified several problems with the monthly mean and climatological Reanalysis fields that may be of concern to researchers. The Tropical hydrological cycle appears to be poorly constrained by the observations employed and is mainly a reflection of model physics (Higgins *et al.* 1996; Trenberth and Guillemot 1996). Trenberth and Guillemot (1996) demonstrate the substantial biases exist in the Reanalysis moisture fields compared to satellite and satellite/radiosonde blend estimates of moisture. Monthly mean tropical Pacific radiative fields have large errors when compared to satellite measurements (Bergman and Hendon 1996). Near-surface Reanalysis winds in the tropical Pacific show large monthly mean differences with the in-situ Tropical Ocean Global Atmosphere (TOGA) Tropical Atmosphere Ocean (TAO) moored buoy array, with the meridional wind difference growing larger away from the equator (Smull and

McPhaden 1996). The overall strength of the tropical Hadley cell appears underestimated by a factor of 2 in some regions in monthly mean NCEP Reanalysis compared to ECWMF Reanalysis (R. Tomas, personal communication).

In light of the identified monthly mean and annual differences between observations and Reanalysis, an examination of the contemporaneous high resolution temporal relationship between different types of observations and Reanalysis appears appropriate, with particular attention to the poorly observed Tropical regions of the globe. In this study, data from three different observing platforms are correlated with Reanalysis fields of zonal and meridional wind, temperature, and SLP. Daily MSU tropospheric temperatures are correlated with layer averaged Reanalysis air temperature. Surface station SLP and air temperature are correlated with Reanalysis SLP and 0.995 sigma level air temperature. TOGA TAO zonal and meridional wind are correlated with Reanalysis 0.995 sigma level and 1000 hPa zonal and meridional wind. Midlatitude SLP, low-level air temperature, and subtropical tropospheric temperature agree well between the Reanalysis and observing platforms. Tropical low–level temperatures correlate poorly. Tropical wind correlations are low in the eastern Pacific and high in the western Pacific.

A.2 Data and Method

The NCEP/NCAR Reanalysis (Kalnay *et al.* 1996) is used from 1979 to 1995. Variables examined in this study include SLP, temperature on pressure levels 700 to 100 hPa evenly spaced at 100 hPa intervals, wind at 1000 hPa, and wind and temperature at the lowest sigma level (terrain following) of 0.995 times the surface pressure for comparison with surface data. The pressure level variables and SLP are class A variables, while the sigma level variables are class B. The use of

the 0.995 sigma level temperature allows simultaneous comparison with the temperature reported at station with varying elevations from mountains to island atolls. For the wind comparison, the 1000 hPa level is categorized as an A variable, while the lowest sigma level wind is categorized as a B variable, so both are examined. The NCEP/NCAR Reanalysis is available on a 2.5 degree global grid at 6 hourly resolution. For comparison with station data, the Reanalysis data are interpolated with a 2-D bicubic spline to the location of the station.

The Microwave Sounding Unit (MSU) daily deep layer temperature has been shown to accurately describe the average tropospheric temperature (Spencer *et al.* 1990; Spencer and Christy 1992). The blend of MSU Channels 2 and 3 (MSU 2/3) provides a tropospheric temperature between 1000 and 300 hPa with a peak weighting at 500 hPa. For comparison, the Reanalysis temperature is averaged between 700 and 300 hPa. To complement their analysis, an average near the peak of the MSU 2/3 weighting should allow a fair comparison of daily fluctuations. In addition, the purpose here is to compare produced temperature not to evaluate the retrieval scheme. Note that MSU 2/3 cannot retrieve temperature through precipitating clouds (Spencer *et al.* 1990), so any signal during precipitation must be the result of interpolation. The MSU 2/3 data is available on a 2.5 degree grid from 27.5°N to 27.5°S around the globe at daily resolution. Missing MSU temperatures were interpolated by NOAA Climate Diagnostics Center.

The NCEP Surface ADP dataset is used for SLP and near-surface air temperature. Stations from 50°N to 50°S and 90°E to 110°W have been quality controlled with maximum values over 3 and 6 hour periods greater than 7 standard deviations removed. 320 stations (stars in Fig. A.1) are used in the analysis from 1980 to 1994. The station data is available at 3 hourly resolution and has been reduced to

6 hourly for comparison with Reanalysis. Between 2925 and 21222 time points are used in the comparisons. At daily resolution, this corresponds to between 780 and 5306 days. All comparisons are done only with available quality-controlled data. Missing values are not interpolated.

The TOGA TAO buoy dataset is used for near-surface winds and compared to NCEP/NCAR Reanalysis of 1000 hPa and 0.995 sigma zonal and meridional winds. The buoy data collection and processing is described by McPhaden (1996). NOAA Pacific Marine Environmental Laboratory performs extensive quality control on the buoy data before dissemination to the scientific community, so no further quality checks were used in this study. The location of the buoys used in this study is indicated on Fig. A.1 by diamonds. The data is daily resolution of varying lengths of record, with some buoy winds available since 1986 and most since 1990. A minimum record of 2 years of data is used, providing 56 buoys for comparison with Reanalysis.

Elevation data is from USGS Bathymetry and Elevation Data. Data is originally NGDC ETOPO5 at 5 minute resolution. The data has been smoothed to 1/10 its original resolution.

Comparison between the observations and Reanalysis is made using the correlation statistic. Correlations of between total time series at each grid point or spatially interpolated Reanalysis and station time series at each location are performed. Correlations between anomalies from the annual cycle are also computed and evaluated. The annual cycle is determined by a least squares fit to the first three harmonics (periods of 365.25, 182.625, and 121.750) and subtracted from the total time series to create the anomaly time series. For the NMC ADP surface station data, separate correlations are computed using the full time resolution and using only times

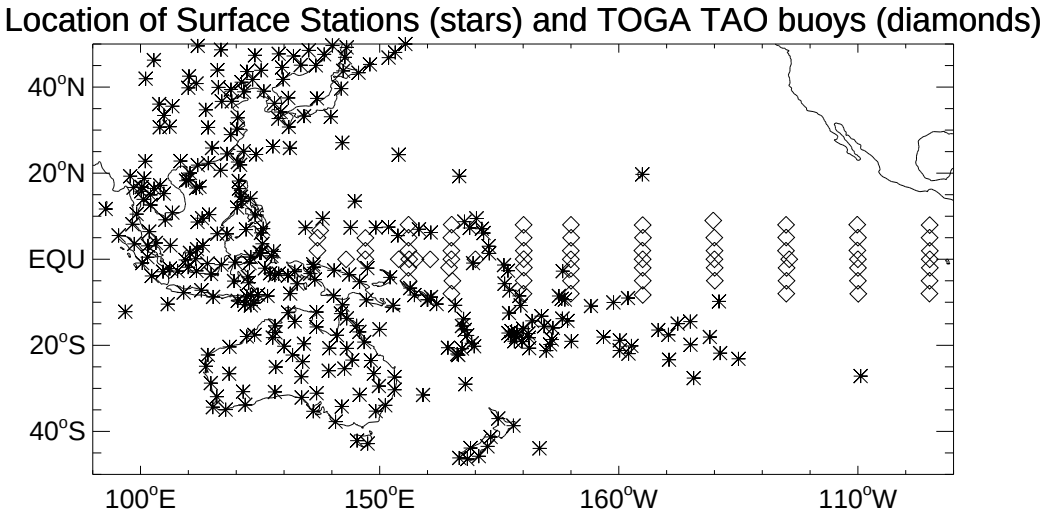

Figure A.1. Location of NMC ADP surface stations (stars) and TOGA TAO Buoys (diamonds) used in the correlation analysis. Only stations and buoys with more than 2 years worth of data were included in the analysis.

at the same synoptic reporting period (0Z, 6Z, 12Z, 18Z). Thus, the relationship between anomalies in the station data and Reanalysis with and without the diurnal cycle can be assessed.

A.3 Results

A.3.1 MSU Comparison

Figure A.2 shows the correlation between anomalies of MSU 2/3 air temperature and Reanalysis layer averaged 700-300 hPa air temperature. The correlations have been stratified by season to account for changing solar heating. The low correlation regions appear to be accounted for by a combination of topography and deep convection.

In Fig. A.2a, the correlation field for anomalies during JJA is shown. The low correlations appear to have local minima over the mountainous regions of the Northern Hemisphere subtropics. Note how the island of Borneo is flanked on three sides by higher correlations, while sharing low values with the convective monsoon region of the South China Sea. The subtropical Northern Hemisphere highlands of Africa along 10°N show low correlation that minimize with the terrain, as do the western Ghats of India and the mountains of Southeast Asia. In addition, generally lower correlation is seen in the off the west coast of Mexico and Africa, over the Bay of Bengal, South China Sea, and central Indian Ocean.

Figure A.2b shows that the regions of low correlation shift southward with the solar cycle. Note that the correlations over south Asia have increased dramatically. Over Africa, the lowest correlations have shifted southward to the central highlands, as well as decreasing over terrain along 20°S. Over South America, the low

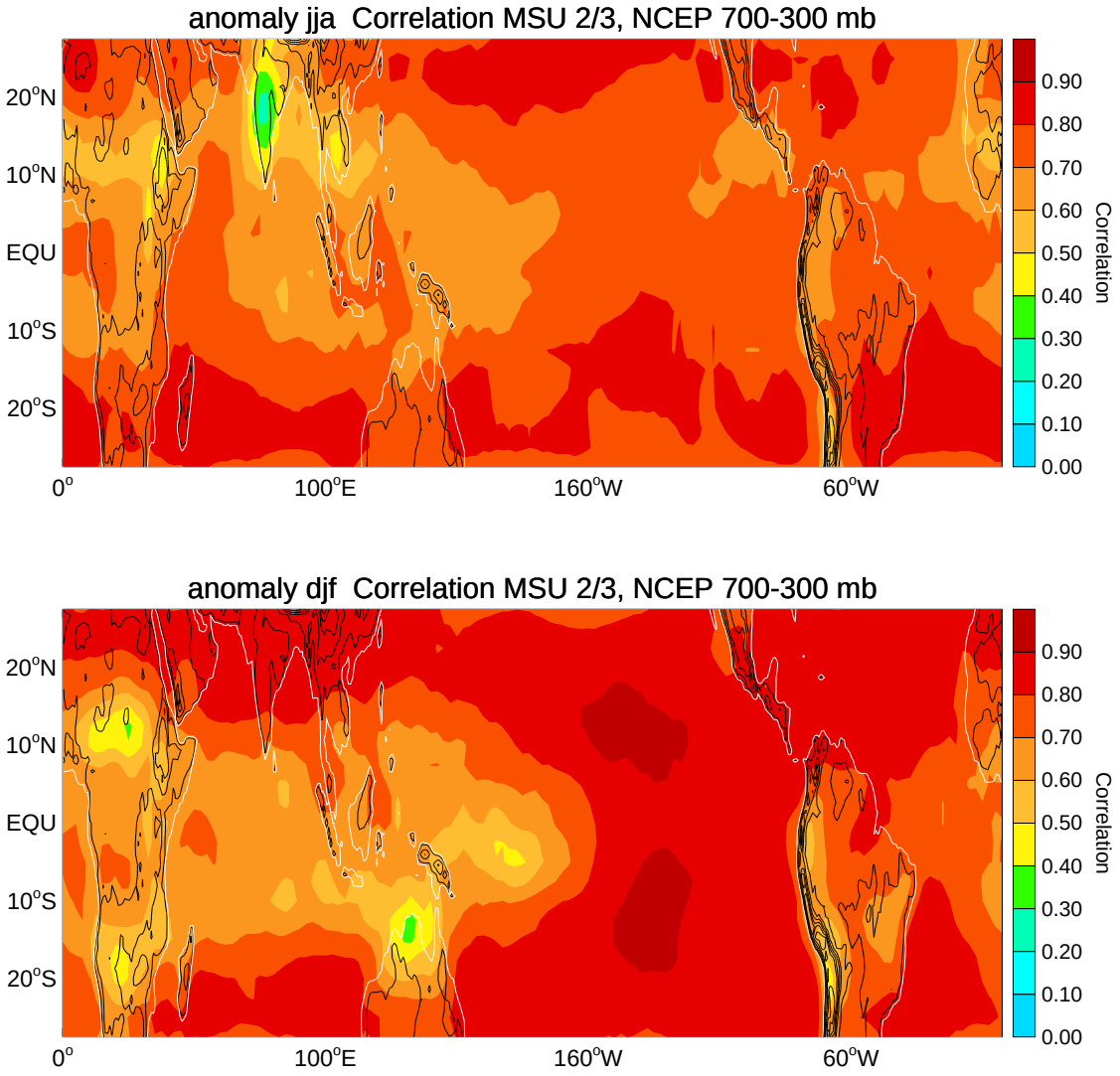

Figure A.2. Filled contours show correlation between anomalies of daily values of MSU Channel 2/3 blend air temperature and NCEP Reanalysis air temperature averaged 700-300 mb from 1979-1993. Filled contour interval is indicated in legend. Elevation contours are indicated in black. Contour interval is 750m beginning at 300m.

correlations are bounded by the elevation contours indicated. In contrast, over Australia and the western Pacific, the low correlations are over the regions of deep convection, but a local minima over continental northern Australia does further indicate that warm land surfaces appear to be leading to differences between the Reanalysis and MSU 2/3 air temperature fluctuations. The low correlation over the relatively flat region of northern Australia appears exceptionally low when compared to the Central American convective and mountainous regions in Fig. A.2a. The convection over the Australia monsoon may be more regular than that of the Mexican monsoon and ITCZ, allowing more MSU 2/3 successful retrievals.

As MSU 2/3 cannot retrieve temperature through precipitating clouds (Spencer *et al.* 1990), any signal during precipitation must be the result of interpolation. However, the NCEP Reanalysis distribution of precipitation does not appear realistic (Higgins *et al.* 1996), so neither set of data may reflect the true state of the atmosphere in these regions during convectively active periods. The differences over the summer mountain regions are not easily accounted for and warrant further investigation. Correlations between total time series have also been examined and have a similar spatial structure (not shown).

Basist and Chelliah (1997) have performed an anomaly correlation analysis of MSU measured-radiance and Reanalysis simulated-radiance. Their spatial distribution of the anomaly correlation broadly corresponds to a combination of Figs. A.2a and b, as Basist and Chelliah (1997) do not show the changing correlation with season. Throughout much of the the Tropics, lower correlatation coefficients are found in A.2 suggesting that a more fair comparison should take into account the weighting distribution of the MSU 2/3 when constructing the NCEP layer-averaged temperature. However, significantly higher correlations in the the eastern Pacific and

the Atlantic are found during DJF (Fig. A.2b) compared to the radiance correlation of Basist and Chelliah (1997).

Basist and Chelliah (1997) have evaluated the standard deviation of MSU measured-radiance and NCEP Reanalysis and find good global agreement. Basist and Chelliah (1997) made several other comparisons and concluded, overall, that the MSU measured radiance and Reanalysis simulated-radiance had excellent agreement. However, changes to the input data to Reanalysis had noticeable effects on the comparison. In particular, the Reanalysis has a cool bias compared to the MSU after 1990. The difference may be attributable to changes in the MSU retrieval around this period, the eruption of Mt. Pinatubo causing errors in the MSU retrieval, or may be a result of declining radiosonde availability arising from the break-up of the former Soviet Union.

A.3.2 Surface Station Comparison Figure A.3 shows the correlation and number of time points used in the correlation between 6 hourly SLP at each station in Fig. A.1 and SLP from NCEP Reanalysis. The Reanalysis has been interpolated to the station locations. The correlation is high for most stations, with a noticeable decrease in correlation in the deep tropical regions. The spread of correlations is much higher in the tropics than in the midlatitudes. Note that the spread in number of observations is also large in the tropics. Also, the number of stations with fewer observations is larger and could be contributing to the spread. Further, the annual cycle and diurnal cycles of pressure have less variance in the tropics, thus a lower signal-to-noise ratio, and this decrease in variance alone could lead to greater decoupling between observations and Reanalysis.

Figure A.4 shows the anomaly correlation (represented by the color of the station location) between the 6 hourly station SLP and Reanalysis SLP and between

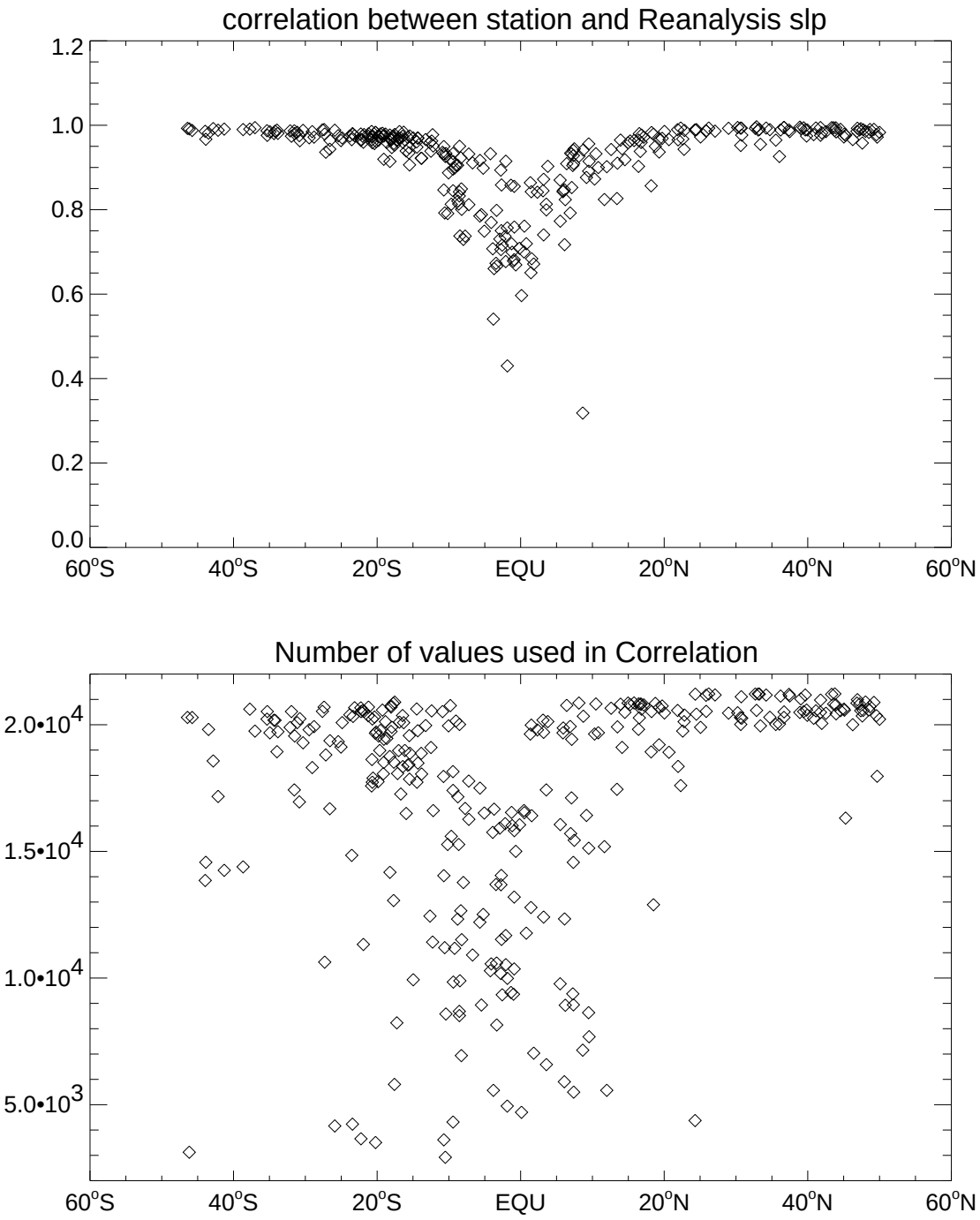

Figure A.3. (a) Correlation between station SLP and NCEP Reanalysis SLP from 6 hourly data for 1979-1994. The correlation values at each station are plotted as a function of latitude. (b) Number of time points used in each correlation.

0Z values only. Only stations that have at least five years worth of observations have been included to eliminate the possible biases of small samples hypothesized to be producing the large spread in the tropical correlations. Changing the conditions for the comparison also allows assessment of the impact of removing the annual cycle and diurnal cycle from the correlation and directly comparing the perturbations. Fig. A.4a shows the correlation when only the annual cycle is removed and all 6 hour time periods are correlated together over the entire record available at the station. The correlation points have been plotted so that low correlations are clearly visible. Throughout the domain, generally high correlations (greater than 0.70) are observed, with Reanalysis correlating at greater than 0.90 with 133 of the stations plotted. Noticeable low correlating stations (indicated by the green dots) are found in the Indonesia region and western South Pacific. The low correlation points are surrounded by considerably higher correlating stations, perhaps indicating that data quality at these stations may be suspect. However, it is curious to note that over most of Indonesia, correlations are generally lower than at the same latitude in the central and western Pacific.

In Fig. A.4b, only the 0Z values have been correlated. While the number of stations correlating with the interpolated Reanalysis at greater than 0.90 has increased to 144, more lower correlating stations are also observed. In particular, a station in the South China Sea correlates at less that 0.30. However, it is nearly adjacent to a station that correlates at 0.90, so its reliability must questioned. The general trend of lower correlations over Indonesia compared to the western and central Pacific is also noticed in the 0Z correlations. In sum, though, the generally high correlations seen comparing total SLP time series, 6 hourly annual mean anomaly, and 0Z anomaly indicate that the Reanalysis agrees well with most of the underlying station

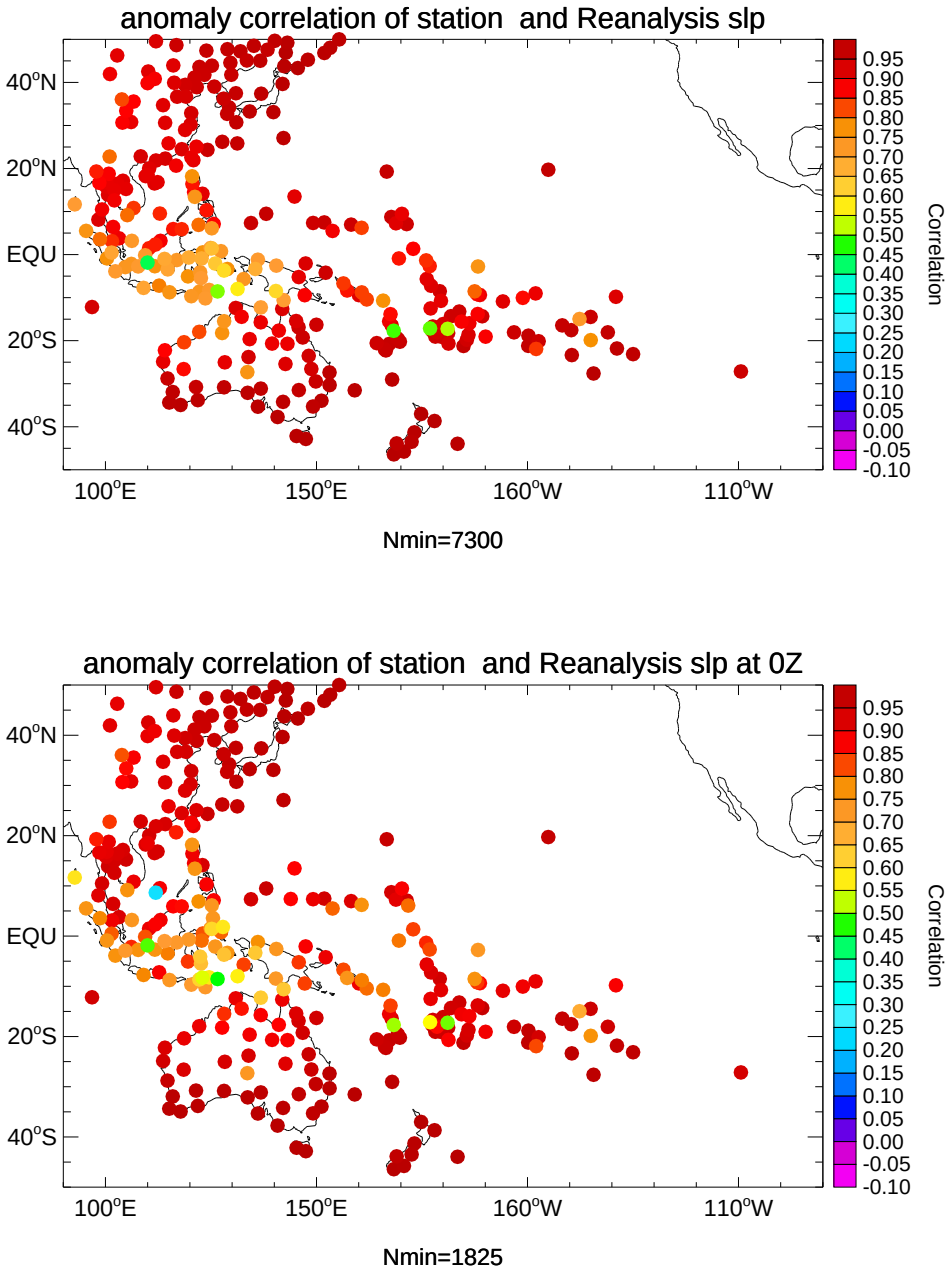

Figure A.4. (a) Map of anomaly correlation between station SLP and NCEP Reanalysis SLP from 6 hourly data for 1979-1994. Anomalies are relative to a 3 harmonic annual cycle. Location of point indicates the station location, and color indicates the correlation. Only stations with at least 5 years of values were plotted. (b) Same as (a) but only using 0Z values.

pressure observations over the entire Pacific Basin domain.

In contrast to the generally high correlations seen for SLP, Fig. A.5 shows that the correlation between station temperature and spatially interpolated Reanalysis 0.995 sigma level temperature is highly variable. A general trend towards decreasing correlation at tropical latitudes is seen, but the spread in correlation near the equator ranges from 0.80 to slightly negative. The Southern Hemisphere midlatitude correlations have greater spread than that seen in the Northern Hemisphere. Only 89 of the 320 stations correlate with the 0.995 sigma air temperature at greater than 0.90.

In Fig. A.6, spatial pattern of the anomaly correlations between station air temperature and Reanalysis 0.995 sigma air temperature is examined. Only stations with more than 5 years worth of records are included in this part of the analysis to eliminate the possible bias of small samples. Fig. A.6a shows the 6 hourly anomaly correlation. While high correlations are seen over the Asian and Australian continents, the tropical correlation is generally low, with few stations correlating at higher than 0.60. Over the domain, only 35 stations correlate greater than 0.80, while 56 correlate at less than 0.30. Correlating only one synoptic reporting period (Fig. A.6b) shows that part of the high correlation at many stations arose from the diurnal cycle. The 0Z-only anomaly correlations are significantly smaller across the domain. Only 6 stations correlate at greater than 0.80, while 106 correlate at less than 0.30. Over the Philippines, Indonesia, and the western and central tropical Pacific correlations are less than 0.30. Correlations along the western coast of Australia are also low compared with southern Australia. An examination of individual time series in all of these regions shows that the Reanalysis 0.995 sigma level air temperature has little variance compared to the poorly correlating stations (not shown).

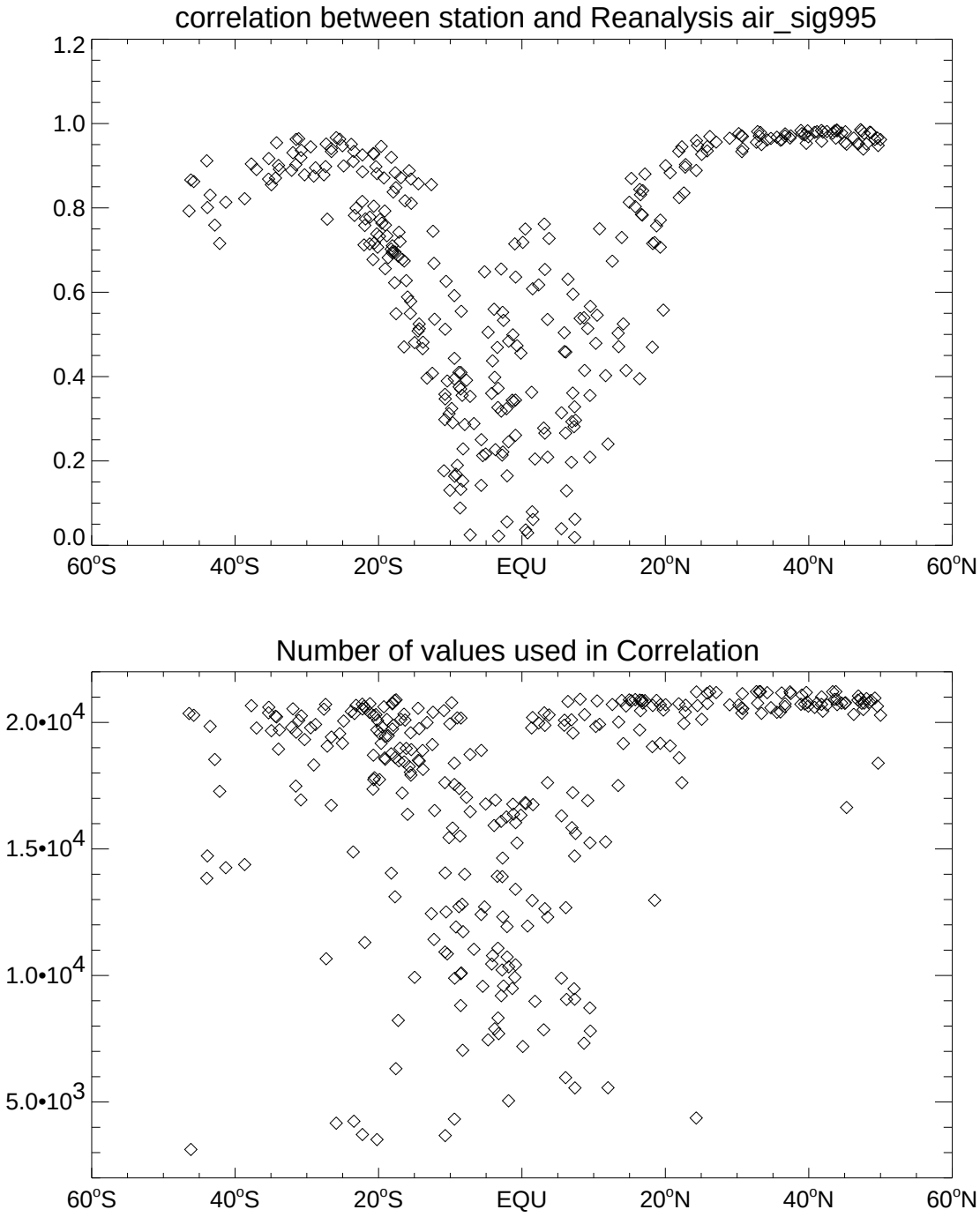

Figure A.5. Same as Fig. A.3 but for the correlation between reported station air temperature and NCEP Reanalysis 0.995 sigma air temperature.

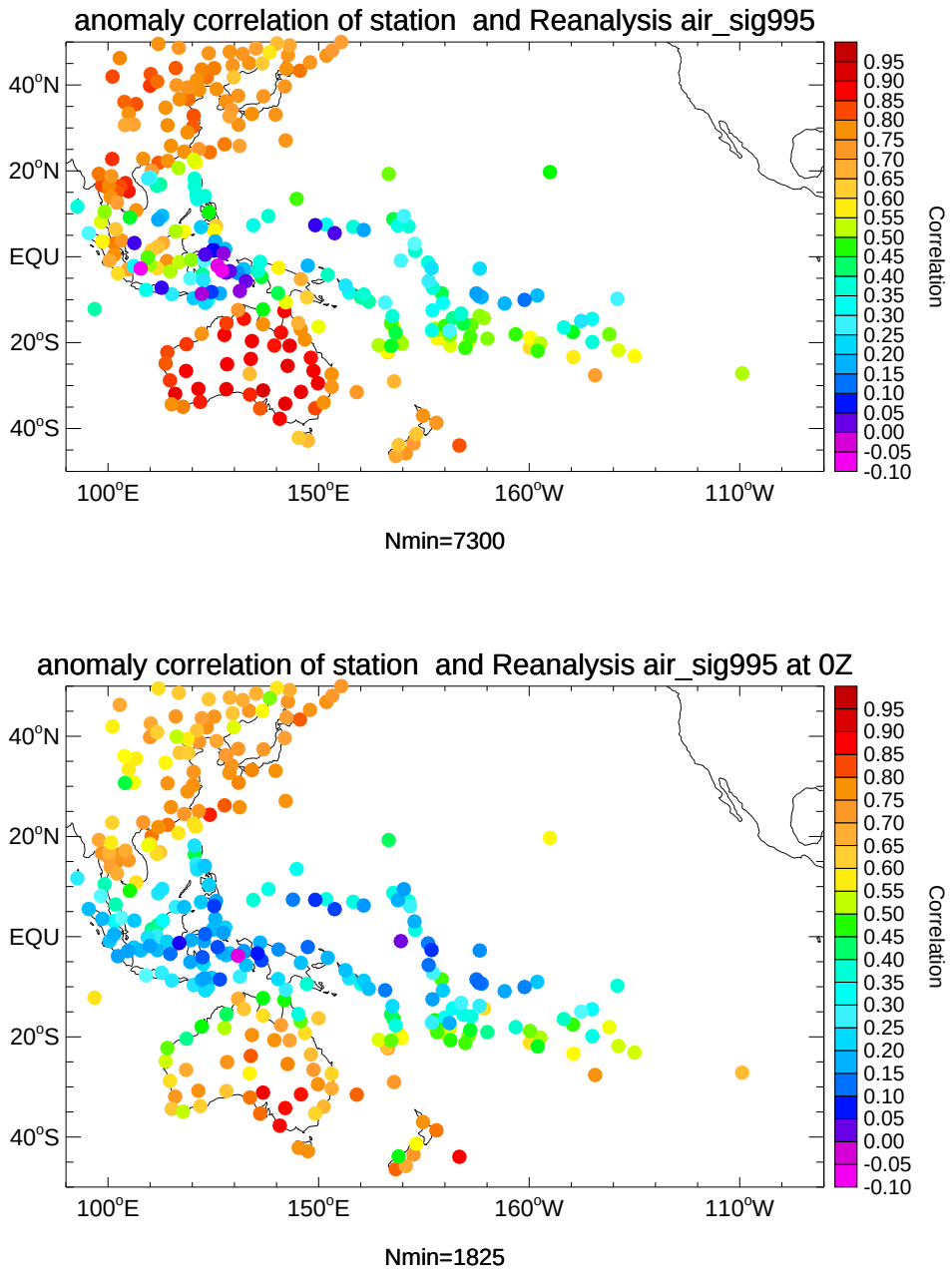

Figure A.6. As in Fig. A.4 but for the correlation between station air temperature and NCEP Reanalysis 0.995 sigma air temperature.

A.3.3 TAO Array Comparison The correlation between daily averaged NCEP Reanalysis wind at the 0.995 sigma level and TOGA TAO near-surface winds (4m) show significant spatial variability across the equatorial Pacific (Fig. A.7). In Fig. A.7a, the meridional wind relationship is examined. Similar to the results of Smull and McPhaden (1996), the correlation between the Reanalysis and TAO measured meridional wind decreases from the western Pacific to the divergent region of the eastern Pacific. In contrast to Smull and McPhaden, the meridional wind correlations are higher in the Northern Hemisphere ITCZ region than to the south. While most of the moderate to low correlating buoys are adjacent along the equator, correlations at two of the buoys are less than 0.30 and are surrounded by higher correlating locations. A far western Pacific buoy correlates at 0.40 while nearby buoys correlate at greater than 0.80. The cause of these isolated low correlations could be instrument noise. However, only 18 of the buoys correlate with the Reanalysis interpolated time series at greater than 0.70 and just 5 at greater than 0.80. The low correlations of 5 buoys along 170°W appears to be more than attributable to measurement error. In general, the very near equatorial meridional wind variations seem to compare poorly east of 170°W. The poor comparison with the eastern Pacific meridional wind field may reflect the hypothesis of (Bergman and Hendon 1996) that Reanalysis errors in the cloud and radiation fields in this region may contribute to an incorrect analysis of the motion fields.

The zonal wind correlations are higher than the meridional wind, but the spatial trends in correlation are similar (Fig. A.7b). The buoys in the western and central Pacific correlate well with the Reanalysis 0.995 sigma level zonal wind. The high correlation of the TAO zonal wind here with the 0.995 sigma level zonal wind stands in contrast to the large annual and monthly mean differences between TAO

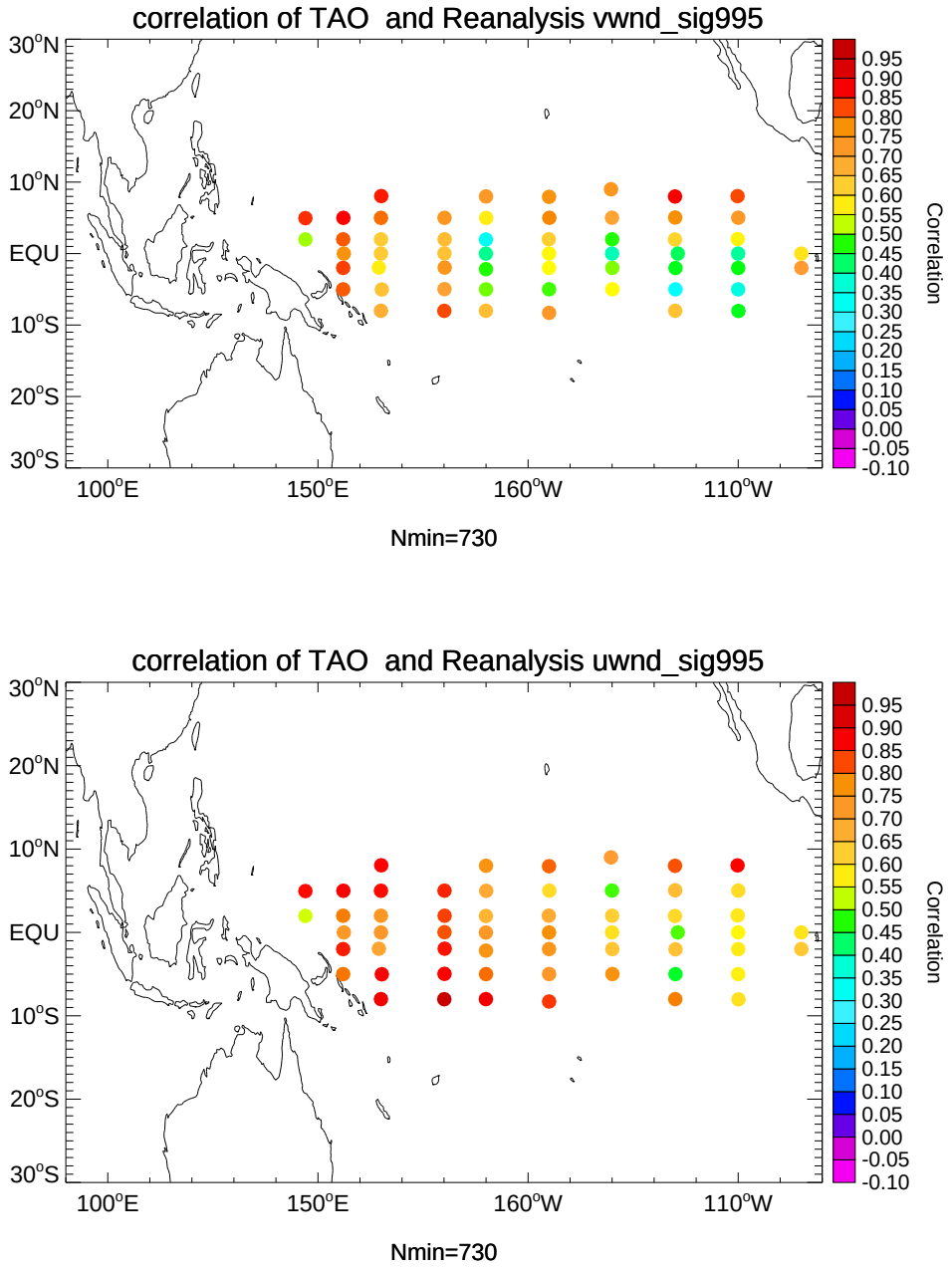

Figure A.7. (a) Map of correlation between daily TAO meridional wind and daily-averaged NCEP Reanalysis 0.995 sigma level meridional wind. Location of point indicates the buoy location and color indicates the correlation. Only buoys with at least 2 years of values were plotted. (b) Same as (a) but for zonal wind.

and Reanalysis found by Smull and McPhaden (1996) in this same region. Smull and McPhaden compared 1993 TAO monthly and annual mean winds to Reanalysis 10m surface wind interpolated to the TAO level of 4m. The differences may arise from the sensitivity of the different levels to errors and parameterization of boundary layer fluxes and radiative fluxes. These errors may play a larger role in creating mean differences than daily variations. Overall, a total of 31 of the 56 buoys correlate with the Reanalysis zonal wind at greater than 0.70 and 13 at greater than 0.80. Several areas of moderate to low correlation are therefore of concern. While the northernmost buoy at 110° correlates at greater than 0.80, the remaining buoys at this longitude correlate at less than 0.65. In both the meridional and zonal wind, 1000 hPa Reanalysis winds interpolated to the buoy locations have lower correlation with every TAO buoy than 0.995 sigma level winds, with the same spatial pattern of correlations (not shown). This indicates that the subjective classification scheme provided by Kalnay *et al.* (1996) may not accurately reflect the reliability of the Reanalysis data for all regions.

When the annual cycle is removed and anomaly wind time series are compared, the correlations between TAO winds and NCEP Reanalysis 0.995 sigma level winds decrease markedly (Fig. A.8). In the anomaly meridional wind field correlation (Fig. A.8a), 16 of the buoys correlate at less the 0.40 and only 7 at greater than 0.70. The near equatorial eastern and central Pacific appear to be largely unrelated to either the meridional or zonal wind anomalies (Fig. A.8b), providing further evidence for the possible decoupling between the analysis and true state of the atmosphere in this region, perhaps owing to errors in the radiation and cloud fields. In contrast, the correlation between the layer averaged 700-300 hPa temperature and the MSU 2/3 blend anomalies has a local maxima in the eastern equatorial Pacific

(Fig. A.2). The mechanisms for a closer analysis of the variations of the lower tropospheric temperature while incorrectly assessing the near–surface wind field are unclear at the present time.

Conversely, in the western Pacific, the correlations are high between the TAO zonal wind anomalies and Reanalysis 0.995 sigma zonal wind anomalies (Fig. A.8b) but are low for the MSU 2/3 comparison with layer averaged temperature anomalies (Fig. A.2). While only 4 buoys have correlations higher that 0.80 (none greater than 0.90), only 2 buoys have correlations less than 0.40 in the entire array. It appears that the zonal wind field is much better analyzed overall than the meridional wind field. The large zonal spatial scale and narrow meridional scale of equatorial disturbances probably contributes to the analysis errors and success in the tropical Pacific.

A.4 Conclusions

Several areas of interesting low and promising high correlations between in-situ and remotely sensed data and the NCEP Reanalysis have been examined. The entire Pacific SLP field appears to be well represented by the Reanalysis, as does the zonal wind field in the tropical western Pacific. The large-scale low correlation in the eastern Pacific when correlating Reanalysis with the TOGA TAO array is of concern. The low correlations in the eastern Pacific may reflect the hypothesis of Bergman and Hendon (1996) that the radiative transfer problems arising from the cloud scheme in the Reanalysis could disrupt the dynamics of the analyzed atmosphere. Also, several buoys have differing correlation values than what appear to be nearby neighbors. Independent wind estimates from high quality stations or wind–profilers may help in

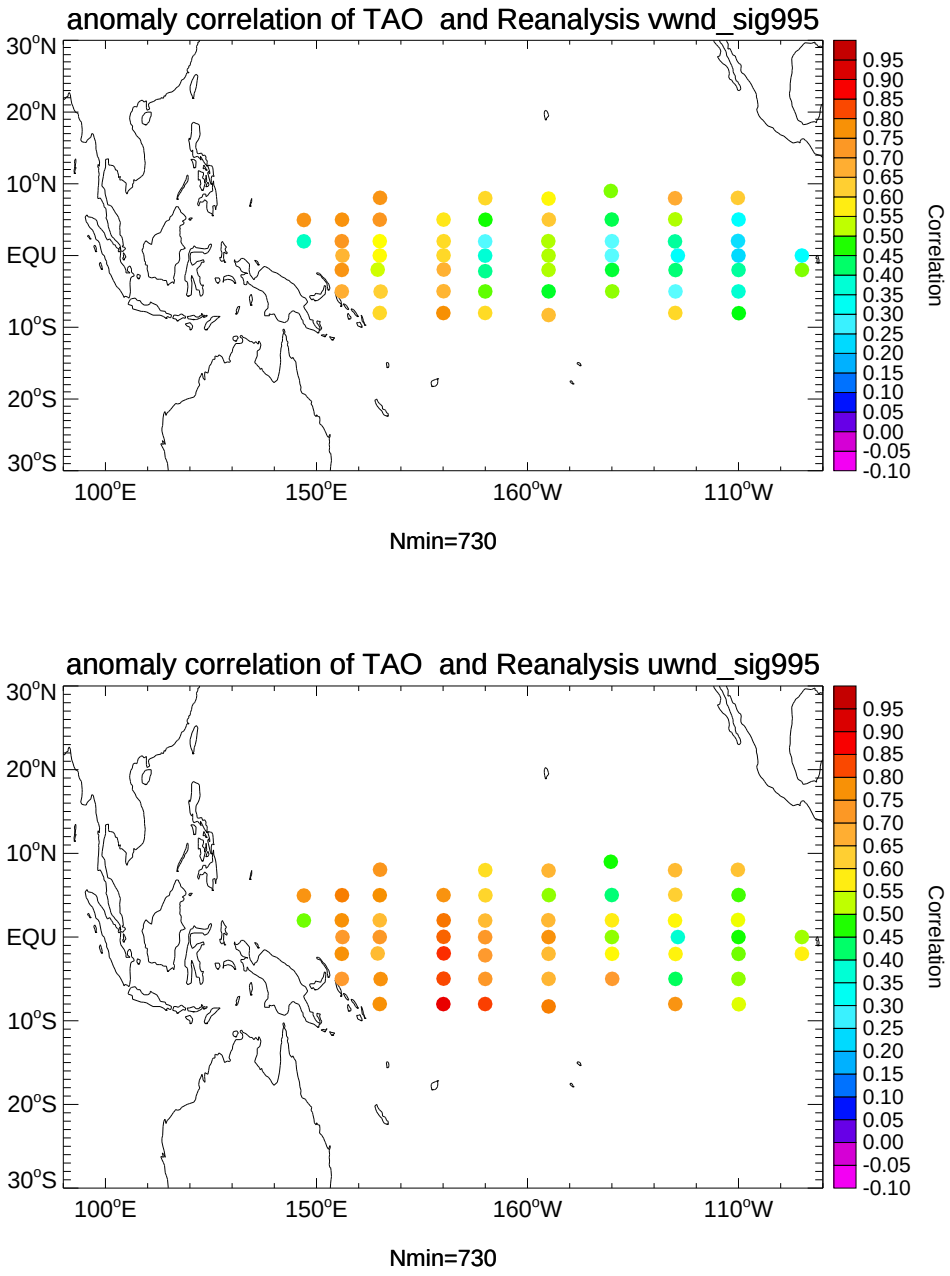

Figure A.8. (a) As in Fig. A.8 but for daily anomalies. (b) Same as (a) but for zonal wind.

resolving the correct temporal variations of the low–level wind field at these locations. A comparison of the 10m and sigma 0.995 level Reanalysis wind field in the tropical Pacific may illuminate the differences found between this study and that of Smull and McPhaden (1996).

High anomaly correlations between station and Reanalysis SLP over East Asia and Australia (Fig. A.4) provide some indication that the Reanalysis can be considered reliable for this class A variable. The steady decline of correlation into the Tropics, especially the low correlations at stations south of Borneo should be investigated further. Also, further inquiry into the noticeable differences in anomaly correlation between nearly adjacent stations in the South China Sea and south Pacific should be made to determine if the stations have errors in their reports.

The low near-surface air temperature correlations in the tropical regions seen in Fig. A.6 across the Pacific warrant further investigation. The 0.995 sigma level may not be the appropriate variable for comparison to the tropical station temperature time series. The Reanalysis 2m or 10m temperature may be a better choice. Unfortunately, the Reanalysis 2m and 10m air temperature contains strong biases from flux adjustment under warm sea surface temperature and low wind speed conditions (W. Ebisuzaki, personal communication), so it is unclear what variable could uniformly be compared between the tropics and midlatitudes to assess near–surface temperature reliability. Even over the continental regions, low correlations exist once the diurnal cycle is removed, such as along west coast of Australia (Fig. A.6b).

The correlation pattern between the MSU 2/3 daily temperature and daily averaged Reanalysis 700-300 hPa layer appears largely determined by the convective and topographically varying regions, with low correlation in regions of deep convection and high topography. The correlations appear to follow the solar cycle, with

warm land surfaces contributing to increasing differences between MSU 2/3 and Reanalysis layer averaged temperature.

The conflicting high and low correlation regions between the three observing platforms warrants further investigation, especially in the Tropics. SLP and deep layer temperature correlations are lower in the western tropical Pacific than in the eastern, while low–level wind correlations are higher in the western Pacific and lower in the eastern. As the SLP and low–level wind are closely linked, the mechanism behind the different pattern of correlation between these two variables is unclear and more wind and pressure measurements from other parts of the Tropics may help elucidate the mechanism separating the Reanalysis from the observations.

APPENDIX B

EAST ASIAN PRESSURE SURGES AND THEIR RELATIONSHIP TO TROPICAL VARIABILITY

East Asian synoptic scale cold air outbreaks accompanied by increasing surface pressure ("pressure surges") are shown to be an important aspect of the subseasonal variability of the winter monsoon system. In this study, adapted from Compo *et al.* (1997), the statistical linear relationship between pressure surges, tropical convection, and tropospheric circulation is assessed using a ten year dataset (1985/86–1994/95) of European Centre for Medium Range Weather Forecasting (ECMWF) gridded operational analyses. From spectral analysis, the pressure, wind, and temperature fluctuations indicative of strong pressure surges are found to have statistically significant spectral peaks at submonthly periods (6 to 30 days). Variability in East Asian pressure and circulation is also documented on synoptic (2 to 6 day) and Madden-Julian (30 to 70 day) timescales. The horizontal and vertical structure and the propagation characteristics of submonthly (6 to 30 day) timescale East Asian pressure surges are discussed. Relationships between East Asian pressure surges in the submonthly band and tropical circulation anomalies are found over the Bay of Bengal, eastern Indian Ocean, Indonesia, and western Pacific regions. Submonthly surges over the South China Sea are related to strong surges or groups of surges and convective activity south of Indonesia, over the South China Sea, the East Indian Ocean, and the Philippine Island regions. Submonthly surges over the Philippine Sea

are related to periods of westerly wind bursts and convective activity in the western Pacific. Upper level wave activity over western Asia precedes submonthly surges. The wave activity amplifies in the region of the Pacific jet stream, and can be traced dispersing equatorward through the region of upper level westerlies over the eastern tropical Pacific.

B.1 Introduction

During the East Asian winter monsoon periods of strong northerly winds and anomalously low temperatures dominate the synoptic weather from Siberia to the South China Sea. Though different definitions of these so-called ”pressure surges” have been proposed, (as discussed,e.g. Boyle and Chen (1987)), consensus exists on a few important characteristics in the region of East Asia: a sharp drop in temperature is accompanied by a strengthening of the climatological northerly winds and an increase in surface pressure. As enumerated by Boyle and Chen, surges have been defined by arbitrary thresholds of 12 to 24 hour temperature changes, wind acceleration, wind speed, surface pressure changes, and station pressure differences. Absolute agreement on a definition for surges is difficult to find, probably because East Asia is an extensive area and individual researchers construct definitions based on the local response to the surge (Boyle and Chen 1987). East Asian pressure surges are also termed ”cold surges” as a decrease in temperature as far south as 17°N accompanies the increasing pressure and northerly winds (Chang *et al.* 1983). Wu and Chan (1995) preferred the term ”northerly surge” to highlight the increase in wind speed that is predominantly from the north. In studying the tropical-midlatitude relationship during surge events, the term ”pressure surge” is probably more applicable, as it will be shown that while these events do not always bring significant temperature perturbations to the near-equatorial tropics, they are usually associated with

non-negligible changes in the tropical pressure and wind fields.

Two separate East Asian regions, the Philippine Sea and the South China Sea, have frequent occurrences of strong, penetrating, pressure surges (Fig. B.1). Both regions represent preferred paths for surges. Between these two principle loci is a relative minimum in surge occurrence (Ding 1990) . During boreal winter, separate local maxima of days with strong northerly winds occur over the South China Sea and Philippine Sea (Ding 1990). Both regions have pressure surge activity related to tropical convection (Williams 1981; Chu 1988; Weickmann and Khalsa 1990; Kiladis *et al.* 1994; Meehl *et al.* 1996).

The life cycle for surges over the South China Sea has received considerably more attention than those over the Philippine Sea. A summary of the conclusions involving South China Sea surges is given below:

(1) **Surges originate from midlatitude activity**. Baroclinic waves in the region of Lake Baikal (Fig. B.1) are enhanced prior to surge occurrence. These upper level waves subsequently strengthen in the Pacific jet region (Chang and Lau 1982; Joung and Hitchman 1982; Lau and Lau 1984; Hsu 1987). The Siberian High is unusually strong prior to surges (Ding 1990; Wu and Chan 1995; Wu and Chan 1997). The East Asian jet stream accelerates and extends eastward prior to and during surge arrival at Hong Kong (Chang and Lau 1980; Chang and Lau 1982; Lau *et al.* 1983; Chang and Lum 1985). The initial acceleration results from midlatitude baroclinic processes while the subsequent strengthening may be a feedback from surge enhancement of tropical convection (Chang and Lum 1985). However, during surges, the jet may strengthen on its own due to baroclinic and barotropic processes without any tropical interaction (Chang and Chen 1992). Hsu *et al.* (1990) and Meehl *et al.* (1996) have

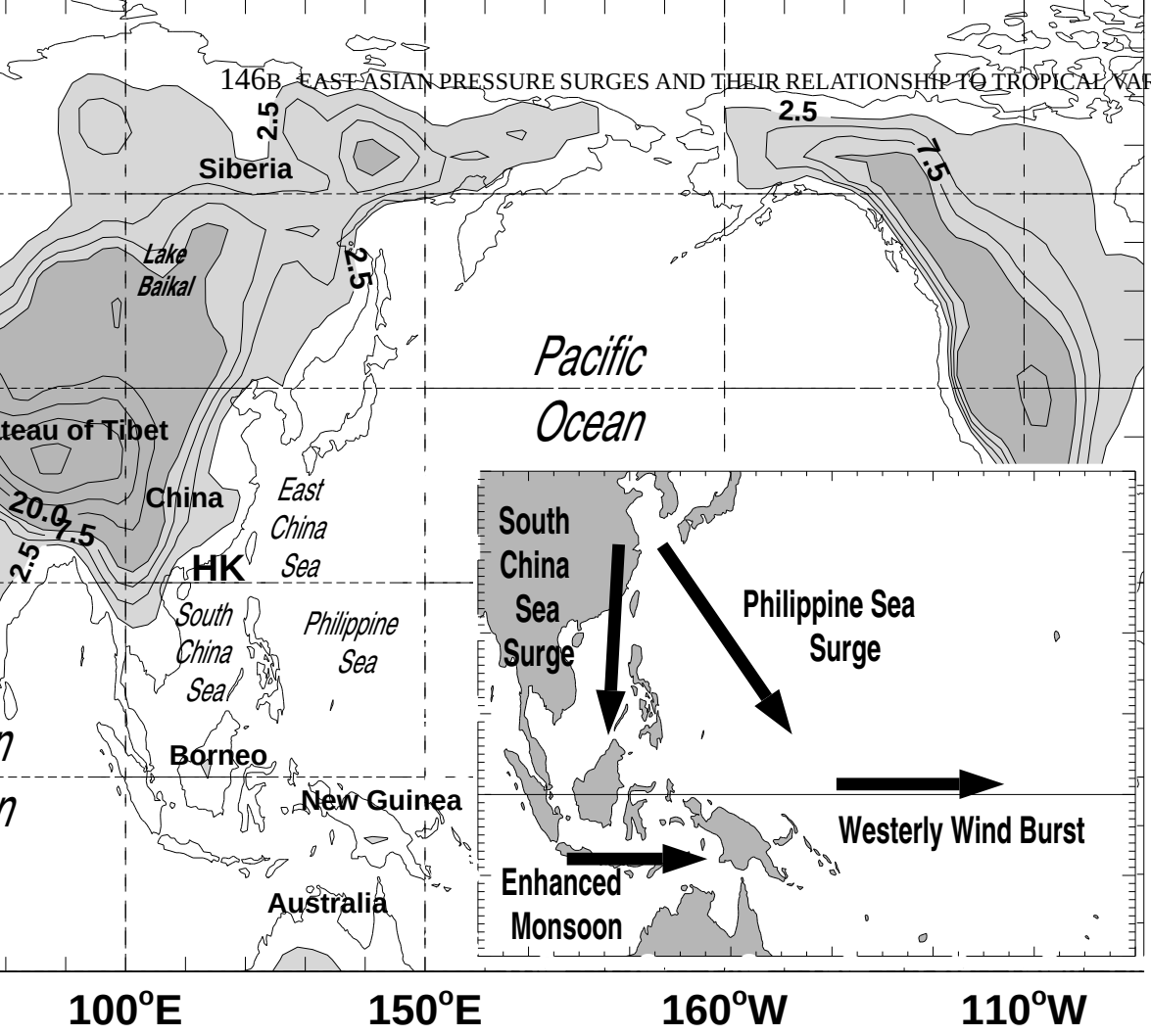

Figure B.1. Map of smoothed orography at 2.5° resolution. Contours interval is 2.5 hm until 10 hm (light gray shading) and 100 hm thereafter (dark gray shading). Geographical features referenced in the text are indicated. The inset shows the regions that previous studies indicate for surge activity and related tropical variability.

suggested that some surges are a response to enhanced subtropical upper-level wave activity forced by convection in the eastern Indian Ocean.

(2) **The surge arrival at Hong Kong is marked by dramatic 12–24 hour changes in synoptic conditions**. Surges at Hong Kong bring decreased near-surface temperature and dewpoint, increased surface pressure, and increased northerly winds within a period of 12–24 hours. The exact timing of changes depends on the definition used (Chang *et al.* 1983; Wu and Chan 1995).

(3) **Surge passage is a two stage process**. A fast southward moving (about 40 m s^{-1}) pressure pulse is followed by a slower moving (10to15 m s^{-1}) pressure increase (Chang *et al.* 1983; Leathers 1986). The second pressure rise is accompanied by a frontal passage with drops in near surface temperature and humidity and strengthening of the climatological northerly winds. Over the Asian land mass the pressure pulse has characteristics similar to an orographic Kelvin wave, whose restoring forces are gravity and the Coriolis effect normal to a barrier (Leathers 1986; Tilley 1990; Reason 1994). Over the South China Sea, the fast moving pulse has been identified as a gravity wave (Chang *et al.* 1983; Webster 1987). The second pressure increase and associated frontal passage have been modeled as a topographic Rossby wave, the atmospheric analogue to the oceanic shelf wave (see Mysak (1980) for a review of the oceanic case), whose restoring force is the orographically augmented gradient of potential vorticity along a sloping bottom surface (Leathers 1986; Hsu 1987; Tilley 1990). In contrast, Colle and Mass (1995) have suggested that Rocky Mountain surges, which appear to be similar to South China Sea surges, were governed by non-linear advection and not orographic Kelvin nor shelf wave dynamics.

(4) **The East Asian meridional divergent circulation is enhanced**. The East Asian meridional divergent circulation, the so-called ”local Hadley cell”, is enhanced in a thermally direct sense during the entire surge event, with maximum amplitude following the surge passage over southern China (Chang and Lau 1980; Chang and Lau 1982; Chu and Park 1984; Davidson *et al.* 1984; Chang and Lum 1985; Chang and Chen 1992; Wu and Chan 1997). Concurrently, upper level divergence over the South China Sea increases. Researchers disagree on the latitudinal extent of the enhancement, however.

(5) **Surges coincide with an increase in convective activity in the South China Sea region**. Separate studies show that following surge passage over southern China, convective activity increases in amplitude and areal extent over several areas: north of Borneo, along the Indochina coast, over the central South China Sea, and over the Philippine archipelago (Ramage 1971; Chang *et al.* 1979; Chang and Lau 1980; Chang and Lau 1982; Murakami 1980; Houze *et al.* 1981; Johnson and Priegnitz 1981; Lau 1982; Kiladis *et al.* 1994; Meehl *et al.* 1996).

(6) **The Australian monsoon becomes active following surge passage of south China**. Australian monsoon westerlies and convection often increase 2–3 days after surge passage is detected at stations along the South China coast (Murakami 1980; Webster 1981; Williams 1981; Love 1985a; Webster 1987). However, McBride (1987) found no obvious association between tropical cyclones, an important component of monsoon activity, and surge occurrence for the Winter MONEX year. In contrast, Love (1985b) presented a composite study and case analysis of East Asian surges that suggests surges do appear

to have an effect on Southern Hemisphere tropical cyclogenesis north of Australia.

Many of the conclusions reached about South China Sea surges depend on different datasets which extend over different time periods. In many of the composite studies performed, the use of different surge definitions leads to completely different surge statistics even within the same year (Boyle and Chen 1987). Several of the studies depend on data from Winter MONEX, which was a weak year for surge activity (Lau and Chang 1987) and, thus, may not accurately represent the surge relationship to tropical activity in general. A study that is independent of definition is needed to find the basic relationships between variables associated with East Asian pressure surges.

To provide an example of the variability of pressure fluctuations over East Asia, a time-latitude diagram along 110°E of SLP anomalies from the climatological seasonal cycle is shown in Fig. B.2. This section is representative of the region from 105°E to 115°E. Using the 5.0 hPa anomaly contour as a reference, Fig. B.2 shows that positive pressure anomalies along East Asia have their origin well north of 50°N and can be traced as far south as 10°N. Negative anomalies also appear to be propagating southwards. Phase lines (solid lines, Fig. B.2) are drawn on the diagram, and several anomaly examples are labeled. There appear to be two classes of anomalies based on southward propagation speeds of 22 m s^{-1} for some shorter duration anomalies and 13 m s^{-1} for other longer duration anomalies. These speeds appear to represent the movement of both negative and positive anomalies. As will be shown in Sec. B.4, the slower speed can be identified with submonthly (6 to 30 days) timescale surges. The faster speed can be associated with anomalies that strongly project on the synoptic (2 to 6 days) timescale.

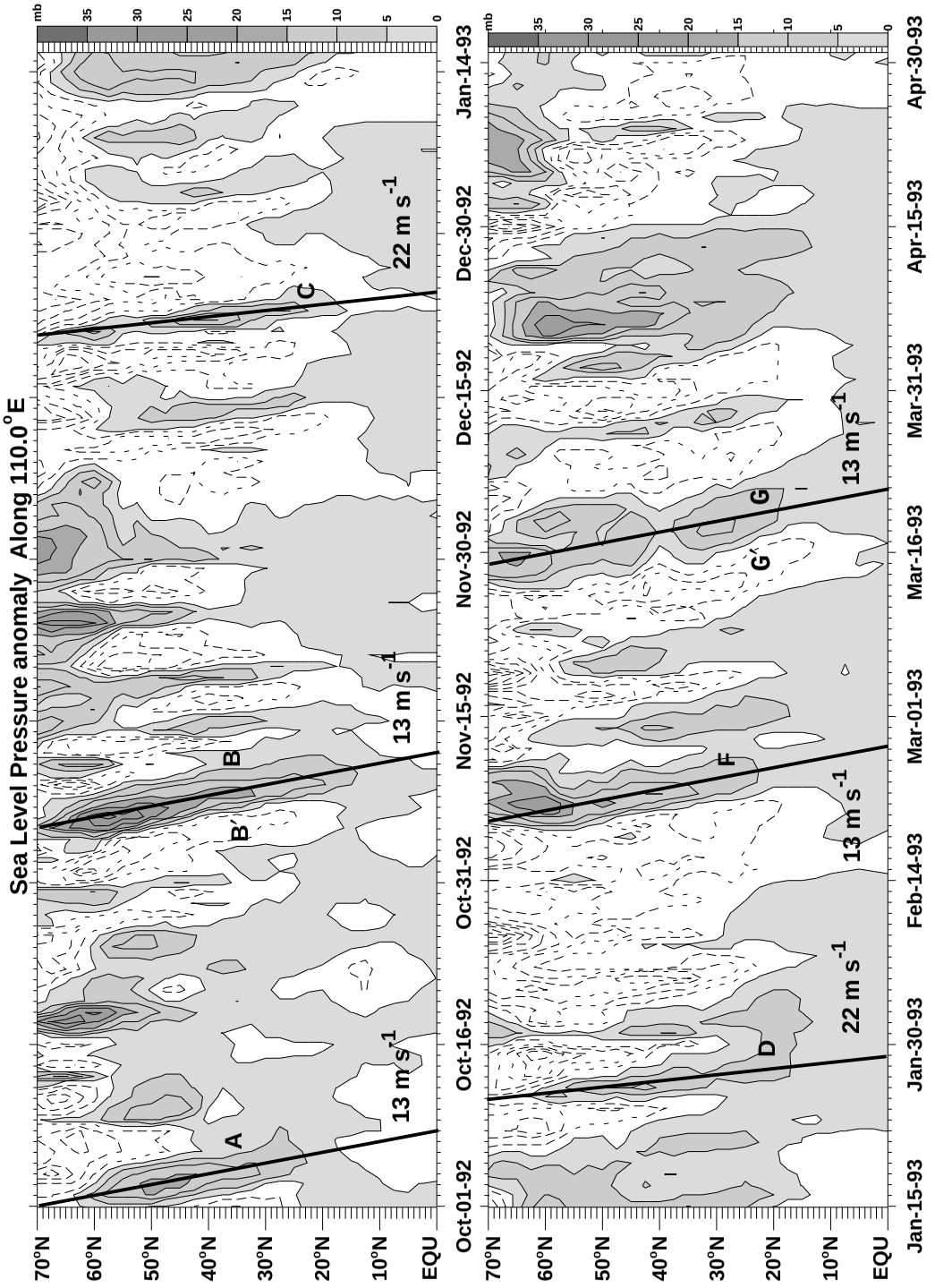

Figure B.2. Hovmoller (latitude versus time) diagram along 110.0°E of SLP anomalies. Anomalies are computed by subtracting a three-harmonic climatological annual cycle from the original timeseries as described in the text.

As an example of the slower speed, we consider surge B from November 3, 1992 to November 13, 1992. A large amplitude negative temperature perturbation (not shown) coincides with the positive pressure perturbation in Fig. B.2. Surge B is a large amplitude positive pressure anomaly in a series of southward propagating positive and negative pressure anomalies from October 1 to November 20, 1992. Surge B appears well described by a 13 m s–1 propagation speed, and a negative pressure anomaly preceding the surge (labeled B) appears also to propagate southward at that speed. While not all anomalies clearly propagate southward, the other labeled anomalies demonstrate the generality of the southward propagation and the two propagation speed estimates for this example period.

Philippine Sea pressure surges have received less attention, perhaps, because they would seem to have less human impact than surges along the densely populated coast of the South China Sea. However, some investigators have shown a relationship between these more eastern pressure surges and the so-called "westerly wind bursts" (Chu 1988; Chu and Frederick 1990; Kiladis *et al.* 1994). These episodes of near-surface enhanced westerlies in the equatorial western Pacific represent a major perturbation to both the atmosphere and the ocean. Westerly wind bursts are sometimes associated with pairs of symmetric tropical cyclones forming on both sides of the equator (Keen 1982). Groups of westerly wind bursts may interact with interannual modes of variability such as the El-Nino Southern Oscillation (ENSO), with westerly bursts in the central Pacific increasing in frequency during the warm phase of ENSO (Murakami and Sumathipala 1989). Oceanic mixing in the western Pacific is increased during periods of the enhanced winds associated with westerly bursts (Lukas and Lindstrom 1991; McPhaden *et al.* 1988;

McPhaden *et al.* 1992). Oceanic equatorial Kelvin waves, which have been hypothesized to play a role in ENSO initiation, have been shown to be initiated by westerly bursts (Knox and Halpern 1982; Giese and Harrison 1990; Kindle and Phoebus 1995).

Chu (1988) and Chu and Frederick (1990) documented westerly wind bursts associated with equatorially propagating Philippine Sea pressure surges. These case studies showed Philippine Sea pressure surges moving southward at 40 m s^{-1} along 135°E preceding an enhanced equatorial sea level pressure (SLP) gradient. Westerly wind and convective anomalies east of New Guinea followed the enhanced SLP gradient. Using cross correlations of outgoing longwave radiation (OLR) and National Meteorological Center analyzed wind fields, Kiladis *et al.* (1994) showed that low level westerly wind anomalies in the region east of New Guinea are associated with Philippine Sea surges and a strengthening of the equatorial SLP gradient.

The sequence of events associated with surge passage over the South China Sea or Philippine Sea occurs on a wide range of temporal scales with periods from 4 days to 30 days (Murakami 1979; Ding 1990; Kiladis *et al.* 1994; Meehl *et al.* 1996). Using data for the period 16 November 1970 to 15 March 1971, Murakami (1979) found spectral peaks are prominent in the meridional wind and latitudinal pressure gradient at synoptic (2 to 6 day) timescales over the East China Sea, the main path for Philippine Sea pressure surges. Murakami also found large power on this timescale in the meridional wind over the South China Sea. In addition, meridional wind and surface pressure time series over the South China Sea have a spectral peak between 20 and 30 days. Co-spectra of fluctuations of meridional wind and temperature between the East China Sea and South China Sea showed the East China

Sea fluctuations leading by 1–3 days. Ding (1990) pointed out a 10–to–20 day period in fluctuations of the Siberian High and pressure surge events. In the present study, the spectral analysis of surges is extended by using 10 winters (December-April), allowing greater confidence in the results. The statistical significance of the spectra is also discussed.

Another important timescale in the tropics is that of the Madden-Julian Oscillation (MJO) or 40 to 50 Day Oscillation (see Madden and Julian (1994) for a review of the phenomena). Some researchers have shown a connection between strong pressure surges and the movement of convection between the eastern Indian and western Pacific Oceans associated with the MJO. Weickmann and Khalsa (1990) documented an MJO event during November/December, 1981, in which an intense pressure surge and cold air outbreak precedes the shift of intraseasonal convection from the eastern Indian Ocean to the western Pacific by 12 days. They conclude that a surge initiated convection in the region of 110°E and was important to the overall eastward movement of this MJO case. Hsu *et al.* (1990) documented a case of a pressure surge occurring in response to a subtropical wave-train in the western Pacific forced by MJO convection in the eastern Indian Ocean. The Indonesian convection activated by the pressure surge was thought to be enhanced by favorable upper level conditions that developed as part of the MJO.

Despite the advances made in previous studies, a number of important questions remain:

(1) What are the timescales associated with surge activity?

(2) What are the basic relationships between surge-associated variables, independent of an arbitrary definition?

(3) Is the tropical response to pressure surges a robust signal?

In the present study, through answering the questions above, we hope to extend understanding of the global and temporal variability related to episodes of East Asian pressure surges. This paper is organized as follows. Section B.2 discusses the data and provides a rationale for the analysis methods used. The timescales present in pressure surge variables are identified through spectral analysis in section B.3. A linear regression analysis is presented in section B.4. In addition, we discuss the horizontal and vertical structure of East Asian pressure surges, the relationship of surges to fluctuations in the East Asian jet streams and upper level baroclinic wave activity, and the correlation between pressure surges and tropical variability in tropospheric circulation and convection. Discussion and comparison with previous work is presented in section B.5.

B.2 Data and Methodology

B.2.1 Data The European Centre for Medium Range Weather Forecasting (ECMWF) gridded global analyses of standard atmospheric variables are used for the period 1 January 1985 to 31 December 1995 to examine East Asian winter monsoon pressure surges. For a detailed description and analysis of this dataset see Trenberth (1991; Trenberth (1992; Trenberth and Guillemot (1995). The twice daily ECMWF analyses are averaged prior to any other processing to remove diurnal fluctuations. A daily OLR dataset produced by NOAA for the same time period is also used. For a description of the interpolation scheme used on this dataset see Liebmann and Smith (1996). Both datasets are on 2.5 by 2.5 grid. No data are missing for the periods under consideration.

B.2.2 Methodology Anomaly time series are constructed by removing the first three harmonics (periods of 365.25, 182.625, and 121.75 days) of the

climatological seasonal cycle using a least squares fit to the entire record of 1 January 1985–31 December 1995. To determine if any significant periods occur in the time series, ten-winter ensemble averages of spectra are computed using 181 days from 15 November to 15 May with a 15 day cosine taper on each end.

Confidence levels for the spectral calculations are determined with Monte Carlo tests assuming a first-order Markov process. At each grid point, for each winter period, 1000 autocorrelated random time series are constructed, using the lag–1 autocorrelation of the anomaly data of that winter. The spectrum for each random time series is computed. The 10 winters are averaged together to produced 1000 ensemble averages at each grid point. A distribution of spectral power is then calculated separately at each frequency.

After examining spectral results, we find significant power at periods between 6 and 30 days in several of the variables associated with surge activity. The choice of this band also eliminates high frequency baroclinic wave activity in the midlatitudes, high frequency mixed Rossby-gravity wave activity in tropics, and the lower frequencies associated with the MJO. The complete record of the anomaly data is temporally filtered into a submonthly (6–30 day) frequency band using a Lanczos digital filter (Duchon 1979) with 121 daily weights. The high number of weights helps eliminate Gibb's ringing in the response of the filter. The response of the filter used is shown in Kiladis and Weickmann (1992). These are the same bands and weights as used in several previous studies, so the results shown here are directly comparable to those works (Kiladis and Weickmann 1992; Kiladis *et al.* 1994; Meehl *et al.* 1996).

The composite relationship between pressure surges and global circulation is determined using the linear regression technique of (Kiladis and Weickmann

1992). The linear regression assesses the statistically significant linear relationship between SLP fluctuations indicative of surges and the global circulation and convective variability. Bandpass filtered SLP at various base points is cross-correlated and linearly regressed against identically filtered OLR and ECMWF analyzed SLP, wind, and temperature. A separate regression coefficient is obtained for each variable at every grid point.

Linear regressions are first performed for grid points covering East Asia. Regressions are separately computed using only three months of each year during the northern hemisphere cool season (SON, OND, NDJ, DJF, JFM, FMA, MAM) for base points spaced every 10 degrees from 50°N to 10°S and 100°E to 150°E (42 points) and compared to determine the seasonality of pressure surges. The regressed patterns for SON and OND were decidedly different from the other three month groupings. The northern hemisphere tropical and midlatitude patterns seen for all of the three month groupings of DJF through FMA were quite similar. Given these results, December through April data, inclusive, are used in the regression results shown here.

Regression of the filtered SLP anomaly against the data at all other grid points permits the local statistical significance of the linear relationship between the SLP anomaly at the base point and the circulation or OLR anomaly to be determined using the ”student t-test.” The number of degrees of freedom at each grid point is derived according to the method of Livezey and Chen (1983). The time-lagged regression is also utilized to provide the temporal evolution of the large-scale circulation and convective anomalies associated with the pressure perturbations. In this way, circulation anomalies that precede surges and those that follow surges can be determined objectively. Wind vectors are plotted where the local correlation of either

the zonal u or meridional v wind component meets or exceeds the 99.5% confidence level, while maps of regressed OLR indicate only those values that meet or exceed the 99.5% confidence level. Contours of SLP and streamfunction are shown without regard to correlation.

The use of the regression method assumes a nearly linear relationship between the predictor and predictand. A nearly linear relationship between SLP, circulation, and wind during pressure surges is apparent in case studies of pressure surges (Chang *et al.* 1983; Chu and Park 1984; Love 1985a). With respect to OLR, the linear assumption is valid to the extent that lower tropospheric wind anomalies associated with pressure surges contribute to convective activity. A direct relationship between pressure surge occurrence, with its accompanying increase in the northeasterly flow over the South China Sea, and an increase in convective activity is observed in case studies (Houze *et al.* 1981; Johnson and Priegnitz 1981). However, nonlinear interactions such as CISK (conditional instability of the second kind), where the feedback of the circulation onto the convection itself Chang and Lim (1988, e.g.,) becomes important, is a likely component of the response to the tropical heating anomaly induced by the pressure surges.

Two base points (15°N, 115°E and 20°N, 140°E) are shown as representative of the results obtained using the 42 SLP base points throughout the East Asian sector. The results highlighted here are qualitatively insensitive to the choice of base point. The South China Sea base point at (15°N, 115°E) represents the northern most base point over the South China Sea that retains a statistically significant relationship to southern hemisphere anomalies south of Indonesia, while the northern hemisphere tropical circulation and convective anomalies are robust and statistically significant

using base points as for north as 50°N over the Asian continent. The regression results at this base point are plotted using a 3.0 hPa anomaly, an anomaly value based on the magnitude of strong surges observed at this latitude (e.g., cases B, F, and G in Fig. B.2). Similar magnitudes of SLP anomalies at this latitude are seen in the composite results of Wu and Chan (1995). The Philippine Sea base point (20°N, 140°E) provides a secondary verification of the reproducibility of the signals observed west of 120°E using the South China Sea base point. Further, a significant relationship observed between Philippine Sea base points and circulation and OLR anomalies in the equatorial western Pacific is not observed with any base points located over continental East Asia or the South China Sea. A Philippine Sea base point is therefore included to illustrate this association. The regression results at the Philippine Sea base point are plotted assuming an anomaly value of 4.0 hPa, which is also consistent with observed cases of surges in this area (not shown).

B.3 Spectral Analysis

Figure B.2 showed variations of SLP anomalies on several timescales. To test the generality of the limited time period examined, the spectral characteristics of the ten-year sample are investigated. Figure B.3(a) shows the latitudinal distribution of SLP spectral power for the boreal winter along 110°E. This meridian covers the western South China Sea and coastal Indochina. North of 40°N, power significant at the 95% level is seen at periods less than 9 days. In the subtropics and tropics, these synoptic-scale peaks diminish in intensity, while the amplitude of the peaks in the submonthly and MJO bands increases. Almost no significant power is seen at synoptic time scale south of 15°N. Two peaks between 10 and 20 days dominate the spectra from 30°N to 10°N. Although not statistically significant until near the equator, there is a broad peak in power between 30 and 40 days at most latitudes,

along with a peak at about 60 days near the equator which is most likely due to the MJO.

Figure B.3(b) shows the latitudinal distribution of 850 hPa meridional wind power as in Fig. B.3(a). The 850 hPa meridional wind displays a larger distribution of significant power at periods less than 6 days than SLP (Fig. B.3 (a)). The peaks seen between 10 and 20 days in Fig. B.3 (a) are also significantly present in the meridional wind. However, the peak at approximately 12 days is only statistically significant at the 90level. The peak around 20 days is significant from 25°N to 5°N, a southward shift from the peak in SLP. Spectra of meridional wind at 200 hPa over the South China Sea and East Asia also show statistically significant peaks at the 95% level between 10 and 20 days (not shown).

As with SLP, spectra of lower tropospheric air temperature between 105°E to 120°E (not shown) exhibit a decrease in significant power at synoptic timescales from the midlatitudes to the deep tropics. Also like SLP, air temperature at 850 hPa has two significant spectral peaks between 10 and 22 days from 35°N to 15°N.

To compare the spectral characteristics of SLP in the South China Sea surge area with that in the Philippine Sea, Fig. B.4(a) shows spectra of SLP as a function longitude along 20°N. This latitude band represents the region influenced by both the Philippine Sea and South China Sea surges. Only periods between 3 and 25 days are shown; most of SLP variance significant at the 95% level is in this range over the South China Sea (Fig. B.3(a)), and this is also true further east. The dominance of two submonthly spectral peaks between 10 and 20 days is apparent from 95°E to 140°E. At the synoptic timescale, the South China Sea region has little variance, but the Philippine Sea region still has many significant peaks. In contrast to the wide longitudinal extent of submonthly power at 20°N, SLP spectra examined south of

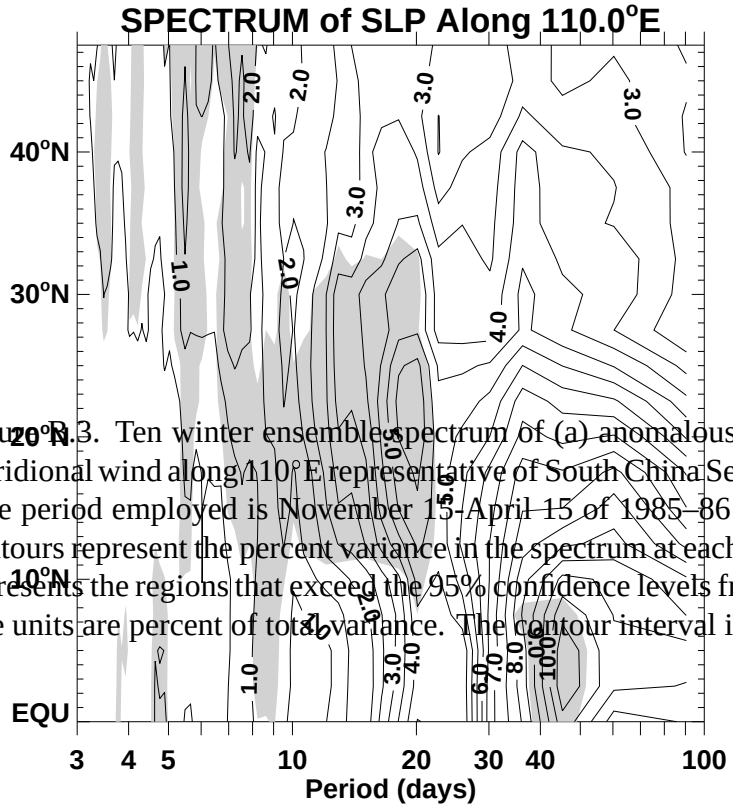

Figure B.3. Ten winter ensemble spectrum of (a) anomalous SLP and (b) 850 hPa meridional wind along 110° E representative of South China Sea pressure surges. The time period employed is November 15-April 15 of 1985–86 to 1994–95. The line contours represent the percent variance in the spectrum at each latitude. The shading represents the regions that exceed the 95% confidence levels from Monte Carlo tests. The units are percent of total variance. The contour interval is 1%.

15°N show significant power in the submonthly band only west of the Philippine Islands.

Zonal wind spectra for the South China Sea and Philippine Sea regions are shown in Fig. B.3(b) along 7.5N as function of longitude. Figure B.3(b) shows that zonal wind fluctuations over the South China Sea have power significant at the 95% at the same periods of the submonthly band as SLP fluctuations to the north (Fig. B.3(a)). The submonthly peaks between 10 and 20 days are largely confined to the South China Sea and Bay of Bengal while the Philippine Sea has significant power at the 19 day peak centered at 125 B.3E. Also, a 22 day peak contains significant power from 135 to 145E. The concomitant significant spectral peaks between SLP and zonal wind imply that the same dynamical forcing may account for the similarities. The significant timescales seen in the spectra suggest that a broad range of scales should be examined and 6 to 30 days appears appropriate for capturing the majority of the significant variance associated with the wind and SLP over East Asia.

B.4 Linear Regression Analysis

Based on the results of the previous section, pressure surge variability in the 6–30 day band is examined. This period range captures the bulk of the statistically significant fluctuations in parameters associated with surges.

B.4.1 Lower Tropospheric Circulation In Fig. B.5 , the lower tropospheric circulation anomalies associated with the evolution of submonthly pressure surges are examined using an SLP base point at 15°N, 115°E. At Day –5 (Fig. B.5(a)), positive pressure anomalies cover northern Asia with a wedge of positive pressure and northerly wind anomalies extending over most of China. The leading edge of the anomaly is marked by the thick dark line (0.5 hPa). Suppressed convective activity (denoted by hatching) is shown over and east of the Philippines and south of India.

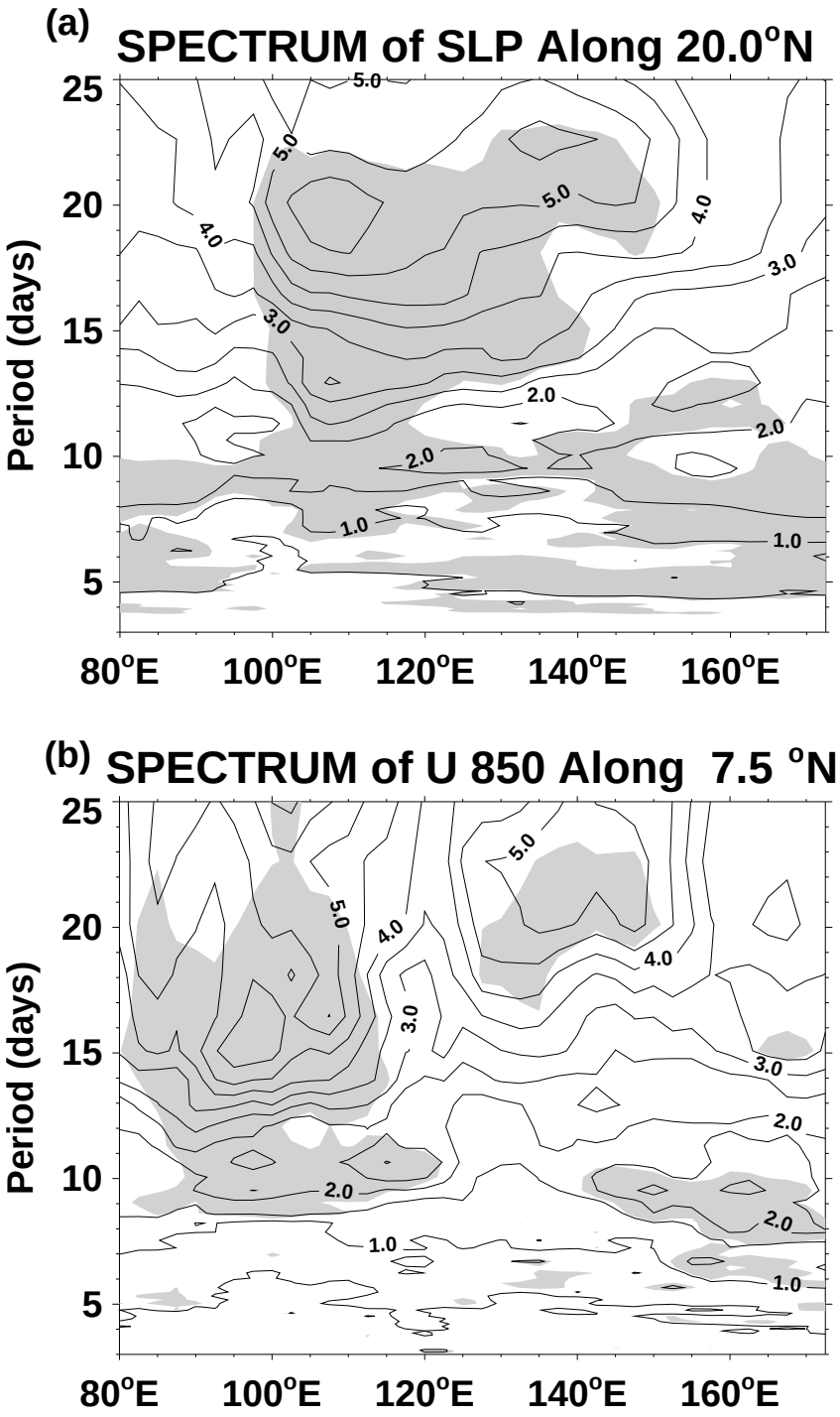

Figure B.4. As in Fig. B.3 but for (a) anomalous SLP along 20°N and (b) anomalous zonal wind along 7.5°N.

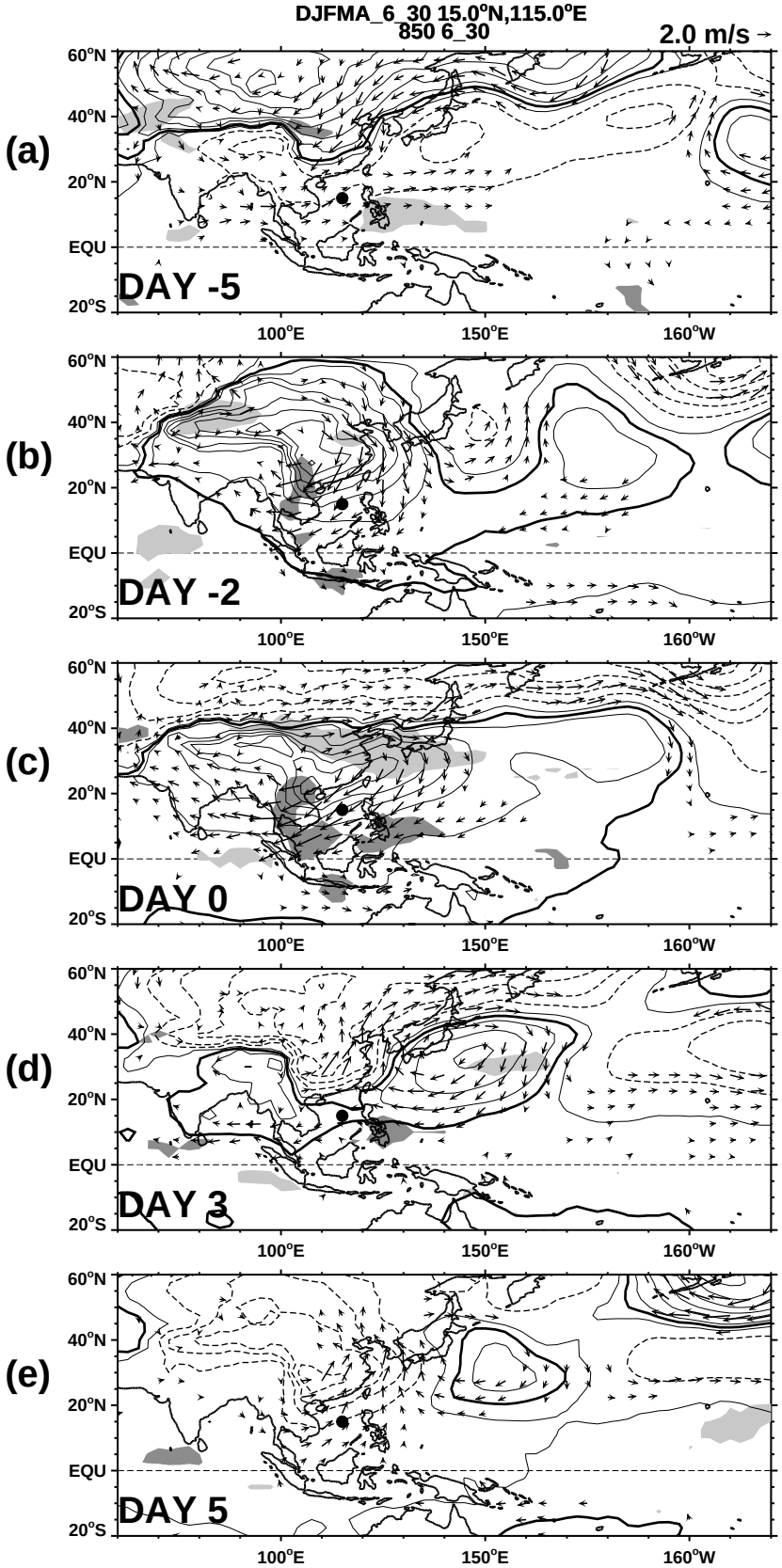

Figure B.5. 6–30 day bandpass filtered SLP, OLR, and 850 hPa wind anomaly fields linearly regressed against SLP at 15°N, 115°E (indicated by the black dot) for (a) 5 days preceding maximum SLP anomaly at the base point, (b) 2 days preceding, (c) day of maximum, and (d) 3 days after maximum. The minimum correlation coefficient for plotting a vector or OLR is that at the 99.5% significance level. The regressed values are based on a typical perturbation of SLP at the base point (3.0 hPa). SLP is plotted without regards to correlation at contour interval 1.0 hPa. The thick line contour indicates the 0.5 hPa level. OLR contour is 8.0 W m^{-2} with negative

At Day –2 (Fig. B.5(b)), the surge has crossed the equator and low level convergence just south of Borneo is indicated by a statistically significant increase in convective activity, as shown by negative values of OLR (shading). Divergence calculations (not shown) on the 850 hPa regressed field also confirm convergence co-located with the negative OLR anomaly. In addition, convective activity is also enhanced over Indochina. The convective activity increases in intensity in the region south of Borneo as low level westerly anomalies strengthen at Day 0 (Fig. B.5(c)). Anomalous convective activity over the southern Philippines and Philippine Sea is accompanied by statistically significant low level easterlies. Northeast of Borneo and over Southeast Asia, convective anomalies have also developed in the increased northeasterly anomalies. The convective activity along the coast of Southeast Asia and over the southern Philippines may be a result of the upslope flow along the orography of that region. Also on Day 0, significant easterly anomalies cover the Bay of Bengal and central India.

By Day +3 (Fig. B.5(d)), the South China Sea surge has weakened, while a positive pressure anomaly has propagated eastward from the China coast, extending the maximum of the enhanced tropical trades eastward and northward. The southerlies seen over China at Day +3 propagate southward. A significant area of negative OLR is observed in the easterly anomalies over Sri Lanka.

In regressions using base points located from the midlatitudes to the equator along the East Asia, it is observed that OLR anomalies over and around the South China Sea basin are significantly correlated to SLP along the path of the pressure surge from 55°N to the equator (not shown). In contrast, OLR anomalies south of the equator in the eastern Indian Ocean and south of Borneo only correlate significantly with SLP fluctuations using base points east of 120°E and south of 20°N. Tropical

and deep tropical base points showed results similar to that of Fig. B.5 . The localization of the correlation indicates that many surges do not penetrate far enough south to affect Southern Hemisphere westerlies and convection.

A significant relationship to convective and wind anomalies in the equatorial western Pacific is observed in Fig. B.6 using a base point located in the Philippine Sea (20°N, 140°E). Qualitatively similar results to those presented here were obtained using base points throughout the Philippine Sea domain as far north as 40°N. At Day –4 (Fig. B.6(a)), the cross-hemispheric influence of the South China Sea pressure surge can be seen in the northerly anomalies over the South China Sea and in the weak westerly anomalies and negative OLR anomalies south of Indonesia. In the western Pacific, however, the westerly anomalies are quite well developed, with negative OLR anomalies stretching from the equator to 20°S near the dateline. The progress of the South China Sea surge at Day –4 can be compared directly with Fig. B.6(b) for Day –2, although the magnitude of the anomalies is weaker here. An anticyclonic anomaly in the Philippine Sea, indicated by the wind vectors and positive OLR anomaly at Day –4, is not observed in Day –2 of Fig. B.5. This anticyclonic anomaly is observed to have propagated northwestward from the equatorial region (not shown).

In Fig. B.6(b) (Day –2), the pressure anomaly s positive over the entire Philippine Sea, with two local maxima: one at 30°N corresponding to a southeastward moving anticyclonic anomaly from the East China Sea and the other at 10N corresponding to the anticyclonic anomaly already present two days previously. The pressure anomaly over the Philippine Sea and South China Sea combine to produce a northeasterly trade surge from 160°E extending into the Bay of Bengal. The westerly wind and OLR anomalies in the central Pacific have propagated westward from

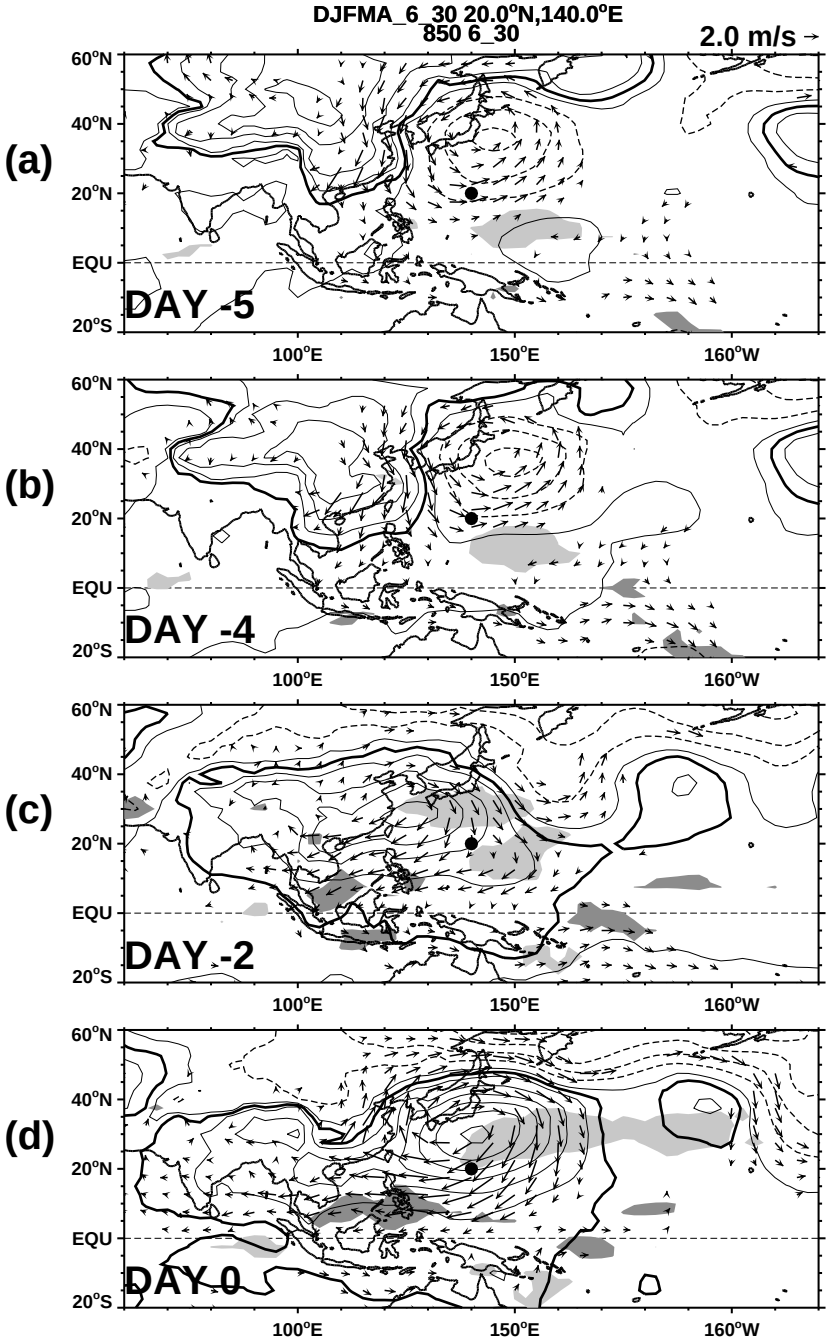

Figure B.6. Same as Fig. B.5 but for an SLP base point at 20°N, 140°E (indicated by the black dot). The regressed values are based on 4.0 hPa anomaly at the base point.

Day –4 to Day –2 and continue to do so to Day 0 (Fig. B.6(c)). Figure B.6(c) can be compared directly with Fig. B.5(c). The negative OLR anomaly in the western Pacific is also present in Fig. B.5(c) but is not accompanied by any significant circulation signal there.

The use of a Philippine Sea base point shows that western Pacific circulation and convective anomalies do have a significant correlation with pressure fluctuations in the Philippine Sea. Figure also shows that the western Pacific equatorial and southern hemisphere anomalies appear to be propagating from the central Pacific to the western Pacific. The evolution and structure of the western Pacific circulation and OLR anomalies in Fig. B.6 are similar to those found by Kiladis and Wheeler (1995), who associated the structure with an equatorial Rossby wave.

The Philippine Sea surge, therefore, appears to be the combination of a westward moving tropical anticyclonic disturbance and a southeastward moving midlatitude anticyclonic disturbance. By tracking the centers of the pressure anomalies from Fig. B.6, the southeastward propagation speed of the Philippine Sea anticyclone is approximately $7 - 8$ m s^{-1} while the tropical anticyclone moves northwestward at approximately $3 - 4$ m s^{-1}.

B.4.2 Upper Tropospheric Circulation Figure B.7 shows the 200 hPa streamfunction and wind vectors of the regression corresponding to Fig. B.5. The upper tropospheric pattern related to pressure surges covers a broader area than that of the lower troposphere. As seen at Day –5 (Fig. B.7(a)) a trough and ridge system is centered over India. In addition, a midlatitude trough/ridge wave pattern over eastern and central Asia is evident. When compared with streamfunction fields at lower levels (not shown), a westward tilt with height of the features is evident, suggesting baroclinic waves within the storm track.

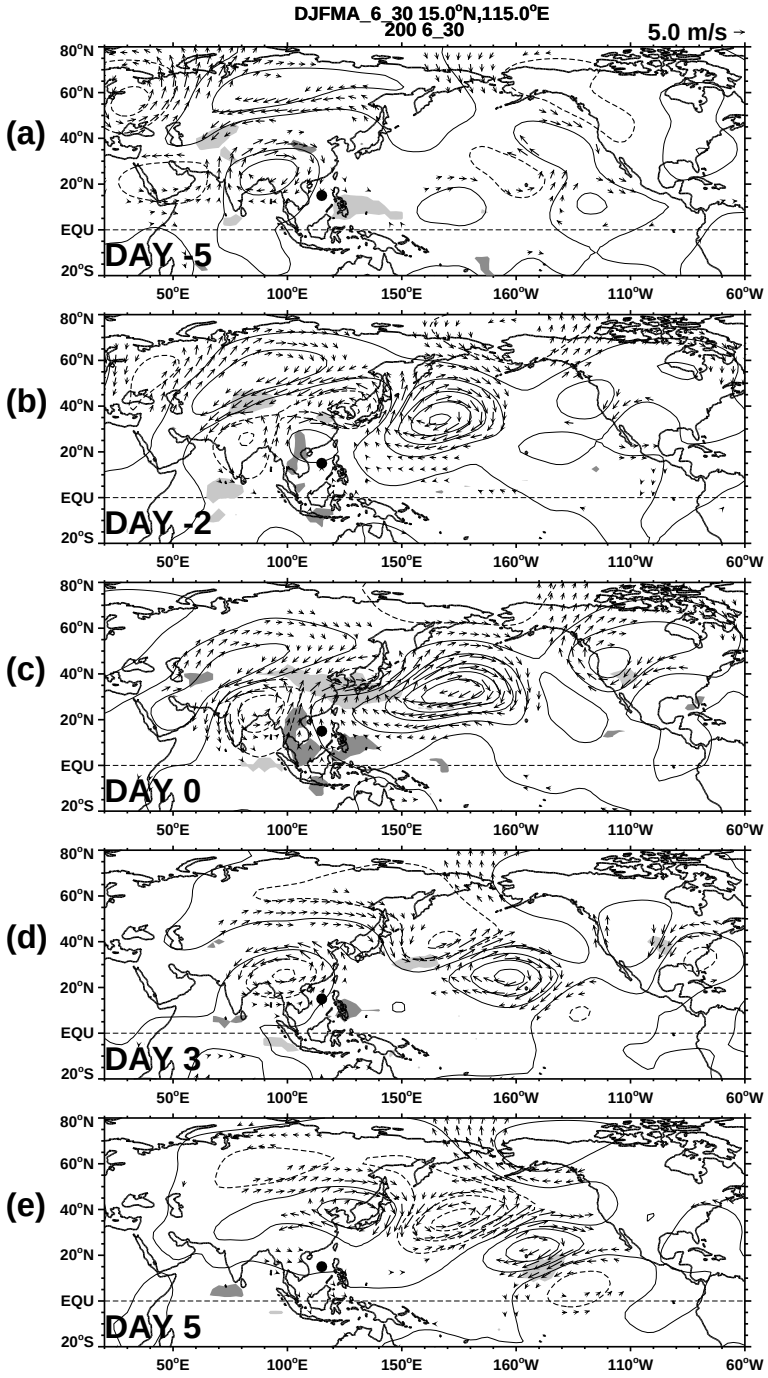

Figure B.7. 6–30 day bandpass filtered OLR and 200 hPa wind anomaly fields corresponding to Fig. B.5 for (a) 5 days preceding maximum SLP anomaly at the base point, (b) 2 days preceding, (c) day of maximum. The minimum correlation coefficient for plotting a vector or OLR is the 99.5% local significance level. Streamfunction is plotted without regards to correlation, interval is 10^6 m^2 s^{-2}. Only every other vector is plotted.

As convective anomalies develop over Southeast Asia, the southern Philippines, and southern Sumatra from Day –2 to 0, a subtropical wave pattern is evident, arcing into the midlatitude jetstream region of the central Pacific. By Day +3 (Fig. B.7(d)), as the convective signal weakens, the wave pattern advances further into the Pacific and circulation centers over India diminish. The wave pattern arcs from Bangladesh to the eastern Pacific similar to several studies examining the propagation of Rossby wave through the eastern Pacific westerly ducts (Webster and Holton 1982; Kiladis and Weickmann 1992; Tomas and Webster 1994). At Day +5 (Fig. B.7(e)) the wave pattern has significant anomalies crossing into the southern hemisphere.

Comparing Figs. B.7 and B.5, the lower tropospheric pressure surge separates from the upper level flow. This separation is apparent comparing Day –5 (Figs. B.7(a) and B.5(a)). While the lower tropospheric flow and upper tropospheric are nearly vertically coincident over northern China on previous days (not shown), at Day –5, the lower tropospheric northeasterly anomalies have advanced to southern China (Fig. B.5(a)), while the upper tropospheric anomalies remain poleward of 40°N (Fig. B.7(a)). At Day –2, the strong, statistically significant northeasterly anomalies over the South China Sea seen in Fig. B.5(b) have no corresponding 200 hPa circulation anomalies in Fig. B.7(b). A statistically significant 200 hPa anomaly over the South China Sea is not evident until Day 0 (Fig. B.7(c)).

Figure B.8 compares regressed values of the 1000 hPa and 200 hPa divergence anomalies with the OLR anomaly at one of the grid points of strong convective activity (10°N, 110°E). Figure B.8 shows that the variations in the local East Asian Hadley cell are strongly correlated to the surface surge–induced variations in the divergent flow, with the surface changes leading the increase in the 200 hPa divergence

of the Hadley circulation by 2 days. The OLR anomaly follows the 1000 hPa increase in convergence by one day, and the 200 hPa divergence anomaly follows the OLR anomaly by one day. As the low-level surge progresses southward from Day –9 to Day –5 (Fig. B.5), no significant 200 hPa signal is present over the South China Sea or Southeast Asia. Together, Figs. B.8 and B.7 indicate that the Hadley cell is near normal preceding the surge and that the upper-level local Hadley cell intensifies following a pressure surge. A region of positive OLR anomalies along northern China at 35°N marks the descending branch of the local Hadley cell (Fig. B.7(c)). The timing of the upper-level intensification of the divergent circulation appears most closely linked to the divergence following the enhanced convection. A consistent 2–day time delay between low-level convergence, convective activity, and upper-level divergence is seen with all base points employed (not shown).

B.4.3 Propagation Characteristics To quantify the southward propagation and magnitude of the South China Sea surge associated perturbations, regressions of SLP and 850 hPa air temperature and meridional wind are calculated as a function of lag and latitude along 110°E using the South China Sea base (15°N, 115°E) point time series of SLP (Fig. B.9). A positive pressure anomaly propagates southward at 8.9 degrees per day or 11.3 m s^{-1}, as indicated by the reference phase line, from the midlatitudes to approximately 15°N. The propagation speed changes south of 15°N to a nearly 40 m s^{-1} southward increase of pressure from 15N to south equator. The two propagation speeds over East Asia are independent of the base point used.

The propagation of the temperature anomaly in Fig. B.9(a) follows the pressure anomaly from 55°N to 10°N along 110°E. North of 55°N, the temperature

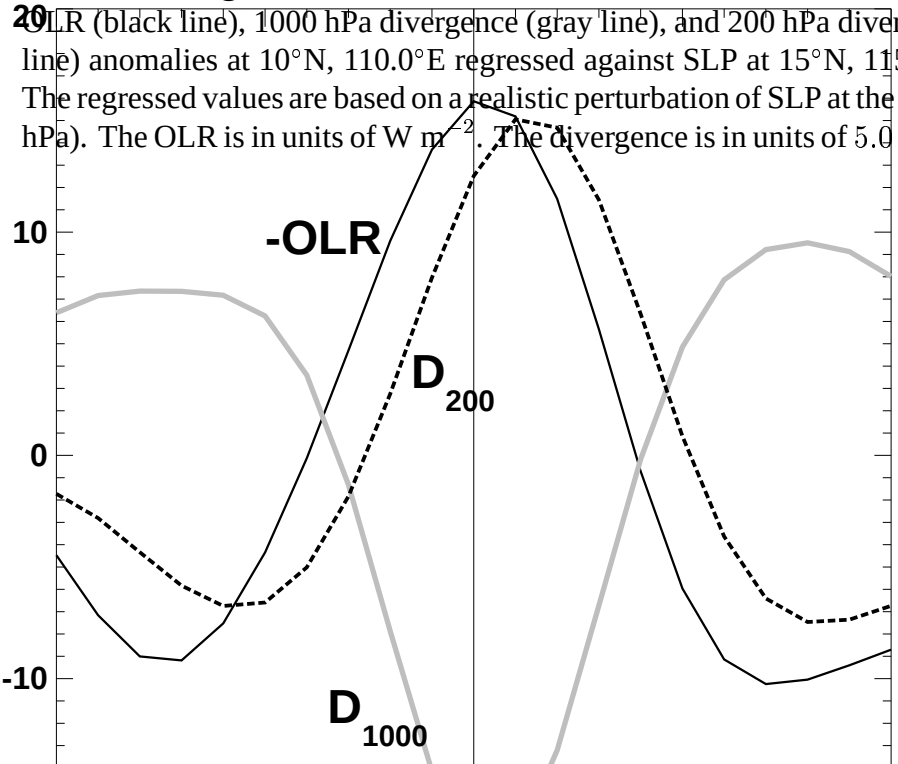

Figure B.8: Lagged covariability regressed values of 6-30 day bandpass filtered OLR (black line), 1000 hPa divergence (gray line), and 200 hPa divergence (dashed line) anomalies at 10°N, 110.0°E regressed against SLP at 15°N, 115°E (Fig. B.5). The regressed values are based on a realistic perturbation of SLP at the base point (3.0 hPa). The OLR is in units of W m^{-2}. The divergence is in units of 5.0×10^{-6} m^2 s^{-2}.

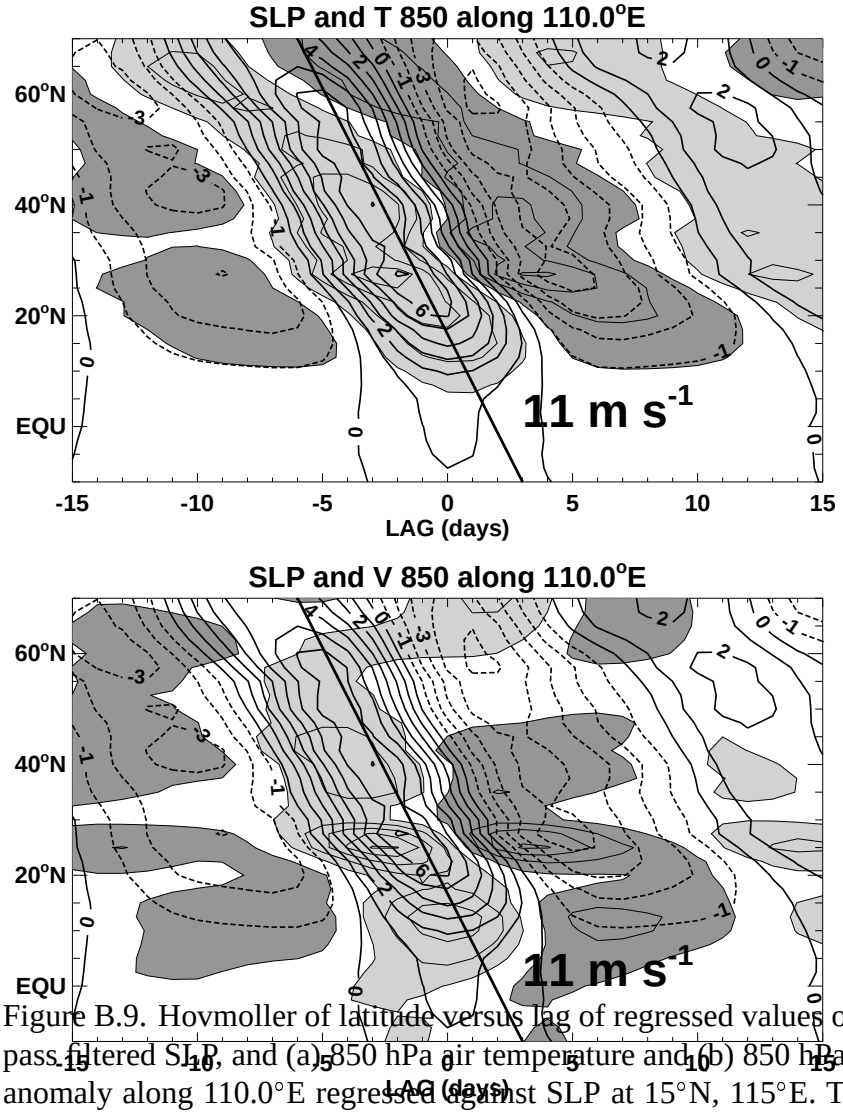

Figure B.9. Hovmoller of latitude versus lag of regressed values of 6–30 day bandpass filtered SLP, and (a) 850 hPa air temperature and (b) 850 hPa meridional wind anomaly along 110.0°E regressed against SLP at 15°N, 115°E. The regressed values are based on a realistic perturbation of SLP at the base point (3.0 hPa). The SLP contour interval (solid lines, positive; dashed lines, negative) is 0.5 hPa. The (a) air temperature and (b)wind contour (filled: dark gray, positive; light gray, negative) is 0.5 (a) C (b) m s^{-1}, with the zero contour suppressed.

anomaly is in quadrature with the pressure anomaly, consistent with eastward propagating baroclinic disturbances. South of 55°N however, the temperature and pressure anomalies are nearly in phase until they reach 15°N, where the rapid southward progression of pressure occurs. The 850 hPa air temperature anomaly of 0.5°C penetrates to 7.5°N. The erosion of the near-surface negative temperature anomaly signal as the air passes over the South China Sea is discussed in the next section.

Chang *et al.* (1983) and Leathers (1986) discussed in detail two events associated with surges. The first event, a fast moving (40 m s^{-1}) positive pressure pulse was associated with a gravity wave motion. The second event was a slower moving positive pressure increase and temperature drop that followed the initial pressure pulse. Chang et al. suggested advection as the mechanism for the southward propagation of the second event in the pressure surge. A clear double maxima is not observed in Fig. B.9. However, a fast moving pressure pulse appears here as the nearly 40 m s^{-1} increase in pressure from 15°N to across the equator, while the second pressure increase appears to be the coincident SLP, temperature, and meridional wind southward propagation seen in Fig. B.9. The propagation speed estimated in Fig. B.9 is consistent with the 13 m s^{-1} estimation in Fig. B.2 and an 11 m s^{-1} estimation of Chang *et al.* (1983), based on irregularly spaced station data from 25N to 5N from the winter of 1978–79. All of these estimations are consistent with a 15 m s^{-1} estimation of Leathers using the same time period as Chang et. al. with points further north (35°N to 29°N). As both the East Asian background and surge-associated lower tropospheric winds are northerly, a non-linear advective mechanism might seem plausible for the southward propagating pressure surges and associated temperature and wind anomalies.

To examine the advection hypothesis, the meridional wind anomaly is

shown in Fig. B.9(b) along the same meridian as considered in Fig. B.9(a). The SLP anomaly is reproduced to simplify comparison. The maxima in meridional wind speed are not in quadrature with the temperature or pressure extrema, as would be necessary if non-linear advection were the primary mechanism. In addition, the maximum meridional wind speed varies along the surge path and is inconsistent with the observed steady southward propagation. The temperature and pressure perturbations associated with negative pressure anomalies are accompanied by southerly wind anomalies. Under the advection mechanism, negative pressure and positive temperature anomalies should show northward movement, instead there appears to be southward phase propagation. Southward phase propagation of negative pressure anomalies is observed in both the pressure anomalies of the case period in Fig. B.2 and the regression of Fig. B.9. Further, the negative pressure anomalies also move southward at the same speed as the surges. The observed propagation speed is faster than both the background meridional velocity and the anomalous meridional velocity, also inconsistent with non-linear advection as a mechanism for the movement of pressure surges.

In contrast to the advection hypothesis, Hsu (1987) and Tilley (1990) suggested the southward propagation of surges as a topographic Rossby wave, also termed a ”shelf wave” (Pedlosky 1987), the atmospheric equivalent to the oceanic ”continental shelf wave” (Mysak 1980). Leathers (1986) suggested that advection explained the southward movement of the negative temperature anomalies but hypothesized that the shelf wave mechanism explained the dynamics of the pressure perturbations. Through this mechanism, the slope of the orography from the East Asian coast to the Himalayas provides an augmented gradient of potential vorticity which acts as a restoring force for perturbations induced either up or down the slope.

As in the general atmospheric Rossby wave case, shelf waves are unidirectional, in the northern hemisphere, they propagate with the greater orographic heights to their right. The scale of the wave is the same as that of the slope.

The evidence presented here supports the hypothesis that pressure surge propagation over continental East Asia may be related to the dynamics of shelf waves. The consistent southward propagation, with the increasing orographic height to the right, observed in Figs. B.2 and B.9 , and the coincident relationship between SLP and meridional wind anomalies support the hypothesis, based on the theoretical discussions by Pedlosky and Mysak. As discussed by Pedlosky, the theoretical spatial scale of the shelf wave in the direction normal to the orography is the scale of the slope. The horizontal scale of the pressure anomaly seen in Fig. B.5 appears to be consistent with the hypothesis that the slope from the Himalayas to the East Asian coast is the appropriate spatial scale for the pressure and wind anomalies over East Asia during a pressure surge. In addition, the vertical structure, considered below, lends further support to the shelf wave hypothesis.

B.4.4 Vertical Structure Latitude-height cross-sections of meridional wind and air temperature along 110°E regressed against the SLP base point of 15°N, 115°E are shown in Fig. B.10. The negative meridional wind anomalies (Fig. B.10(a)) associated with the surge occur between 22.5°N and the equator and extend up to 700 hPa. The positive meridional wind anomalies also proceeding southward have similar dimensions, though only those anomalies between 35°N and 45°N exceed a statistically significant correlation of 0.2. Above 500 hPa, the significant subtropical southerlies occur between 27.5°N and 5°N at 200 and 300 hPa. In subsequent days, the lower tropospheric northerlies decrease in intensity, while the upper level southerlies appear to increase in response to the convective anomalies,

as shown in Fig. B.7.

While the regressed meridional circulation anomalies have distinct lower tropospheric and upper tropospheric signals over the whole of East Asia, the temperature anomalies (Fig. B.10(b)) appear coherent from the surface to above 500 hPa in the midlatitudes but are shallower towards the equator. The positive temperature anomaly associated with negative pressure anomalies (compare with Fig. B.9(a)) extends to 500 hPa. North of 30°N, the mid-tropospheric negative temperature anomaly lags behind the anomaly near the surface, providing further evidence of a separation between the near-surface surge and the upper level wave activity. South of 30°N, the negative temperature anomaly at 850 hPa is co-located with the meridional wind anomalies and has approximately the same vertical extent, but at 1000 hPa, negative anomalies less than –0.5°C terminate at 10°N. Cross–sections taken over the center of the South China Sea (11°5E, not shown) indicate that the 0.5°C temperature perturbation has maximum southward extent of only 15°N at 1000 hPa and at 10°N at 850 hPa. The low level warming of the surge over the open water is probably due to air-sea interaction modifying the near surface cold air anomaly. Thus, as originally observed in two cases by Chang *et al.* (1979), the temperature signal associated with a pressure surge has deep tropical penetration only near and over the land region of the Indochina Peninsula. Over the South China Sea, the cold air is quickly modified, and the near surface signal is lost.

Comparing Fig. B.10(a) and B.10(b), the vertical change in the phase relationship between the temperature and meridional wind anomalies south of 45N is consistent with the hypothesis that different dynamical mechanisms may govern the southward propagation of the anomalies. The vertical structure of the meridional wind anomalies seen in Fig. B.10(a) appears similar to the predicted effect of stable

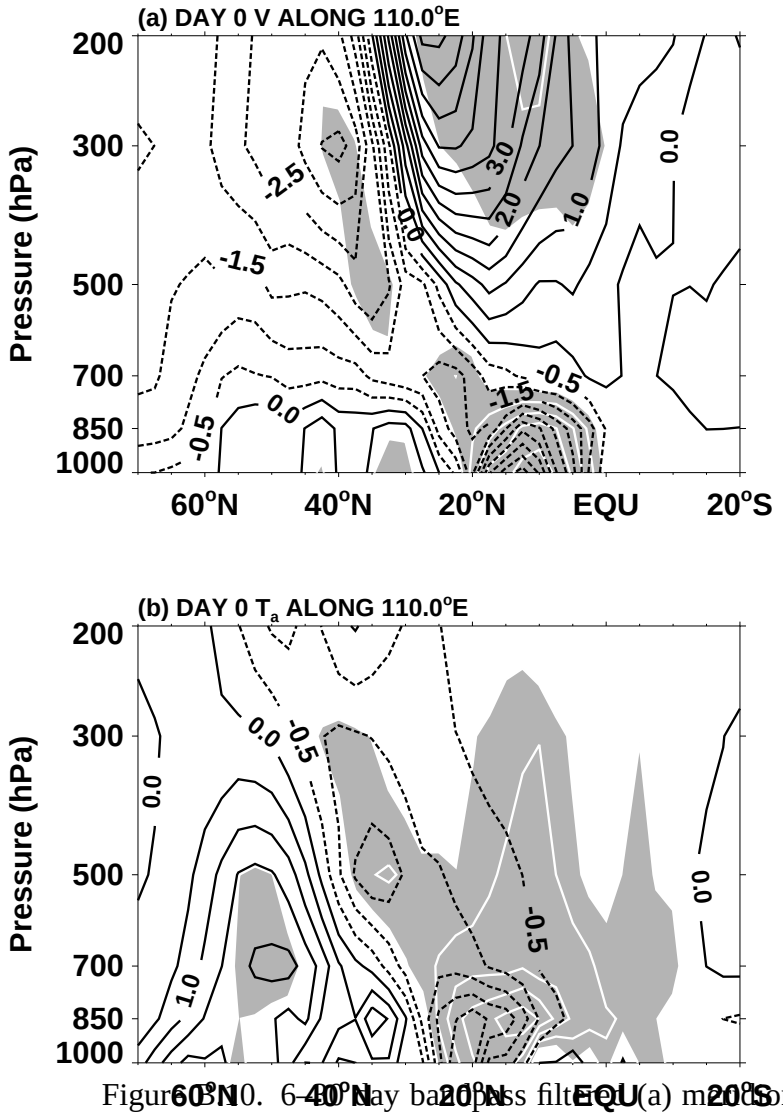

Figure B.10. 6–40 day bandpass filtered (a) meridional wind and (b) air temperature as a function of latitude and height along 110°E linearly regressed about SLP at 15°N, 115°E for Day 0 corresponding to Fig. B.5. The line contour represents the regressed value for a realistic perturbation of SLP at the base point (3.0 hPa). The line contour interval is 0.5 (a) m s^{-1} (b) 0.5°C. The shading represents the magnitude of the correlation coefficient with interval 0.1 and a minimum contour of 0.2.

stratification on barotropic shelf wave structure as modeled numerically by Wang and Mooers (1976) and Huthnance (1978). Both studies demonstrated that intermediate stratification combined with a sloped bottom surface induced bottom trapping of the velocity anomalies. In Fig. B.10(a), the vertical extent of the meridional wind anomalies in the lower troposphere is confined to near the surface. While not considered in either modeling study, the limited vertical extent of the lower tropospheric temperature anomaly (Fig. B.10(b)) does appear consistent with the hypothesis of bottom trapping.

B.5 Discussion

The results found above corroborate some earlier findings on pressure surges, however, significant differences were found as well. We now attempt to develop a more consistent morphology of surges by answering the questions posed at the beginning of the paper.

(1) What are the timescales associated with surge activity?

East Asian pressure surges are the dominant mode of submonthly variability in the East Asian winter monsoon system. As shown in section B.3, the circulation variability associated with pressure surges occurs on synoptic (2 to 6 day) and submonthly (6 to 30 day) timescales. The spectral results of Figs. B.3 and B.4 demonstrate a localization of statistically significant power in timescales between synoptic (2 to 6 days), submonthly (6 to 30 days) and the MJO (30 to 70 days). The spectra demonstrate that peaks in submonthly power significant at the 95% level are localized to an area from the Bay of Bengal to the Philippine Sea from 30N to the equator. The regression results (Fig. B.5) show that submonthly spectral power is maximum in the regions found as

the dominant path for South China Sea surges. The submonthly peaks also extended into the region of the Philippine Sea, but power decreases east of 140°E. In both the synoptic and submonthly bands, Murakami (1979) found similar spectral peaks with a single winter record over the South China, Philippine, and East China Seas. The hovmöllerdiagrams in Fig. B.9 indicate a roughly 15–day periodicity for South China Sea surges, but the asymmetry in the duration of positive and negative pressure, temperature, and wind anomalies suggests that a given case of a pressure surge will not adhere precisely to this period. Thus, a single discrete time scale cannot be assigned to surges. Rather, pressure surges are a relatively broadband phenomena in the submonthly range.

(2) What are the basic relationships between surge-associated variables, independent of an arbitrary definition?

With the current results, we can now describe the variability between circulation and temperature that shows a statistically significant relationship with East Asian pressure fluctuations. The pressure patterns observed in Figs. B.5 and B.6 represent the dominant evolution of pressure anomalies during the northern hemisphere cool season. Previous studies using rotated empirical orthogonal function analysis on SLP found similar patterns to those seen here in the time evolution of pressure perturbations (Hsu and Wallace 1985). Based on the propagation characteristics seen in Figs. B.2 and B.9 , the South China Sea surge signal shows three different regional characteristics as it moves equatorward. North of 45°N, the pressure and temperature signal are in quadrature, as would be expected from eastward moving baroclinic waves. Over mainland China, the low-level surge signal in pressure, temperature, and wind are almost

in phase and appear to propagate much faster than the mean or anomaly advective speed would explain. In some cases, (Fig. B.2), we estimate two propagation speeds that are reasonably described by either 13 m s^{-1} or 22 m s^{-1}, with larger anomalies in pressure being associated with the slower propagation speed. Based on the regression results, the submonthly timescale surge signal propagates at a speed on the order of 11 m s^{-1} (Fig. B.9). The vertical structure of the surge suggests bottom trapping of the low-level surge anomalies (Fig. B.10), consistent with the modeling work of Wang and Mooers (1976) and Huthnance (1978). The regression results further support for the hypothesis that surges propagate with a shelf wave-like mechanism, whereby the augmentation of the potential vorticity gradient by the sloped surface from the East Asian coast to the Himalayan Plateau acts as the restoring force for a southward propagating disturbance. A full comparison of the results of the present study with shelf wave theory is currently being undertaken.

At the south China coast, the low-level surge propagation speed becomes much larger and pressure, temperature, and wind fluctuations are nearly in phase (Fig. B.9). An initial pressure increase rapidly spreads over the whole of the South China Sea (Fig. B.9) with meridional wind anomalies spreading southward at nearly the same rate. The temperature anomalies appear to retain their speed of propagation, and a second, slower propagating increase of pressure is seen by examining the 1.0 hPa anomaly line. Ramage (1971) observed the rapid spreading of the northerly winds associated with surge from 25°N to the equator occurring at speeds much faster than the advective speed. Williams (1981), Chang *et al.* (1983), and Webster (1987), showed cases of the initial pressure rise associated with surges propagating southward at 40 m s^{-1} from

25°N to the equator. Using a linear shallow water model on a beta-plane, Lim and Chang (1981) and Zhang and Webster (1992) viewed surge effects over the South China Sea as the transient response of an adjustment to a pressure wind imbalance. Chang *et al.* (1983) attributed the rapid southward propagation over the South China Sea to gravity wave motions based on the speed and isallobaric angle of wind vectors. In Fig. B.9, we also estimate the speed of surge propagation after leaving the southern Chinese coast to be 40 m s^{-1}. The slower propagating SLP, temperature, and wind anomaly anomaly is estimated to propagate southward at 11 m s^{-1}.

The 1000 hPa air temperature perturbation associated with the submonthly pressure surges does not penetrate as far south over the South China Sea as the 850 hPa perturbation (Fig. B.10(b)). This statistically significant modification of the surge temperature anomaly at 1000 hPa corroborates the previous study of Chang *et al.* (1979) that showed, using two case studies, a decrease in temperature associated with pressure surges was not detectable with station data from islands in the South China Sea. They hypothesized that air-sea interactions quickly modify the temperature of the air mass, leaving only the pressure and wind perturbations.

In Fig. B.7, the jet anomalies over the Pacific shows an out-of-phase relationship with the jet anomalies directly over East Asia. The structure of the East Asian jet anomalies appears closely tied to the subtropical and midlatitude upper-level eastward moving waves that merge off the East Asian coast. These results corroborate the previous studies of the surge relationship to Asian jet anomalies that used shorter records (Chang and Lau 1980; Chang and Lau 1982).

The local East Asian Hadley cell is weak before surges commence (Figs. B.5(a), B.7(a), B.8). Strong subsidence, as indicated by the 200 hPa circulation of Fig. B.7(c) and positive OLR anomalies in the midlatitudes, occur following the surge-induced initiation of convection in the southeast Asian region. This result is in contrast to the findings of Chang and Lau (1980), who showed that subsidence in the midlatitudes, associated with the downward branch of the local Hadley cell, increased prior to the surge. Instead, the changes in the 200 hPa circulation divergence field seen in Fig. B.8, in conjunction with the presence of a large-scale positive OLR anomaly in the midlatitudes of Fig. B.7(c), suggest that the upper-level perturbations to the Hadley cell follow the surge-induced convective anomalies.

(3) Is the tropical response to pressure surges a robust signal?

On the submonthly timescale, pressure surges occur over the South China Sea and the Philippine Sea. (Figs. B.5 and B.6). Figs. B.5 and B.9 provide statistical support for previous work demonstrating that South China Sea pressure surges are associated with southward propagating positive pressure anomalies with concurrent negative temperature perturbations and northerly wind anomalies. The submonthly timescale pressure surges are identified as those surges that have deep tropical and cross-hemispheric effects in convective and tropospheric circulation anomalies. The surge relationship to tropical and circulation convection over the Philippine Sea, South China Sea, Indochina, and eastern Indian Ocean is a statistically robust signal found to be statistically significant using base points over East Asia from 55°N southward. In contrast, the southern hemisphere signal of enhanced convective activity and westerlies is only observed with base points over the South China Sea south of 20°N.

Fig. B.5 shows that from the Indochina Peninsula to the Philippines, and in the Indonesian monsoon regions, convective activity increases following the enhancement of the climatological northeasterly monsoon flow associated with a South China Sea pressure surge. This result compares favorably with the previous results of Houze *et al.* (1981), Johnson and Priegnitz (1981), and Chang and Chen (1992). Our results also corroborate the OLR-based statistical work of Kiladis *et al.* (1994), and Meehl *et al.* (1996), but the area of statistically significant increased convective activity associated with South China Sea surges seen in Figs. B.5 and B.6 covers a much larger area than that found in those studies.

The submonthly Philippine Sea surge relationships to western Pacific circulation and convection seen in Fig. B.6, in particular to the equatorial westerly wind anomalies, have several features in common with the equatorial Rossby wave structure identified by Kiladis and Wheeler (1995). Upper level wave activity associated with surges is seen in Fig. B.7. The correlation of upper level wave activity showing propagation into the westerly duct region demonstrates that low-level pressure surges are an indicator of large-scale submonthly variability throughout the troposphere, confirming that the similar findings of Lau and Lau (1984) and Joung and Hitchman (1982) on the synoptic timescale are present in the much larger submonthly timescale. In contrast to the case studies of Chu (1988) and Chu and Frederick (1990), no fast southward propagating Philippine Sea surge signal preceding westerly anomalies in the western Pacific is observed on either the synoptic or submonthly timescales. The statistically significant linear association between Philippine Sea surges and western Pacific westerly wind anomalies appears to lie in the coincident timing and

interaction of Philippine Sea surges with westward propagating equatorial disturbances. These westward propagating equatorial disturbances appear similar to the equatorial Rossby waves found by Kiladis and Wheeler (1995). Further study is underway to determine the exact nature of the coincident association between these features and the East Asian pressure surges over the South China Sea and Philippine Sea.

APPENDIX C

WAVELET ANALYSIS

A practical step-by-step guide to wavelet analysis is given,[1] with examples taken from time series of the El Niño-Southern Oscillation (ENSO). The guide includes a comparison to the windowed Fourier transform, the choice of an appropriate wavelet basis function, edge effects due to finite-length time series, and the relationship between wavelet scale and Fourier frequency. New statistical significance tests for wavelet power spectra are developed by deriving theoretical wavelet spectra for white and red noise processes and using these to establish significance levels and confidence intervals. It is shown that smoothing in time or scale can be used to increase the confidence of the wavelet spectrum. Empirical formulae are given for the effect of smoothing on significance levels and confidence intervals. Extensions to wavelet analysis such as filtering, the power hovmöller, cross-wavelet spectra, and coherence are described.

The statistical significance tests are used to give a quantitative measure of changes in ENSO variance on interdecadal time scales. Using new datasets that extend back to 1871, the NINO3 sea surface temperature and the Southern Oscillation Index show significantly higher power during 1880-1920 and 1960-1990, and lower power during 1920-1960, as well as a possible 15-year modulation of variance. The power hovmöller of sea level pressure shows significant variations in 2–8

[1] Adapted from Torrence and Compo (1997), available at URL: "http://paos.colorado.edu/research/wavelets/".

year wavelet power in both longitude and time.

C.1 Introduction

Wavelet analysis is becoming a common tool for analyzing localized variations of power within a time series. By decomposing a time series into time-frequency space, one is able to determine both the dominant modes of variability and how those modes vary in time. The wavelet transform has been used for numerous studies in geophysics, including tropical convection (Weng and Lau 1994), the El Niño-Southern Oscillation (Gu and Philander 1995; Wang and Wang 1996), atmospheric cold fronts (Gamage and Blumen 1993), central England temperature (Baliunas *et al.* 1997), the dispersion of ocean waves (Meyers *et al.* 1993), wave growth and breaking (Liu 1994), and coherent structures in turbulent flows (Farge 1992). A complete description of geophysical applications can be found in Foufoula-Georgiou and Kumar (1995), while a theoretical treatment of wavelet analysis is given in Daubechies (1992).

Unfortunately, many studies using wavelet analysis have suffered from an apparent lack of quantitative results. The wavelet transform has been regarded by many as an interesting diversion that produces colorful pictures yet purely qualitative results. This misconception is in some sense the fault of wavelet analysis itself, as it involves a transform from a one-dimensional time series (or frequency spectrum) to a diffuse two-dimensional time-frequency image. This diffuseness has been exacerbated by the use of arbitrary normalizations and the lack of statistical significance tests.

In a previous article in the **Bulletin**, Lau and Weng (1995) provided an excellent introduction to wavelet analysis. However, their paper did not provide all

of the essential details necessary for wavelet analysis, and avoided the issue of statistical significance.

The purpose of this paper is to provide an easy-to-use wavelet analysis toolkit, including statistical significance testing. The consistent use of examples of the El Niño-Southern Oscillation (ENSO) provides a substantive addition to the ENSO literature. In particular, the statistical significance testing allows greater confidence in the previous wavelet-based ENSO results of Wang and Wang (1996). The use of new datasets with longer time series permits a more robust classification of interdecadal changes in ENSO variance.

The first section describes the datasets used for the examples. Section C.3 describes the method of wavelet analysis using discrete notation. This includes a discussion of the inherent limitations of the windowed Fourier transform (WFT), the definition of the wavelet transform, the choice of a wavelet basis function, edge effects due to finite-length time series, the relationship between wavelet scale and Fourier period, and time-series reconstruction. Section C.4 presents the theoretical wavelet spectra for both white-noise and red-noise processes. These theoretical spectra are compared to Monte Carlo results and are used to establish significance levels and confidence intervals for the wavelet power spectrum. Section C.5 describes time or scale averaging to increase significance levels and confidence intervals. Section C.6 describes other wavelet applications such as filtering, the power hovmöller, cross-wavelet spectra, and wavelet coherence. The summary contains a step-by-step guide to wavelet analysis.

C.2 Data

Several time series will be used for examples of wavelet analysis. These include the NINO3 sea surface temperature (SST), used as a measure of the amplitude of the El Niño-Southern Oscillation (ENSO). The NINO3 SST index is defined as the seasonal SST averaged over the central Pacific (5°S–5°N, 90°W–150°W). Data for 1871–1996 are from an area-average of the UK Meteorological Office GISST2.3 (Rayner *et al.* 1996), while data for January–June 1997 are from the Climate Prediction Center (CPC) optimally-interpolated NINO3 SST index (courtesy D. Garrett at CPC, NOAA, USA). The seasonal means for the entire record have been removed to define an anomaly time series. The NINO3 SST is shown in the top plot of Fig. C.1a.

Gridded sea level pressure (SLP) data is from the UKMO/CSIRO historical GMSLP2.1f (courtesy D. Parker and T. Basnett, Hadley Centre for Climate Prediction and Research, UKMO, UK). The data is on a 5 degree global grid, with monthly resolution from January 1871 to December 1994. Anomaly time series have been constructed by removing the first three harmonics of the annual cycle (periods of 365.25, 182.625, and 121.75 days) using a least-squares fit.

The Southern Oscillation Index is derived from the GMSLP2.1f, and is defined as the seasonally-averaged pressure difference between the eastern Pacific (20°S, 150°W) and the western Pacific (10°S, 130°E).

C.3 Wavelet Analysis

This section describes the method of wavelet analysis, includes a discussion of different wavelet functions, and gives details for the analysis of the wavelet power spectrum. Results in this section are adapted to discrete notation from the continuous formulae given in Daubechies (1990). Practical details in applying wavelet analysis are taken from Farge (1992), Weng and Lau (1994), and Meyers *et al.*

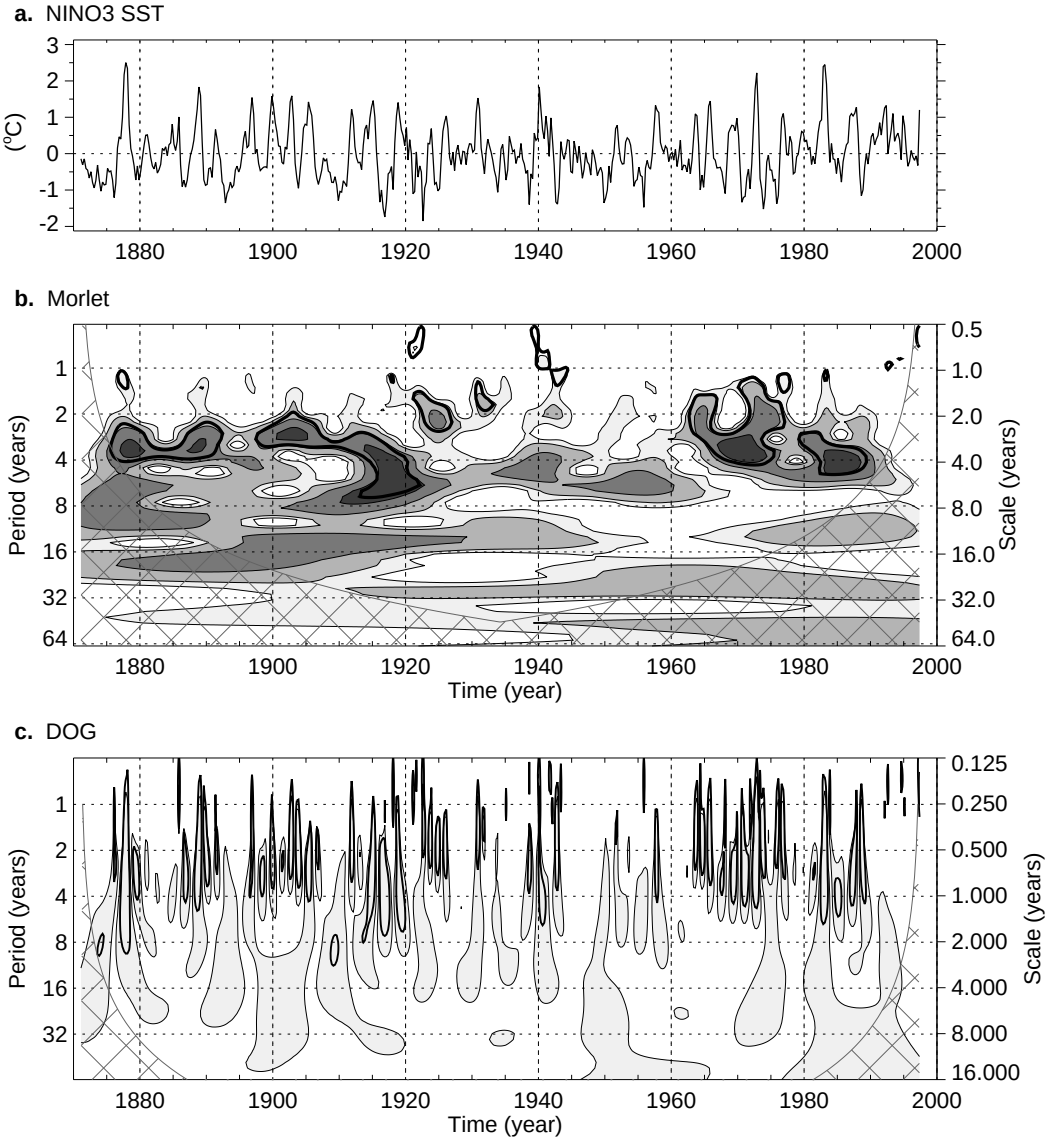

Figure C.1. (a) the NINO3 SST time series used for the wavelet analysis. (b) the local wavelet power spectrum of (a) using the Morlet wavelet, normalized by $1/\sigma^2$ ($\sigma^2 = 0.54°\mathrm{C}^2$). The left axis is the Fourier period (in years) corresponding to the wavelet scale on the right axis. The bottom axis is time (year). The shaded contours are at normalized variance of 1, 2, 5, and 10. The thick contour encloses regions of greater than 95% confidence for a red-noise process with a lag-1 coefficient of 0.72. Cross-hatched regions on either end indicate the "cone of influence," where edge effects become important. (c) Same as (b) but using the real-valued Mexican hat wavelet (DOG $m = 2$). The shaded contour is at normalized variance of 2.0.

(1993). Each section is illustrated with examples using the NINO3 SST.

C.3.1 Windowed Fourier Transform The Windowed Fourier Transform (WFT) represents one analysis tool for extracting local-frequency information from a signal. The Fourier transform is performed on a sliding segment of length T from a time series of time step δt and total length $N\delta t$, thus returning frequencies from T^{-1} to $(2\delta t)^{-1}$ at each time step. The segments can be windowed with an arbitrary function such as a boxcar (no smoothing) or a Gaussian window (Kaiser 1994).

As discussed by Kaiser (1994), the WFT represents an inaccurate and inefficient method of time-frequency localization, as it imposes a scale or "response interval" T into the analysis. The inaccuracy arises from the aliasing of high and low frequency components which do not fall within the frequency range of the window. The inefficiency comes from the $T/(2\delta t)$ frequencies which must be analyzed at each time step, regardless of the window size or the dominant frequencies present. In addition, several window lengths must usually be analyzed to determine the most appropriate choice. For analyses where a predetermined scaling may not be appropriate because of a wide range of dominant frequencies, a method of time-frequency localization that is scale independent, such as wavelet analysis, should be employed.

C.3.2 Wavelet Transform The **wavelet transform** can be used to analyze time series that contain non-stationary power at many different frequencies (Daubechies 1990). Assume that one has a time series, x_n, with equal time spacing δt and $n = 0 \ldots N-1$. Also assume that one has a **wavelet function**, $\psi_0(\eta)$, that depends on a non-dimensional "time" parameter η. To be "admissible" as a wavelet, this function must have zero mean and be localized in both time and frequency space

(Farge 1992). An example is the Morlet wavelet, consisting of a plane wave modulated by a Gaussian:

$$\psi_0(\eta) = \pi^{-1/4} e^{i\omega_0\eta} e^{-\eta^2/2}, \tag{C.1}$$

where ω_0 is the non-dimensional frequency, here taken to be 6 to satisfy the admissibility condition (Farge 1992). This wavelet is shown in Fig. C.2a.

The term "wavelet function" is used generically to refer to either orthogonal or non-orthogonal wavelets. The term "wavelet basis" refers only to an orthogonal set of functions. The use of an orthogonal basis implies the use of the **discrete wavelet transform**, while a non-orthogonal wavelet function can be used with either the discrete or the **continuous wavelet transform** (Farge 1992). In this paper only the continuous transform is used, although all of the results for significance testing, smoothing in time and scale, and cross wavelets are applicable to the discrete wavelet transform.

The continuous wavelet transform of a discrete sequence x_n is defined as the convolution of x_n with a scaled and translated version of $\psi_0(\eta)$:

$$W_n(s) = \sum_{n'=0}^{N-1} x_{n'} \psi^* \left[\frac{(n'-n)\delta t}{s} \right], \tag{C.2}$$

where the (*) indicates the complex conjugate. By varying the **wavelet scale** s and translating along the **localized time index** n, one can construct a picture showing both the amplitude of any features versus the scale and how this amplitude varies with time. The subscript 0 on ψ has been dropped to indicate that this ψ has also been normalized (see next section). Although it is possible to calculate the wavelet transform using (C.2), it is considerably faster to do the calculations in Fourier space.

To approximate the continuous wavelet transform, the convolution (C.2) should be done N times for each scale, where N is the number of points in the time series (Kaiser 1994). (The choice of doing all N convolutions is arbitrary, and one

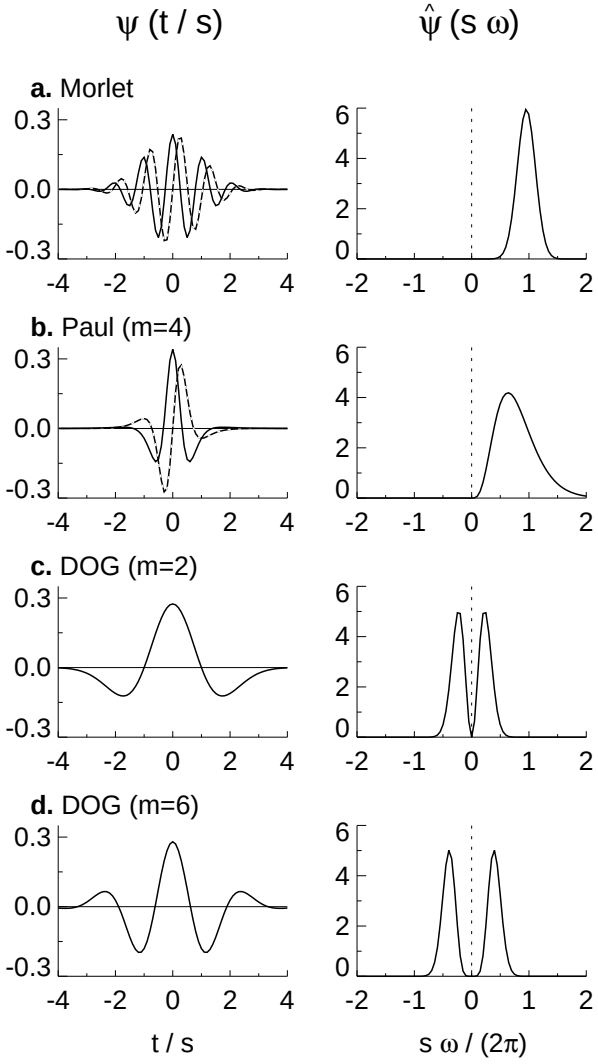

Figure C.2. Four different wavelet bases, from Table C.1. The plots on the left give the real part (solid) and imaginary part (dashed) for the wavelets in the time domain. The plots on the right give the corresponding wavelets in the frequency domain. For plotting purposes, the scale was chosen to be $s = 10\delta t$. (a) Morlet, (b) Paul ($m = 4$), (c) Mexican Hat (DOG $m = 2$), (d) DOG ($m = 6$).

could choose a smaller number, say by skipping every other point in n). By choosing N points, the convolution theorem allows us do all N convolutions simultaneously in Fourier space using a discrete Fourier Transform (DFT). The DFT of x_n is:

$$\widehat{x}_k = \frac{1}{N}\sum_{n=0}^{N-1} x_n e^{-2\pi i k n/N}, \tag{C.3}$$

where $k = 0 \ldots N-1$ is the frequency index. In the continuous limit the Fourier transform of a function $\psi(t/s)$ is given by $\widehat{\psi}(s\omega)$. By the convolution theorem, the wavelet transform is the inverse Fourier transform of the product:

$$W_n(s) = \sum_{k=0}^{N-1} \widehat{x}_k \widehat{\psi}^*(s\omega_k) e^{i\omega_k n\delta t}, \tag{C.4}$$

where the angular frequency is defined as:

$$\omega_k = \begin{cases} \frac{2\pi k}{N\delta t} & : \quad k \leq \frac{N}{2} \\ -\frac{2\pi k}{N\delta t} & : \quad k > \frac{N}{2} \end{cases} . \tag{C.5}$$

Using (C.4) and a standard Fourier transform routine, one can calculate the continuous wavelet transform (for a given s) at all n simultaneously and efficiently.

C.3.3 Normalization To ensure that the wavelet transforms (C.4) at each scale s are directly comparable to each other and to the transforms of other time series, the wavelet function at each scale s is normalized to have unit energy:

$$\widehat{\psi}(s\omega_k) = \left(\frac{2\pi s}{\delta t}\right)^{1/2} \widehat{\psi}_0(s\omega_k). \tag{C.6}$$

Examples of different wavelet functions are given in Table C.1 and illustrated in Fig. C.2. Each of the unscaled $\widehat{\psi}_0$ are defined in Table C.1 to have $\int_{-\infty}^{+\infty} |\widehat{\psi}_0(\omega')|^2 \, d\omega' = 1$, i.e. they have been normalized to have unit energy.

Using these normalizations, at each scale s one has:

$$\sum_{k=0}^{N-1} |\widehat{\psi}(s\omega_k)|^2 = N, \tag{C.7}$$

Table C.1. Three wavelet basis functions and their properties. Constant factors for ψ_0 and $\widehat{\psi}_0$ ensure a total energy of unity.

Name	$\psi_0(\eta)$	$\widehat{\psi}_0(s\omega)$	e-folding time τ_s	Fourier Wavelength λ
Morlet ($\omega_0 =$ frequency)	$\pi^{-1/4} e^{i\omega_0\eta} e^{-\eta^2/2}$	$\pi^{-1/4} H(\omega) e^{-(s\omega-\omega_0)^2/2}$	$\sqrt{2}\, s$	$\frac{4\pi s}{\omega_0+\sqrt{2+\omega_0^2}}$
Paul ($m =$order)	$\frac{2^m i^m m!}{\sqrt{\pi(2m)!}}(1-i\eta)^{-(m+1)}$	$\frac{2^m}{\sqrt{m(2m-1)!}} H(\omega)(s\omega)^m e^{-s\omega}$	$s/\sqrt{2}$	$\frac{4\pi s}{2m+1}$
DOG ($m =$derivative)	$\frac{(-1)^{m+1}}{\sqrt{\Gamma(m+\frac{1}{2})}} \frac{d^m}{d\eta^m}(e^{-\eta^2/2})$	$\frac{i^m}{\sqrt{\Gamma(m+\frac{1}{2})}}(s\omega)^m e^{-(s\omega)^2/2}$	$\sqrt{2}\, s$	$\frac{2\pi s}{\sqrt{m+\frac{1}{2}}}$

$H(\omega) =$ Heaviside step function, $H(\omega) = 1$ if $\omega > 0$, $H(\omega) = 0$ otherwise.
DOG = derivative of a Gaussian. $m = 2$ is the Marr or Mexican hat wavelet.

where N is the number of points. Thus, the wavelet transform is weighted only by the amplitude of the Fourier coefficients $\widehat{x}_k$ and not by the wavelet function. If one is using the convolution formula (C.2), the normalization is:

$$\psi\left[\frac{(n'-n)\delta t}{s}\right] = \left(\frac{\delta t}{s}\right)^{1/2} \psi_0\left[\frac{(n'-n)\delta t}{s}\right] \tag{C.8}$$

where $\psi_0(\eta)$ is normalized to have unit energy.

C.3.4 Wavelet Power Spectrum Because the wavelet function $\psi(\eta)$ is in general complex, the wavelet transform $W_n(s)$ is also complex. The transform can then be divided into the real part, $\Re\{W_n(s)\}$, and imaginary part, $\Im\{W_n(s)\}$, or amplitude, $|W_n(s)|$, and phase, $\tan^{-1}(\Im\{W_n(s)\}/\Re\{W_n(s)\})$. Finally, one can define the **wavelet power spectrum** as $|W_n(s)|^2$. For real-valued wavelet functions such as the DOG (derivatives of a Gaussian) the imaginary part is zero and the phase is undefined.

To make it easier to compare different wavelet power spectra, it is desirable to find a common normalization for the wavelet spectrum. Using the normalization in (C.6), and referring to (C.4), the **expectation value** for $|W_n(s)|^2$ is equal to N times the expectation value for $|\widehat{x}_k|^2$. For a white-noise time series this expectation value is σ^2/N, where σ^2 is the variance. Thus, for a white noise process, the expectation value for the wavelet transform is $|W_n(s)|^2 = \sigma^2$ at all n and s.

Figure C.1b shows the normalized wavelet power spectrum, $|W_n(s)|^2/\sigma^2$, for the NINO3 SST time series. The normalization by $1/\sigma^2$ gives a measure of the power **relative to** white noise. In Fig. C.1b most of the power is concentrated within the El Niño-Southern Oscillation (ENSO) band of 2–8 years, although there is appreciable power at longer periods. The 2–8 year band for ENSO agrees with other studies (Trenberth 1976), and is also seen in the Fourier spectrum in Fig. C.3. With wavelet analysis, one can see variations in the frequency of occurrence and amplitude

of El Niño (warm) and La Niña (cold) events. During 1875–1920 and 1960–1990 there were many warm and cold events of large amplitude, while during 1920–1960 there were few events (Torrence and Webster 1997). From 1875–1910, there was a slight shift from a period near four years to a period closer to two years, while from 1960–1990 the shift is from shorter to longer periods.

These results are similar to those of Wang and Wang (1996), who used both wavelet and waveform analysis on ENSO indices derived from the COADS dataset. Wang and Wang's analysis showed reduced wavelet power before 1950, especially 1875–1920. The reduced power is possibly due to the sparseness and decreased reliability of the pre-1950 COADS data (Folland *et al.* 1984). With the GISST2.3 data, the wavelet transform of NINO3 SST in Fig. C.1b shows that the pre-1920 period has equal power to the post-1960 period.

C.3.5 Wavelet Functions One criticism of wavelet analysis is the arbitrary choice of the wavelet function, $\psi_0(\eta)$. (It should be noted that the same arbitrary choice is made in using one of the more traditional transforms such as the Fourier, Bessel, Legendre, etc.) In choosing the wavelet function, there are several factors which should be considered (for more discussion see Farge 1992):

(1) **Orthogonal or non-orthogonal**. In orthogonal wavelet analysis, the number of convolutions at each scale is proportional to the width of the wavelet basis at that scale. This produces a wavelet spectrum which contains discrete "blocks" of wavelet power, and is useful for signal processing as it gives the most compact representation of the signal. Unfortunately for time-series analysis, an

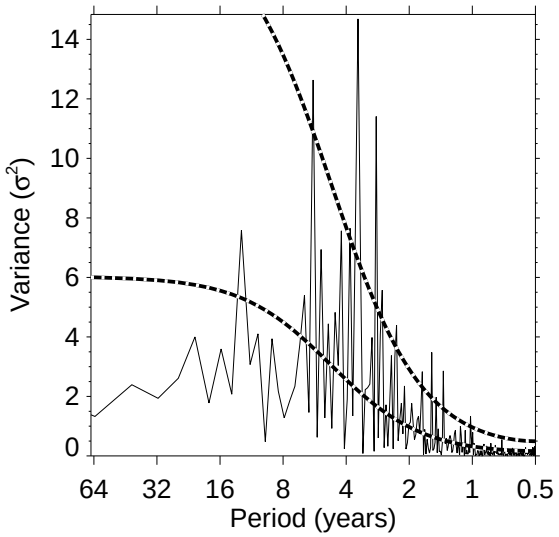

Figure C.3. Fourier power spectrum of NINO3 SST (solid), normalized by $N/(2\sigma^2)$. The lower dashed line is the mean red noise spectrum from (C.16) assuming a lag-1 of $\alpha = 0.72$. The upper dashed line is the 95% confidence spectrum.

aperiodic shift in the time series produces a different wavelet spectrum. Conversely, a non-orthogonal analysis (such as used in this study) is highly redundant at large scales, where the wavelet spectrum at adjacent times is highly correlated. The non-orthogonal transform is useful for time-series analysis where smooth, continuous variations in wavelet amplitude are expected.

(2) **Complex or real**. A complex wavelet function will return information about both amplitude and phase and is better adapted for capturing oscillatory behavior. A real wavelet function returns only a single component and can be used to isolate peaks or discontinuities.

(3) **Width**. For concreteness, the width of a wavelet function is defined here as the e-folding time of the wavelet amplitude. The resolution of a wavelet function is determined by the balance between the width in real space and the width in Fourier space. A narrow (in time) function will have good time resolution but poor frequency resolution, while a broad function will have poor time resolution yet high frequency resolution.

(4) **Shape**. The wavelet function should reflect the type of features present in the time series. For time series with sharp jumps or steps one would choose a boxcar-like function such as the Harr, while for smoothly-varying time series one would choose a smooth function such as a damped cosine. If one is primarily interested in wavelet power spectra, then the choice of wavelet function is not critical, and one function will give the same **qualitative** results as another (see discussion of Fig. C.1 below).

Four common non-orthogonal wavelet functions are given in Table C.1. The Morlet and Paul wavelets are both complex, while the DOG (derivatives of a Gaussian) are real-valued. Pictures of these wavelet in both the time and frequency

domain are shown in Fig. C.2. Many other types of wavelets exist such as the Haar and Daubechies, most of which are used for orthogonal wavelet analysis (e.g. Weng and Lau 1994; Mak 1995; Lindsay *et al.* 1996). For more examples of wavelet bases and functions see Kaiser (1994).

For comparison, Fig. C.1c shows the same analysis as in C.1b, but using the Mexican hat wavelet (DOG, m=2) rather than the Morlet. The most noticeable difference is the fine-scale structure using the Mexican hat. This is because the Mexican hat is real-valued, and captures both the positive and negative oscillations of the time series as separate peaks in wavelet power. The Morlet wavelet is both complex and contains more oscillations than the Mexican hat, and hence the wavelet power combines both positive and negative peaks into a single broad peak. A plot of the real or imaginary part of $W_n(s)$ using the Morlet would produce a plot similar to Fig. C.1c. Overall, the same features appear in both plots, approximately at the same locations, and with the same power. Comparing Figs. C.2a and c, the Mexican hat is narrower in time-space yet broader in spectral-space than the Morlet. Thus, in Fig. C.1c the peaks appear very sharp in the time direction, yet are more elongated in the scale direction. Finally, the relationship between wavelet scale and Fourier period is very different for the two functions (see section C.3.8).

C.3.6 Choice of Scales Once a wavelet function is chosen, it is necessary to choose a set of scales s to use in the wavelet transform (C.4). For an orthogonal wavelet one is limited to a discrete set of scales as given by Farge (1992). For non-orthogonal wavelet analysis, one can use an arbitrary set of scales to build up a more complete picture. It is convenient to write the scales as fractional powers of two:

$$s_j = s_0 2^{j\delta j}, \quad j = 0, 1, \ldots, J \tag{C.9}$$

$$J = \delta j^{-1} \log_2(N\delta t/s_0)\,, \tag{C.10}$$

where s_0 is the smallest resolvable scale, and J determines the largest scale. The s_0 should be chosen so that the equivalent Fourier period (see section C.3.8) is approximately $2\delta t$. The choice of a sufficiently small δj depends on the width in spectral-space of the wavelet function. For the Morlet wavelet a δj of about 0.5 is the largest value that still gives adequate sampling in scale, while for the other wavelet functions a larger value can be used. Smaller values of δj give finer resolution.

In Fig. C.1b, $N = 506$, $\delta t = 1/4$ year, $s_0 = 2\delta t$, $\delta j = 0.125$ and $J = 56$, giving a total of 57 scales ranging from 0.5 years up to 64 years. This value of δj appears adequate to provide a smooth picture of wavelet power.

C.3.7 Cone of Influence (COI) Because one is dealing with finite-length time series, errors will occur at the beginning and end of the wavelet power spectrum, as the Fourier transform in (C.4) assumes the data is cyclic. One solution is to pad the end of the time series with zeroes before doing the wavelet transform, and then remove them afterwards (for other possibilities such as cosine-damping see Meyers *et al.* 1993). In this study, the time series is padded with sufficient zeroes to bring the total length N up to the next-higher power of two, thus limiting the edge effects and speeding up the Fourier transform.

Padding with zeroes introduces discontinuities at the endpoints and, as one goes to larger scales, decreases the amplitude near the edges as more zeroes enter the analysis. The **cone of influence** (COI) is the region of the wavelet spectrum in which edge effects become important, and is defined here as the e-folding time for the autocorrelation of wavelet power at each scale (see Table C.1). This e-folding time is chosen so that the wavelet power for a discontinuity at the edge drops by a factor e^{-2}, and ensures that the edge effects are negligible beyond this point. For

cyclic series (such as a longitudinal strip at a fixed latitude), there is no need to pad with zeroes and there is no COI.

The size of the COI at each scale also gives a measure of the decorrelation time for a single spike in the time series. By comparing the width of a peak in the wavelet power spectrum with this decorrelation time, one can distinguish between a spike in the data (possibly due to random noise) and a harmonic component at the equivalent Fourier frequency.

The COI is indicated on Figs. C.1b and C.1c by the cross-hatched regions. The peaks within these regions have presumably been reduced in magnitude due to the zero padding. Thus, it is unclear whether the decrease in 2–8 year power after 1990 is a true decrease in variance or an artifact of the padding. Note that the much narrower Mexican hat wavelet in Fig. C.1c has a much smaller COI, and is thus less affected by edge effects.

C.3.8 Wavelet Scale and Fourier Frequency An examination of the wavelets in Figure C.2 shows that the peak in $\widehat{\psi}(s\omega)$ does not necessarily occur at a frequency of s^{-1}. Following the method of Meyers *et al.* (1993), the relationship between the **equivalent Fourier period** and the wavelet scale can be derived analytically for a particular wavelet function by substituting a cosine wave of a known frequency into (C.4) and computing the scale s at which the wavelet power spectrum reaches its maximum. For the Morlet wavelet with $\omega_0 = 6$ this gives a value of $\lambda = 1.03s$, where λ is the Fourier period, indicating that for the Morlet wavelet the wavelet scale is almost equal to the Fourier period. Formulae for other wavelet functions are given in Table C.1, while Fig. C.2 gives a graphical representation.

In Figs. C.1b, c the ratio of Fourier period to wavelet scale can be seen by

a comparison of the left and right axes. For the Morlet the two are nearly identical, while for the Mexican hat the Fourier period is four times larger than the scale. This ratio has no special significance, and is due solely to the functional form of each wavelet function. However, one should certainly convert from scale to Fourier period before plotting, as presumably one is interested in equating wavelet power at a certain time and scale with a (possibly short-lived) Fourier mode at the equivalent Fourier period.

C.3.9 Reconstruction Since the wavelet transform is a band-pass filter with a known response function (the wavelet function), it is possible to **reconstruct** the original time series using either deconvolution or the inverse filter. This is straightforward for the orthogonal wavelet transform (which has an orthogonal basis) but for the continuous wavelet transform it is complicated by the redundancy in time and scale. However, this redundancy also makes it possible to reconstruct the time series using a completely different wavelet function, the easiest of which is a delta (δ) function (Farge 1992). In this case, the reconstructed time series is just the sum of the real part of the wavelet transform over all scales:

$$x_n = \frac{\delta j \, \delta t^{1/2}}{C_\delta \, \psi_0(0)} \sum_{j=0}^{J} \frac{\Re\{W_n(s_j)\}}{s_j^{1/2}}. \tag{C.11}$$

The factor $\psi_0(0)$ removes the energy scaling, while the $s_j^{1/2}$ converts the wavelet transform to an energy density. The factor C_δ comes from the reconstruction of a δ-function from its wavelet transform using the function $\psi_0(\eta)$. This C_δ is a constant for each wavelet function, and is given in Table C.2. Note that if the original time series were complex, then the sum of the complex $W_n(s)$ would be used instead.

To derive C_δ for a new wavelet function, first assume a time series with a δ-function at time $n = 0$, given by $x_n = \delta_{n0}$. This time series has a Fourier transform

Table C.2: Empirically-derived factors for four wavelet bases.

Name	C_δ	γ	δj_0	$\psi_0(0)$
Morlet ($\omega_0 = 6$)	0.776	2.32	0.60	$\pi^{-1/4}$
Paul ($m = 4$)	1.132	1.17	1.5	1.079
Marr (DOG $m = 2$)	3.541	1.43	1.4	0.867
DOG ($m = 6$)	1.966	1.37	0.97	0.884

C_δ = reconstruction factor.
γ = decorrelation factor for time-averaging.
δj_0 = factor for scale-averaging.

$\widehat{x}_k = N^{-1}$, constant for all k. Substituting $\widehat{x}_k$ into (C.4), at time $n = 0$ (the peak) the wavelet transform becomes:

$$W_\delta(s) = \frac{1}{N} \sum_{k=0}^{N-1} \widehat{\psi}^*(s\omega_k). \tag{C.12}$$

The reconstruction (C.11) then gives:

$$C_\delta = \frac{\delta j \, \delta t^{1/2}}{\psi_0(0)} \sum_{j=0}^{J} \frac{\Re\{W_\delta(s_j)\}}{s_j^{1/2}}. \tag{C.13}$$

The C_δ is scale-independent and is a constant for each wavelet function.

The total energy is conserved under the wavelet transform, and the equivalent of **Parseval's theorem** for wavelet analysis is:

$$\sigma^2 = \frac{\delta j \, \delta t}{C_\delta N} \sum_{n=0}^{N-1} \sum_{j=0}^{J} \frac{|W_n(s_j)|^2}{s_j}, \tag{C.14}$$

where σ^2 is the variance, and a δ-function has been assumed for reconstruction. Both (C.11) and (C.14) should be used to check wavelet routines for accuracy and to ensure that sufficiently small values of s_0 and δj have been chosen.

For the NINO3 SST, the reconstruction of the time series from the wavelet transform has a mean-square error of 1.4%, or $0.087°$C.

C.4 Theoretical Spectrum and Significance Levels

To determine significance levels for either Fourier or wavelet spectra, one first needs to choose an appropriate background spectrum. It is then assumed that different realizations of the geophysical process will be randomly distributed about this mean or expected background, and the actual spectrum can be compared against this random distribution. For many geophysical phenomena, an appropriate background spectrum is either white noise (with a flat Fourier spectrum) or red-noise (increasing power with decreasing frequency).

A previous study by Qiu and Er (1995) derived the mean and variance of the local wavelet power spectrum. In this section the theoretical white and red noise wavelet power spectra are derived, and compared to Monte Carlo results. These spectra are used to establish a **null hypothesis** for the significance of a peak in the wavelet power spectrum.

C.4.1 Fourier Red Noise Spectrum Many geophysical time series can be modeled as either white noise or red noise. A simple model for red noise is the univariate lag-1 autoregressive (AR(1), or Markov) process:

$$x_n = \alpha x_{n-1} + z_n, \tag{C.15}$$

where α is the assumed lag-1 autocorrelation, $x_0 = 0$, and z_n is taken from Gaussian white noise. Following Gilman *et al.* (1963), the discrete Fourier power spectrum of (C.15) is:

$$P_k = \frac{1-\alpha^2}{1+\alpha^2-2\alpha\cos(2\pi k/N)}, \tag{C.16}$$

where $k = 0 \ldots N/2$ is the frequency index. Thus, by choosing an appropriate lag-1 autocorrelation, one can use (C.16) to model a red-noise spectrum. Note that $\alpha = 0$ in (C.16) gives a white-noise spectrum.

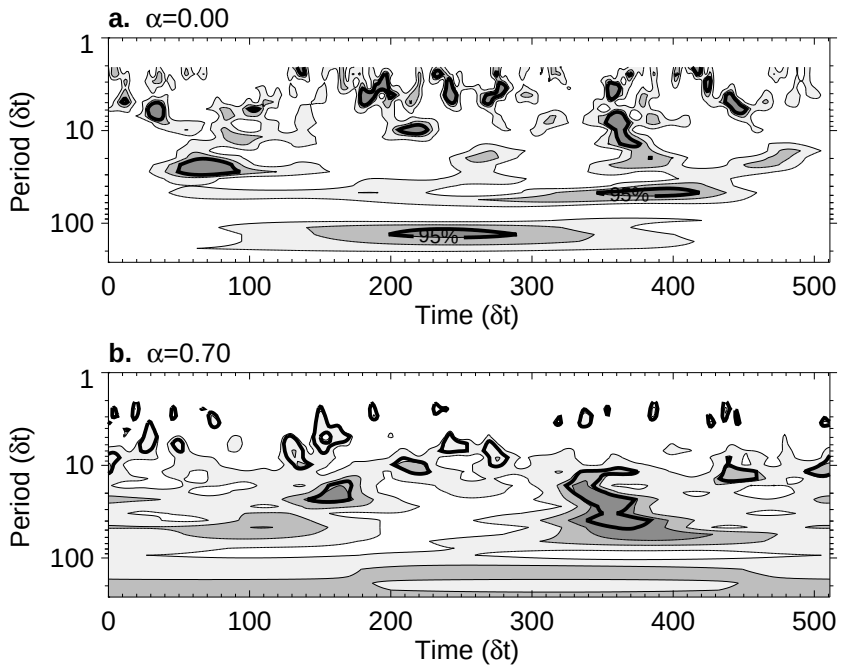

Figure C.4. (a) The local wavelet power spectrum for a Gaussian white noise process of 512 points, one of the 100,000 used for the Monte Carlo simulation. The power is normalized by $1/\sigma^2$, and contours are at 1, 2, and 3. The thick contour is the 95% confidence level for white noise. (b) Same as (a) but for a red-noise AR(1) process with lag-1 of 0.70. The contours are at 1, 5, and 10. The thick contour is the 95% confidence level for the corresponding red-noise spectrum.

The Fourier power spectrum for the NINO3 SST is shown by the thin line in Fig. C.3. The spectrum has been normalized by $N|\widehat{x}_k|^2/\sigma^2$, where N is the number of points and σ^2 is the variance of the time series. Using this normalization, white noise would have an expectation value of 1 at all frequencies. The red-noise background spectrum for $\alpha = 0.72$ is shown by the lower dotted curve in Fig. C.3. This red-noise was estimated from $(\alpha_1 + \sqrt{\alpha_2})/2$, where α_1 and α_2 are the lag-1 and lag-2 autocorrelations of the NINO3 SST. One can see the broad set of ENSO peaks between 2–8 years, well above the background spectrum.

C.4.2 Wavelet Red Noise Spectrum The wavelet transform in (C.4) is a series of band-pass filters of the time series. If this time series can be modeled as a lag-1 AR process, then it seems reasonable that the **local wavelet power spectrum**, defined as a vertical slice through Fig. C.1b, is given by (C.16). To test this hypothesis, 100,000 Gaussian white noise time series and 100,000 AR(1) time series were constructed, along with their corresponding wavelet power spectra. Examples of these white and red noise wavelet spectra are shown in Fig. C.4. The local wavelet spectra were constructed by taking vertical slices at time $n = 256$. The lower smooth curves in Figs. C.5a and C.5b show the theoretical spectra from (C.16). The dots show the results from the Monte Carlo simulation. On average, the local wavelet power spectrum is identical to the Fourier power spectrum given by (C.16).

Therefore, the lower dashed curve in Fig. C.3 also corresponds to the red-noise local wavelet spectrum. A random vertical slice in Fig. C.1b, would be **expected** to have a spectrum given by (C.16). As will be shown in section C.5.1, the average of all the local wavelet spectra tends to approach the (smoothed) Fourier spectrum of the time series.

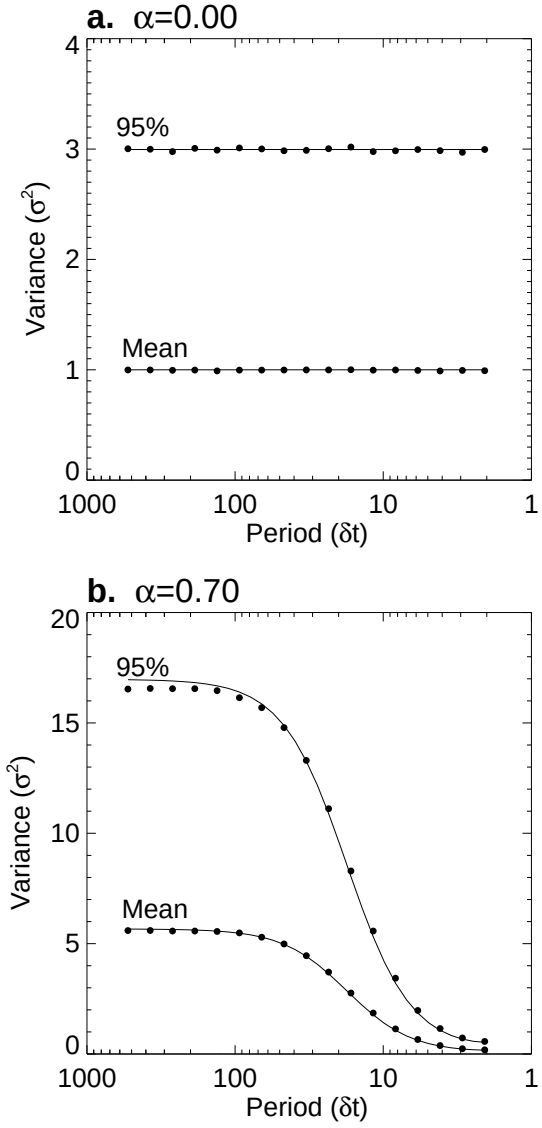

Figure C.5. (a) Monte Carlo results for local wavelet spectra of white noise ($\alpha = 0.0$). The lower thin line is the theoretical mean white-noise spectrum, while the black dots are the mean at each scale of 100,000 local wavelet spectra. The local wavelet spectra were slices taken at time $n = 256$ out of $N = 512$ points. The top thin line is the 95% confidence level, equal to $\chi^2_2(95\%)$ times the mean spectrum. The black dots are the 95% level from the Monte Carlo runs. (b) Same as (a) but for red noise of $\alpha = 0.70$.

C.4.3 Significance Levels The null hypothesis is defined for the wavelet power spectrum as follows: It is assumed that the time series has a mean power spectrum, possibly given by (C.16); if a peak in the wavelet power spectrum is significantly above this background spectrum, then it can be assumed to be a true feature with a certain percent confidence. For definitions, "significant at the 5% level" is equivalent to "the 95% confidence level", and implies a test against a certain background level, while the "95% confidence **interval**" refers to the range of confidence about a given value.

The normalized Fourier power spectrum in Fig. C.3 is given by $N|\widehat{x}_k|^2/\sigma^2$, where N is the number of points, $\widehat{x}_k$ is from (C.3), and σ^2 is the variance of the time series. If x_n is a normally distributed random variable, then both the real and imaginary parts of $\widehat{x}_k$ are normally distributed (Chatfield 1989). Since the square of a normally-distributed variable is chi-square distributed with one **degree of freedom** (DOF), then $|\widehat{x}_k|^2$ is chi-square distributed with two DOF, denoted by χ^2_2 (Jenkins and Watts 1968). To determine the 95% confidence level (significant at 5%), one multiplies the background spectrum (C.16) by the 95th percentile value for χ^2_2 (Gilman *et al.* 1963). The 95% Fourier confidence spectrum for the NINO3 SST is the upper dashed curve in Fig. C.3. Note that only a few frequencies now have power above the 95% line.

In the previous section, it was shown that the local wavelet spectrum follows the mean Fourier spectrum. If the original Fourier components are normally distributed, then the wavelet coefficients (the band-passed inverse Fourier components) should also be normally distributed. If this is true then the wavelet power spectrum, $|W_n(s)|^2$, should be χ^2_2 distributed. The upper curves in Figs. C.5a and C.5b show the 95% Fourier red-noise confidence level versus the 95% level from the

Monte Carlo results of the previous section. Thus, at each point (n, s) in Fig. C.1b, assuming a red-noise process, the distribution is χ^2_2. Note that for a wavelet transform using a real-valued function, such as the Mexican Hat shown in Fig. C.1c, there is only one degree of freedom at each point, and the distribution is χ^2_1.

In summary, assuming a mean background spectrum, possibly red noise (C.16), the distribution for the **Fourier power spectrum** is:

$$\frac{N|\widehat{x}_k|^2}{\sigma^2} \Rightarrow \frac{1}{2} P_k \chi^2_2, \tag{C.17}$$

at each frequency index k, and "$\Rightarrow$" indicates "is distributed as". The corresponding distribution for the **local wavelet power spectrum** is:

$$\frac{|W_n(s)|^2}{\sigma^2} \Rightarrow \frac{1}{2} P_k \chi^2_2, \tag{C.18}$$

at each time n and scale s. The $1/2$ removes the DOF factor from the χ^2 distribution. (For a real wavelet the distribution on the right-hand-side would be $P_k \chi^2_1$). The value of P_k in (C.18) is the mean spectrum at the Fourier frequency k that corresponds to the wavelet scale s (see section C.3.8). Aside from the relation between k and s, Eqn. (C.18) is independent of the wavelet function. After finding an appropriate background spectrum, and choosing a particular confidence for χ^2 such as 95%, one can then calculate (C.18) at each scale and construct 95% confidence contour lines.

As with Fourier analysis, smoothing the wavelet power spectrum can be used to increase the DOF and enhance confidence in regions of significant power. Unlike Fourier, smoothing can be performed in either the time or scale domain. Significance levels and DOF for smoothing in time or scale are discussed in section C.5.

Inside the COI, the distribution is still χ^2, but if the time series has been padded with zeroes, then the mean spectrum is reduced by a factor of $(1 - \frac{1}{2} e^{-2t/\tau_s})$,

where τ_s is from Table C.1 and t is the distance (in time) from either the beginning or end of the wavelet power spectrum.

The 95% confidence level for the NINO3 SST is shown by the thick contours on Figs. C.1b and C.1c. During 1875–1910 and 1960–1990 the variance in the 2–8 year band is significantly above the 95% confidence for red noise. During 1920–1960 there are a few isolated significant regions, primarily around two years, and at the edge of the usual 2–8 year ENSO band. The 95% confidence implies that 5% of the wavelet power should be above this level. In Fig. C.4b, approximately 5% of the points are contained within the 95% contours. For the NINO3 wavelet spectrum 4.9% of the points are above 95%, implying that for the NINO3 time series a test of enclosed area cannot distinguish between noise and signal. However, the spatial distribution of variance can also be examined for randomness. In Fig. C.4b the variance shows a gradual increase with period, with random distributions of high and low variance about this mean spectrum. In Figs. C.1b and c the significant regions are clustered together in both period and time, indicating less randomness of the underlying process.

C.4.4 Confidence Interval The **confidence interval** is defined as the probability that the true wavelet power at a certain time and scale lies within a certain interval about the estimated wavelet power. Rewriting (C.18) as:

$$\frac{|W_n(s)|^2}{\sigma^2 P_k} \Rightarrow \frac{\chi_2^2}{2}, \tag{C.19}$$

one can then replace the theoretical wavelet power $\sigma^2 P_k$ with the **true wavelet power**, defined as $\mathcal{W}_n^2(s)$. The confidence interval for $\mathcal{W}_n^2(s)$ is then:

$$\frac{2}{\chi_2^2(p/2)}|W_n(s)|^2 \leq \mathcal{W}_n^2(s) \leq \frac{2}{\chi_2^2(1-p/2)}|W_n(s)|^2, \tag{C.20}$$

where p is the desired significance ($p = 0.05$ for the 95% confidence interval) and $\chi^2_2(p/2)$ represents the value of χ^2 at $p/2$. Note that for real-valued wavelet functions, the right-hand side of (C.19) becomes χ^2_1, and the factor of 2 is removed from the top of (C.20). Using (C.20) one can then find confidence intervals for the peaks in a wavelet power spectrum, to compare against either the mean background or against other peaks.

C.4.5 Stationarity It has been argued that wavelet analysis requires the use of non-stationary significance tests (Lau and Weng 1995). In defense of the use of stationary tests such as those given above, the following points are noted:

(1) A non-arbitrary test is needed. The assumption of stationary statistics provides a standard by which any non-stationarity can be detected.

(2) The test should be robust. It should not depend upon the wavelet function or upon the actual distribution of the time series, other than the assumption of a background spectrum.

(3) A non-Monte Carlo method is preferred. In addition to the savings in computation, the chi-square test simplifies comparing one wavelet transform with another.

(4) Many wavelet transforms of real data appear similar to transforms of red-noise processes (compare Figs. C.1b and C.4b). It is therefore difficult to argue that large variations in wavelet power imply non-stationarity.

(5) One needs to ask what is being tested. Is it non-stationarity? Or low-variance versus high-variance periods? Or changes in amplitude of Fourier modes? The chi-square test gives a standard measure for any of these possibilities.

In short, it appears wiser to assume stationarity and design the statistical tests accordingly. If the tests show large deviations, such as the changes in ENSO variance seen

in Fig. C.1b and c, then further tests can be devised for the particular time series.

C.5 Smoothing in Time and Scale

C.5.1 Averaging in Time (Global Wavelet Spectrum) If a vertical slice through a wavelet plot is a measure of the local spectrum, then the **time-averaged wavelet spectrum** over a certain period is:

$$\overline{W}_n^2(s) = \frac{1}{n_a} \sum_{n=n_1}^{n_2} |W_n(s)|^2, \tag{C.21}$$

where the new index n is arbitrarily assigned to the midpoint of n_1 and n_2, and $n_a = n_2 - n_1 + 1$ is the number of points averaged over. By repeating (C.21) at each time step, one creates a wavelet plot smoothed by a certain window.

The extreme case of (C.21) is when the average is over all the local wavelet spectra, which gives the **global wavelet spectrum**:

$$\overline{W}^2(s) = \frac{1}{N} \sum_{n=0}^{N-1} |W_n(s)|^2. \tag{C.22}$$

In Fig. C.6, the thick solid line shows the normalized global wavelet spectrum, $\overline{W}^2(s)/\sigma^2$, for the NINO3 SST. The thin solid line in Fig. C.6 shows the same spectrum as in Fig. C.3, but smoothed with a 5-point running average. Note that as the Fourier spectrum is smoothed, it approaches the global wavelet spectrum more and more closely, with the amount of necessary smoothing decreasing with increasing scale. A comparison of Fourier spectra and wavelet spectra can be found in Hudgins *et al.* (1993), while a theoretical discussion is given in Perrier *et al.* (1995). Percival (1995) shows that the global wavelet spectrum provides an unbiased and consistent estimation of the true power spectrum of a time series. Finally, it has been suggested that the global wavelet spectrum could provide a useful measure of the background spectrum, against which peaks in the local wavelet spectra could be tested (Kestin *et al.* 1998).

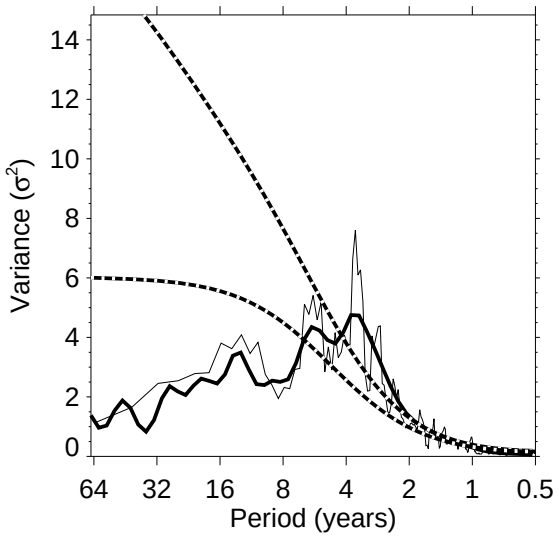

Figure C.6. Fourier power spectrum from Fig. C.3, smoothed with a 5-point running average (thin solid line). The thick solid line is the global wavelet spectrum for the NINO3 SST. The lower dashed line is the mean red-noise spectrum, while the upper dashed line is the 95% confidence level for the global wavelet spectrum, assuming $\alpha = 0.72$.

By smoothing the wavelet spectrum using (C.21), one can increase the degrees of freedom of each point and increase the significance of peaks in wavelet power. To determine the degrees of freedom (DOF), one needs the number of independent points. For the Fourier spectrum (Fig. C.3), the power at each frequency is independent of the others, and the average of the power at M frequencies, each with two DOF, is χ^2 distributed with $2M$ degrees of freedom (Spiegel 1975). For the time-averaged wavelet spectrum, one is also averaging points that are χ^2_2 distributed, yet Figs. C.1b and C.4 suggest that these points are no longer independent, but are correlated in both time and scale. Furthermore, the correlation in time appears to lengthen as scale increases and the wavelet function broadens. Designating ν as the degrees of freedom (DOF), one expects $\nu \propto n_a$ and $\nu \propto s^{-1}$. The simplest formula to consider is to define a decorrelation length $\tau = \gamma s$ such that $\nu = 2n_a \delta t/\tau$. However, Monte Carlo results show that this τ is too abrupt at small n_a or large scales; even though one is averaging points which are highly correlated, some additional information is gained.

The Monte Carlo results are given in Fig. C.7, which shows the mean and 95% levels for various n_a. These curves are best described by the distribution $P_k \chi^2_\nu/\nu$, where P_k is the original assumed background spectrum, and χ^2_ν is the chi-square distribution with ν degrees of freedom, where

$$\nu = 2\sqrt{1 + \left(\frac{n_a \delta t}{\gamma s}\right)^2}. \tag{C.23}$$

Note that for a real-valued function such as the Mexican hat, each point only has one DOF, and the factor of 2 in (C.23) is removed. The decorrelation factor γ is determined empirically by an iterative fit of absolute error to the 95% Monte Carlo level, and is given in Table C.2 for the four wavelet functions. The relative error (or percent difference) between the Monte Carlo and the χ^2_ν/ν distribution was everywhere

less than 7% for all scales and n_a values. The thin lines in Fig. C.7 show the results of (C.23) using the Morlet wavelet. Note that even the white noise process has more stringent 95% confidence levels at large scales compared to small. As a final note, if the points going into the average are within the cone of influence, then n_a is reduced by approximately one half of the number within the COI, to reflect the decreased amplitude (and information) within that region.

A different definition of the global wavelet spectrum, involving the discrete wavelet transform and including a discussion of confidence intervals, is given by Percival (1995). An example using Percival's definition can be found in Lindsay *et al.* (1996).

The 95% confidence line for the NINO3 global wavelet spectrum is shown by the dashed line in Fig. C.6. Only the broad ENSO peak remains significant, although note that power at other periods can be less than significant globally, but still show significant peaks in local wavelet power.

C.5.2 Averaging in Scale To examine fluctuations in power over a range of scales (a band), one can define the **scale-averaged wavelet power** as the weighted sum of the wavelet power spectrum over scales s_1 to s_2:

$$\overline{W}_n^2 = \frac{\delta j \, \delta t}{C_\delta} \sum_{j=j_1}^{j_2} \frac{|W_n(s_j)|^2}{s_j}. \tag{C.24}$$

Comparing (C.24) and (C.14), the scale-averaged wavelet power is a time series of the average variance in a certain band. Thus the scale-averaged wavelet power can be used to examine modulation of one time series by another, or modulation of one frequency by another within the same time series.

As an example of averaging over scale, Fig. C.8 shows the average of Fig. C.1b over all scales between 2–8 years (actually 2–7.34 years), which gives a measure of the average ENSO variance versus time. The variance plot shows a

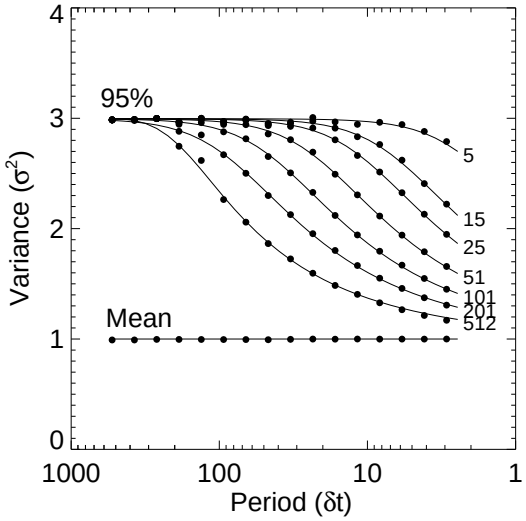

Figure C.7. Monte Carlo results for the time-averaged wavelet spectra (C.21) of white noise using the Morlet wavelet. The numbers to the right of each curve indicate n_a, the number of times that were averaged, while the black dots are the 95% level for the Monte Carlo runs. The top thin lines are the 95% confidence from (C.23). The lower thin line is the mean white-noise spectrum, while the black dots are the means of the Monte Carlo runs (all of the means are identical).

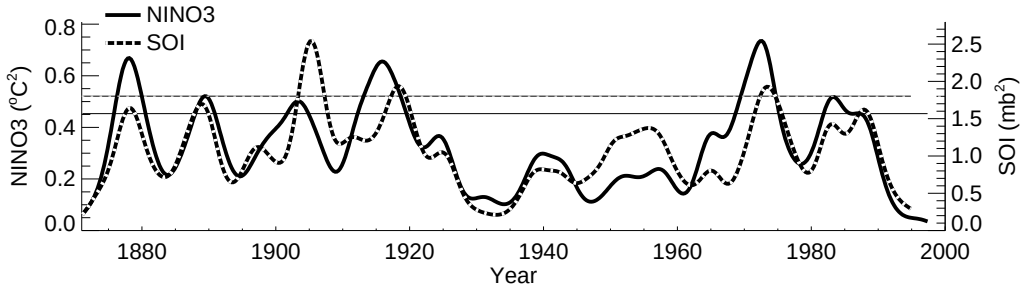

Figure C.8. Scale-averaged wavelet power (C.24) over the 2–8 year band for the NINO3 SST (solid) and the SOI (dashed). The thin solid line is the 95% confidence level from (C.26) for NINO3 SST (assuming red-noise $\alpha = 0.72$), while the thin dashed line is the 95% level for the SOI (red noise $\alpha = 0.61$).

distinct period between 1920–1960 when ENSO variance was low. Also shown in Fig. C.8 is the variance in the Southern Oscillation Index (SOI), which correlates well with the changes in NINO3 SST variance (0.72 correlation). Both time series show consistent interdecadal changes, including a possible modulation in ENSO variance with a 15-year period. To examine more closely the relation between NINO3 SST and the SOI, one could use the cross-wavelet spectrum (see section C.6.3).

As with time-averaged wavelet spectrum, the degrees of freedom (DOF) are increased by smoothing in scale, and an analytical relationship for significance levels for the scale-averaged wavelet power is desirable. Again, it is convenient to normalize the wavelet power by the expectation value for a white noise time series. From (C.24), this expectation value is $(\delta j\, \delta t\, \sigma^2)/(C_\delta\, S_{avg})$, where σ^2 is the time-series variance and S_{avg} is defined as:

$$S_{avg} = \left(\sum_{j=j_1}^{j_2} \frac{1}{s_j} \right)^{-1} . \tag{C.25}$$

The black dots in Fig. C.9 show the Monte Carlo results for both the mean and the 95% level of scale-averaged wavelet power as a function of various n_a, where $n_a = j_2 - j_1 + 1$ is the number of scales averaged. Using the normalization factor for white-noise, the distribution can be modeled as:

$$\frac{C_\delta\, S_{avg}}{\delta j\, \delta t\, \sigma^2}\, \overline{W}_n^2 \Rightarrow \overline{P}_k \frac{\chi_\nu^2}{\nu}, \tag{C.26}$$

where the scale-averaged theoretical spectrum is now given by:

$$\overline{P}_k = S_{avg} \sum_{j=j_1}^{j_2} \frac{P_k}{s_j}. \tag{C.27}$$

Note that for white noise this spectrum is still unity (due to the normalization). The degrees of freedom ν in (C.26) is modeled as:

$$\nu = \frac{2 n_a S_{avg}}{S_{mid}} \sqrt{1 + \left(\frac{n_a \delta j}{\delta j_0} \right)^2}, \tag{C.28}$$

where $S_{mid} = s_0 2^{0.5(j_1+j_2)\delta j}$. The factor S_{avg}/S_{mid} corrects for the loss of DOF that arises from dividing the wavelet power spectrum by scale in (C.24) and is observed in the Monte Carlo results. Note that for a real-valued function such as the Mexican hat, each point only has one DOF, and the factor of 2 in (C.28) is removed. The decorrelation distance δj_0 is determined empirically by an iterative fit of absolute error between (C.28) and the 95% level of the Monte Carlo results, and is given in Table C.2. The thin lines in Fig. C.9 show the results of (C.28) for the Morlet, Paul $(m = 4)$, DOG2, and DOG6 wavelet functions. For these wavelets, the relative error between the χ^2_ν distribution using (C.28) and the Monte Carlo results is less than 1.5%. It should be noted that (C.28) is valid only for confidences of 95% or less. At higher confidence levels the distribution begins to deviate significantly from χ^2, and (C.28) is no longer valid.

In Fig. C.8 the thin solid and dashed lines show the 95% confidence levels for the NINO3 SST and the SOI using (C.25)–(C.28). In this case, $\delta j = 0.125$, the sum was between periods 2–8 years (actually 2.1–7.6 years), $n_a = 16$, $S_{avg} = 0.221 years$, $S_{mid} = 3.83 years$, $\delta j_0 = 0.60$, and $\nu = 6.44$. Since the two time series do not have the same variance or the same red-noise background, the 95% lines are not equal.

C.6 Extensions to Wavelet Analysis

C.6.1 Filtering As discussed in section C.3.9, the wavelet transform (C.4) is essentially a band-pass filter of uniform shape and varying location and width. By summing over a subset of the scales in (C.11), one can construct a **wavelet-filtered** time series:

$$x'_n = \frac{\delta j \, \delta t^{1/2}}{C_\delta \, \psi_0(0)} \sum_{j=j_1}^{j_2} \frac{\Re\{W_n(s_j)\}}{s_j^{1/2}}. \tag{C.29}$$

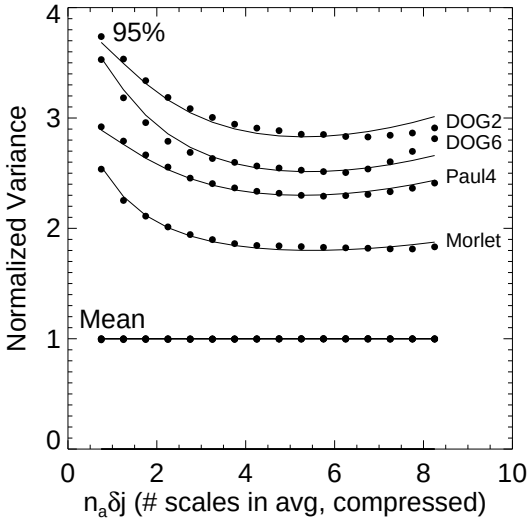

Figure C.9. Monte Carlo results for the wavelet spectra averaged over n_a scales from (C.24), using white noise. The average from (C.24) is centered on scale $s = 16\delta t$ for convenience, but the results are independent of the center scale. To make the graph independent of the choice for δj, the x-axis has been compressed by the Monte Carlo δj of 0.25. The top black dots are the 95% level for the Monte Carlo runs, while the lower black dots are the means. The means for all four wavelet bases are all the same, while the 95% level depends on the width of the basis in Fourier space, with the Morlet being the most narrow. The top thin lines are the 95% confidence from (C.28). The lower thin line is the mean white-noise spectrum.

This filter has a response function given by the sum of the wavelet functions between scales j_1 and j_2.

This filtering can also done on both the scale and time simultaneously by defining a threshold of wavelet power. This "de-noising" removes any low-amplitude regions of the wavelet transform which are presumably due to noise. This technique has the advantage over traditional filtering in that it removes noise at all frequencies, and can be used to isolate single events which have a broad power spectrum or multiple events which have varying frequency. A more complete description including examples is given in Donoho and Johnstone (1994).

Another filtering technique involves the use of the two-dimensional wavelet transform. An example can be found in Farge *et al.* (1992), where two-dimensional turbulent flows are "compressed" using an orthonormal wavelet packet. This compression removes the low-amplitude "passive" components of the flow, while retaining the high-amplitude "dynamically-active" components.

C.6.2 Power Hovmöller By scale-averaging the wavelet power spectra at multiple locations, one can assess the spatial and temporal variability of a field of data. Figure C.10a shows a **power hovmöller** (time-longitude diagram) of the wavelet variance for sea level pressure (SLP) anomalies in the 2–8 year band at each longitude. The original time series at each longitude is the average SLP between 5°S and 15°S. At each longitude the wavelet power spectrum is computed using the Morlet wavelet, and the scale-averaged wavelet power over the 2–8 year band is calculated from (C.24). The average-wavelet-power time series are combined into a two-dimensional contour plot as shown in Fig. C.10a. The 95% confidence level is computed using the lag-1 autocorrelation at each longitude and Eqn. (C.26).

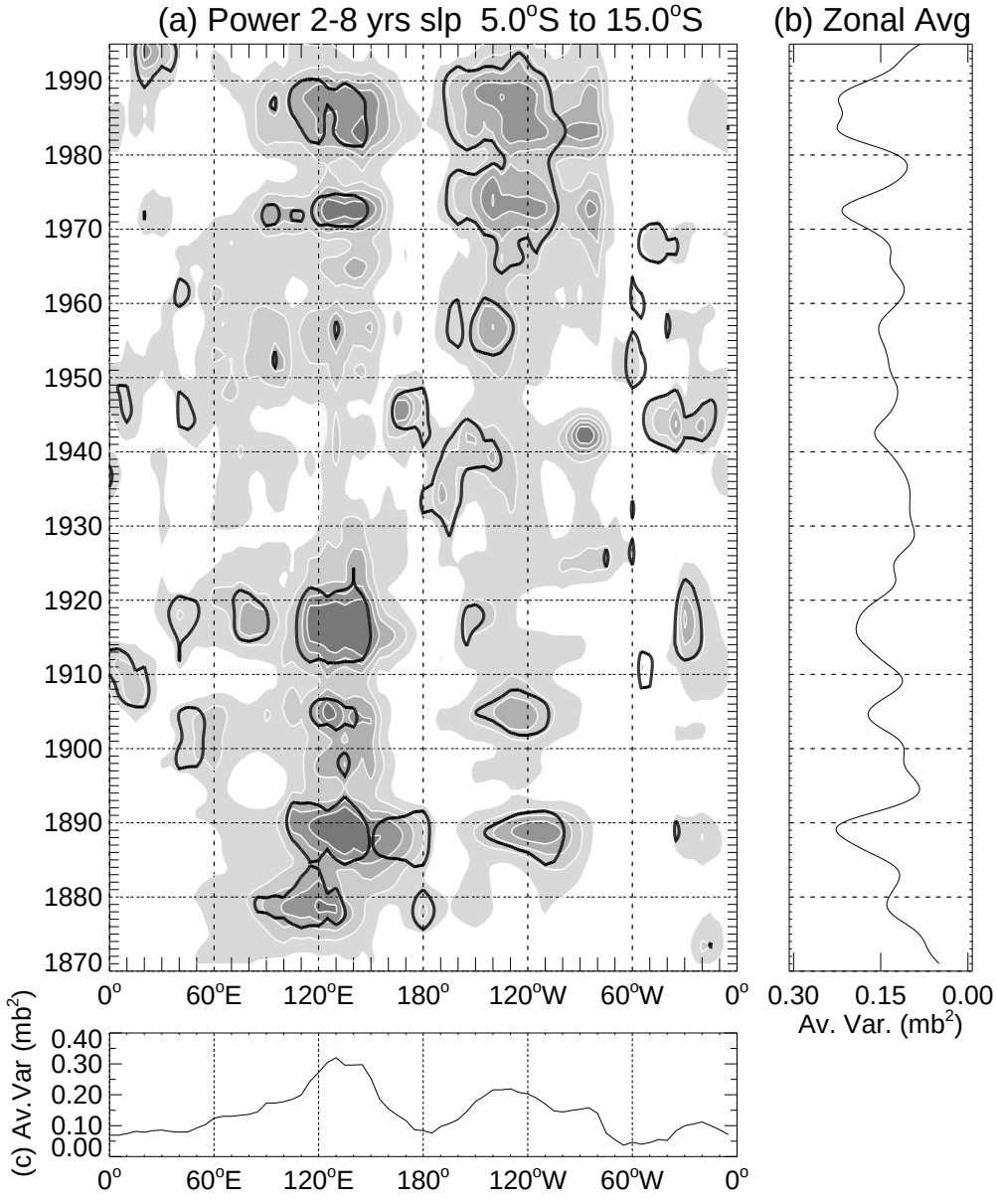

Figure C.10. (a) Power hovmöller of 2–8 year averaged wavelet power in SLP. The original time series at each longitude is the average SLP between 5°S and 15°S. The contour interval is 0.1 mb^2. The thick contour is the 95% confidence level, using the corresponding red-noise spectrum at each longitude. (b) The average of (a) over all longitudes. (c) The average of (a) over all times.

Several features of Fig. C.10 demonstrate the usefulness of wavelet analysis. Fig. C.10c shows the time-averaged 2–8 year power as a function of longitude. Broad local maxima at 130°E and 110°W reflect the power associated with the Southern Oscillation. This longitudinal distribution of power is also observed in the 2–8 year band for Fourier spectra at each longitude (not shown). The zonal average of the power hovmöller (Fig. C.10b), gives a measure of global 2–8 year variance in this latitude band. Comparing this to Fig. C.8, one can see that the peaks in zonal-average power are associated with the peaks in NINO3 SST variance, and hence, the 2–8 year power is dominated in this latitude band by ENSO.

With the power hovmöller in Fig. C.10a, the temporal variations in ENSO-associated SLP fluctuations can be seen. While the low power near the dateline region is apparent throughout the record, the high power regions fluctuate on inter-decadal time-scales. From the 1870's to the 1920's, strong decadal fluctuations in 2–8 year power are observed in the Australian region. In contrast, the eastern Pacific fluctuations are strong only through 1910 and appear to have little power in the 1915 to 1930 period. The generally low power observed in Figs. C.1 and C.8 between 1930 and 1950 mainly reflects a lack of power in the Australian region, with the eastern Pacific having some significant fluctuations in the 1940s. The large-zonal-scale fluctuations in both regions return in the 1950s, with the strongest amplitudes after 1970. The diminished power after 1990 is within the COI, yet may reflect the changes in ENSO structure and evolution seen in recent years (Wang 1995).

C.6.3 Cross-Wavelet Spectrum Given two time series X and Y, with wavelet transforms $W_n^X(s)$ and $W_n^Y(s)$, one can define the **cross-wavelet spectrum** as $W_n^{XY}(s) = W_n^X(s)W_n^{Y*}(s)$, where $W_n^{Y*}(s)$ is the complex conjugate of

$W_n^Y(s)$. The cross-wavelet spectrum is complex, and hence one can define the **cross-wavelet power** as $|W_n^{XY}(s)|$.

Confidence levels for the cross-wavelet power can be derived from the square-root of the product of two chi-square distributions (Jenkins and Watts 1968). Assuming both wavelet spectra are χ^2 distributed with ν DOF, the probability distribution is given by:

$$f_\nu(z) = \frac{2^{2-\nu}}{\Gamma^2\left(\frac{\nu}{2}\right)} z^{\nu-1} \mathrm{K}_0(z), \tag{C.30}$$

where z is the random variable, Γ is the Gamma function, and $\mathrm{K}_0(z)$ is the modified Bessel function of order zero. The cumulative distribution function is given by the integral, $p = \int_0^{Z_\nu(p)} f_\nu(z)\, dz$, where $Z_\nu(p)$ is the confidence level associated with probability p. Given a probability p, this integral can be inverted to find the confidence level $Z_\nu(p)$.

If the two time series have theoretical Fourier spectra P_k^X and P_k^Y, say from (C.16), then the cross-wavelet distribution is

$$\frac{|W_n^X(s) W_n^{Y*}(s)|}{\sigma_X \sigma_Y} \Rightarrow \frac{Z_\nu(p)}{\nu} \sqrt{P_k^X P_k^Y}, \tag{C.31}$$

where σ_X and σ_Y are the respective standard deviations. For $\nu = 1$ (real wavelets), $Z_1(95\%) = 2.182$, while for $\nu = 2$ (complex wavelets), $Z_2(95\%) = 3.999$.

Figure C.11a shows the wavelet power spectrum of NINO3 SST using the Paul ($m = 4$) wavelet, while Fig. C.11b shows the wavelet power for the Southern Oscillation Index (SOI). Note that the narrow width in time of the Paul gives better time localization than the Morlet, but poorer frequency localization. Finally, Fig. C.11c shows the cross-wavelet power for the NINO3 SST and the SOI, and indicates large covariance between the time series at all scales between 2–8 years. The 95% confidence level was derived using (C.31), and assuming red noise spectra (C.16) with $\alpha = 0.72$ for NINO3 SST and $\alpha = 0.61$ for the SOI.

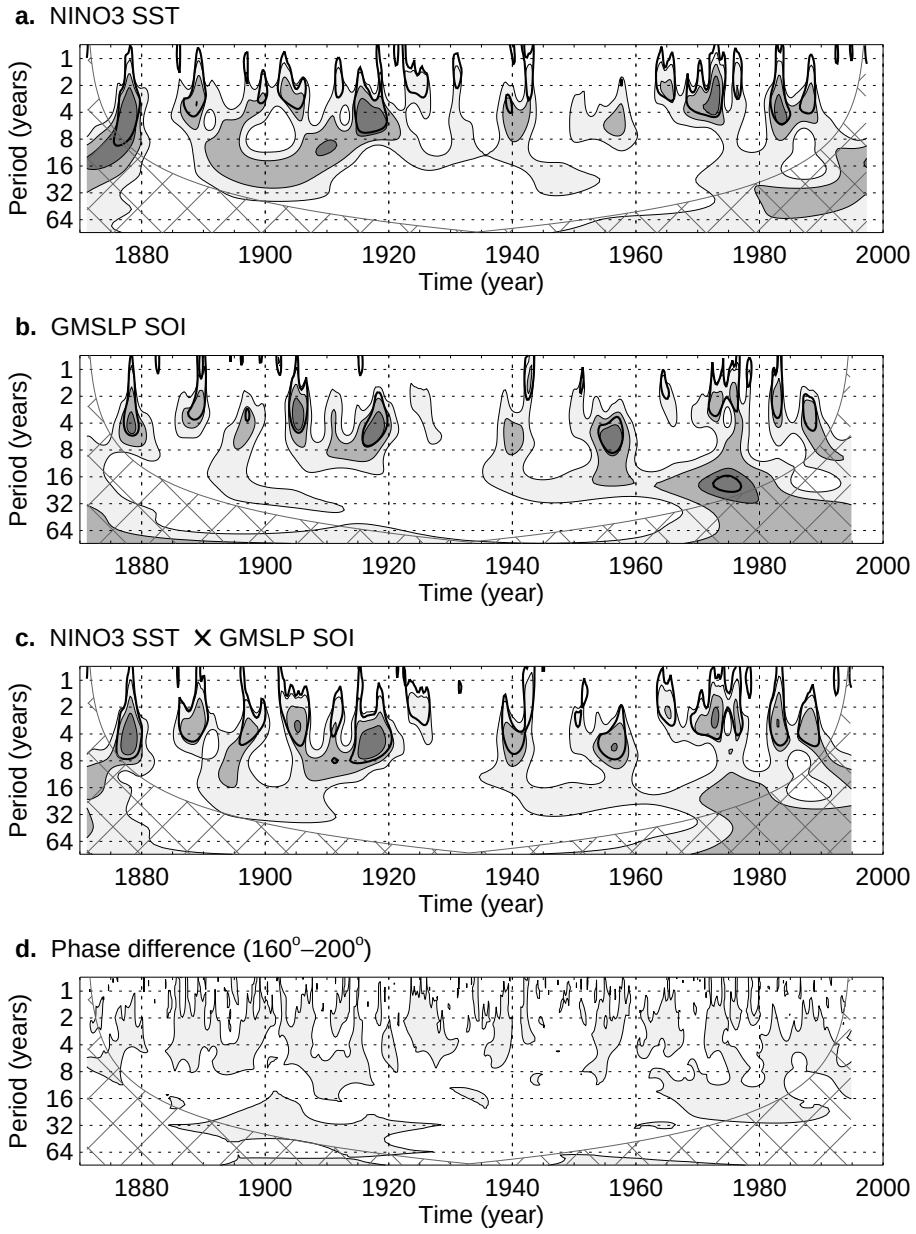

Figure C.11. (a) The wavelet spectrum for the NINO3 SST using the Paul ($m = 4$) wavelet. The contours are at normalized variance of 2, 5, and 10, while the thick contour is the 95% confidence level (red noise $\alpha = 0.72$). (b) Same as (a) but for the GMSLP SOI (red noise $\alpha = 0.61$). (c) The cross-wavelet power for the NINO3 SST and the SOI. Contours are at 2, 5, and 10, while the thick contour is the 95% confidence from (C.31), with the red noise given in (a) and (b). (d) The phase difference between NINO3 SST and the SOI, with the filled contour enclosing regions between 160°–200°.

C.6.4 Wavelet Coherence and Phase Another useful quantity from Fourier analysis is the **coherence**, defined as the square of the cross-spectrum normalized by the individual power spectra. This gives a quantity between 0 and 1, and measures the cross-correlation between two time series as a function of frequency. Unfortunately, as noted by Liu (1994), this coherence is identically one at all times and scales. In Fourier analysis this problem is circumvented by smoothing the cross-spectrum before normalizing. For wavelet analysis, it is unclear what sort of smoothing (presumably in time) should be done to give a useful measure of coherence. This smoothing would also seem to defeat the purpose of wavelet analysis by decreasing the localization in time. Liu (1994) suggests plotting the real and imaginary parts (the **co-** and **quadrature-** wavelet spectra) separately, and also plotting the **coherence phase**, defined as $\tan^{-1}(\Im\{W_n^{XY}(s)\}/\Re\{W_n^{XY}(s)\})$.

The co- and quadrature-wavelet spectra for the NINO3 SST and the SOI (not shown) do not appear to give any additional information, especially in conjunction with the coherence phase shown in Fig. C.11d. The shaded region in Fig. C.11d shows where the phase difference between NINO3 SST and the SOI is between 160° and 200°. It is well known that the NINO3 SST and the SOI are out of phase, yet this shows that the time series are within $\pm 20°$ of being 180° out of phase over all periods between 2–8 years. Furthermore, this out-of-phase behavior is consistent with changes in the cross-wavelet power, with periods of low variance, say between 1920–1960, associated with more random phase differences.

C.7 Summary

Wavelet analysis is a useful tool for analyzing time series with many different time scales or changes in variance. The steps involved in using wavelet analysis

are as follows:[2]

(1) Find the Fourier transform of the (possibly padded) time series,
(2) Choose a wavelet function and a set of scales to analyze,
(3) For each scale, construct the normalized wavelet function using (C.6),
(4) Find the wavelet transform at that scale using (C.4),
(5) Determine the cone-of-influence and the Fourier wavelength at that scale.
(6) After repeating steps 3–5 for all scales, remove any padding, and contour plot the wavelet power spectrum.
(7) Assume a background Fourier power spectrum (e.g. white or red noise) at each scale, then use the chi-squared distribution to find the 95% confidence (5% significance) contour.

For other methods of wavelet analysis such as the orthogonal wavelet transform see Farge (1992). The results presented in section C.4 on statistical significance testing are presumably valid for higher-dimensional wavelet analysis (assuming an appropriate background spectrum can be chosen), but this has not been tested and is left to future research. More research is also needed on the properties and usefulness of the cross-wavelet, wavelet coherence, and co- and quadrature-spectrum.

In the wavelet analysis of NINO3 sea surface temperature (SST), the Southern Oscillation Index (SOI), and the sea level pressure (SLP), it was found that the variance of the El Niño-Southern Oscillation changed on interdecadal time scales, with a period of low variance from 1920–1960. Using both the filtered 2–8 year variance and the cross-wavelet power, the changes in NINO3 SST variance appear to be well correlated with changes in the SOI. The SLP power hovmöller suggests that these changes are planetary in scale, while Torrence and Webster (1997) use wavelet analysis to show that interdecadal changes in ENSO are also related to

[2] Software and examples are available from the authors at URL: “http://paos.colorado.edu/research/wavelets/”.

changes in Indian monsoon variance. Further studies are necessary to determine the extent and possible causes of these interdecadal changes.

It is hoped that the analysis presented here will prove useful in studies of non-stationarity in time series, and the addition of statistical significance tests will improve the quantitative nature of wavelet analysis. Future studies using wavelet analysis can then concentrate on the results rather than simply the method.